# Misfit Induced Elastic Strain at Interfaces and its Impact on Ionic Conductivity

## An Investigation on Thin Film Multilayers

Vom Fachbereich Biologie und Chemie genehmigte

**Dissertation**

von
**Dipl.-Chem. Nicole Schichtel**
geboren am 09.12.1981 in Dillenburg

angefertigt am
Physikalisch-Chemischen Institut
der Justus-Liebig-Universität Gießen
unter Anleitung von
Prof. Dr. rer. nat. Jürgen Janek

Gießen 2010

# Misfit Induced Elastic Strain at Interfaces and its Impact on Ionic Conductivity

## An Investigation on Thin Film Multilayers

Vom Fachbereich Biologie und Chemie genehmigte

**Dissertation**

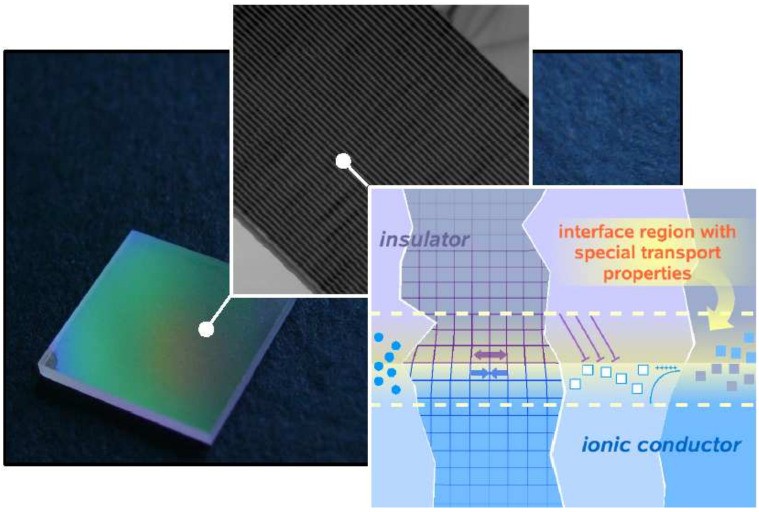

von
**Dipl.-Chem. Nicole Schichtel**
geboren am 09.12.1981 in Dillenburg

angefertigt am
Physikalisch-Chemischen Institut
der Justus-Liebig-Universität Gießen
unter Anleitung von
Prof. Dr. rer. nat. Jürgen Janek

Gießen 2010

| | |
|---|---|
| Dekan | Prof. Dr. Volkmar Wolters |
| | |
| 1. Gutachter | Prof. Dr. Jürgen Janek |
| 2. Gutachter | P.D. Dr. Carsten Korte |

Arbeit eingereicht am 12. April 2010
Tag der mündlichen Prüfung: 10. Juni 2010

“We’re so busy watching out for what’s just ahead of us that we don’t take time to enjoy where we are.”

Calvin from Bill Watterson´s “Calvin & Hobbes”

# Acknowledgement

- First of all, my thanks go to Prof. Dr. Jürgen Janek for offering me the opportunity for my PHD in the Institute of Physical Chemistry, JLU Gießen and to PD Dr. Carsten Korte, who supervised my work and helped to solve all kinds of difficult problems.
- Many thanks appertain to Prof. Dr. Dietrich Hesse and Dr. Nikolai Zakharov, Max-Planck-Institut für Mikrostrukturphysik Halle, for numerous TEM and HRTEM measurements, which were essential for the structural characterisation of my samples.
- I also like to thank Dr. Eckhard Pippel, Max-Planck-Institut Halle, for STEM, EELS and HREDX measurements with the TITAN 80-300 (samples YSc150-2 and YLu150) and Dr. Martin Zimmermann, Bruker AXS, for the pole figure measurements.
- Very detailed HRTEM, HRSTEM and EELS measurements (samples YSc50-3 and YLu50-3) were also performed by Dr. Benjamin Butz, Karlsruher Institut für Technologie (KIT), Laboratorium für Elektronenmikroskopie. Many thanks for that!
- For the TOF-SIMS measurements, thanks go to Dr. Marcus Rohnke, Alexander Rein and Sven Steinmüller.
- Of course I want to thank all my colleagues in the Institute of Physical Chemistry for a very friendly working atmosphere and the staff of the fine mechanics and electronic workshop for their hands-on support.
- Special thanks go to Michael, for motivating me and helping me to stay the course.
- Last but not least I want to thank my parents who always supported me.

# Abstract

Thin film multilayers consisting of 9.5 mol-% $Y_2O_3$ doped $ZrO_2$ (YSZ) and different rare earth oxides ($RE_2O_3$) with RE = Sc and Lu were prepared on (0001) sapphire substrates using pulsed laser deposition (PLD). These geometrically well defined samples serve as model systems for the investigation of structural influences, especially elastic lattice strain, on ionic transport in interfaces between two different materials. The interface density was varied by varying the number of individual layers while keeping the total thickness of the multilayers constant. To influence the grain boundary density of the typically polycrystalline samples, two different deposition rates, 10 Hz and 2 Hz, were used for the preparation of the samples.

Structural characterisation of the samples was performed using X-ray diffraction (XRD), scanning electron microscopy (SEM) and (high-resolution) transmission electrons microscopy ((HR)TEM) methods. For the electrochemical characterisation, mainly AC impedance measurements were applied.

All multilayer samples were crystalline directly after deposition and exhibit a columnar grain structure. The interfaces between YSZ and the rare earth oxides are sharp. Furthermore, the multilayers are highly textured and show a distinct orientation relationship between the substrate, YSZ and the rare earth oxides. For RE = Sc, the texture is better developed than for RE = Lu.

Based on considerations concerning the influence of mismatch induced interfacial lattice strain on ionic transport, a decrease in total conductivity with increasing interface density was expected for RE = Sc, where a compressive lattice strain is present near the interfaces in YSZ. These assumptions could be proved by the electrochemical investigations. For RE = Lu, a small increase of the conductivity was expected because of the small positive misfit between $Lu_2O_3$ and YSZ. However, a small decrease was found instead for the samples deposited at 10 Hz. The investigations on samples deposited at 2 Hz result in data being difficult to analyse. Whereas a strong decrease of the conductivity for RE = Sc is in accordance with the expectations, the values obtained for RE = Lu were too scattered to allow a definite interpretation.

# Zusammenfassung

Der Gegenstand der vorliegenden Arbeit sind Dünnfilm-Multischichtsysteme, bestehend aus 9.5 mol-% $Y_2O_3$ dotiertem $ZrO_2$ und verschiedenen Seltenerdoxiden ($RE_2O_3$) mit RE = Sc und Lu. Die Multischichten wurden mittels gepulster Laserdeposition (PLD) auf (0001) Saphir Substraten abgeschieden. Sie dienen als geometrisch wohldefinierte Modellsysteme für die Untersuchung von strukturellen Einflüssen, insbesondere von elastischen Gitterverspannungen, auf den Ionentransport in Phasengrenzen. Die Grenzflächendichte in den Proben konnte variiert werden, indem die Anzahl der Einzelschichten bei gleichbleibender Gesamtdicke verändert wurde. Um zusätzlich Einfluss auf die Korngrenzdichte in den typischerweise polykristallinen Proben zu nehmen, wurden zwei verschiedene Depositionsraten, 2 Hz und 10 Hz, für den PLD-Prozess benutzt.

Mittels Röntgendiffraktometrie (XRD), Rasterelektronenmikroskopie (SEM) und (hochauflösender) Transmissionselektronenmikroskopie ((HR)TEM) wurden die Proben strukturell charakterisiert. Die elektrochemische Charakterisierung wurde hauptsächlich durch Impedanz-Spektroskopie vorgenommen.

Alle Proben besaßen bereits direkt nach der Deposition eine kristalline Struktur, gekennzeichnet durch kolumnares Kornwachstum. Die Grenzflächen zwischen YSZ und den Seltenerdoxiden sind scharf. Zudem sind die Multischichten hochtexturiert und zeigen eine strikte Orientierungsbeziehung zwischen dem Substrat, YSZ und den Seltenerdoxiden. Dabei war die Textur für Proben mit RE = Sc besser ausgebildet als für Multischichten mit RE = Lu.

Basierend auf theoretischen Überlegungen über den Einfluss von fehlpassungsinduzierten Gitterverspannungen in Grenzflächennähe auf den ionischen Transport erwartete man eine Abnahme der Gesamtleitfähigkeit mit zunehmender Grenzflächendichte für RE = Sc, da in diesem System eine kompressive Gitterverspannung in den YSZ Schichten nahe den Phasengrenzen existiert. Diese Annahme wurde durch die Leitfähigkeitsmessungen bestätigt. Für RE = Lu ist hingegen ein leichter Anstieg der Gesamtleitfähigkeit zu erwarten da zwischen YSZ und $Lu_2O_3$ eine geringe dilative Fehlpassung vorliegt. Tatsächlich wurde eine leichte Verringerung der Leitfähigkeit für die Proben festgestellt, die mit 10 Hz abgeschieden wurden.

Die Untersuchungen der mit 2 Hz abgeschiedenen Multischichtproben lieferten Ergebnisse, die nur schwer zu analysieren sind. Während die starke Abnahme der Leitfähigkeit mit steigender Grenzflächendichte, die für RE = Sc gefunden wurde, mit den Erwartungen übereinstimmt, ist die Streuung der Werte für RE = Lu zu groß, um eine verlässliche Aussage zuzulassen.

# Table of Contents

I Introduction 1

1 Introduction 3

II Literature Review 7

2 Conductivity Investigations on Geometrically Well Ordered Thin Film Systems 9
  2.1 Investigations on Single Layer Systems . . . . . . . . . . . . . . . 9
  2.2 Investigations on Multilayer Systems . . . . . . . . . . . . . . . . . 13

III Theoretical Considerations 19

3 Interfaces in Crystalline Solids 21
  3.1 Structural Properties of Interfaces . . . . . . . . . . . . . . . . . . 21
    3.1.1 Classification of Interfaces and General Concepts . . . . . 21
    3.1.2 Strain and Dislocations at Interfaces . . . . . . . . . . . . 26
  3.2 Impact of Interface Properties on Ionic Conductivity . . . . . . . 35
    3.2.1 The Space Charge Concept . . . . . . . . . . . . . . . . . 36
    3.2.2 The Influence of Lattice Strain and Dislocations. . . . . . 38

4 Material Properties 43
  4.1 Structural Relationship between the Rare Earth Oxides and YSZ 43
  4.2 Transport Phenomena . . . . . . . . . . . . . . . . . . . . . . . . 46
    4.2.1 Transport Properties of Yttria-Stabilized Zirconia (YSZ) . 46
    4.2.2 Transport Properties of Bixbyite Type Rare Earth Sesquioxides . . . . . . . . . . . . . . . . . . . . . . . . . . 48
    4.2.3 Transport in Thin Film Multilayer Systems . . . . . . . . 51

5 Electrochemical Impedance Spectroscopy 53
  5.1 Basics of Electrochemical Impedance Spectroscopy (EIS) . . . . . 53
  5.2 The Representation of Microstructure in EIS . . . . . . . . . . . 55

IV Experiments and Results 59

**6 Sample Preparation 61**

**7 Structural Investigations 63**
7.1 Methods . . . . . 63
7.1.1 X-Ray Diffraction (XRD) . . . . . 63
7.1.2 Scanning Electron Microscopy (SEM) . . . . . 63
7.1.3 Transmission Electron Microscopy ((HR)TEM, (HR)STEM, EELS and SAED) . . . . . 64
7.1.4 Time-of-Flight Secondary Ion Mass Spectroscopy (TOF-SIMS) . . . . . 65
7.2 Results . . . . . 66
7.2.1 YSZ | $Sc_2O_3$ Multilayers . . . . . 66
7.2.2 YSZ | $Lu_2O_3$ Multilayers . . . . . 94

**8 Electrochemical Investigations 115**
8.1 Measurement Setup . . . . . 115
8.2 Results . . . . . 118
8.2.1 Sapphire Substrate and Sample Holder . . . . . 118
8.2.2 Rare Earth Oxides . . . . . 119
8.2.3 YSZ | $Sc_2O_3$ Multilayers . . . . . 119
8.2.4 YSZ | $Lu_2O_3$ Multilayers . . . . . 126

**V Discussion and Outlook 133**

**9 Discussion of the Results 135**
9.1 Structural Properties of the Multilayers . . . . . 135
9.1.1 Orientation Relationships . . . . . 135
9.1.2 Layer Morphology and Dislocation Density . . . . . 140
9.1.3 The Grain Boundary Structure . . . . . 144
9.1.4 Microstrain in the Multilayers . . . . . 146
9.1.5 Interdiffusion at the Interfaces . . . . . 147
9.2 Ionic Conductivity . . . . . 149
9.2.1 General Remarks . . . . . 149
9.2.2 Derivation of a Suitable Equivalent Circuit . . . . . 150
9.2.3 Expectations for the Strain Induced Change of the Ionic Conductivity . . . . . 152
9.2.4 Comparison of the Different Systems . . . . . 154
9.2.5 The Influence of Grain Boundaries . . . . . 158
9.2.6 The Role of Space Charge Regions . . . . . 159

**10 Open Questions - Further Required Investigations 161**

**11 Conclusion 163**

**12 Appendix 165**
12.1 Fourier Filtering Details . . . . . . . . . . . . . . . . . . . . . . . 165
12.2 TOF-SIMS: Additional Graphical Material . . . . . . . . . . . . . . 166
12.3 HRTEM Mictrographs . . . . . . . . . . . . . . . . . . . . . . . . . 166
12.4 Sample Data . . . . . . . . . . . . . . . . . . . . . . . . . . . . . . 170
12.5 List of Abbreviations and Symbols . . . . . . . . . . . . . . . . . . 175

**Bibliography 177**

# Part I

# Introduction

# 1 Introduction

Due to the need for increased performance combined with preferably small devices, miniaturised structures play a major role in today‘s electronic applications. By decreasing the outer dimensions, the fraction of surfaces and interfaces compared to the total volume gets larger, giving interfaces an increasing role considering the overall performance and stability of a system. It is therefore important to gain a detailed insight in the properties of interfaces, including structural properties as well as interfacial transport mechanisms. Especially the ionic transport properties of interfaces are interesting: They may on the one hand be crucial for the design of solid electrolyte systems with a preferably high ionic conductivity at low temperatures and on the other hand the knowledge of these properties can help to reduce unwanted degradation processes.

In order to selectively investigate interfaces, suitable model systems have to be found which allow the experimental separation of interface properties from bulk- or grain boundary effects. Geometrically disordered (composite) systems, such as have been in the focus of many investigations [1–4], are difficult to control with respect to the density of interfaces and their orientation in relation to the direction of the current flow. Thin films of an (ionically) conducting material, deposited on a suitable substrate, are a simple approach to obtain geometrically ordered and well-defined model systems. A number of publications is available dealing with investigations on thin film samples consisting of a single layer of well-known solid electrolytes such as doped ceria or zirconia on a preferably insulating substrate [5–9].

To increase the impact of the interfaces on the experimentally accessible overall system properties, the thickness of the thin film has to be decreased. Measuring the system properties in relation to the interface density (the film thickness) then allows to separate the interface part from the bulk (or volume) part.

A major problem of thin film measurements is the high sample resistance, which is an inevitable consequence of reducing the film thickness. On the one hand, this leads to an increased uncertainty of the results obtained by AC as well as DC conductivity measurements because the measured current signals will be very low. On the other hand, conduction through the substrate is no longer negligible if the resistance of the thin film is in the same order of magnitude as that of the substrate. Even if the conductivity of the substrate material is several orders of magnitude lower than the conductivity of the film, one has to take into account that the substrate thickness is also typically two to three orders of magnitude higher. In order to reduce the error caused by conduction through the substrate

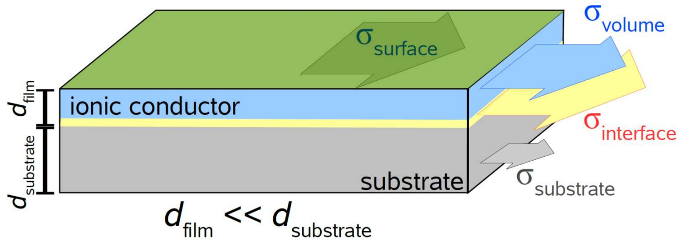

(a)

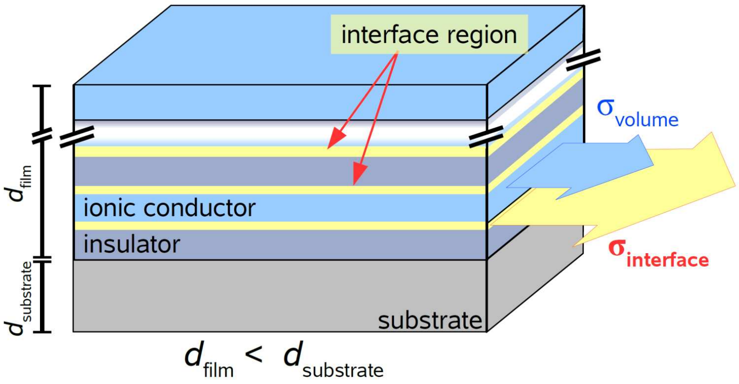

(b)

**Figure 1.1:** Different sample designs for the investigation of interface transport properties. a) Single layer setup: The conductivity $\sigma$ of the substrate in this cell is not negligible when the deposited film is very thin. b) Multilayer setup: The impact of interfaces on the total conductivity can be varied by varying the number of individual layers but keeping the total thickness $d_{\mathrm{film}}$ of the multilayer constant. In this case, contributions from the sample surface, the substrate/film interface and the substrate bulk conductivity can be neglected.

to under 1 %, a minimum film thickness is needed for a given substrate thickness and given conductivities[1]. For example, if we assume the substrate to be 1 mm thick and the conductivity of the film to be five orders of magnitude higher than the substrate conductivity, the minimum film thickness is 1 µm.

Another problem of a single film setup is that it is asymmetric with regard to the involved interfaces: part of the observed interface effect is caused by the substrate/film interface, another part is due to the film/gas interface. Both parts cannot be expected to be equal.

These problems can be avoided in multilayer systems where thin films of an ionic conductor are alternately deposited to films of an insulating material (see figure 1.1). The volume fraction of ionic conductor/insulator interfaces compared to the

---

[1] It can be calculated as:

$$\frac{d_{film}}{d_{substrate}} > 100\frac{\sigma_{film}}{\sigma_{substrate}} \tag{1.1}$$

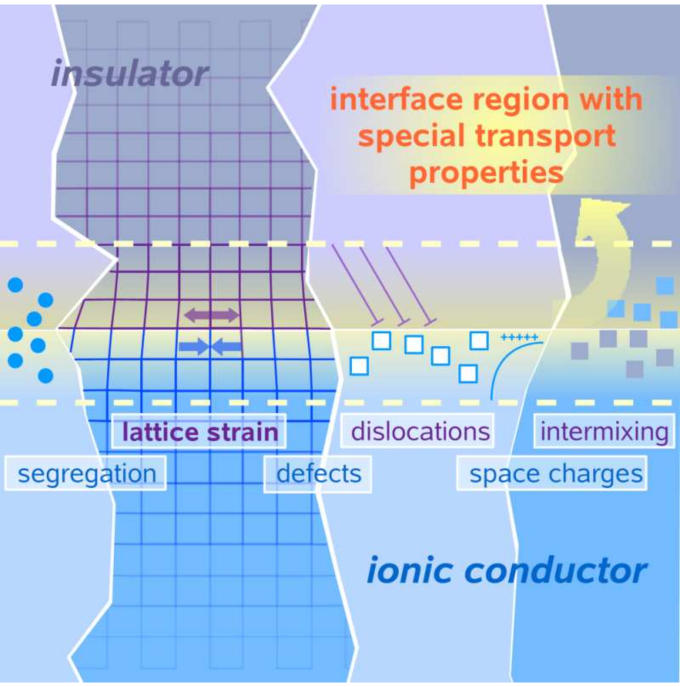

**Figure 1.2:** Scheme showing an interface region between two crystalline layers. Several aspects of disorder may be found: intermixing, segregation, build up of dislocations, formation of various point defects, space charge layers or strained and deformed crystal lattices.

bulk phases can easily be varied by increasing the number of individual layers but keeping the total thickness of the multilayer constant. In addition to that, the influence of the substrate/film and the film/gas interfaces is negligible when the number of individual layers is high. In recent years, the number of publications dealing with investigations on multilayers has risen (for example [10–12], for a survey see also [13]).

Controversial opinions exist about the origin of the observed transport properties of interfaces. As interfaces exhibit special structural and thermodynamic characteristics, several possible reasons may be taken into account (see figure 1.2). Often, intermixing of adjacent materials or segregation leads to the formation of additional phases in the interface region. Structural defects like dislocations or lattice deformations may influence the mobility of ionic charge carriers. Specific accumulation or depletion of one charge carrier at the interface leads to the formation of space charge regions.

The concept of space charge regions has been described in detail in many publications [14–17]. In contrast to this, structural effects are often neglected or only insufficiently described. The first systematic attempt to analyse the influence of the interface structure on the ionic conductivity by investigating multilayer systems has been presented by A. Peters and C. Korte [18, 19]. Multilayers consisting of calcia-stabilized zirconia (CSZ) | $Al_2O_3$ or yttria-stabilized zirconia (YSZ) | $Y_2O_3$, both deposited on sapphire substrates, where used for the investigations. However, the structural properties of these two systems are quite different, leading to completely different interfacial structures and a high degree of disorder in the case of CSZ | $Al_2O_3$.

The role of the present work is to further clarify the influence of structural parameters of interfaces on the ionic conductivity, using ionic conductor/insulator multilayers with YSZ as ionic conductor. Special attention is paid to the role of lattice strain. In order to investigate strain effects, the density of strain-releasing lattice defects like misfit dislocations has to be kept low. This can be realised if the misfit between the insulating layers and YSZ is small enough to be compensated mainly by strain. Rare earth sesquioxides of the Bixbyite structure are suitable insulators, because they are structurally related to YSZ and usually have low conductivities [20–23]. A systematic variation of the strain present at the interfaces can be accomplished by choosing different rare earth oxides, exhibiting a different misfit towards YSZ. Here, $Sc_2O_3$ and $Lu_2O_3$ are studied. By detailed structural analyses and conductivity measurements, compared to a suitable theoretical model, the extend to which lattice strain may enhance or diminish the interface conductivity is to be determined.

# Part II

# Literature Review

# 2 Conductivity Investigations on Geometrically Well Ordered Thin Film Systems

The most simple sample design for geometrically well ordered systems are single thin films deposited by pulsed laser deposition, electron beam evaporation or sputtering on a single crystalline substrate. The film thickness can be varied easily and the conductivity can be measured as a function of film thickness. Therefore, numerous publications can be found dealing with investigation on this type of systems. However, single thin films have an asymmetric arrangement of interfaces: one interface between substrate and film and one interface between film and gas atmosphere (surface). Those two interfaces are usually totally different in their structure as well as in their conductivity properties. Multilayer samples provide a means of investigating the impact of interfaces between two distinct materials on the total sample behaviour, avoiding the influence of the sample surface or the film/substrate interface, by just varying the number of alternating layers and thereby the interface density. Those systems have gained more and more interest in recent years and the number of publications has risen.

For the sake of shortness, only references which directly deal with investigations on the interface conductivity in YSZ will be presented.

## 2.1 Investigations on Single Layer Systems

In 2004, Kosacki et al. measured the in-plane conductivity of thin films of 10 mol-% $Y_2O_3$ doped $ZrO_2$ with thicknesses varying from 15 nm to 2 µm in the temperature range of 400 °C - 800 °C [5, 6]. The thin films, deposited by PLD on (001) MgO, were highly texurised and epitactic. According to Kosacki, the number of grain boundaries parallel to the substrate is negligible. In spite of the large misfit between the thin film and the substrate, leading to about 22 % strain, Kosacki stated that he found little evidence for dislocation arrays.

AC impedance measurements, using silver electrodes, showed an enhancement of the conductivity when decreasing the film thickness below 60 nm, up to a maximum value of 0.6 S/cm at 800 °C, and correspondingly a decrease in activation energy down to 0.62 eV for the thinnest (15 nm thick) film (see figure 2.1). The conductivity was interpreted as ionic conduction because it was not dependent on the oxygen partial pressure within the range of $p_{O_2} = 10^{-24}$ atm - 1 atm.

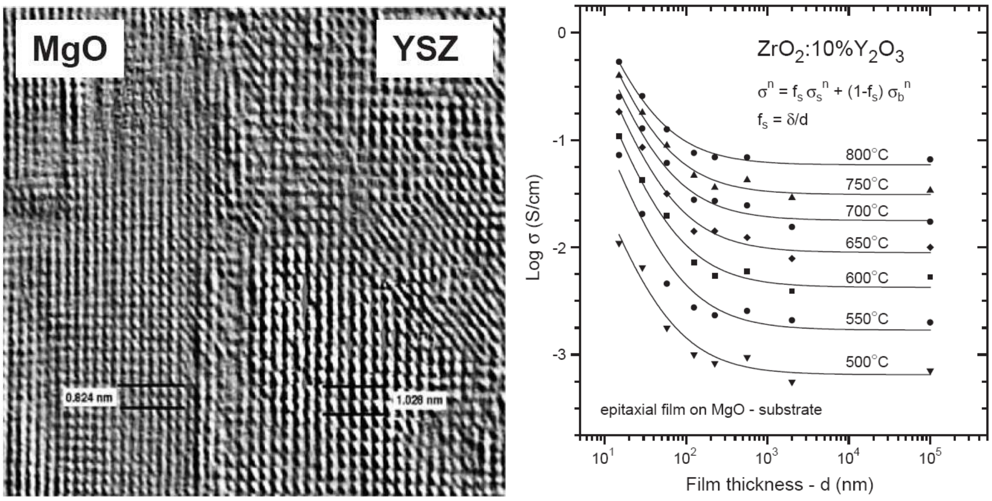

(a) (b)

**Figure 2.1:** a) HRTEM picture of one of KOSACKI´S samples, showing the MgO/YSZ interface (cross section). b) Total conductivity of the samples plotted as a function of sample thickness and temperature. Pictures taken from [6].

Furthermore, the contribution of the surface path to the total conductivity was estimated as small since a segregation of Yttrium and impurities such as $SiO_2$ and CaO was found which reduces the conductivity. The observed linear relationship between the total conductivity and the film thickness was interpreted using a so called "rule of mixtures model" [24, 25] for the analysis of different contributions to the total conductivity, assuming that the bulk and interfacial conduction paths are parallel:

$$\sigma^n = \sigma_s^n f_s + \sigma_b^n (1 - f_s) \qquad f_s = \frac{\delta}{d} \tag{2.1}$$

$\sigma_s$ denotes the interface conductivity, $\sigma_b$ the bulk conductivity. $\delta$ is the thickness of the interface, $d$ the layer thickness. $n$ is an exponent describing the nature of the connection between the two conduction paths, being 1 for a parallel connection and $-1$ for a series connection. The experimentally determined value of $n$ was 0.31. Using the values obtained by this model, a purely interfacial conductivity was calculated being over three orders of magnitude higher than the bulk conductivity and having an activation energy of 0.45 eV.

Concerning the physical reason of the conductivity enhancement, it was noted that $\delta$, estimated as 1.6 nm, was similar to the thickness of space charge regions in grain boundaries of YSZ (reported to be 1 nm - 2 nm [27]). Therefore, space charge effects are discussed. But the high misfit strain at the YSZ | MgO interface was also mentioned as a possible influencing variable because it should reduce the activation energy for ion hopping. In spite of KOSACKI´S earlier

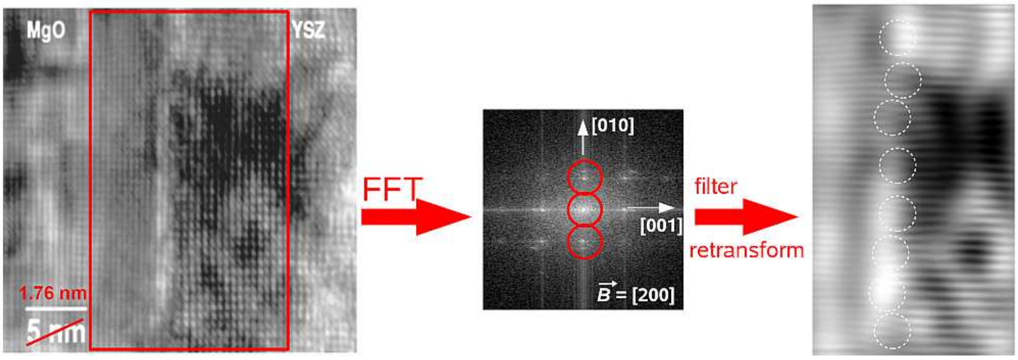

**Figure 2.2:** By Fourier transformation, filtering of the marked reflexes and re-transformation, dislocations can be made visible in the TEM picture of Kosacki´s sample. TEM picture taken from [5], Fourier transform processing by C. Korte (see [26]).

report, taking a closer look at the TEM micrograph of the MgO | YSZ interface, a quite regular array of dislocations can be revealed by Fourier transformation and filtering, so that only the vertical reflexes are preserved (see figure 2.2, for a detailed description see [26]). These dislocations may have an influence on the measured conductivities, too. Also, the scale seems to be wrong when compared to the lattice spacings in the micrograph, but this mistake was corrected by Kosacki in 2005 [6].

Similar measurements were reported by Guo et al. in 2005 [7]. He investigated a sample with a 12 nm and another with a 25 nm thick polycrystalline film of 8-mol% $Y_2O_3$ doped $ZrO_2$ on (001) MgO substrates, prepared by PLD. The YSZ layers were oriented parallel to the substrate ((001) YSZ || (001) MgO) and a dislocation network was found, due to the high compressive strain in YSZ (see figure 2.3a)).
Measuring the in-plane conductivity between 550 °C and 750 °C (evaporated Pt electrodes), he found conductivities lowered by a factor 4 compared to microcrystalline bulk ceramic and the activation energy to be higher (figure 2.3b)). Furthermore, the conductivity was not dependent on the film thickness or humidity of the atmosphere. Therefore, proton conduction could be excluded (as was also found by Kosacki et al.). Guo also excluded an influence of the MgO | YSZ interface on the conductivity. He ascribed the decrease of the conductivity to space charge effects at the grain boundaries. As was shown before [27, 28], grain boundaries in YSZ have a higher activation energy for ionic transport across if compared to the bulk transport. This is because vacancies are adsorbed in the grain boundary core, which is then positively charged. A vacancy depletion in the space charge region and the creation of a Schottky barrier are the result. According to Guo, the space charge region in YSZ can reach a width of 5 nm - 8 nm. In addition to this, the bulk conductivity is also lowered when the grain size is below 41 nm. Then, a size dependent segregation

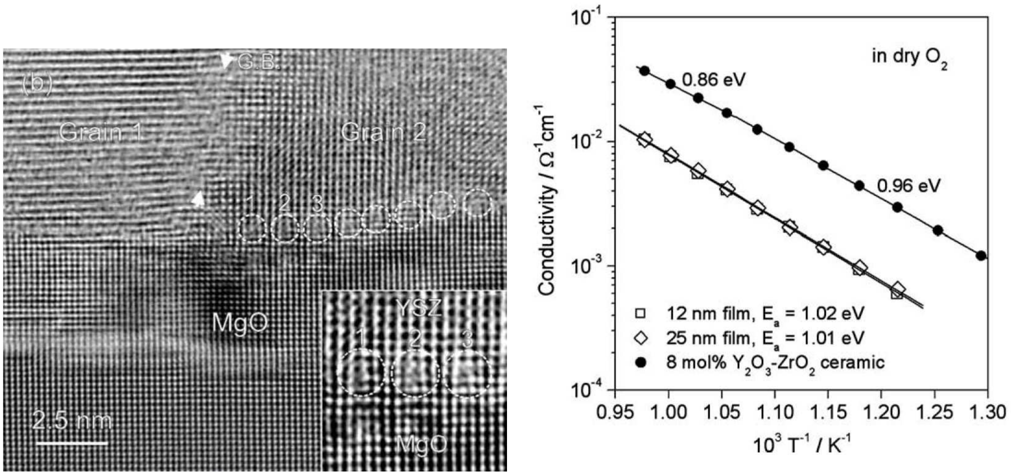

(a) (b)

**Figure 2.3:** a) HRTEM picture of the 12 nm thick YSZ film investigated by Guo et al. (cross section). Dislocations are marked by dashed circles b) Temperature dependent conductivity for both samples in comparison with data for bulk YSZ ceramic. Pictures taken from [7].

of dopants occurs, which is denoted as the bulk "de-doping" effect. This effect was also demonstrated for Ca in $TiO_2$ by Terwilliger and Chiang [29] and for nanocrystalline Gd doped $CeO_2$ ceramics by Chiang and Lavik [30].

In 2006, Karthikeyan et al. investigated polycrystalline thin films of 9.5 mol-% doped YSZ, prepared by electron beam evaporaton and with thicknesses between 17 nm and 210 nm [8]. (001) MgO and (0001) $Al_2O_3$ were used as substrates. The in-plane AC impedance was measured in the temperature range of 700 °C - 940 °C in air using Pt electrodes. Karthikeyan again found an increase of the total conductivity with decreasing layer thickness, independent of the choice of the substrate. He identified the conductivity as ionic conductivity by analysing the frequency dependence of the imaginary part of the modulus $M´´$ and the dielectric constant $\epsilon´´$. If an ionic conduction mechanism is present, $M´´$ as a function of frequency should show a peak but no corresponding peak should be found for $\epsilon´´$. The increase in conductivity was explained by the formation of space charge layers at the substrate/film interface and the grain boundaries since the Debye length in YSZ was estimated to be of a few nm [31] and therefore in the range of the layer thickness for the thinnest layers. Later, Karthikeyan corrected his statement of the Debye length, stating that the value of a few nanometres corresponds to pure zirconia and that it is expected to be smaller in doped zirconia because of a several orders of magnitude higher defect concentration [32]. As alternative explanations, segregation and strain effects are mentioned, causing modified defect concentrations at the interfaces.

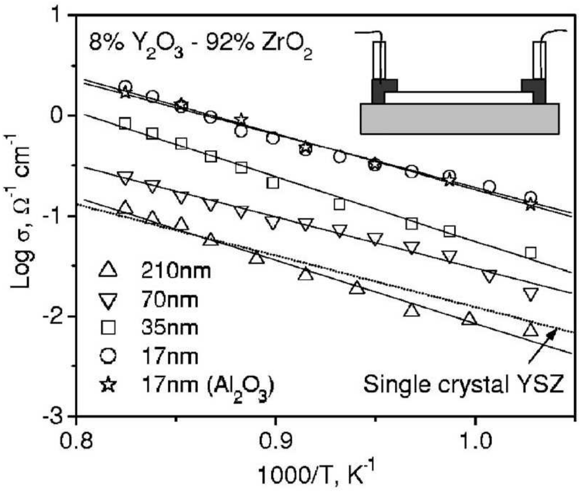

**Figure 2.4:** Temperature dependent conductivity of YSZ thin films, being 17 nm - 210 nm thick, as measured by KARTHIKEYAN et al.Picture taken from [8]

## 2.2 Investigations on Multilayer Systems

N. SATA et al. reported in 2000 on the conductivity properties of polycrystalline $CaF_2/BaF_2$ heterostructures [10]. Thin film multilayers of the two moderate, anti-Frenkel disordered fluoride conductors were prepared using electron beam epitaxy. The individual layer thickness in the samples ranged from 2 nm - 500 nm. $(01\bar{1}2)$ $Al_2O_3$ and $SiO_2$ were used as substrates. AC impedance measurements were carried out between 100 °C and 540 °C, using Pt electrodes applied to the surface of the multilayers. An increase in conductivity with increased interface density was found (see figure 2.5a)). In samples with single layer thicknesses over 50 nm, the increase was linear with respect to the interface density. When the individual layers where thinner than 50 nm, the increase in conductivity was even more pronounced. The linear increase of the conductivity was explained in terms of space charge layers at the interfaces. These lead to a locally enhanced charge carrier mobility. With increasing density of interfaces, the space charge layers have an increasing influence on the overall transport properties. Also, a redistribution of $F^-$ ions from $BaF_2$ to $CaF_2$ takes place leading to an increased vacancy concentration in $BaF_2$ dominating the conduction at lower temperatures and an increased interstitial concentration in $CaF_2$, dominating the high temperature conductivity. The more pronounced conductivity enhancement in samples with individual layer thicknesses below 50 nm (spacings below four times the Debye length of about 15 nm) was ascribed to a specific nanosize effect: overlapping space charge regions lead to layers which are charged on the whole. In this case, the multilayer must be treated as a system with specific conductivity properties. Decreasing the thickness of the individual layers below 8 nm, a decrease in conductivity was observed, likely being caused by a structural breakdown of the

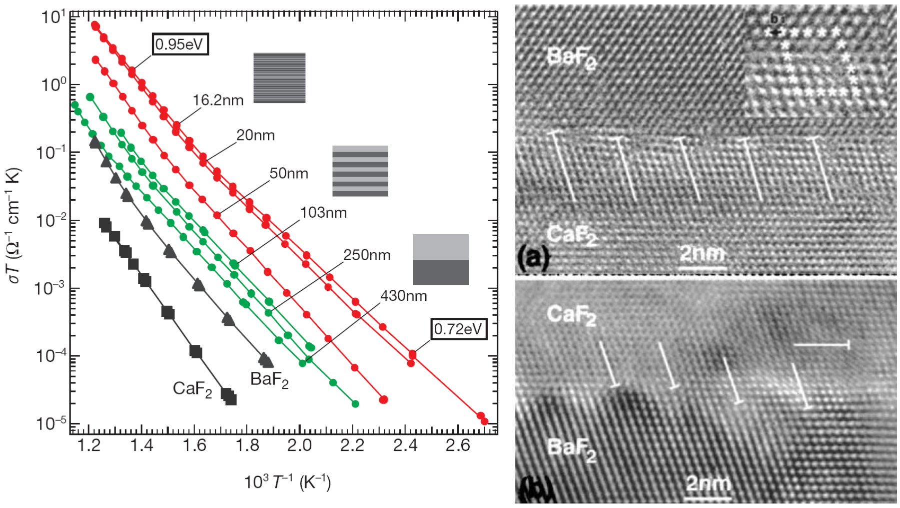

(a) (b)

**Figure 2.5:** a) Conductivity results for different CaF$_2$/BaF$_2$ multilayers. The denoted thicknesses refer to the CaF$_2$-BaF$_2$ double layer period. b) HRTEM of the interfaces between the two fluoride conductors (cross sectional view). The inset in the upper picture shows the Burgers vector for a dislocation. The lower picture shows a wavy interface and an example for a nearly horizontally aligned dislocation. Pictures taken from a) [10] b) [33].

multilayer structure.

A detailed investigation of the structural properties of the CaF$_2$/BaF$_2$ multilayers was reported in 2004 [33]. The orientation relationship between the substrate and the different phases in the multilayers was described as (0112) Al$_2$O$_3$ $\parallel$ (111) CaF$_2$/BaF$_2$ and $[2\bar{1}\bar{1}0]$ Al$_2$O$_3$ $\parallel$ $[11\bar{2}]$ CaF$_2$/BaF$_2$. In samples with thicker individual layers, the interfaces were flat and sharp. When the single layer thickness was decreased, the layers became more and more wavy, leading finally to discontinuous layers and to the mentioned breakdown of the multilayer structure. The high mismatch of 14 % between the two materials was partly released through regularly arranged dislocations at the interfaces (see figure 2.5b)), partly through a deformation of the lattices in the vicinity of the interface (the CaF$_2$ lattice was compressed, the BaF$_2$ lattice dilated). At the wavy layer interfaces, a second type of dislocation was observed, the corresponding Burgers vector being oriented more or less perpendicular to the interface. It is noted that the observed deformation of the crystal lattices and the dislocations may also have an effect on the conductivity, but the contribution of this effect to the overall behaviour was not analysed further.

Multilayers of two ionic conductors, CeO$_2$ and ZrO$_2$, either pure or both doped with 12 % Gd, were prepared by Azad, Wang et al. in 2005 also using molecular beam epitaxy and (0001) $Al_2O_3$ substrates [11, 34]. The conductivity was measured for the Gd doped system. The multilayers had a total thickness of about 155 nm and contained 2, 4, 8, 10 or 16 single layers. As in the fluoride system described above, the authors found a significant increase of the conductivity with decreasing single layer thickness (see figure 2.6a)). A maximum of the conductivity was observed for the sample with 10 individual layers. Strain effects were mentioned as a possible reason for the decline of the conductivity in the sample with 16 layers, but no further explanation was given.

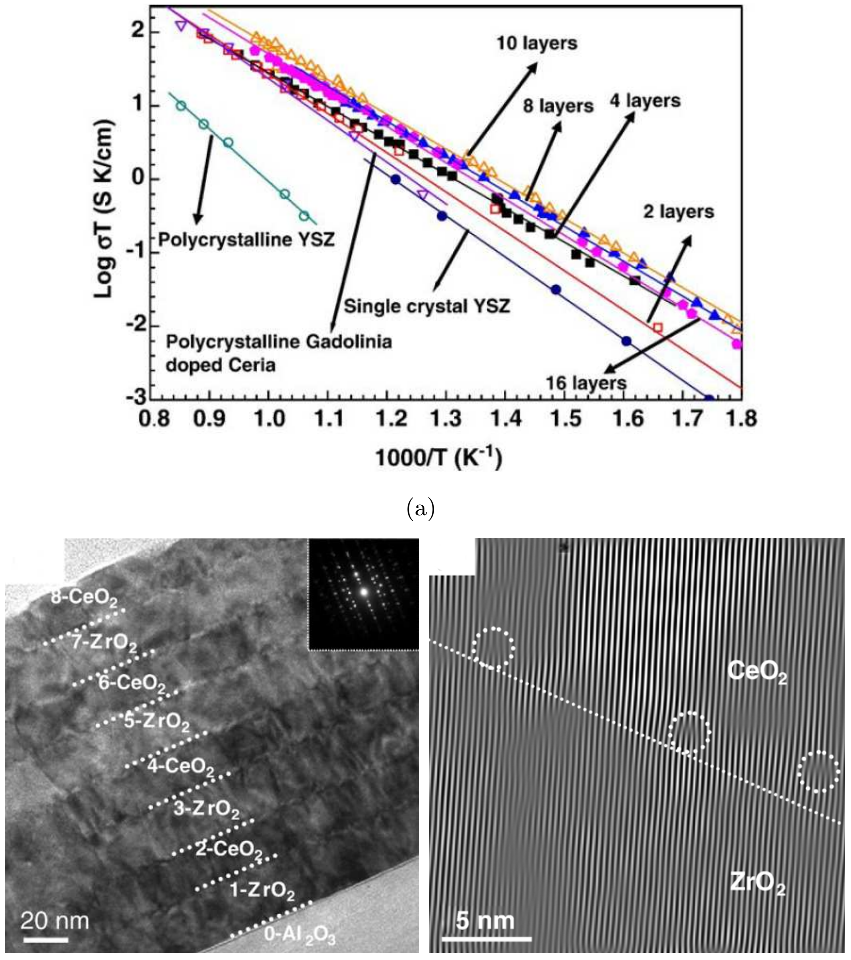

(a)

(b)

(c)

**Figure 2.6:** a) Conductivity versus temperature plots for different multilayers of Gd doped ceria and zirconia, investigated by Azad et al.b) Bright field TEM micrograph of a multilayer containing 8 individual layers. c) Fourier filtered HRTEM micrograph showing dislocations at an interface between Gd:$CeO_2$ and Gd:$ZrO_2$. Pictures taken from [35].

Structural analysis [35] of the multilayers showed that both materials were highly textured. Mainly the (111) orientation could be found. Only a small fraction of the crystallites had a (100) orientation. The orientation relationship was described as [110] $ZrO_2$ ∥ [110] $CeO_2$ and (002) $ZrO_2$ ∥ (002) $CeO_2$. A theoretical misfit of of 5.3 % was calculated for the given material combination. A closer look at the interfaces revealed a regular arrangement of dislocations, spaced at intervals of about 7 nm (see figure 2.6b,c). This distance is larger than theoretically expected from the mismatch, so there must be some residual strain at the interfaces if no other mechanism for the strain release takes place. XPS depth profiling and EDX measurements in STEM analysis indicated that $CeO_2$ is enriched in oxygen vacancies due to the higher solubility of Gd in $CeO_2$. Also, an asymmetric segregation of Gd was found on top of the $ZrO_2$ layers, which is expected to lead to an enhanced defect concentration at the interfaces. Together with the observed dislocations, this was given as the reason for the conductivity enhancement. Space charge effects were said to play a minor role due to the short Debye length of ca. 0.1 nm in materials with such a high carrier concentration as those used in these studies.

In 2008, Karthikeyan et al. investigated YSZ | $SiO_2$ (or $Al_2O_3$) superlattices on (001) MgO [12]. The individual YSZ layers were 3 nm to 33 nm thick. They found both cubic and tetragonal phases in the polycrystalline YSZ, which they also reported earlier for single layer experiments [8]. AC impedance measurements were performed from 670-930 °C using porous Pt electrodes. A nearly five fold increase of the conductivity was observed when the YSZ layer thickness was decreased to 3 nm, similar for all temperatures and not dependent on the chemical nature of the amorphous insulating layer (see figure 2.7).

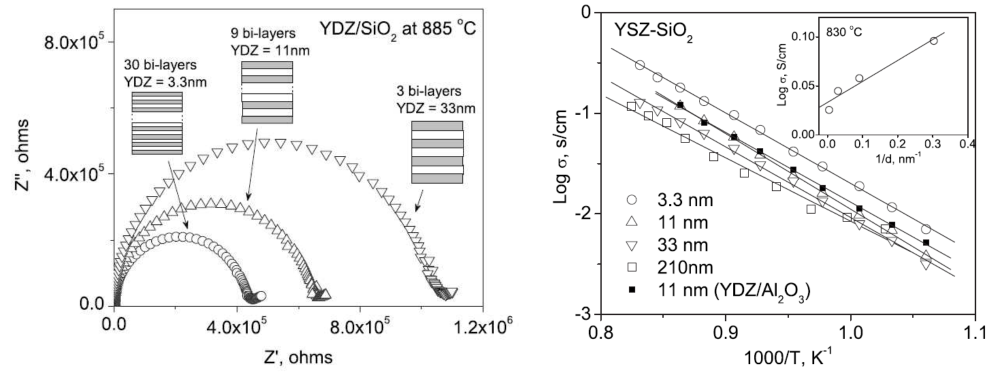

(a) (b)

**Figure 2.7:** a) Nyquist plots of different YSZ / $SiO_2$ multilayers. b) Plot of the temperature dependent conductivity of the multilayers. The multilayer with $Al_2O_3$ as insulating layer is shown for comparison. The inset shows the variation of the conductivity with varying single layer thickness at 830 °C. Pictures taken from [12].

An activation energy of about 1.3 eV for the total conductivity was measured, which is higher than the typical value for bulk YSZ (around 1.1 eV, see [36–38]). Using an equation[1] based on the rule of mixtures model in equation 2.1, they calculated the interfacial and volume part of the conductivity, respectively. At 830 °C, the conductance of the interfaces was $7.2 \cdot 10^{-9}$ S and an average activation energy of about 1.4 eV for the interfacial path was estimated. The activation energy changed with temperature and reached a value of 1.1 eV at temperatures over 800 °C. The enhancement of the conductivity was related to interface effects, but no explanation was given what these interface effects in detail are.

A very controversially discussed work was published by Garcia-Barriocanal et al. in 2008 [39]. Using RF sputtering, they deposited tri- and multilayered samples ($SrTiO_3$(10 nm) | [8 mol-% YSZ (1-62 nm) | $SrTiO_3$(10 nm)]$\times n$, $n = 1 - 5$) on (100) $SrTiO_3$ substrates. Using XRD and HRTEM, they found that the very thin YSZ layers grew perfectly coherent on $SrTiO_3$, being rotated by 45° around the $c$-axis and because of the rather high mismatch of 7 % strained in the $ab$-plane. They also reported the individual layers to be continuous and flat, even the 1 nm thick film (1 nm $\approx$ 2 unit cells YSZ, see figure 2.8a)). In the thicker films, strain was released through the evolution of a granular morphology and the loss of coherency, but the films were still highly textured.

AC impedance measurements revealed a very high increase of the conductivity for the trilayered samples with 1 nm - 30 nm thick YSZ films (figure 2.8b)). At about 280 °C, this enhancement was reported to be nearly eight orders of magnitude with conductivities of about $10^{1.5}$ S/cm for the trilayer with the 1 nm thick YSZ film. This is an even one order of magnitude higher value as has been reported for the superionic cation conductors $\alpha$-AgI and $RbAg_4I_5$ [40, 41]. The DC conductance was three to four orders of magnitude lower than the AC conductance, which was interpreted as proof for an ionic transport mechanism. Multilayers were measured to analyse the dependence of the conductance on the number of interfaces, which resulted in a linear plot. The conductance showed no dependency on the thickness of the YSZ layers, which may be a proof that the observed effect is purely due to an interfacial mechanism (see figure 2.8b).

Using EELS, the authors identified the terminating layer of the $SrTiO_3$ phases as a $TiO_2$ plane (the Ti signal had a higher intensity at the interfaces than the Sr signal). They also detected an enhanced concentration of oxygen vacancies at the interfaces between YSZ and $SrTiO_3$. The oxidation state of Ti was reported to be unchanged. This high degree of disorder and depletion of oxygen at the interfaces was given as an explanation for the conductivity enhancement. However, no clear proof was presented that the measured conductivity of these samples is really of ionic nature.

---

[1] derived by Korte in [18], see also section condmultilayer

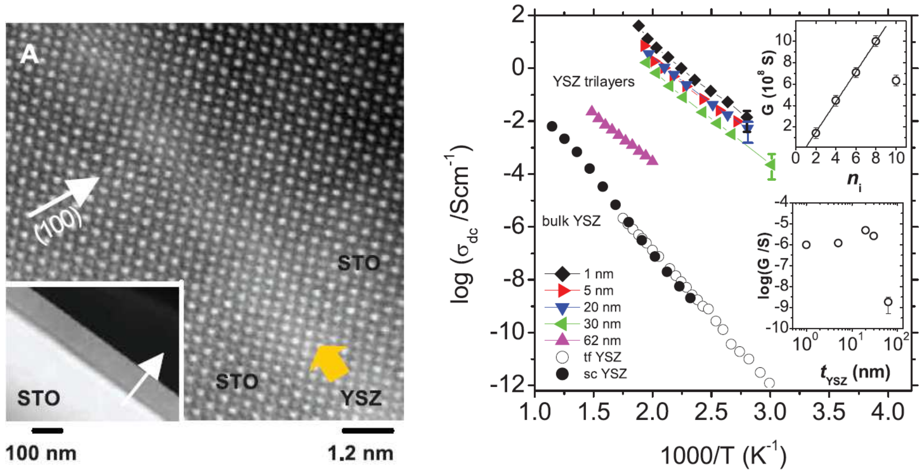

(a)

(b)

**Figure 2.8:** a) Z-contrast scanning transmission electron microscopy (STEM) picture of a superlattice with 9 YSZ layer (1 nm thick) embedded in 10 nm thick $SrTiO_3$ layers. The white arrow indicates the growth direction, the yellow arrow marks the YSZ layer. b) Logarithm of the low frequency (DC) conductivity of the trilayers versus temperature. Data from bulk single crystal (sc) and a thin film (tf) being 700 nm thick are given for comparison. The upper inset shows the relation of the conductance G on the number of interfaces. The lower inset shows the dependence of the conductance in the trilayers on the thickness of the YSZ layer. Pictures taken from [39].

A common feature in all the publications presented here is that the conductivity changes significantly with increasing interface density or decreasing layer thickness; in most cases an enhancement was measured. If a detailed description of the interfacial effects is given, the space charge model is the most popular explanation. However, in almost all publications also structural changes at the interfaces such as dislocations or strained lattices were reported. But the role of these structural changes was not further investigated. This shows how important it is to have a closer look at the effect of interfacial defects and strain on conductivity, especially since the space charge model may not be suitable for materials like YSZ, due to the high carrier concentration and therefore small Debye length. Apart from the overview given here, a review of different publications on ionic conduction in two-dimensional heterostructures can also be found in [13].

# Part III

# Theoretical Considerations

# 3 Interfaces in Crystalline Solids

## 3.1 Structural Properties of Interfaces

### 3.1.1 Classification of Interfaces and General Concepts

A general, physical description of an interface may be given in terms of a boundary separating two different phases. If it separates phases in different aggregate states (solid-liquid, solid-gas or liquid-gas interfaces), we normally speak of a surface. Interfaces separating two solids from each other may divide two different materials (heterophase boundary) or two different domains of the same material (homophase boundary), including grain boundaries, stacking faults or inversion domain boundaries [42]. Especially in heterophase boundaries, a great variety of interface structures and geometries may be found, depending on the structure, the mutual orientation, the elastic properties and the dimensions of the adjoining phases.

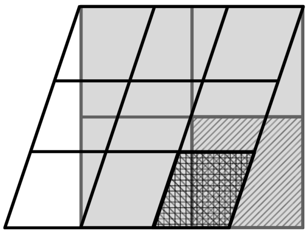

**Figure 3.1:** Scheme showing the concept of commensurability. Both unit cells (marked by different hatchings) cover the same area when the in-plane lattice constants of the smaller one are multiplied by three and by two for the larger one.

The geometric relation of two lattice planes meeting at an interface can be described using the concept of commensurability. In commensurate interfaces, the relation of the different lattice constants is such that a common planar unit cell in the interface plane can be found. This means that congruence between adjoining planes of different unit cells can be achieved by multiplying the lattice parameters of one or both unit cells by small integers (see figure 3.1). Atomic positions on both sides of a commensurate interface are long range ordered parallel to the interface. Sometimes, a long range ordered interface can only be created if an additional twist or tilt misorientation is introduced. This leads to more complex relations between the lattice parameters, because now also the tilt and twist angles have to be taken into account. Commensurability is a necessary premise for coherency, as explained below.

In most cases, commensurate interfaces can not be formed if the lattice parameters of the bulk phases are assumed. Nevertheless, a matching of the lattice planes may be created by an elastic deformation of the adjoining crystals at the interface. Typically, one crystal lattice is dilated, the other compressed, leading to strained regions inside the crystals extending from the interface into the volume. How far these regions actually are extended depends on the elastic properties as well as on the outer dimensions of the two adjoining phases. Three different types of interfaces can be classified [43]:

### Bulk Interfaces

If the interface is embedded on both sides in bulk material, either situated between thick layers or separating large crystallites (see figure 3.2a)), the strain energy involved in the deformation of the adjoining crystal lattices is very large. Thus, the compensation of the mutual lattice mismatch takes place by the creation of misfit dislocations.

### Semi-bulk Interfaces

In the case of a thin film or a crystallite with a small volume compared to the contact area joining a bulk phase or a large crystallite, an overall structural distortion of the thin film or the small crystallite can be expected (see figure 3.2b)). The thin film or small crystallite will adopt the lattice spacings of the bulk phase or the large crystallite.

### Thin Film Interfaces

At an interface between two thin films or small crystallites, both phases will show an overall distortion of the lattice parameters, the extent of the distortion for each phase being determined by the structural misfit between the two phases and their elastic properties (see figure 3.2c)). Again, a mutual lattice parameter will be established but no relaxation into the volume takes place. If the thin films are not restrained by a rigid substrate, the mismatch will also be compensated by a bending of the films.

A special case of bulk-like interfaces are those separating columnar grains where the contact are between the grains is very small but the extension of the grains perpendicular to the interface is large. Directly at the interface, the mismatch can be compensated by a deformation of the adjoining crystal lattices, but in contrast to thin film interfaces the lattice deformation declines with increasing distance to the interface (see figure 3.3). The extent of the deformed lattice regions depends on the size of the contact area in relation to the size of the crystallite and of course on the elastic constants of the involved materials. If the contact area is increased, the strain energy rises and dislocations are formed.

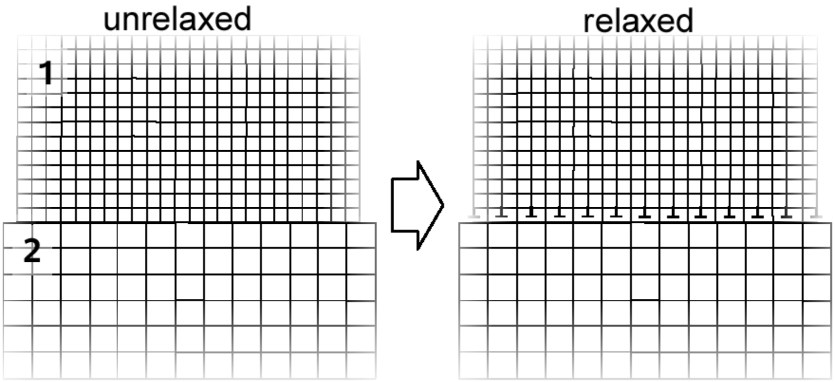

(a) bulk interface

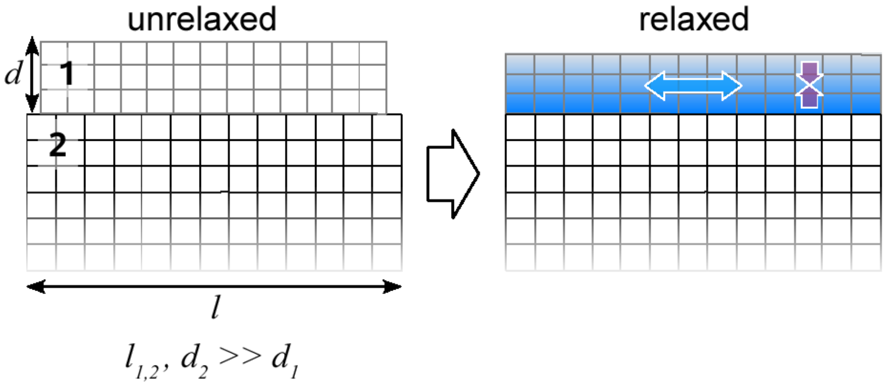

(b) semi-bulk interface

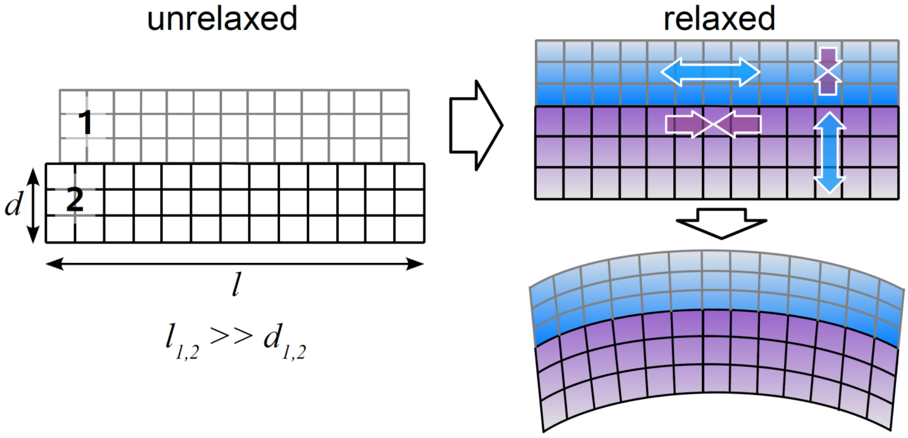

(c) thin film interface

**Figure 3.2:** Three different kinds of interfaces. Strained regions are marked blue for tensile strain and red for compressive strain. Whereas in bulk interfaces the lattice is able to relax into the volume and adopt the bulk lattice parameter, in semi-bulk or thin film interfaces one or both adjacent phases are deformed at a whole.

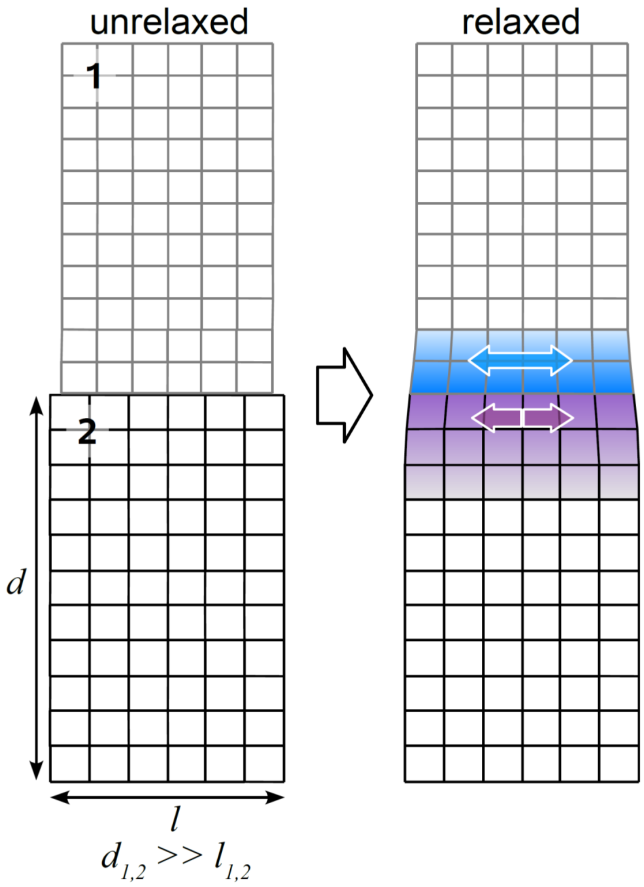

**Figure 3.3:** Lattice deformation of an interface between columnar grains.

The bulk interface is the limiting case for very large contact areas.

The mismatch $f_{12}$ between two phases is crucial for evaluating the extent of interfacial strain and the density of strain induced structural defects. It can be described by relating the difference in the lattice distances parallel to the interface in both phases (1 and 2) to the lattice parameter of one phase, taking into account the commensurability conditions:

$$f_{12} = \frac{d_{hkl,2} - d_{hkl,1}}{d_{hkl,1}} \tag{3.1}$$

The presence of structural defects and their density along an interface are important for the concept of coherency [43], defining coherent, semicoherent and incoherent interfaces.

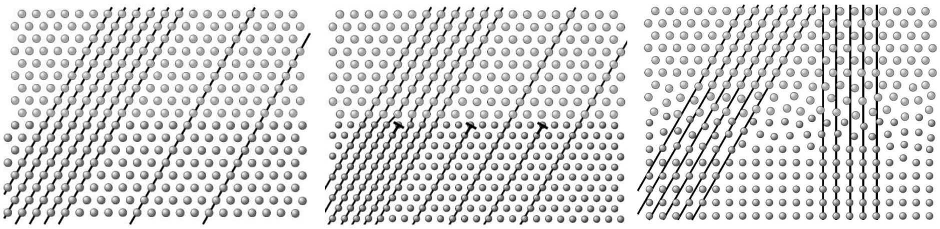

(a) coherent interface (b) semicoherent interface (c) incoherent interface

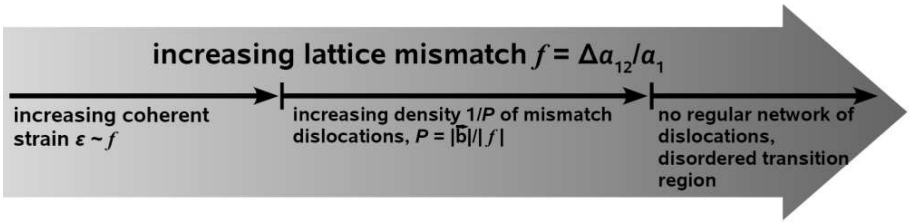

**Figure 3.4:** Scheme describing the concept of coherency. Pictures a)-c) after [26].

The coherency concept describes microstructural properties of an interface on an atomic level (figure 3.4), provided there is no tilt or twist misorientation present. An interface is called coherent if all correspondent lattice planes and atom lines are continuous across the interface. This involves an atom-by-atom matching across the interface. Contrary to this, incoherent interfaces show no continuity of lattice planes at all, a disordered transition region can often be observed. Across semicoherent interfaces, dislocation lines appear in regular intervals. Between these linear defects, correspondent lattice planes match across the interface.

## 3.1.2 Strain and Dislocations at Interfaces

### Strain in Coherent Interfaces

In systems with a small misfit, interfaces are coherent and the misfit is compensated by elastically strained lattices (see figure 3.4a)). Two types of strain may occur with respect to one phase: compressive and dilatative strain. The first leads to shorter, the second to larger lattice spacings.
The elastic parameters governing strain are anisotropic in most crystalline solids. However, for the sake of simplicity only isotropic strains will be used in the following treatment.

Isotropic Elasticity Theory [44]

When a force is exerted on a crystal lattice, the atomic positions will be displaced, the displacement being defined as $\vec{u} = (u_x + u_y + u_z)$. The acting force $\vec{F}$ usually is referred to in terms of stress $\sigma_{ij} = \vec{F} \Big/ A$. $i$ denotes the direction of $\vec{F}$, $j$ defines the direction perpendicular to the surface A on which the force is applied (see figure 3.5). The three normal stress components are $\sigma_{xx}$, $\sigma_{yy}$ and $\sigma_{zz}$ (see figure 3.5a)). In addition to this, there are six shear stress components with $i \neq j$ (see figure 3.5b)). If no net rotational force moment is acting, we find:

$$\sigma_{xy} = \sigma_{yx}, \quad \sigma_{xz} = \sigma_{zx}, \quad \sigma_{yz} = \sigma_{zy} \tag{3.2}$$

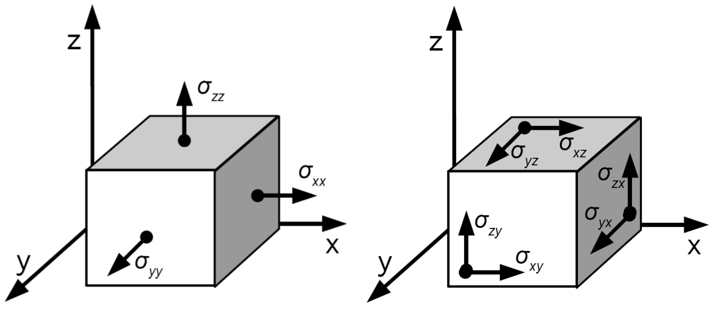

(a) (b)

**Figure 3.5:** a) The normal stress components acting on a volume element. b) The six different shear stress components. The stresses acting on opposed surfaces are different in sign.

In literature, the shear stresses are also denoted as $\tau_{ij}$.

The deformation caused by stress, the strain $\varepsilon$, can be calculated as the partial derivatives of the displacement components:

$$\varepsilon_{xx} = \frac{\partial u_x}{\partial x}, \quad \varepsilon_{yy} = \frac{\partial u_y}{\partial y}, \quad \varepsilon_{zz} = \frac{\partial u_z}{\partial z} \tag{3.3}$$

The shear components of the strain are:

$$\begin{aligned} \varepsilon_{xy} = \varepsilon_{yx} &= \frac{1}{2}\left(\frac{\partial u_x}{\partial y} + \frac{\partial u_y}{\partial x}\right) \\ \varepsilon_{xz} = \varepsilon_{zx} &= \frac{1}{2}\left(\frac{\partial u_x}{\partial z} + \frac{\partial u_z}{\partial x}\right) \\ \varepsilon_{zy} = \varepsilon_{yz} &= \frac{1}{2}\left(\frac{\partial u_z}{\partial y} + \frac{\partial u_y}{\partial z}\right) \end{aligned} \tag{3.4}$$

A volume change $\mathit{\Delta} V$ of the deformed crystal is related to the total strain $\varepsilon$ by the trace of the strain tensor:

$$\frac{\mathit{\Delta} V}{V_0} = (\varepsilon_{xx} + \varepsilon_{yy} + \varepsilon_{zz}) = \varepsilon \tag{3.5}$$

$V_0$ is the volume of the undeformed crystal. Along one dimension this would be equal to $\frac{\mathit{\Delta} l_i}{l_{0i}} = \varepsilon_i$.
In linear elasticity, the relationship between $\sigma$ and $\varepsilon$ is *Hooke´s Law*. If applied to isotropic solids, it takes the form:

$$\begin{aligned} \sigma_{xx} &= 2\mathrm{G}\varepsilon_{xx} + \lambda\left(\varepsilon_{xx} + \varepsilon_{yy} + \varepsilon_{zz}\right) \\ \sigma_{yy} &= 2\mathrm{G}\varepsilon_{yy} + \lambda\left(\varepsilon_{xx} + \varepsilon_{yy} + \varepsilon_{zz}\right) \\ \sigma_{zz} &= 2\mathrm{G}\varepsilon_{zz} + \lambda\left(\varepsilon_{xx} + \varepsilon_{yy} + \varepsilon_{zz}\right) \\ \sigma_{xy} &= 2\mathrm{G}\varepsilon_{xy}, \quad \sigma_{xz} = 2\mathrm{G}\varepsilon_{xz}, \quad \sigma_{yz} = 2\mathrm{G}\varepsilon_{yz} \end{aligned} \tag{3.6}$$

$\lambda$ and G are the *Lamé constants*. $\lambda$ is the first *Lamé constant* and G is the second *Lamé constant*, which is also known as the *shear modulus*. They are related to *Young´s modulus* Y and *Poisson´s ratio* $\nu$:

$$\mathrm{Y} = \frac{\sigma}{\varepsilon} = 2\mathrm{G}\left(1 + \nu\right), \quad \nu = -\frac{\varepsilon_{transverse}}{\varepsilon_{axial}} = \lambda/2\left(\lambda + \mathrm{G}\right) \tag{3.7}$$

The effective isotropic pressure acting on a volume element in a crystal under stress is:

$$p = -\frac{1}{3}\left(\sigma_{xx} + \sigma_{yy} + \sigma_{zz}\right) \tag{3.8}$$

The energy contributed by elastic strain to the internal energy of the crystal is given by:

$$E_{elast} = \frac{1}{2} \int \sum_{i=xyz} \sum_{j=xyz} \sigma_{ij} \varepsilon_{ij} dV \tag{3.9}$$

The volume $V$ in the integral is the volume of the undeformed system.

### Biaxially Strained Thin Films

For the case of an interface between two thin films (referred to as 1 and 2), we neglect all shear components. We further simplify our considerations by introducing a purely biaxial strain situation, that means for the strain in each phase: $\varepsilon_{xx,i} = \varepsilon_{yy,i} = \varepsilon_i$. The stress components are:

$$\sigma_{xx,i} = \sigma_{yy,i} = -\frac{\mathrm{Y}_i}{1-\nu_i}\varepsilon_i \quad \text{and} \quad \sigma_{zz,i} = 0 \tag{3.10}$$

$\frac{\mathrm{Y}_i}{1-\nu_i} = 2\mathrm{G_i}(1+\nu_i)/(1-\nu_i)$ is often referred to as biaxial modulus $\mathrm{M}_i$ in literature, $i$ denotes phase 1 or 2. There is a maximum to the strain which can be compensated at an interface without the generation of misfit dislocations. In a thin film system, both phases contribute to the strain compensation. For coherent interfaces, the following condition is fulfilled [45–47]:

$$\varepsilon_1 - \varepsilon_2 = \varepsilon_{max} \tag{3.11}$$

The strain in phase 1 necessarily is opposite in sign to the strain in phase 2; equation 3.11 can also be written as the sum of the absolute values of $\varepsilon_1$ and $\varepsilon_2$ . If no external forces are applied, $\varepsilon_{max}$ is equal to the misfit $f$. If the net force on any atomic plane perpendicular to the interface is zero, then $\sigma_1 h_1 + \sigma_2 h_2 = 0$. $h_i$ is the film thickness. If we use the biaxial modulus M instead of Y, this is equal to:

$$\mathrm{M}_1\varepsilon_1 h_1 + \mathrm{M}_2\varepsilon_2 h_2 = 0 \tag{3.12}$$

The strain in both phases can then be calculated:

$$\begin{aligned} \varepsilon_1 &= \frac{\varepsilon_{\max}}{1 + \frac{\mathrm{M}_1}{\mathrm{M}_2}(h_1/h_2)} \\ \varepsilon_2 &= -\varepsilon_{\max}\frac{\frac{\mathrm{M}_1}{\mathrm{M}_2}(h_1/h_2)}{1 + \frac{\mathrm{M}_1}{\mathrm{M}_2}(h_1/h_2)} \end{aligned} \tag{3.13}$$

The elastic energy $E_{elast}$ in the thin film system can be calculated using equations 3.9, 3.12 and 3.13:

$$\begin{aligned} E_{elast} &= \frac{1}{2}\sum_i (\sigma_{xx,i}\varepsilon_{xx,i} + \sigma_{yy,i}\varepsilon_{yy,i}) A h_i \\ \tilde{E}_{elast} &\equiv \frac{E_{elast}}{A} = \frac{\mathrm{M}_1 \varepsilon_{\max}^2 h_1}{1 + \frac{\mathrm{M}_1}{\mathrm{M}_2}(h_1/h_2)} \end{aligned} \tag{3.14}$$

If $h_2 \to \infty$, which would be the case for a thin film (1) on a thick substrate (2), then equation 3.14 simplifies to:

$$\tilde{E}_{elast} = \mathrm{M}_1 \varepsilon_{\max}^2 h_1 \tag{3.15}$$

That means the elastic strain energy $E_{elast}$ per unit area in the thin film is linearly dependent on the film thickness $h_1$.

### Strain Release through Misfit Dislocations

If the strain at an interface exceeds the maximum value $\varepsilon_{\max}$, dislocations are formed and part of the misfit strain is released. Two types of dislocations can be distinguished: edge and screw dislocations (pure edge and screw dislocations are extreme cases, often mixed types can be found). However, only edge dislocations can act to release local lattice strain. Therefore the following treatment will be limited to edge dislocations.

#### Strain Energy of Dislocations

Dislocations are themselves sources of strain fields. The strain “above” an edge dislocation, where an extra half plane of atoms is inserted in the crystal lattice, is compressive. Below this extra half plane, the lattice is dilatatively strained. This is shown in figure 3.6a).

The stress field around an edge dislocation can be illustrated by the elastic distortion of an isotropic cylindrical ring, as shown in figure 3.6b). The ring is slitted (L,M,N,O mark the radial slit parallel to the $z$-axis) and the faces of the slit are displaced against each other in $x$-direction by a distance $b$, which corresponds to the Burgers vector of the dislocation. No disarrangement takes place in the $z$-direction, therefore all strain components in this direction are zero. The compo-

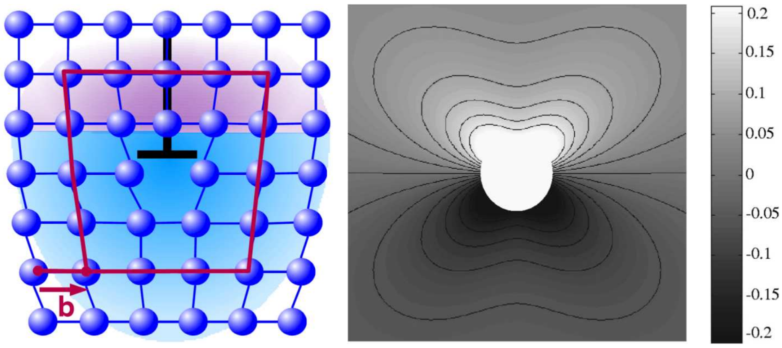

(a) (b)

**Figure 3.6:** a) Schematic picture of the strained crystal lattice around an edge dislocation with Burgers vector $\vec{b}$. Blue: tensile strain; red: compressive strain. b) Calculated strain field $\varepsilon_{xx}(x, y)$ around an isolated edge dislocation extending in the $z$-direction of an infinite elastic medium. Continuum elasticity theory was used for the calculation. The picture shows an area in the $x, y$-plane and has the size $16\vec{b}^2$ ($\vec{b}$ extends in the horizontal paper plane). Maximum tensile strain corresponds to white, maximum compressive strain to black. The white space at the centre represents the dislocation core, where the calculation produces a singularity. Picture taken from [45].

nents of the stress field can be calculated using continuum elasticity theory [44], which is the basis of all following calculations:

$$
\begin{aligned}
\sigma_{xx} &= -Dy\frac{\left(3x^2+y^2\right)}{\left(x^2+y^2\right)^2} \\
\sigma_{yy} &= Dy\frac{\left(x^2-y^2\right)}{\left(x^2+y^2\right)^2} \\
\sigma_{xy} &= \sigma_{yx} = Dy\frac{\left(x^2-y^2\right)}{\left(x^2+y^2\right)^2} \\
\sigma_{zz} &= \nu\left(\sigma_{xx}+\sigma_{yy}\right) \\
\sigma_{xz} &= \sigma_{zx} = \sigma_{yz} = \sigma_{zy} = 0
\end{aligned}
\qquad (3.16)
$$

The abbreviation $D$ is defined as $D = \frac{G\vec{b}}{2\pi(1-\nu)}$.

$\sigma_{xx}$ acts parallel to the slip vector and is therefore the largest contribution. The slip plane is defined as $y = 0$. Immediately above and below the slip plane, the maximum compressive ($\sigma_{xx} < 0$) and the maximum tensile ($\sigma_{xx} > 0$) stress is

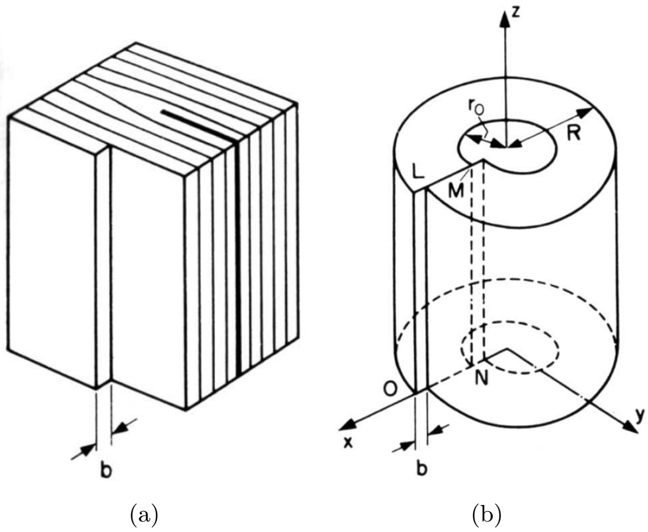

(a) (b)

**Figure 3.7:** a) Schematic picture of an edge dislocation. b) Lattice distortion produced by an edge dislocation, simulated by the elastic distortion of a cylindrical ring. $b$ denotes the Burgers vector in a), respectively the displacement in $x$-direction in b). Taken from [44].

found. This nicely compares to figure 3.6b), where the calculated strain field $\varepsilon_{xx}$ in the $x, y$-plane around an isolated edge dislocation is shown [45][1].
The magnitude of the strain in figure 3.6b) is brightness encoded, ranging from white (max. tensile strain) to black (max. compressive strain).
The effective pressure caused by the dislocation can be calculated by equation 3.8. The result is:

$$p = \tfrac{2}{3}\left(1+\nu\right) D \frac{y}{\left(x^2+y^2\right)} \tag{3.18}$$

It can easily be seen that the pressure gets smaller when the distance from the dislocation line axis (the $z$-axis of the cylindrical ring) gets larger. If $x$ or $y$ approach zero, this equation can no longer be applied. It is only valid if the distance from the line axis exceeds the dislocation core radius $r_0$.
The distortion of the crystal lattice by a dislocation adds an extra strain energy to the total energy, which divides into two parts:

$$E_{total} = E_{core} + E_{elastic}$$

---

[1] The equation used for this calculation in the cited literature source is:

$$\varepsilon_{xx} = \frac{\vec{b}}{4\pi\left(1-\nu\right)} \frac{y\left(x^2-y^2\right)}{\left(x^2+y^2\right)^2} + \frac{\vec{b}}{2\pi} \frac{y}{x^2+y^2} \tag{3.17}$$

$\vec{b}$ is the Burgers vector, extending in $x$ direction.

$E_{elastic}$ may be interpreted as the work needed in displacing the slit faces by $b$ against the resisting internal stresses. The internal stresses on $y = 0$ build up from zero to their final values during the displacement process. For an infinitesimal element $dA$ of the area of the slit plane L M N O in figure3.7b), the work is thus:

$$dE_{elast} = \tfrac{1}{2}\sigma_{xy} b dA \tag{3.19}$$

The total strain energy per unit length of dislocation can be gained by integration of equation 3.19 along the $x$-direction from $r_0$ to the crystal radius $R$ (which is defined as the distance to the next (inner) surface or the next dislocation line):

$$E_{elast} = \frac{G\vec{b}^2}{4\pi\left(1-\nu\right)} \int\limits_{r_0}^{R} \frac{dx}{x} = \frac{G\vec{b}^2}{4\pi\left(1-\nu\right)} \ln\left(\frac{R}{r_0}\right) \tag{3.20}$$

Since $E_{elast}$ is proportional to $\vec{b}^2$, dissociation of a dislocation into two dislocations with a smaller Burgers vector, for example into two Shockley partials creating a stacking fault, leads to a lowering of the energy. It also leads to an increased dislocation mobility because of an extension of the dislocation core [48].

Typically, crystals do not contain only one isolated dislocation. If several dislocations are present, they are often arranged so that the superimposed long-range elastic fields cancel each other and the energy per dislocation is reduced. The value for $R$ would then be approximately half the average spacing of the dislocations when the dislocations are placed at random.

The core energy of a dislocation can only be estimated coarsely, and it varies as the dislocation moves through the crystal. Estimated values for $E_{core}$ are 0.1-0.3 aJ [44] for each atom plane that is threaded by the dislocation. Compared to the values for $E_{elast}$, which are in the order of 1 aJ (6 eV) per atomic plane, these values are small.

As was mentioned above, a pure edge dislocation is an extreme case. Often a dislocation exhibits edge and screw parts. The elastic strain energy per unit length of a screw dislocation is lower than that of an edge dislocation by $1/(1-\nu)$. The total elastic energy of a mixed type dislocation is simply the sum of edge and screw parts because there is no interaction between these two different strain fields. A more detailed calculation of the strain energy of both types of dislocations can be found in [44].

### Critical Layer Thickness for the Emergence of Dislocations

As derived in section 3.1.2, the strain energy of a thin film system with coherent interfaces increases proportionally to the film thickness. Once the strain energy exceeds a certain value, it is energetically more favourable to introduce misfit dislocations. The film thickness marking this threshold is the critical film thickness $h_c$. Basically, $h_c$ can be calculated by setting the elastic strain energy of the thin film system (see equation 3.14) equal to the energy of an isolated misfit dislocation (equation 3.20) or a dislocation network (depending on the way in which dislocations are introduced to the system) and minimizing the total energy. Several theoretical models have been developed dealing with the details of this calculation and mainly differing in the way the dislocations are considered. One has to distinguish between purely thermodynamic models considering only equilibrium states and models which also comprise kinetic considerations dealing with activation barriers for the nucleation and movement of dislocations and thereby also allowing solutions for metastable states.

Two well-known thermodynamic models are the Van-der-Merwe (VM) [49, 50] and the Matthews and Blakeslee (MB) [51–54] theory. Both theories do not consider nucleation mechanisms for dislocations. Van-der-Merwe made the first approach by calculating critical values for the misfit between a substrate and a thin film of a given thickness assuming an equilibrium between the interfacial energy (with or without misfit dislocations present in the interface) and the areal strain energy density in the film. The MB theory considers the forces acting on threading dislocations which bend into the interface plane creating misfit dislocations when $h > h_c$ [2]. It yields the following result for $h_c$:

$$h_c = \frac{\left|\vec{b}\right| \left(1 - \nu \cos^2 \alpha\right)}{2\pi f (1+\nu) \cos\lambda} \ln \frac{h_c}{\left|\vec{b}\right|} + 1 \tag{3.21}$$

The interfacial strain $\varepsilon$ is replaced by the misfit $f$. $\nu$ is Poisson´s ratio, $\vec{b}$ is the dislocations Burgers vector, $\alpha$ is the angle between the dislocation line and its Burgers vector and $\lambda$ is the angle between the slip direction of the interface and the slip plane normal projected into the interface. Equation 3.21 applies to systems where the elastic properties of the adjoining materials can be treated as equal and isotropic. It is implicit with reference to $h_c$ and has to be solved numerically.

The result from the MB theory applies to the case of a thin film on a much thicker substrate. It was generalised by Freund and Nix [46] for systems with compliant substrates and epitaxial thin films. They obtain the following result for the maximum mismatch strain $\varepsilon_{max}$ which can be compensated without introducing dislocations:

$$\varepsilon_{max} = \frac{\left[b_x^2 + b_y^2 + (1-\nu)\, b_z^2\right]}{8\pi\,(1+\nu)} \frac{t_s + t_f}{t_s t_f} \ln \frac{t_s t_f}{r_0\,(t_s + t_f)} \tag{3.22}$$

$b_{x,y,z}$ are the three components of the Burgers vector, $t_{s,f}$ is the thickness of the substrate, respectively the thin film and $r_0$ is the core radius of the dislocation.

---

[2] The MB theory is based on investigations on GaAs - $\mathrm{GaAs_{0.5}P_{0.5}}$

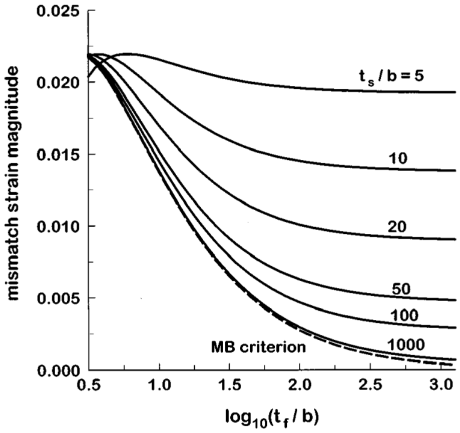

**Figure 3.8:** Plot illustrating the critical thickness condition for relaxation in cubic materials by the formation of 60° dislocations in a (100) interface, as derived by FREUND and NIX (taken from [46]). The magnitude of mismatch strain $|\varepsilon_{max}|$ at which the critical thickness condition in equation 3.22 is fulfilled is shown in relation to the film thickness $t_f$ normalised by the length of the Burgers vector and for several values of the normalised substrate thickness $t_s/b$.

The results for different values of $t_f$ and $t_s$ are shown in figure 3.8. For the case of a much thicker substrate, the terms $(t_s + t_f)$ and $t_s$ vanish; the resulting equation is equal that obtained by the MB theory.

Using the results of FREUND and NIX, only a coarse estimate can be made of $h_c$ in systems were films of similar thickness meet at an interface. The reason is that the equation for the self-energy of a dislocation used by FREUND and NIX is only an approximation and the greatest difference to the more exact result obtained within the framework of elastic dislocation theory [55] occurs when $t_s = t_f$, at least for the case of a screw dislocation ($b_x = b_y = 0$). The problem is that exact solutions for the self energy of any other dislocation types are hard to obtain.

In contrast to the VM and MB theories, PEOPLE and BEAN [56, 57] assumed the films to be initially free of dislocations and considered mechanisms for their nucleation, concentrating on screw dislocations because these have the lowest energy density[3] and are therefore expected to nucleate first. Dislocations are supposed to be formed when the areal strain energy density in the film (calculated according to VAN DER MERWE) exceeds the energy density associated with the generation of an isolated screw dislocation at a distance from the free surface

---

[3] Energy densities of screw, edge and half-loop dislocations have been calculated by NABARRO [58]

equal to the film thickness $h$. The obtained result for the critical layer thickness is:

$$h_c \simeq \left(\frac{1-\nu}{1+\nu}\right)\left(\frac{1}{16\pi\sqrt{2}}\right)\left[\frac{\vec{b}^2}{a}\right]\left[\left(\frac{1}{f^2}\right)\ln\left(\frac{h_c}{\vec{b}}\right)\right] \tag{3.23}$$

$a$ is the bulk lattice constant of the film. The authors compared this result to experimental data of the system $\mathrm{Ge}_x\mathrm{Si}_{1-x}$ films on Si substrates and found an excellent agreement.
Of course, a lot more literature exists dealing with critical layer thicknesses in thin film systems, for example [47] or [59], which either adopt one of the presented theories or use slight variations. Marée et al. focus on dislocation slip mechanisms in semiconductor systems and investigate differences in strain accommodation for compressive and tensile strain [48]. Chidambarrao et al. [60] take into account the influence of the orientation of epithreading [4] dislocations and the growth temperature of the thin films and find that non-equilibrium states can be frozen-in because of the energy barrier existent for the nucleation of dislocations. His findings apply to a growth temperature range around 500 °C and are therefore not reported in detail here.
In general, the agreement between theoretical and experimental results is much better for metals than for semiconductor systems [43]. This can be explained on one hand by the large perfection of semiconductor substrates and growth methods which require the homogeneous nucleation of dislocations instead of glide mechanisms and on the other hand in terms of friction forces (Peierls-Nabarro friction stress) reducing the mobility of dislocations [48]. A closer analysis, including kinetic considerations of strain relaxation and the influence of friction stress, can be found in [61].

## 3.2 Impact of Interface Properties on Ionic Conductivity

Interfaces are not only characterised by structural differences to the bulk, they also exhibit special thermodynamic properties like chemical potentials for defects and charge carriers. Charge carrier concentrations as well as the mobilities of the charge carriers in the interface are different from the those in the bulk. This leads to special ionic and electronic conductivities. Either an enhancement or a blocking effect is found compared to the bulk. Blocking effects are typically observed for grain boundaries in YSZ [27, 62–64] and when transport takes place across the interfaces. For transport along the interfaces, an enhancement was observed in several heterogeneous systems (see part II or for example [10,65,66]). The special design of systems typically combining an insulator with an ionic conductor is often

---

[4] threading dislocations generated not in the substrate but in the thin film epilayer

referred to as heterogeneous doping (for example [31, 67, 68]). A very popular model used to explain the transport properties of interfaces is the space charge concept, which will therefore be briefly presented in the following. After that, the influence of structural parameters like lattice strain and misfit dislocations on the conductivity will be discussed using simple kinetic considerations.

### 3.2.1 The Space Charge Concept

The space charge concept was first used by Wagner to explain conductivity effects in semiconductor heterophases [69]. Since then, important theoretical work has been performed by MAIER et al. [14,15,17,31,70–72] and JIANG and WAGNER [1]. The space charge model describes the special defect chemistry of interfaces. According to this model, charge carriers can be adsorbed or depleted in the interface, depending on whether the interactions of the given interface with different charged defects are attractive or repulsive. Adsorption of one charge carrier in the interface core results in an increasing concentration of oppositly charged carriers in the regions adjacent to the interface. This leads to the formation of a space charge region in the dimension of the materials Debye length. An accumulation of one charge carrier in the space charge zone leads to an extrinsically increased local conductivity of this carrier compared to the volume value. Depletion of a charge carrier, on the other hand, leads to decreased interfacial conductivity. The effect on conductivity parallel to the interfaces can best be expressed in terms of an excess conductance $\Delta Y^{\|}$ ($Y^{\|} = \sigma^{\|}/L$, $L =$ layer thickness), describing the additional interfacial contribution to the total conductance. For the case that one charge carrier ($i$) dominates (which is valid for most practically important materials) and is accumulated in the space charge zone, $\Delta Y^{\|}$ can be expressed by [73]:

$$\mathit{\Delta} Y_i^{||} \simeq e_0\,(2\lambda)\,u_i\sqrt{(c_{i0}c_{i\infty})} \tag{3.24}$$

$e_0$ is the electron charge, $u_i$ is the defect mobility, $c_{i0}$ is the charge carrier concentration in the first layer next to the interface and $c_{i\infty}$ is the bulk concentration. For the minority charge carrier ($k$), which is depleted in the space charge zone, one obtains:

$$-\mathit{\Delta} Y_k^{||} \simeq e_0\,(2\lambda)\,u_k c_{k\infty} \ll \mathit{\Delta} Y_i^{||} \tag{3.25}$$

which is a small, negative quantity. These equations show what is almost self-evident: the effect of space charge regions is most important for materials with low charge carrier concentrations and therefore large extensions of the space

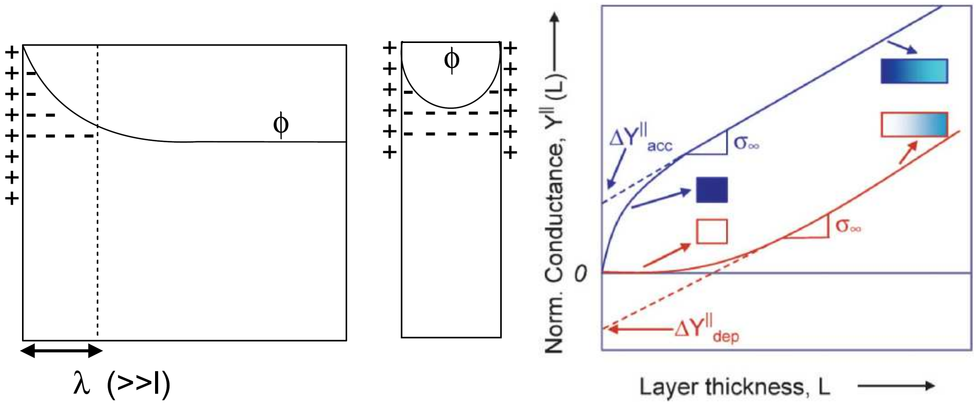

(a) (b)

**Figure 3.9:** a) Space charge regions inside a crystal. The effect of space charges dominates the interfacial conductivity if $\lambda$ is larger than the extension $l$ of structurally distorted regions at the interface. Right hand side: overlapping space charge regions at interface distances below $2\lambda$. Taken from [16]. b) Normalised conductance as a function of layer thickness. The excess conductance $\Delta Y^{\|}$ is positive for an accumulation effect and negative for a depletion effect. If the layer thickness is larger than the space charge zone, the behaviour is linear. Taken from [13].

charge zones[5].

With growing concentration of interfaces (declining size of crystallites or layers in thin film samples), the interface conductivity has a growing impact on the total conductivity. This is considered as a trivial size effect. So called "true" size effects appear at microstructural dimensions were space charge regions overlap [16, 75, 76]. An example for systems with overlapping space charge regions are layered structures with individual layer thicknesses in the dimension of or below the Debye length $\lambda$. In these systems, electrochemical potentials and charge carrier concentrations differ distinctly from bulk values everywhere in the material.

A schematic picture of the space charge layers at a boundary inside a crystal is shown in figure 3.9a) [16], for overlapping as well as non-overlapping space charge regions. In this scheme, $\Phi$ is the electric potential, $\lambda$ is the Debye length (the extension of the space charge layer) and $l$ is the extension of structurally perturbed regions (MAIER supposed $l$ to be significantly smaller than $\lambda$ in this picture; however, this is only the case for materials were the charge carriers are highly diluted).

---

[5] For 2 mol% $Y_2O_3$ doped $ZrO_2$, GUO et al. determined the effective thickness of the space charge layers to be around 2-4 nm [64], whereas in 16 mol% Fe-doped $SrTiO_3$, the space charge layers were found to be about 70 nm [74].

Figure 3.9b) [13] depicts the effect of space charge regions on the geometrically normalised conductance $Y^{\parallel}$[6] parallel to an interface in relation to the layer thickness $L$. Above a given layer thickness where neighbouring space charge regions do not overlap, $Y^{\parallel}$ rises linearly with $L$ (bulk behaviour). A steep increase of $Y^{\parallel}$ is found for small values of $L$ if an accumulation effect prevails in the space charge regions. At such small values of the layer thickness, the space charge regions of neighbouring interfaces overlap. The value of $L$ at which $Y^{\parallel}$ starts to increase linearly can therefore be interpreted as the thickness of the space charge layers if no other effect is present which alters the interface conductance. The excess conductance $\Delta Y^{\parallel}$ is defined as the difference between the value obtained by extrapolation of the linear behaviour and the actual value of $Y^{\parallel}$ for $L = 0$. It is positive for an accumulation effect. If the major charge carrier is depleted in the space charge region, the characteristics of $Y^{\parallel}$ for small values of $L$ is more flat compared to the linear characteristics and $\Delta Y^{\parallel}$ is negative.

### 3.2.2 The Influence of Lattice Strain and Dislocations.

The Effect of Pressure and Strain

Several investigations have been made concerning the effect of hydrostatic pressure on the (self-)diffusion in metals, for example [77, 78] or [79]. Similarly, the pressure dependency of the ionic conductivity has been investigated for different materials [80–83]. The observed effects are related to the prevailing transport mechanism. For impurity doped NaCl, KCl and RbCl, for example, in which the extrinsic conductivity is based on a vacancy mechanism, a decrease in conductivity with increasing pressure was reported [84]. A study of the influence of compressive strain on Ge and impurity diffusivity in SiGe/Si superlattices was carried out by COWERN et al. [85]. They found an enhanced diffusivity for a vacancy mechanism, but a decrease for interstitial transport. The effects were explained in terms of the formation volume for the relevant mobile species. Comprehensive studies analysing the relation between pressure and ionic conductivity in alkali halides by discussing the formation as well as migration volumes of defects using different theoretical approaches have been undertaken by YOON and LAZARUS [86]. AZIZ presented a thermodynamic formalism to calculate the formation and migration volumes as well as the change in diffusivity for vacancy and interstitial mechanisms, differentiating between hydrostatic pressure and biaxial stress states [87]. Investigations on M-$\beta$-aluminas with M = Na, K and Li focused on the influence of pressure in connection with the

---

[6] $Y^{\parallel} = \Delta z / R^{\parallel} \Delta y$, $\Delta z$ and $\Delta y$ being the geometrical parameters perpendicular to the film thickness $L$ and $R^{\parallel}$ being the resistance parallel to the film.

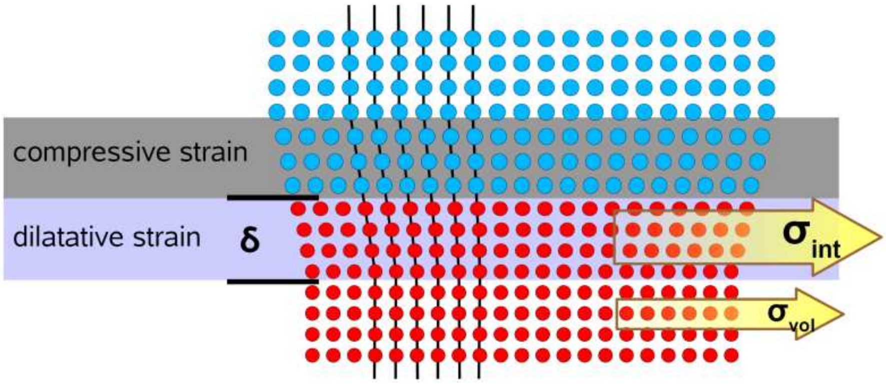

**Figure 3.10:** Example showing different types of strain at an interface. The dilatatively strained lattice region $\delta$ shows wider lattice spacings, the compressively strained region is more narrow compared to the relaxed volume phase. Figure after [26].

size of the migrating cation: The conductivity decreased with increasing pressure for M = K but increased for M = Li, whereas no effect was found for Na [88].

Simple thermodynamic considerations may be applied to derive an expression for the relation between the ionic conductivity and the strain present in a layered system with a given misfit between the layers. As shown by equation 3.8, elastic stress and strain in a crystal lattice lead to an effective pressure acting on the crystal volume. Compressive strain corresponds to an increased pressure $p$, tensile strain to a decreased $p$ (see figure 3.10). We can therefore start analysing the effect of strain by considering the effect of pressure.

In case of an extrinsic oxygen ion conductor and a vacancy based transport mechanism, the following equation is valid for $\sigma_{\mathrm{O}^{2-}}$:

$$\sigma_{\mathrm{O}^{2-}} = \frac{\sigma^0_{\mathrm{O}^{2-}}}{T} \exp\left(-\frac{\Delta G^{\mathrm{M}}_{\mathrm{V}_{\mathrm{O}}^{\cdot\cdot}}}{RT}\right) \tag{3.26}$$

$\Delta G^{\mathrm{M}}_{\mathrm{V}_{\mathrm{O}}^{\cdot\cdot}}$ is the free enthalpy of migration for oxygen vacancies. $\sigma^0_{\mathrm{O}^{2-}}$ includes the extrinsically fixed oxygen vacancy concentration $c_{\mathrm{V}_{\mathrm{O}}^{\cdot\cdot}}$, a geometry factor, the jump distance and the vibration frequency (which is normally assumed to be of the order of the Debye frequency [84]). If we assume the quantities in the preexponential factor $\sigma^0_{\mathrm{O}^{2-}}$ as pressure independent, respectively their pressure

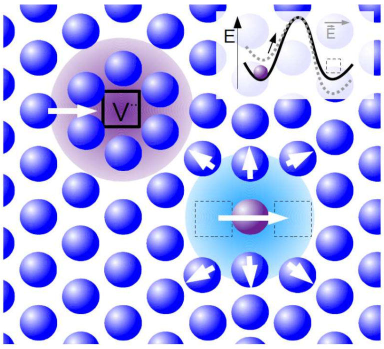

**Figure 3.11:** Schematic picture of the lattice deformation caused by a vacancy and a jump process of an ion to a neighbouring lattice side, illustration the migration volume. The inset shows the energy barrier which has to be overcome during the jump process. Black line: diffusion process; grey dashed line: electric field driven migration.

dependence to be small, the pressure dependence of the ionic conductivity $\sigma_{O^{2-}}$ yields as follows[7]:

$$\left(\frac{\partial \ln \sigma_{O^{2-}}}{\partial p}\right)_T = -\frac{\mathit{\Delta} V^{\mathrm{act}}_{\mathrm{V}_{\mathrm{O}}^{\cdot\cdot}}}{RT} \approx -\frac{\mathit{\Delta} V^{\mathrm{M}}_{\mathrm{V}_{\mathrm{O}}^{\cdot\cdot}}}{RT} \tag{3.28}$$

$\mathit{\Delta} V^{\mathrm{act}}_{\mathrm{V}_{\mathrm{O}}^{\cdot\cdot}}$ is the activation volume for the transport of oxygen vacancies. It can be separated into the defect formation volume $\mathit{\Delta} V^{\mathrm{f}}_{\mathrm{V}_{\mathrm{O}}^{\cdot\cdot}}$ and the migration volume $\mathit{\Delta} V^{\mathrm{M}}_{\mathrm{V}_{\mathrm{O}}^{\cdot\cdot}}$. In an extrinsic oxygen ion conductor, where the oxygen vacancy concentration is fixed by the dopant level and thus is not pressure dependent, the volume of defect formation can be neglected. The value of $\mathit{\Delta} V^{\mathrm{M}}_{\mathrm{V}_{\mathrm{O}}^{\cdot\cdot}}$ depends on the local deformation of the lattice during the jump process (see figure 3.11). In case of a vacancy mechanism it is always positive.

For reasons of simplicity, isotropic mechanic properties are assumed. The isotropic pressure $p$ in a biaxial strained thin film system in a region of a phase 1 close to the interface can be calculated as follows:

$$p = -\frac{2}{3}\frac{\mathrm{Y}_1}{1-\nu_1}\varepsilon_{12} \tag{3.29}$$

For coherent interfaces, the biaxial elastic strain $\varepsilon_{12}$ in phase 1 is proportional to the lattice misfit $f_{12}$. In case of columnar crystallites, where the strain is

---

[7] A more exact expression would be:

$$\left(\frac{\partial \ln \sigma_{O^{2-}}}{\partial p}\right)_T = -\frac{\mathit{\Delta} V^{\mathrm{M}}_{\mathrm{V}_{\mathrm{O}}^{\cdot\cdot}}}{RT} + \left(y_{\mathrm{G}} - \frac{2}{3}\right)\kappa_{\mathrm{T}} \tag{3.27}$$

with $y_{\mathrm{G}}$ being the Grüneisen constant and $\kappa_{\mathrm{T}}$ the isothermal compressibility.

located near the interfaces and a relaxation takes place into the volume, the change of the ionic conductivity when we move from the grain volume ($\sigma_{\mathrm{vol}}$) to an elastically strained region close to the phase boundary ($\sigma_{\mathrm{int}}$) can be estimated from equations (3.28) and (3.29), substituting $\varepsilon_{12}$ by $f_{12}$:

$$\ln \sigma_{\mathrm{int}} - \ln \sigma_{\mathrm{vol}} = \ln \frac{\sigma_{\mathrm{int}}}{\sigma_{\mathrm{vol}}} \propto \mathit{\Delta} V^{\mathrm{M}}_{\mathrm{V}_{\mathrm{O}}^{\cdot\cdot}} f_{12} \tag{3.30}$$

A linear dependence of the logarithm of the interfacial conductivity $\sigma_{\mathrm{int}}$ on the lattice misfit $f_{12}$ results.

### The Effect of Dislocations

Dislocations may present new pathways for transport and thereby also influence ionic conductivity. If the transport preferably takes place along dislocation lines, the conductivity should be linearly related to the interface density $P$:

$$P = \frac{f_{12}}{\vec{b}} \tag{3.31}$$

In systems where the contribution of dislocations and other lattice defects to the change in transport properties at interfaces is larger than the effect of strain induced lattice deformation, we should expect the highest interfacial conductivities for incoherent or dislocation rich semicoherent interfaces. If, on the other hand, strain effects exert a major influence on transport, the biggest effect should be observed in coherent systems with a large mismatch or in comparable semicoherent systems with a low density of dislocations.

# 4 Material Properties

## 4.1 Structural Relationship between Bixbyite Type Rare Earth Oxides and Fluorite Type Zirconium Oxide

$ZrO_2$ exists in three different crystallographic modifications. At temperatures below 1170 °C, the monoclinic structure is stable. Between 1170 °C and 2370 °C, a tetragonal structure is found. The cubic structure of the $CaF_2$-type is stable at temperatures above 2370 °C [89–92]. In $Y_2O_3$ doped $ZrO_2$ (fully stabilised: minimum 7-8 mol-% [62], typically 9.5 mol-% $Y_2O_3$), the cubic structure with the space group $Fm\overline{3}m$ is stabilised at room temperature. The cubic face centred (fcc) cation sublattice can be described in terms of edge linked octahedrons, anions are place in tetrahedral interstices (see figure 4.1a); the anion sublattice is primitive cubic. The sesquioxides ($RE_2O_3$) of the heavy Lanthanoides crystallise preferentially in the also cubic bixbyite structure ($\alpha$-$Mn_2O_3$ type, $Ia\overline{3}$). The fluorite and the bixbyite structure are crystallographically related: the bixbyite type can be deduced from the fluorite type by doubling the lattice parameter (see figure 4.1b). 16 oxygen ions are removed from the cell. Finally, a relaxation of the anion positions and a transformation of the axes of (+1/4, +1/4, +1/4) takes place to yield the real structure (figure 4.1c).

The relationship of the lattice parameters between YSZ and $RE_2O_3$ is $a_{RE_2O_3} \approx 2a_{YSZ}$, establishing a 2:1 commensurability. Interfaces between YSZ and $RE_2O_3$ are expected to be preferentially coherent or semicoherent, depending on the mutual lattice mismatch of the oxides. Structural data for relevant materials are given it table 4.1.

A. Peters [19] found that the preferred orientation relationship in the multilayer system YSZ | $Y_2O_3$ on (0001) sapphire substrates is $Al_2O_3$ (0001) ∥ $Y_2O_3$ (111) ∥ YSZ (111). Due to the similarity of the rare earth oxides used in this work compared to $Y_2O_3$, identical orientation relationships can be expected if the same substrates are used. The relevant lattice planes for calculating the misfit are those perpendicular to the (111) axis, namely the lattice planes $(\bar{1}10)$ and $(11\bar{2})$. The misfit $f$ between YSZ and $RE_2O_3$ is given in table 4.2. It is calculated using equation 4.1 and considering the 2:1 commensurability between the lattice spacings of YSZ and the rare earth oxides as mentioned above.

$$f = \frac{d_{(\bar{1}10)}(\mathrm{RE_2O_3}) - 2 \cdot d_{(\bar{1}10)}(\mathrm{YSZ})}{2 \cdot d_{(\bar{1}10)}(\mathrm{YSZ})} \cdot 100\% \tag{4.1}$$

| Material | Structure Type | $a$ [Å] |
|---|---|---|
| YSZ (9.5 mol% $Y_2O_3$) | $CaF_2$ | 5.143 [93] |
| $Sc_2O_3$ | $\alpha$-$Mn_2O_3$ | 9.8460 [94] |
| $Lu_2O_3$ | $\alpha$-$Mn_2O_3$ | 10.3910 [94] |
| $Y_2O_3$ | $\alpha$-$Mn_2O_3$ | 10.604 [95] |

**Table 4.1:** Summary of structural data for YSZ and the rare earth oxides used for the multilayer systems, including $Y_2O_3$.

| Material | $d_{(\bar{1}10)}$ [Å] | $d_{(11\bar{2})}$ [Å] | Mismatch [%] |
|---|---|---|---|
| YSZ (9.5 mol-% $Y_2O_3$) | 3.6367 | 2.0996 | |
| $Sc_2O_3$ | 6.9622 | 4.0196 | –4.28 |
| $Lu_2O_3$ | 7.3475 | 4.2421 | 1.02 |
| $Y_2O_3$ | 7.4982 | 4.3291 | 3.09 |

**Table 4.2:** Mismatch between YSZ and the different rare earth oxides $RE_2O_3$, calculated for the $(\bar{1}10)$ plane.

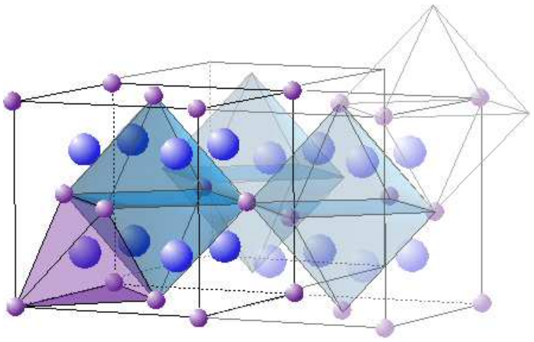

(a) $CaF_2$ structure type

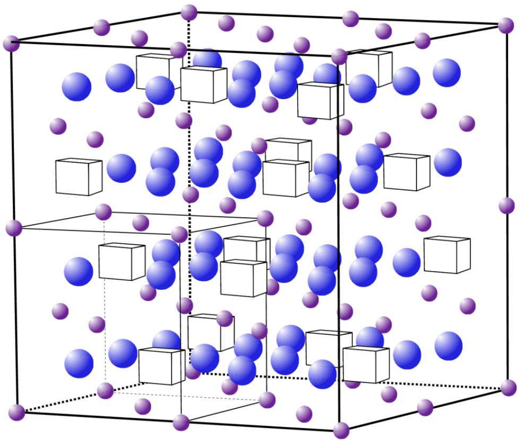

(b) simplified, Bixbyite-like structure

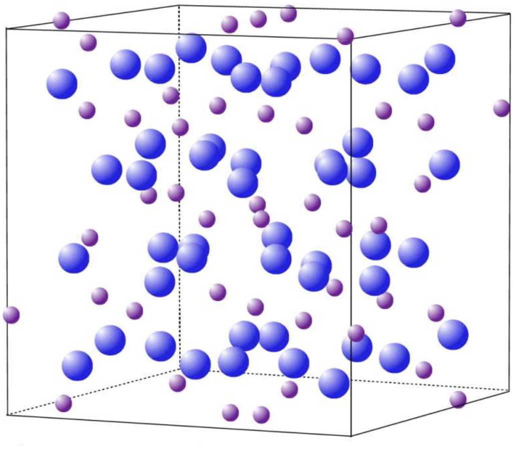

(c) Bixbyite structure type

**Figure 4.1:** Comparison of the unit cells of YSZ ($CaF_2$ - structure) and $RE_2O_3$ (Bixbyite structure). Blue spheres: oxygen ions; red spheres: metal ions. a) $CaF_2$ structure type. b) Simplified (not realistic!) structure, constructed out of 8 unit cells of the fluorite structure type. The introduced oxygen vacancies are displayed by white cubes. c) Real bixbyite structure. The atomic radii are not displayed realistic in the pictures above.

## 4.2 Transport Phenomena

### 4.2.1 Transport Properties of Yttria-Stabilized Zirconia (YSZ)

Pure $ZrO_2$ is an oxygen ion conductor of the anti-Frenkel disorder type [96, 97]. Between 700 °C and 1000 °C and in an oxygen partial pressure range of $10^{-22} \leq p_{O_2} \leq 1$ atm, it also shows electronic conduction [98] with an $n$ to $p$-type transition at $10^{-16}$ atm [99].

The predominant ionic defect reaction in pure $ZrO_2$ is the formation of interstitial oxygen ions ($\mathrm{O}_i''$), creating oxygen vacancies ($\mathrm{V}_\mathrm{O}^{\cdot\cdot}$) on regular lattice sites.

$$\mathrm{O}_\mathrm{O}^\times + \mathrm{V}_i^\times \rightleftharpoons \mathrm{O}_i'' + \mathrm{V}_\mathrm{O}^{\cdot\cdot} \tag{4.2}$$

The minor charge carriers are electronic defects (electrons in the conduction band $\mathrm{e}_\mathrm{CB}'$ and electron holes in the valence band $\mathrm{h}_\mathrm{VB}^{\cdot}$):

$$\mathrm{e}_\mathrm{VB}^\times + \mathrm{h}_\mathrm{CB}^\times \rightleftharpoons \mathrm{e}_\mathrm{CB}' + \mathrm{h}_\mathrm{VB}^{\cdot} \tag{4.3}$$

For small variations of the oxygen partial pressure around the value where a stoichiometric composition of $ZrO_2$ can be found (intrinsic region), the concentration of the ionic defects is constant and the conductivity is independent of $p_{\mathrm{O}_2}$. Under oxidizing or reducing conditions, the ionic defect concentrations and thereby the ionic conductivity become dependent on $p_{\mathrm{O}_2}$. Also, the minor charge carriers get an increasing impact on the total conductivity. Oxygen incorporation (oxidizing regime) or excorporation (reducing regime) can be described as:

$$\begin{aligned} &\tfrac{1}{2}\mathrm{O}_2(g) + \mathrm{V}_\mathrm{O}^{\cdot\cdot} + 2\mathrm{e}' \rightleftharpoons \mathrm{O}_\mathrm{O}^\times \\ &\tfrac{1}{2}\mathrm{O}_2(g) + \mathrm{V}_\mathrm{O}^{\cdot\cdot} \rightleftharpoons \mathrm{O}_\mathrm{O}^\times + 2\mathrm{h}^{\cdot} \end{aligned} \tag{4.4}$$

Doping $ZrO_2$ with aliovalent cations such as $Y^{3+}$, $Sc^{3+}$ or $Ca^{2+}$ stabilizes the cubic structure at room temperature and leads to an increased vacancy concentration. Highly doped zirconia therefore shows a considerable, predominantly ionic conduction [90]. A maximum for the ionic conduction exist at dopant levels of 12-13 % for $Y_2O_3$ stabilised $ZrO_2$ [101]. Increasing the dopant concentration above this level leads to the so-called negative dopant effect: less mobile defects associates between $\mathrm{Y}_\mathrm{Zr}'$ and $\mathrm{V}_\mathrm{O}^{\cdot\cdot}$ [102–104] are formed which results in a reduction of the ionic conductivity:

$$\mathrm{Y}_\mathrm{Zr}' + \mathrm{V}_\mathrm{O}^{\cdot\cdot} \rightleftharpoons \{\mathrm{Y}_\mathrm{Zr}\mathrm{V}_\mathrm{O}\}^{\cdot} \tag{4.5}$$

In doped $ZrO_2$, the region where the ionic conductivity is virtually independent on $p_{\mathrm{O}_2}$ is enlarged because the vacancy concentration is controlled extrinsically by the dopant content:

$$\mathrm{Y}_2\mathrm{O}_3 \xrightarrow{\mathrm{ZrO}_2} 2\mathrm{Y}_\mathrm{Zr}' + 3\mathrm{O}_\mathrm{O}^\times + \mathrm{V}_\mathrm{O}^{\cdot\cdot} \tag{4.6}$$

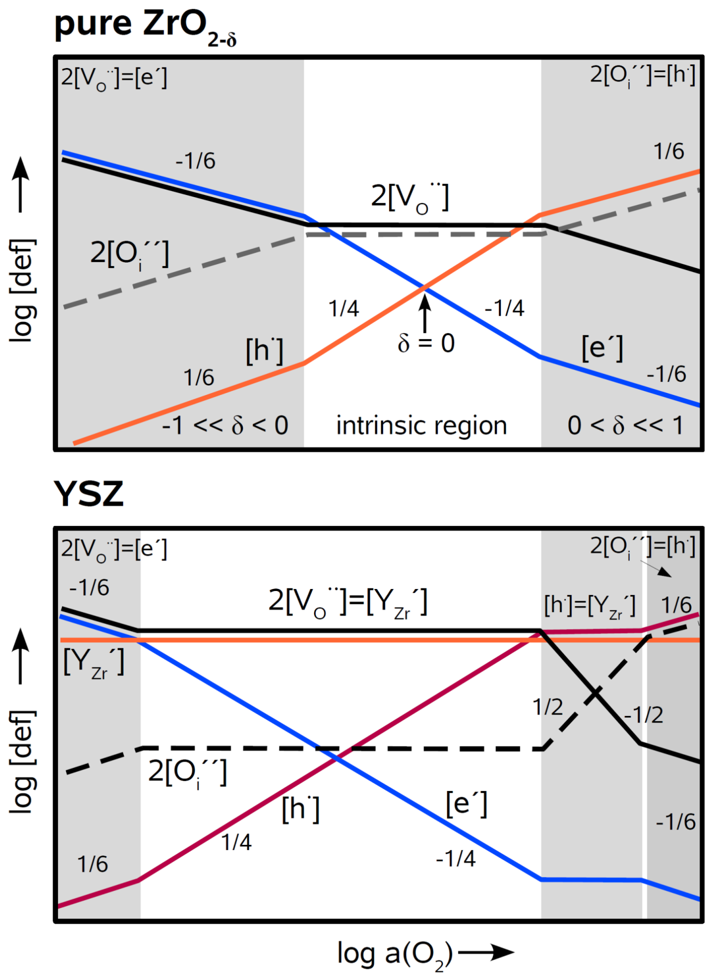

**Figure 4.2:** Kroeger-Vink diagrams for pure and yttria stabilized zirconia. The numbers in the diagrams represent the slopes (not shown realistically), the white area corresponds to the intrinsic regions. The oxidizing (high $p_{O_2}$) and reducing (low $p_{O_2}$) regimes are marked grey. After [100]

The defect concentrations in relation to the oxygen activity are depicted schematically in the Kroeger-Vink diagram for YSZ (see figure 4.2). A more detailed description of the defect equilibria in pure and doped $ZrO_2$ and the mathematical steps for creating the Kroeger-Vink diagram can be found for example in [100].

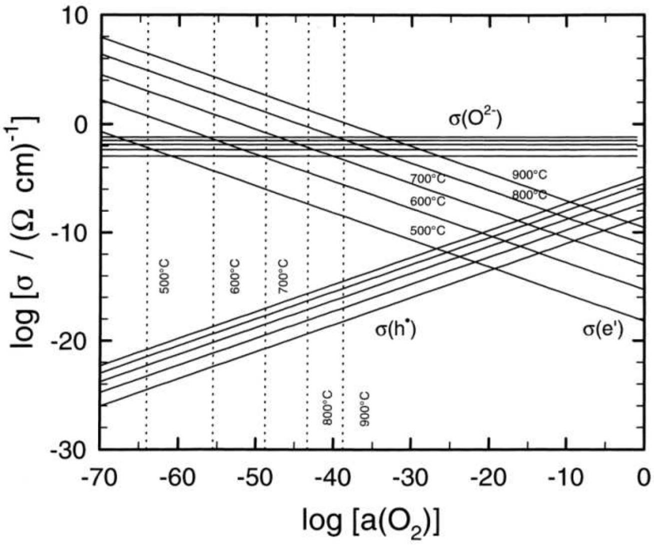

**Figure 4.3:** Conductivity of 8 mol-% yttria-stabilized zirconia in relation to the oxygen partial pressure and for different temperatures. Graph from [105], data from [106].

An overview of the electronic and ionic conductivities in relation to the oxygen partial pressure and at different temperatures is given for 8-mol % YSZ in figure 4.3. At ambient oxygen partial pressures, the electronic conductivity in YSZ is much smaller than the ionic conductivity (at least two orders of magnitude). According to Park and Blumenthal [106], the ionic transference number is greater than 0.99. This is due to the trapping of electronic charge carriers on appropriate lattice sites, namely at normal zirconium sites as $(\mathrm{Z}_{Zr}^{\times} - e')'$ and at yttrium ions on zirconium sites as $(\mathrm{Y}'_{Zr} - h^{\bullet})^0$. Therefore, when considering charge transport, electrons, respectively electron holes, can be neglected as long as the oxygen partial pressure is not very low or very high.

### 4.2.2 Transport Properties of Bixbyite Type Rare Earth Sesquioxides ($RE_2O_3$)

The rare earth oxides employed in this work have quite low total conductivities of about $10^{-7}$ S/cm to $10^{-6}$ S/cm at 1073 K (see figure 4.4), so they can safely be regarded as insulators. The major charge carriers in these rare earth oxides are electronic defects [20,22], leading to a p-type conduction. From the difference between the DC and AC conductivity at 10 kHz, the partial ionic conduction in $Y_2O_3$ and $Nd_2O_3$ was estimated to be about 30 % of the total conduction at temperatures over 700 °C in air [22]. Tare and Schmalzried [21] found $Gd_2O_3$, $Dy_2O_3$, $Sm_2O_3$ and $Y_2O_3$ to be pure ionic conductors in the oxygen partial pressure regime $p_{O_2} = 10^{-5} - 10^{-17}$ atm by measuring the EMF of electrochemical cells with the rare earth oxides as solid electrolytes at temperatures between 940 K and 1133 K. At higher oxygen partial pressures, the major charge carriers were found to be electron holes. However, no transference numbers or detailed values for the partial ionic or electronic conductivities were given in any of these publications.

Yun et al. [23] measured the conductivities of pure and CaO-doped $Lu_2O_3$. The result for pure $Lu_2O_3$ can be seen in figure 4.4 a). Comparable to Tare and Schmalzried, they found ionic conduction at oxygen partial pressures below $10^{-4}$ atm, the measured conductivities being independent of $p_{O_2}$ in this pressure range. At higher $p_{O_2}$, a p-type semiconductor behaviour was observed with an activation energy of 1.92 eV.

Subba Rao et al. explained the p-type electronic conduction with an oxygen excess in the rare earth oxides. Oxygen entering the crystal structure produces cation vacancies and electron holes [22]:

$$\tfrac{3}{4}\mathrm{O_2}(g) \xrightarrow{\mathrm{RE_2O_3}} \tfrac{3}{2}\mathrm{O_O^{\times}} + \mathrm{V_{RE}'''} + 3\mathrm{h^{\cdot}} \tag{4.7}$$

The resulting partial pressure dependency of the conductivity is:

$$\sigma \propto [\mathrm{h^{\cdot}}] \propto p_{O_2}^{1/5.3} \tag{4.8}$$

which was also found experimentally at temperatures between 400 °C and 700 °C and pressures ranging between 2 mmHg and 100 mmHg by the authors. However, the formation of threefold negatively charged cation vacancies does not seem very probable. An alternative mechanism would be the incorporation of oxygen at structural vacancies in the bixbyite lattice (compare to figure 4.1), leading to twofold negatively charged interstitial oxygen ions:

$$\tfrac{1}{2}\mathrm{O_2}(g) + V_i^{\times} \rightleftharpoons \mathrm{O_i''} + 2\mathrm{h^{\cdot}} \tag{4.9}$$

The relation between conductivity and oxygen partial pressure is then:

$$\sigma \propto [\mathrm{h^{\cdot}}] \propto p_{O_2}^{1/6} \tag{4.10}$$

Experimentally, a $1\,{}^{1}\!/6$ dependence of the conductivity on $p_{O_2}$ is hard to discern from the relation given by Subba Rao.

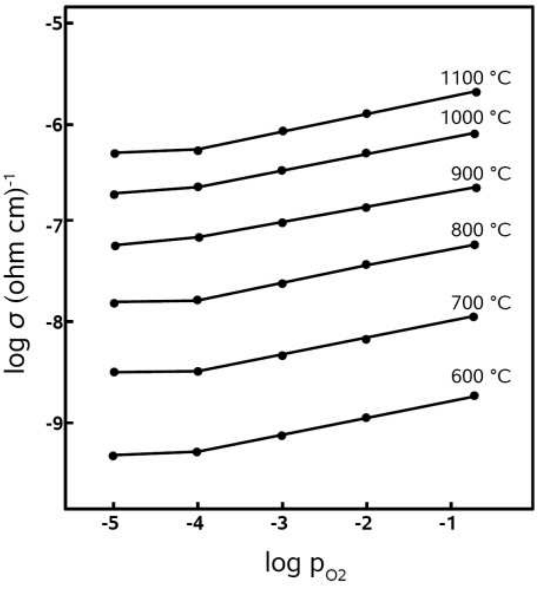

(a)

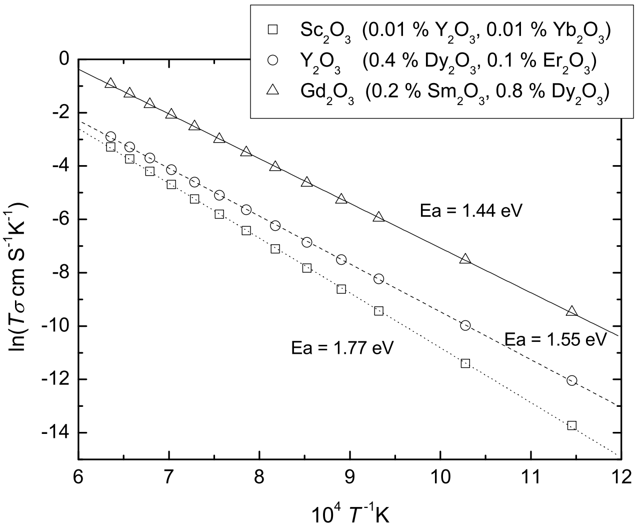

(b)

**Figure 4.4:** a) Total conductivity of pure $Lu_2O_3$, for different oxygen partial pressures and temperatures. After [23]. b) Total conductivity according to the measurements by NODDACK et al. [20]. The corresponding activation energies are also shown.

Noddack et al. measured the conductances of pressed pills of several rare earth oxides, including $Sc_2O_3$, $Y_2O_3$ and $Gd_2O_3$ [20]. Based on the data of his DC measurements at different temperatures in air, the conductivities were calculated and plotted in figure 4.4 b). He interpreted the conductivities to be of electronic character.

### 4.2.3 Transport in Thin Film Multilayer Systems

To derive an expression for the total conductivity $\sigma_{\text{tot}}$ of thin film multilayers, we assume the different transport paths to be parallel and independent from each other. One has to consider basically two contributions: the volume conductivity $\sigma_{\text{vol}}$ and the conductivity of the phase boundaries (referred to as interfaces) $\sigma_{\text{int}}$. However, the resulting equation would only be valid for single crystalline films. Thin films deposited by PLD or similar evaporation techniques are typically polycrystalline and show a columnar grain structure. Responsible for this is the characteristic growth process starting with small islands of material which gradually merge and continue growing perpendicular to the substrate. One therefore also has to consider the conductivity along grain boundaries $\sigma_{\text{gb}}$. If we calculate the total current from all parallel conduction paths, we obtain:

$$I = \sigma_{\text{tot}} A_{\text{tot}} \frac{U}{b} = (\sigma_{\text{vol}} A_{\text{vol}} + \sigma_{\text{int}} A_{\text{int}} + \sigma_{\text{gb}} A_{\text{gb}}) \frac{U}{b} \tag{4.11}$$

$b$ is the sample thickness parallel to the current direction. In a system with $n$ layers of an ionic conductor alternating with $n+1$ layers of an insulator, the lateral surfaces $A_i$ in equation 4.11 can easily be calculated using the width $l$ of the sample, the mean thickness $d$ of the ion conducting layers and the thickness $\delta$ of the interfacial regions (see figure 4.5a) for a schematic picture of the geometric parameters in a multilayer sample). The total lateral surface of the grain boundaries can be calculated if the thickness of the grain boundaries $\delta'$ and their volume density $c_{\text{gb}}$ is known. $c_{\text{gb}}$ should be constant for samples which were prepared using identical deposition parameters and annealing procedures.
The following equations for the different $A_i$ are obtained:

$$\begin{aligned}
A_{\text{tot}} &= A_{\text{vol}} + A_{\text{gb}} + A_{\text{int}} \\
A_{\text{vol}} &= nl\ (d-2\delta)(1-\delta' c_{\text{gb}}) \\
A_{\text{int}} &= nl\ 2\delta\,(1-\delta' c_{\text{gb}}) \\
A_{\text{gb}} &= n\ 2\,(d-\delta)\,\delta' c_{\text{gb}}
\end{aligned} \tag{4.12}$$

The full theoretical expression for $\sigma_{\text{tot}}$ is then:

$$\begin{aligned}
\sigma_{\text{tot}} = \sigma_{\text{vol}} &+ 2\delta\,(\sigma_{\text{int}} - \sigma_{\text{vol}})\,\tfrac{1}{d} \\
&+2\delta' c_{\text{gb}}\,(\sigma_{\text{gb}} - \sigma_{\text{vol}}) \\
&-4\delta\delta' c_{\text{gb}} \left[\tfrac{1}{2}(\sigma_{\text{int}} + \sigma_{\text{gb}}) - \sigma_{\text{vol}}\right] \tfrac{1}{d}
\end{aligned} \tag{4.13}$$

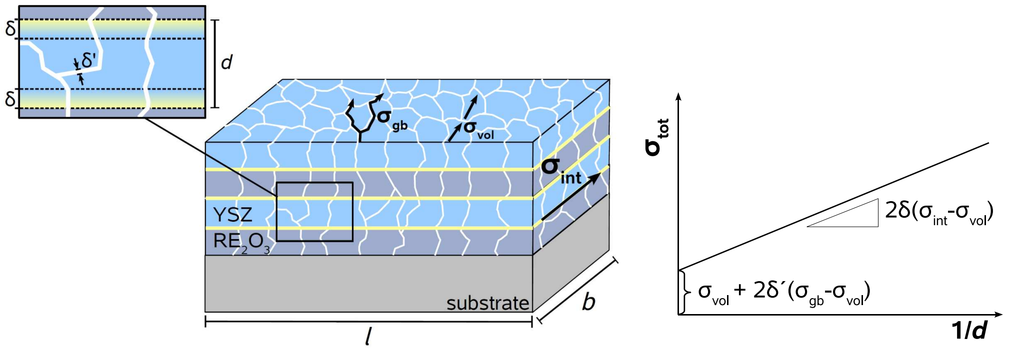

(a) (b)

**Figure 4.5:** a) Schematic picture of a thin film multilayer system containing different pathways for ionic (and electronic) transport. b) Expected linear relationship between $\sigma_{\mathrm{tot}}$ and the reciprocal film thickness $1/d$.

The last term in equation 4.13 is small if compared to the first two terms (see also [107]) and can be neglected.
When the total conductivity $\sigma_{\mathrm{tot}}$ is plotted in relation to the reciprocal film thickness $1/d$ of the conducting layers, a linear relation with the slope $2\delta\,(\sigma_{\mathrm{int}} - \sigma_{\mathrm{vol}})$ is obtained. The intercept is given by $\sigma_{\mathrm{vol}} + 2\delta' c_{\mathrm{gb}}\,(\sigma_{\mathrm{gb}} - \sigma_{\mathrm{vol}})$ (see figure 4.5b)).

If we assume that the contribution of the grain boundaries to the total conductivity is not dependent on $d$, we can define a volume conductivity $\sigma'_{\mathrm{vol}}$ as the combination of the "real" volume conductivity and the grain boundary contribution. $\sigma'_{\mathrm{vol}}$ is then simply given by $\sigma'_{\mathrm{vol}} = \lim_{d\to\infty} \sigma_{\mathrm{tot}}$, which corresponds to the y-axis intercept of the plot in figure 4.5b). The equation for $\sigma_{\mathrm{tot}}$ then simplifies to:

$$\sigma_{\mathrm{tot}} = \sigma'_{\mathrm{vol}} + 2\delta\,(\sigma_{\mathrm{int}} - \sigma_{\mathrm{vol}})\,\frac{1}{d} \tag{4.14}$$

Equation 4.13 is only valid if $2\delta < d$. For $2\delta > d$ the total conductivity is equal to $\sigma_{\mathrm{int}}$ (neglecting the grain boundary contribution). In this case, the dependence on the reciprocal film thickness can not be assumed to be linear any more. To describe the dependence in this region, a specific transport model for the interfaces has to be found.

# 5 Electrochemical Impedance Spectroscopy

## 5.1 Basics of Electrochemical Impedance Spectroscopy (EIS)

A straightforward method for the measurement of conductivities is a simple DC-experiment; the slope of the current-voltage relation directly delivers the conductance 1/R. The problem is that only the total conductance can be measured, but in most cases not only the bulk conductivity of the sample material contributes to the overall response. There is also a contribution of the grain and phase boundaries as well as the electrodes. Side effects of DC measurements are polarisation phenomena and sample degradation through electric field driven reactions.

By performing AC impedance measurements, these disadvantages can be avoided. The different contributions to the overall resistive and dielectric behaviour can be analysed.

The basis of impedance spectroscopy is the analysis of the sample using an AC voltage $U(t)$, sweeping the frequency $\nu$, and detecting the corresponding AC current $I(t)$. The sample response can be simulated by an electric circuit consisting of resistances, capacities and inductances. In analogy to Ohm´s law, the complex AC resistance, the impedance $Z$, is given by:

$$Z = Z' + jZ'' = \frac{U\left(t\right)}{I\left(t\right)}, \quad U\left(t\right) = U_0 \cdot e^{j\omega t}, \quad I\left(t\right) = I_0 \cdot e^{j\omega t+\varphi} \tag{5.1}$$

$Z'$ denotes the real part, $Z''$ the imaginary part of $Z$. $j$ is the imaginary number $\sqrt{-1}$. $\omega$ is the radial frequency: $\omega = 2\pi\nu$; $\varphi$ is the phase shift of the current toward the voltage. $U_0$ and $I_0$ are the maximum amplitudes.

For the three basic components of a circuit, the ohmic resistance $R$, the capacitance $C$ and the inductance $L$, $Z$ is given by:

$$\begin{aligned} &R\!: \quad Z = R \\ &C\!: \quad Z = -j/\omega C \\ &L\!: \quad Z = j\omega L \end{aligned} \tag{5.2}$$

It can be seen that the impedance of a resistor $R$ only has a real part whereas the capacitance $C$ and the inductance $L$ only have an imaginary part (see also [41]).

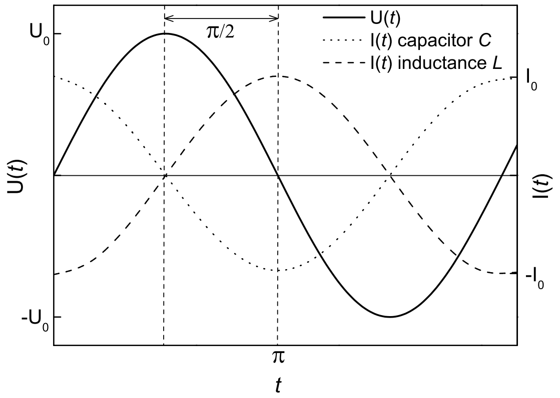

**Figure 5.1:** Relation between an applied sinus shaped voltage and the current for an ideal capacitor $C$ and an ideal inductance $L$.

The impedance of a capacitor vanishes at high frequencies, that of an inductive element at low frequencies. $\varphi$ has the value of $-\pi/2$ for an ideal capacitor and $+\pi/2$ for an ideal inductance (see figure 5.1).

The total impedance of a circuit where all elements are connected in series can be calculated by the sum of the individual impedances: $Z = \sum\limits_i Z_i$. If the elements are connected in a parallel circuit, the inverse values have to be summed: $Z^{-1} = \sum\limits_i Z_i^{-1}$.

A very simple equivalent circuit is the parallel $(RC)$ element, a parallel connection of a resistor and a capacitor. A $(RC)$ element may represent a homogeneous sample with completely non-polarising, ideal electrodes and a geometric capacitance given by the sample surfaces. In more complex samples, a combination of $(RC)$ elements can be used, each representing parts of the sample, for example grain boundaries or non-ideal electrodes.

Non-ideal (distributive) resistive or capacitive behaviour can be expressed by the constant phase element (CPE). The CPE exhibits a constant $\varphi$ between 0 and $-\pi/2$. $R$ and $C$ can be interpreted as limiting cases of an CPE. A special CPE is the Warburg Impedance $W$ for which $\varphi = -\pi/4$. $W$ is often used to represent diffusion phenomena.

$Z$ is often plotted in the Nyquist plot, where $-Z''$ is assigned to the y-axis and $Z'$ to the x-axis. The angle of $Z$ toward the x-axis represents $\varphi$. In this plot, $R$ is represented through an x-axis intercept, $C$ and $L$ through y-axis intercepts, negative for $C$ and positive for $L$. A parallel $(RC)$ element leads to a semi circle. The frequency at the maximum of the circle, $\omega_{max}$, corresponds to the inverse relaxation time $\tau^{-1} = (RC)^{-1}$. Another commonly used depiction is the Bode plot, in which $|Z|$ is plotted versus $\nu$ (see figure 5.2).

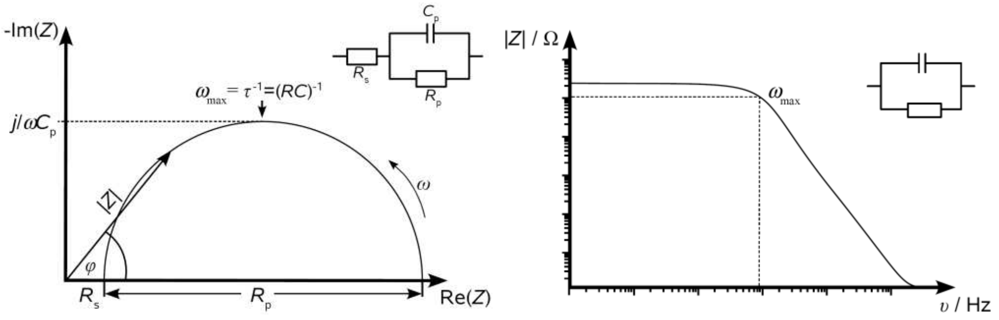

(a) Nyquist Plot

(b) Bode Plot

**Figure 5.2:** a) Nyquist plot of a parallel $(RC)$ element in a serial connection with a resistance. b) Bode plot of a parallel $(RC)$ element. $\tau$ denotes the relaxation time of the $(RC)$ element.

## 5.2 The Representation of Microstructure in EIS

To interpret the impedance spectra of ceramic electrolytes, one has to consider the typically non-homogeneous, polycrystalline microstructure of these materials. Layer models are an early and very simple approach to this problem. In the *series layer model* [108] (see Figure 5.3 a)) two phases are stacked alternately in layers parallel to the electrodes. The two phases may correspond to grain interiors and grain boundaries, respectively. When voltage is applied, charge carriers have to move through both phases. The complex conductivity $\Psi = \sigma_i + j\omega\epsilon_i$ in the series layer model is given by:

$$\Psi_s^{-1} = x_1\Psi_1^{-1} + x_2\Psi_2^{-1} \tag{5.3}$$

$\sigma_1$ is the DC conductivity, $\epsilon_i$ is the permittivity and $x_{1,2}$ are the volume fractions of the phases. The corresponding impedance plot shows two semicircles and the equivalent circuit is a series combination of two parallel $(RC)$ elements (see figure 5.3d)). If the time constants $\tau$ of both elements differ because of differences in $\epsilon_i$, the two arcs will be well resolved in the impedance spectrum and the conductive properties of both phases can be separated. If they differ in $\sigma_i/x_i$, they can be resolved in the Modulus[1] spectrum [109].

In the *parallel layer model* (see Figure 5.3 b)), the two phases are stacked in layers perpendicular to the electrode surfaces, leading to two independent conduction paths for the charge carriers. A parallel combination of two parallel $(RC)$ elements, which transform to a single $(RC)$ element, is the corresponding equivalent

---

[1] Modulus $M = j\omega C_0 Z$, $C_0$ = capacitance of the empty cell

circuit (see figure 5.3e)). The complex conductivity is given by a linear mixing rule:

$$\Psi_p = x_1\Psi_1 + x_2\Psi_2 \tag{5.4}$$

The two conduction paths cannot be separated in the impedance spectrum because only one relaxation time is found. For most of the common ceramic electrolytes, the parallel layer model fails to describe the conductive behaviour.

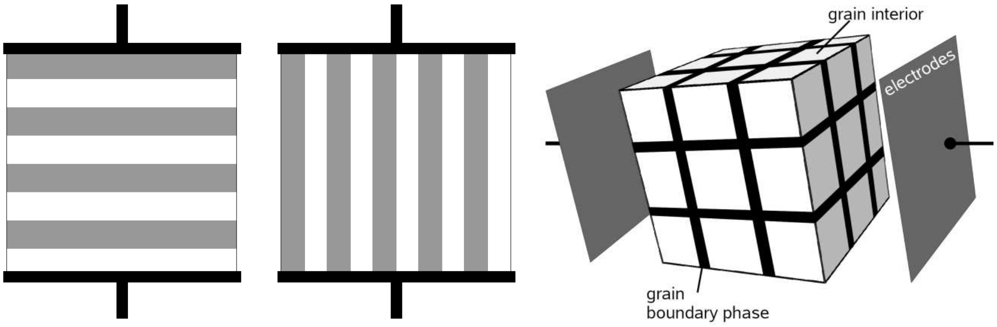

(a) series layer model (b) parallel layer model (c) brick layer model

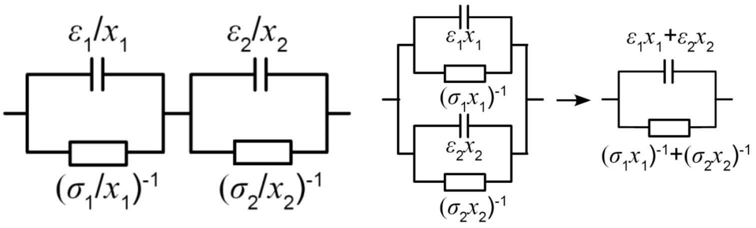

(d) equivalent circuit (a) (e) equivalent circuit (b)

**Figure 5.3:** Different models for the structural properties of ceramic electrolytes. a) - b) series and parallel layer model, c) brick layer model, d) - e) equivalent circuits for a) and b), respectively.

Both layer models describe extreme cases unlikely for real materials. A more realistic description is achieved by the *brick layer model* [110] [111] [63] (see Figure 5.3 c)). The cube shaped grains with thickness $D$ are separated by flat boundaries with a thickness $d$, thus giving the volume fraction of the grain boundary phase as $3d/D$. Two conduction paths are possible: either through the grains and across the grain boundaries or along the grain boundaries parallel to the current direction. If the conductivity of the grain interior $\sigma_{gi}$ is significantly larger than the grain boundary conductivity $\sigma_{gb}$, then the resistive behavior of the brick layer model can be described as:

$$\Psi_{bl}^{-1} = \Psi_{gi}^{-1} + \frac{x_{gb}}{3}\Psi_{gb}^{-1} \tag{5.5}$$

This is equivalent to the series layer model in which the grain boundary resistance is weighted by one third (because the grain boundaries block the transport in only one of three possible directions) [111]. The equivalent circuit is the same as in figure 5.3d) but with the resistive and capacitive elements of the first semicircle being $(\sigma_{gi})^{-1}$ and $c_{gi} = \epsilon_{gi}$, and for the second semicircle $(3\sigma_{gb}/x_{gb})^{-1}$ and $c_{gb} = 3\epsilon_{gb}/x_{gb}$, respectively.
From these relations we can derive an expression for the volume fraction of the grain boundaries:

$$x_{gb} = \frac{3d}{D} = 3\frac{c_{gi}}{c_{gb}}\frac{\varepsilon_{gb}}{\varepsilon_{gi}} \tag{5.6}$$

This equation shows how the volume fraction of the grain boundaries and the grain boundary thickness can be estimated from impedance measurements if one assumes $\epsilon_{gb} \approx \epsilon_{gi}$.

If, on the other hand, $\sigma_{gb}$ dominates, the conduction will take place along the grain boundaries. The complex conductivity is then given by:

$$\Psi_{bl} = \Psi_{gi} + \frac{2x_{gb}}{3}\Psi_{gb} \tag{5.7}$$

This is equivalent to the parallel layer model with a two-thirds weighting of the grain boundary conductance term. No estimations on the microstructure can be made from the electric properties in this case.
A network of both conduction paths can be found if there is no dominating part. The complex conductivity for all ratios of $\sigma_{gb}/\sigma_{gb}$ can be described by [112]:

$$\psi_{bl} = \left(\psi_{gi}^{-1} + \frac{x_{gb}}{3}\psi_{gb}^{-1}\right)^{-1} + \frac{2}{3}x_{gb}\psi_{gb} \tag{5.8}$$

A comprehensive treatment of the concepts and applications of impedance spectroscopy, focusing on solid state systems, can be found in [113].

# Part IV

# Experiments and Results

# 6 Sample Preparation

All samples were prepared by pulsed laser deposition (PLD) on sapphire (0001) substrates[1]. A special deposition chamber equipped with a mirror system to allow either simultaneous or automatically controlled alternate deposition from two different targets[2] was used (figure 6.2). The targets were mounted on a rotating carrier for a uniform material removal. Substrate temperatures up to 950 °C and base pressures down to $10^{-6}$ mbar can be reached. The distance between the substrate and the targets is about 4.5 cm (depending on the size of the targets).

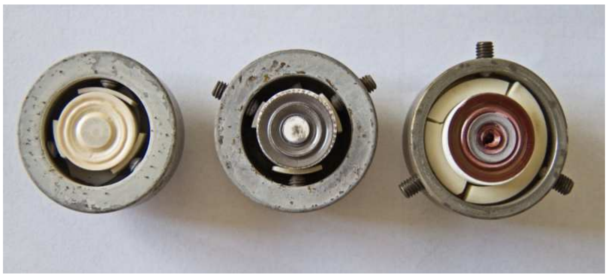

**Figure 6.1:** Targets used for the preparation from left to right: YSZ, $Sc_2O_3$, $Lu_2O_3$.

All multilayers were deposited at 800 °C[3] and a background gas pressure of $6.0 \cdot 10^{-2}$ mbar oxygen, using a pulse rate of 10 Hz and a pulse energy of 250 mJ. A pulse rate of 2 Hz was applied to yield high quality samples with improved epitaxy and bigger grains. An overview over all samples and the specific deposition parameters is given in tables 12.1 - 12.4.

After deposition, the samples were annealed at 800 °C in air for 48 h (10 Hz deposition) or 99 h (2 Hz deposition) to improve crystallinity and ensure an uniform oxidation state.

---

[1] CrysTec GmbH, Köpenicker Str. 325, D-12555 Berlin

[2] Targets of rare earth oxides were prepared from powders by ball milling, pressing and sintering at temperatures around 1400 °C. Oxide powders were obtained from Chempur Feinchemikalien und Forschungsbedarf GmbH, Postfach 410450, D-76204 Karlsruhe, Germany. All oxides were 99.99+ % pure. YSZ targets were supplied by HTM Reetz GmbH, Köpenicker Str. 325, D-12555 Berlin.

[3] The actual temperature at the sample surface may have been lower due to a low heat transfer

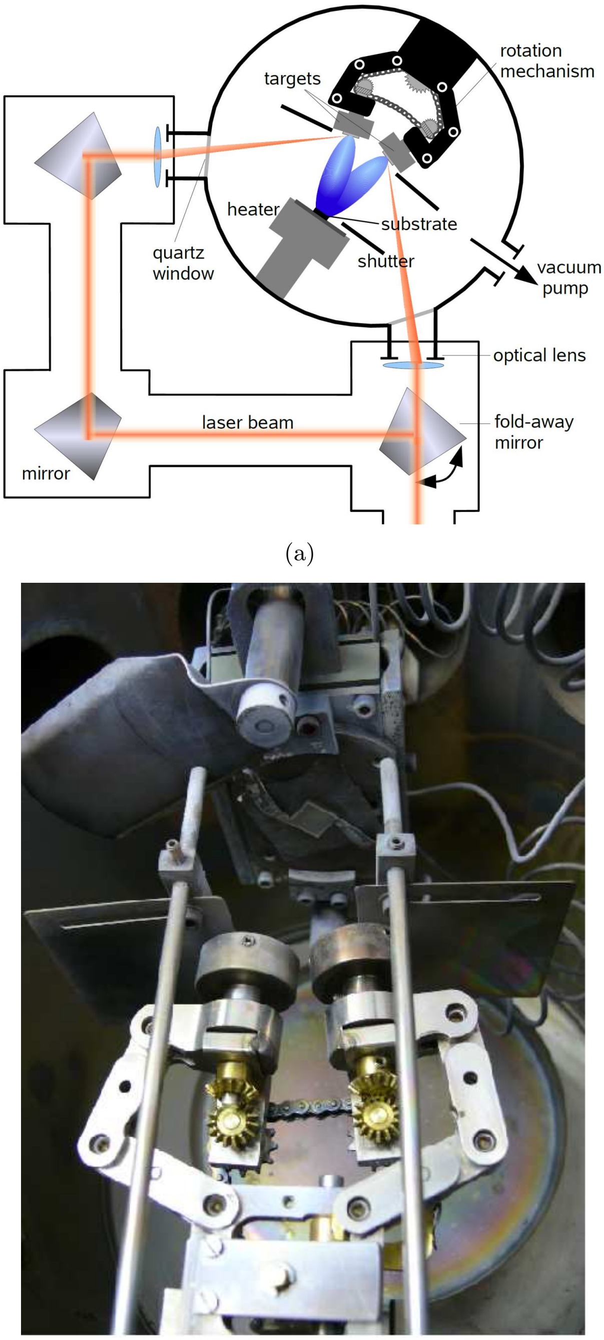

(a)

(b)

**Figure 6.2:** a) Scetch of the high-vacuum chamber used for PLD-preparations. b) Photo showing the interior of the PLD chamber.

# 7 Structural Investigations

## 7.1 Methods

### 7.1.1 X-Ray Diffraction (XRD)

All samples were characterised by X-ray powder diffraction[1] directly after preparation and after annealing at 800 °C for 48 h (respectively 99 h) in air. A Bragg-Brentano geometry, together with a Cu K-alpha ($\lambda = 1.5404$ Å) irradiation source at 40 kV and 30 mA, were used. Routine scans were performed from 20° to 90°, skipping the region between 41.5° and 42.5° due to the high intensity of the (0006) sapphire substrate peak. A step width of 0.03° and an integration time of 2 s were used.

Using the same setup, rocking curves were measured. X-ray source, sample and detector were aligned such that the reflection terms were fulfilled for the (111) YSZ or the (222) $Sc_2O_3$ signal. Then the sample was tilted from $\theta = -5°$ to $\theta = +5°$ and the intensity recorded.

For an extended characterisation of the sample texture, pole figures were recorded by Dr. Martin Zimmermann, Bruker AXS, from $\Psi = 0°$ to $+80°$ and from $\Phi = 0°$ to $360°$[2].

Peak widths and positions were determined by fitting the signal with a Pseudo-Voigt function, using the free software *Fityk 0.7.7*.

### 7.1.2 Scanning Electron Microscopy (SEM)

Scanning electron microscopy[3] was used to determine individual layer thicknesses and investigate the overall structure of the multilayers. Pictures were recorded at an accelerating voltage of 10 kV using the secondary electron or the backscattered electron detector.

The samples were prepared for the SEM investigations as follows: A (1×10) mm$^2$ slice of the sample was cut in half. The coated sides of both halves were glued together[4] and the lateral surface was polished. First by a mechanical polish using diamond polishing foils with grain sizes from 15 µm down to 0.1 µm. Secondly, to improve the result an ion beam milling system[5] was used. A 10 h milling

---

[1] SIEMENS Kristalloflex D500

[2] Bruker D8 Discover, Cu-$K_\alpha$ radiation

[3] LEO Gemini 982, Zeiss

[4] glue: M-Bond 610, Vishay, Electronic GmbH, Geheimrat-Rosenthal-Str. 100, Selb, D-95100, Germany

[5] Bal-Tec RES 101 (Leica Microsystems)

procedure with 2.7 kV gun voltage and 1.7 mA ion current was applied. The guns were place opposite to each other at an angle of 4° toward the sample surface and the sample rotated with a speed of 2 rpm.

After polishing, a carbon coating was applied as electronically conducting layer.

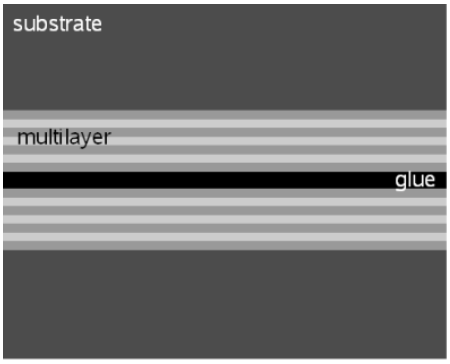

**Figure 7.1:** Scheme showing a sample prepared for SEM measurements (top view).

### 7.1.3 Transmission Electron Microscopy ((HR)TEM, (HR)STEM, EELS and SAED)

Investigations by transmission electron microscopy ((HR)TEM and SAED) were performed by Prof. Dietrich Hesse and Dr. Nikolai Zakharov, Halle[6] with a PHILIPS CM20T and a JEOL 4010 (high resolution).

HR-STEM, EELS and HR-EDX measurements were performed by Dr. Eckhard Pippel, Halle[7] and Dr. Benjamin Butz, Karlsruhe[8], with an aberration-corrected ($C_s$ probe corrector) FEI Titan 80-300 operating at 300 kV.

The reflections in the SAED images were identified by comparing them to a simulated diffraction pattern. Such patterns were created using the software *JSV 1.08 lite*. In SAED exposures with a known original size, it was also possible to measure the distance of the signals to the centre of the SAED and their mutual angle. To calculate the $d_{(hkl)}$ values from the measured distances, the following equation was used:

$$\mathrm{R}d_{(hkl)} = \lambda \mathrm{L} \tag{7.1}$$

---

[6] Prof. Dr. Dietrich Hesse, Dr. Nikolai Zakharov, Max-Planck Institut für Mikrostrukturphysik, Weinberg 2, D-06120 Halle

[7] Dr. Eckhard Pippel, Max-Planck-Institut für Mikrostrukturphysik, Weinberg 2, D-06120, Halle

[8] Dr. Benjamin Butz, Laboratorium für Elektronenmikroskopie, Karlsruher Institut für Technologie (KIT), Engesserstraße 7, D-76131 Karlsruhe

R is the distance of the reflections to the centre of the SAED, $\lambda$ is the wavelength of the electrons and L is the camera length. L was 1 m for all investigated SAED images and $\lambda$ was $2.51 \cdot 10^{-2}$ Å.
Fast Fourier transformations of areas in HRTEM images were created using the software *Image J.* This software allows to directly measure the $d_{(hkl)}$ values and the mutual angle of the reflections.

### 7.1.4 Time-of-Flight Secondary Ion Mass Spectroscopy (TOF-SIMS)

TOF-SIMS[9] was used to obtain information about contaminations present in the multilayer samples. Dynamic TOF-SIMS measurements were performed to record depth profiles, starting from the sample surface. Different ion sources were available for sputtering: Cs and $O_2$. A $Bi^+$ source was used for analysis, the accelerating voltage being 25 kV for the all investigated samples.

The depth of the profile craters was measured using a standard profilometer[10]. Correlating the measured depth with the associated SIMS profile allowed to assign a length scale to the x-axis.

---

[9] TOF.SIMS 5 from ION TOF
[10] Alpha-Step IQ, KLA Tencor

## 7.2 Results

### 7.2.1 YSZ | $Sc_2O_3$ Multilayers

#### X-Ray Diffraction

All samples of this system were crystalline directly after deposition. A narrowing of the reflections in the diffractograms and an increase of the signal intensity could be achieved by further annealing of the samples, indicating grain growth and an improvement of crystallinity. The proportion of the signal intensities compared to each other did not change markedly. This means that the orientation of the single grains was determined during the film growth process and did not change during heat treatment.

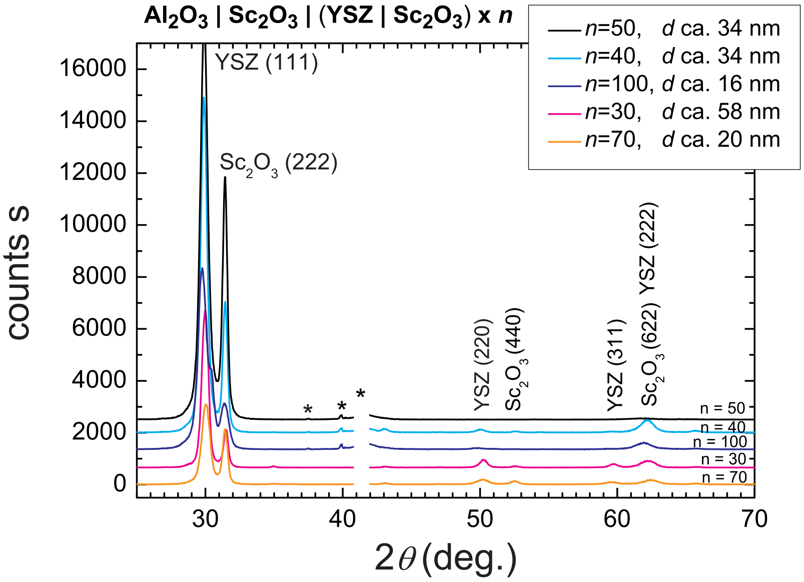

**Figure 7.2:** Overview showing the XRD results for different samples of the system YSZ | $Sc_2O_3$, deposited at 2 Hz. $d$ refers to the thickness of the YSZ layers. "$*$" denotes the position of substrate reflections.

In all diffractograms, the (111) (or (222)) reflection dominates for both phases (see figures 7.2 and 7.3). Thus, the multilayers are highly textured and a preferred axial orientation relationship exists between the substrate, YSZ and $Sc_2O_3$:

$$(0001)\ \mathrm{Al_2O_3} \parallel (111)\ \mathrm{Sc_2O_3} \parallel (111)\ \mathrm{YSZ}$$

Only the sample with $n = 5$ YSZ layers, deposited at 10 Hz, shows small amounts of other orientations. These are:

$$(0001)\ \mathrm{Al_2O_3} \parallel (100)\ \mathrm{Sc_2O_3} \parallel (100)\ \mathrm{YSZ}$$

**Mean Lattice Dilatation in the System YSZ | $Sc_2O_3$**

| | 10 Hz deposition rate | | 2 Hz deposition rate | |
|---|---|---|---|---|
| **YSZ** | $\Delta a$ [%] | FWHM [°] | $\Delta a$ [%] | FWHM [°] |
| as deposited | 1.42 | 0.87 | 1.36 | 0.79 |
| after annealing | 0.80 | 0.73 | 0.55 | 0.57 |
| **$Sc_2O_3$** | | | | |
| as deposited | 0.68 | 0.69 | 0.16 | 0.52 |
| after annealing | 0.52 | 0.66 | 0.11 | 0.51 |

**Table 7.1:** Mean dilatation $\Delta a$ of the measured lattice parameters of YSZ and $Sc_2O_3$ from the literature values and mean FWHM values of the (111) YSZ, respectively the (222) $Sc_2O_3$ reflection.

$$(0001)\ Al_2O_3 \parallel (311)\ Sc_2O_3 \parallel (311)\ \mathrm{YSZ}$$

Also, a very small amount of the orientation

$$(0001)\ Al_2O_3 \parallel (110)\ Sc_2O_3 \parallel (110)\ \mathrm{YSZ}$$

was found.

As can easily be seen in figure 7.3b), the $2\theta$ value of the (111) YSZ (or (222) $Sc_2O_3$) reflections deviates slightly from the literature value and is also different for the different multilayer samples. This is due to a varying mean lattice parameter $a$ perpendicular to the film plane. On average, the mean lattice parameter $a$ of YSZ was dilatated in all YSZ | $Sc_2O_3$ multilayer samples, $\Delta a$ being over 1 % directly after deposition[11]. This out-of-plane dilatation corresponds to a compression of the in-plane lattice parameter, being interconnected by the Poisson´s ratio $\nu$.
$\Delta a$ could be significantly reduced by the heat treatment, as can be seen in table 7.1. The mean dilatation of the samples which were deposited at 2 Hz is smaller than that of the samples deposited at 10 Hz. The same is observed for the mean FWHM (Full Width at Half Maximum) value of the (111) YSZ signals. The lattice parameters and FWHM values for every sample before and after annealing can be found in the appendix in tables 12.1 and 12.2.

---

[11] The mean lattice parameter can be calculated by determining the exact position of the YSZ (111) reflection and using the appropriate quadratic form of Bragg´s equation. The quadratic form of Bragg´s equation for cubic crystal systems is given by:

$$a = \frac{\lambda}{2\sin\theta}\sqrt{(h^2 + k^2 + l^2)} \tag{7.2}$$

The small offset, which was always present in the XRD measurements, was determined by comparing the position of the small but often sharp Wolfram $L_{\alpha 2}$ satellite reflection of the (0006) sapphire substrate reflection to literature value.

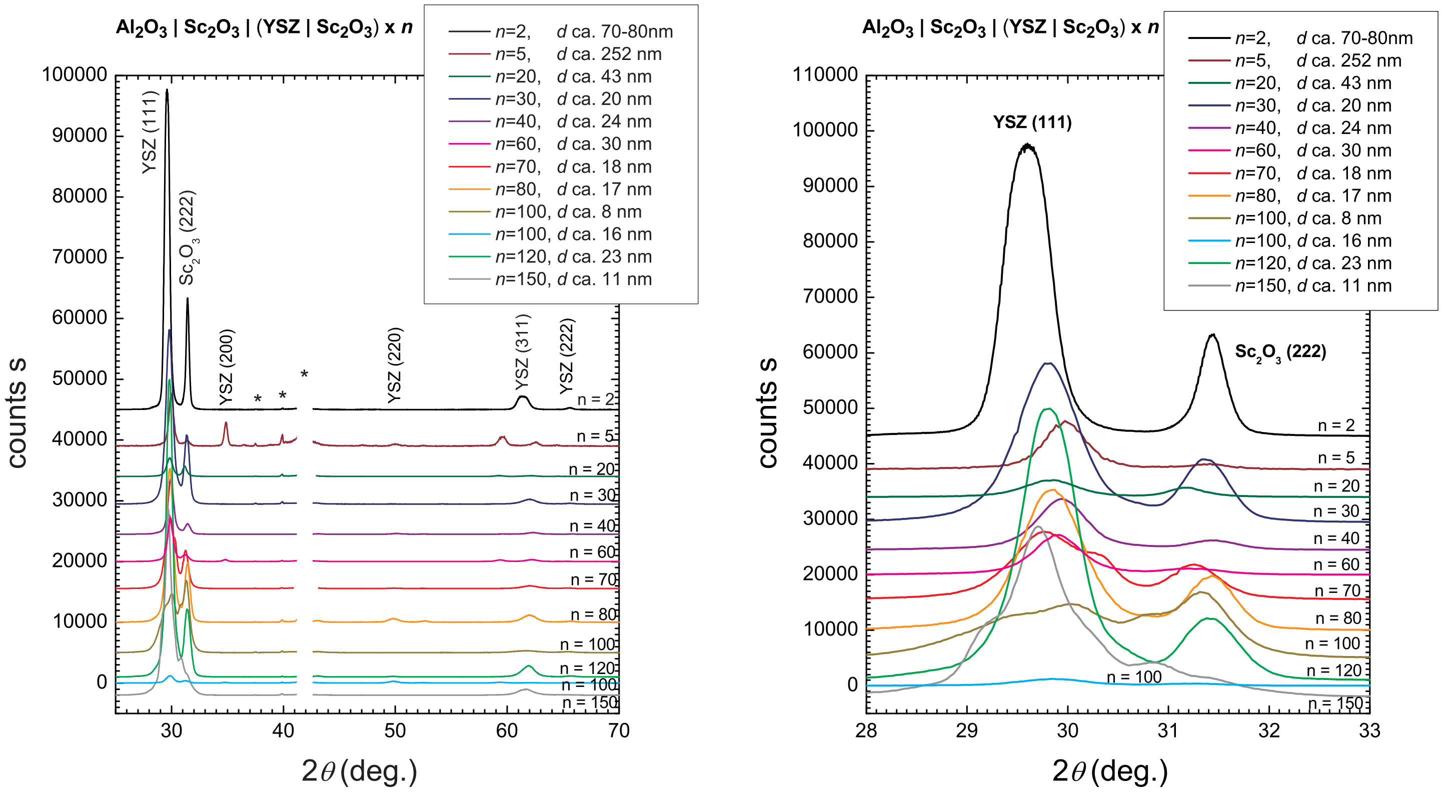

(a)

(b)

**Figure 7.3:** Overview showing the results of XRD measurements for different samples of the system YSZ | Sc$_2$O$_3$, deposited at 10 Hz. b) Enlarged part of a), showing the (111) YSZ respectively (222) Sc$_2$O$_3$ reflexes. "∗" denotes the position of substrate reflections.

The out-of-plane lattice dilatation in the $Sc_2O_3$ layers can be determined in the same way as has been done for YSZ. The results are shown in the lower part of table 7.1. The mean lattice dilatation in the $Sc_2O_3$ layers is smaller than in the YSZ layers, both directly after deposition and after heat treatment. The mean FWHM values are also somewhat smaller.

In many XRD measurements of multilayer samples with single layer thicknesses below 20 nm, shoulders appear at the (111) YSZ, respectively (222) $Sc_2O_3$ signals. In the measurement for the sample with $n = 100$ and $d = 8$ nm, both peaks clearly split up ($d$ always refers to the thickness of the individual YSZ layers). A reasonable explanation for this signal structure is a convolution with superlattice peaks. These peaks can only be resolved if the superlattice period is small enough to produce significant signal distance. A detailed diffractogramm showing the splitted peaks together with a fitting result is presented in figure 7.4. The superlattice peaks appear at a middle distance of 0.645 ° from the main signals. Calculating the $d$-value of the superlattice and assuming a 3rd order reflection, a value of 20.54 nm is obtained. One period in the superlattice can be assumed as the width of a double layer consisting of one layer of YSZ and $Sc_2O_3$ each. According to SEM, this double layer is about 22 nm wide, which is in good agreement with the value obtained from the superlattice reflections.

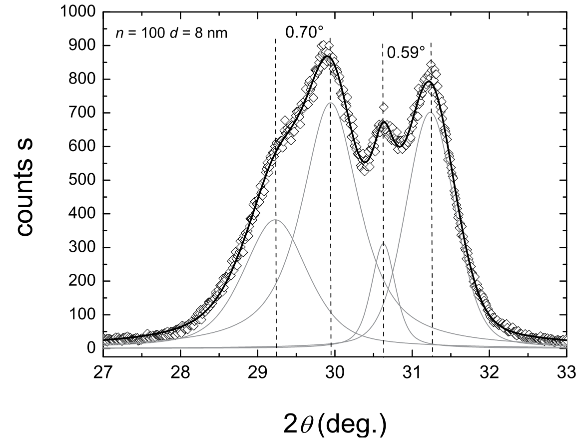

**Figure 7.4:** Superstructure peaks in a multilayer with $n = 100$ individual YSZ layers and double layer thickness of about 22 nm ($d \approx 8$ nm for YSZ). Fitting result: black envelope line and peaks. A Pseudo-Voigt function was used for the fit.

### Texture Analysis

Rocking curve measurements of the (111) YSZ and (222) $Sc_2O_3$ signal were performed to evaluate the tilt misorientation of the crystallites. For a sample with thick YSZ layers (70-80 nm, figure 7.5b)), a FWHM value of 1.93° was found for the (111) YSZ signal. The FWHM value for the (222) $Sc_2O_3$ reflection

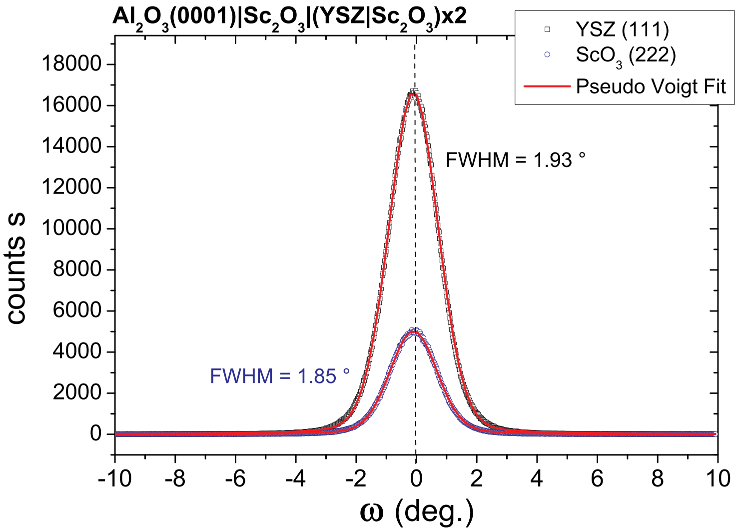

(a)

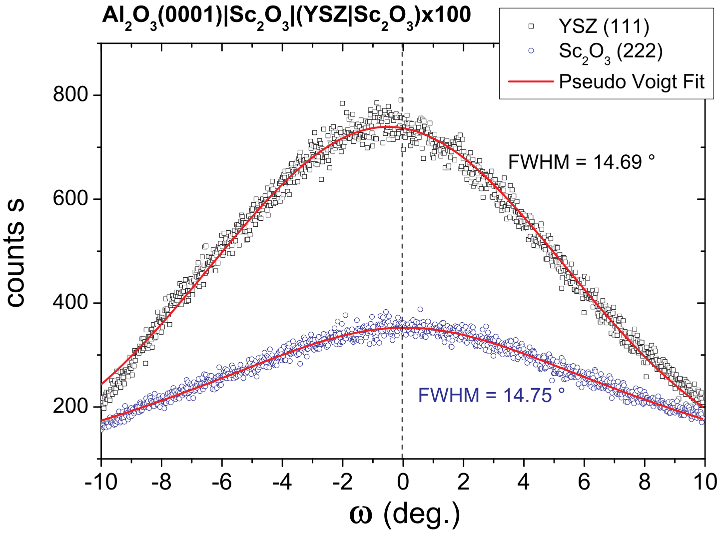

(b)

**Figure 7.5:** a) Rocking curve for the sample YSc2 with 2 individual YSZ layers and a layer thickness of 70-80 nm (YSZ); b) result for the sample YSc1002 with 100 individual YSZ layers, being about 15 nm thick. Both samples were deposited at 10 Hz.

was slightly lower, being 1.85°. These values indicate that the tilt misorientation of the crystallites is small when the individual layers of the multilayer are thick. In a sample with thin individual layers (about 15 nm, figure 7.5a)), a broad (111) YSZ signal was obtained, the FWHM value being 14.69°. For the (222) $Sc_2O_3$ reflection, a FWHM value of 14.75° was determined. Thus, the tilt misorientation must be much larger when the individual layers of the multilayer are thin.

A more detailed analysis of the sample texture was obtained by pole figure measurements. The result for the sample YSc50-3 (50 YSZ layers, $d \approx 34$ nm, deposited at 2 Hz), is shown in figure 7.6. In agreement with X-ray powder diffraction, the orientation along the [111] direction is found to be the preferred one for YSZ as well as for $Sc_2O_3$.

The dispersion of the maximum signal intensity (dark red area) around the centre of the [111] pole figure can roughly be estimated to be between $\Delta\Psi = 5°$ and 10°, being somewhat asymmetric (see figure 7.6 a, b). It is due to tilt misorientation in the samples. The pole figures showing the signal intensities for the [110] direction show broadened maxima at $\Psi \approx 35°$ and at six different positions of the azimuthal (in-plane) angle $\Phi$ (see figure 7.6 c, d). These positions are identical for YSZ and $Sc_2O_3$. That means that firstly a preferred azimuthal orientation exists and secondly that it is the same for both phases. Taking into account the symmetry of the {220} YSZ and {440} $Sc_2O_3$ planes, the six maxima represent two variants of the preferred azimuthal rotation of the individual crystallites. These variants are rotated by 60°, which for reasons of symmetry in this case is the same as a mirror inversion.

However, the pole figures do not deliver any information on whether the rotational variant of the crystallites changes at a phase boundary or if within one columnar grain both YSZ and $Sc_2O_3$ show exactly the same variant of the azimuthal orientation. Thus, two different possibilities exist for the azimuthal orientation relationship between both phases:

(i) $[\bar{1}10]$ $Sc_2O_3$ $\parallel$ $[\bar{1}10]$ YSZ

(ii) $[1\bar{1}0]$ $Sc_2O_3$ $\parallel$ $[\bar{1}10]$ YSZ

The azimuthal orientation relationships (i) and (ii) are depicted schematically in figure 7.7. The cubes represent the orientation of the cubic elementary cells in the different crystal lattices without taking into account any size parameters. Of course, all variants of (i) and (ii) which can be obtained by a simple 60° rotation (creation of a mirror image) of both phases are also possible.

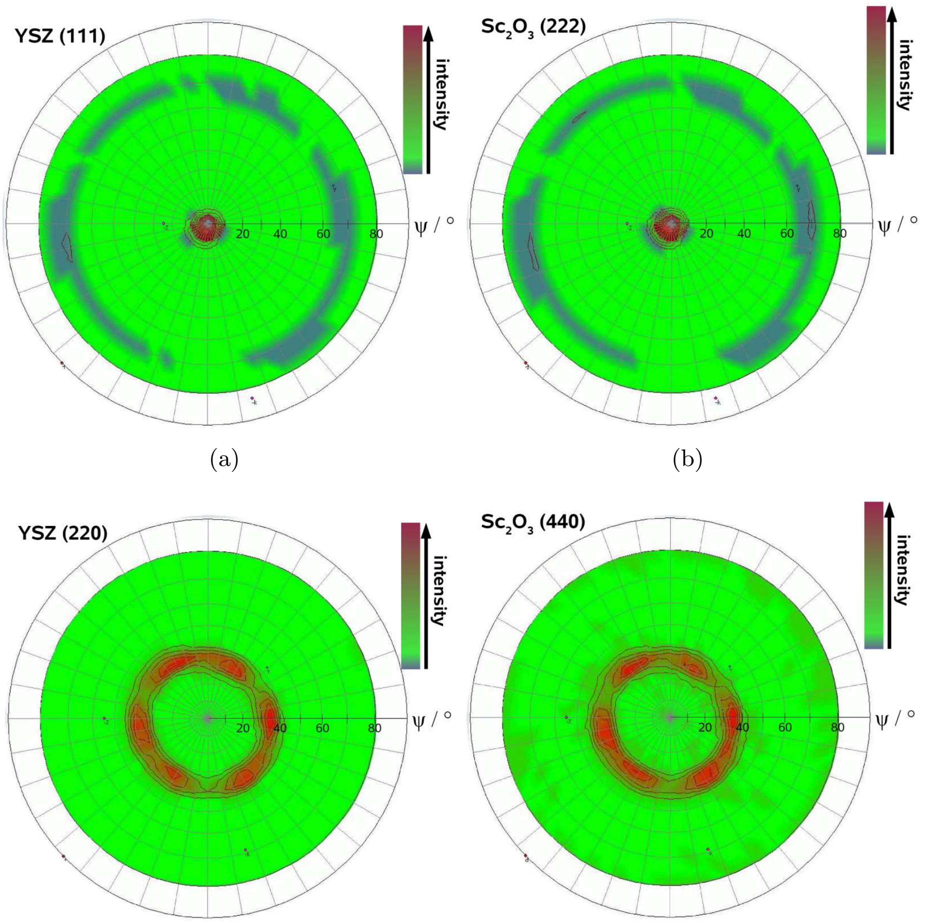

(a) (b)

(c) (d)

**Figure 7.6:** a), b) Pole figure for the YSZ (111) and $Sc_2O_3$ (222) reflexes. c), d) Pole figure for the (220) YSZ and (440) $Sc_2O_3$ reflexes. The intensity of the signals is colour coded, bright red denoting highest, grey lowest intensity. The investigated sample (YSc50-3) was deposited at 2 Hz.

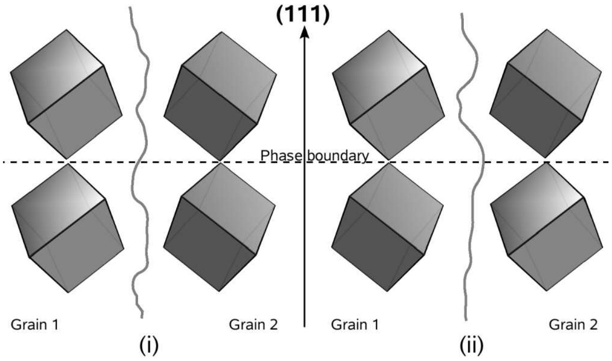

**Figure 7.7:** Possible variants for the azimuthal orientation relationship between YSZ and $Sc_2O_3$ in the multilayers, derived from pole figure measurements.

### SEM Measurements

SEM investigations of sample cross sections did not only reveal the thickness of the individual YSZ layers as given in the appendix in tables 12.1 and 12.2, but also delivered information on the overall morphological structure of the multilayers. Channeling contrasts in the BSE (back scattered electrons) mode indicate a columnar structure of the crystallites (see figure 7.8).

In the SEM images, one can see that the individual layers are completely flat near the substrate, but get more and more wavy with increasing distance to the substrate and increasing thickness of the whole multilayer system (see figure 7.8 and 7.9). This effect is more strongly pronounced in samples with small layer thicknesses and a high number of layers. It is visible in samples deposited at 10 Hz as well as in those deposited at 2 Hz, but the effect is stronger in samples deposited at 2 Hz. In the shown examples, the sample YSc100-2 with 100 individual layers of each phase ($d \approx 16$ nm, deposited at 10 Hz) has very flat individual layers in the lower part of the multilayer (close to the substrate, see figure 7.8). At about half of the total multilayer thickness, the layers start to get more and more wavy. The sample YSc 30 with 30 individual layers of each phase and with a thickness of the YSZ layers being about twice the value of the sample YSc100-2 ($d \approx 28$ nm, deposited at 10 Hz), shows only weak undulations in the topmost layers. In contrast to this, the sample YSc303, deposited at 2 Hz, shows very strong undulations of the individual layers at some distance to the substrate despite a layer thickness of $d = 58$ nm (see figure 7.9). The columnar structure in this sample coarsens with increasing distance to the substrate, so that the columns in the lower part of figure 7.9 (near to the sample surface) are clearly identifiable. The surface of the multilayer is buckled. A high degree of tilt misorientation can be anticipated at the boundaries between the individual columns. All YSZ | $Sc_2O_3$ multilayers which were deposited at 2 Hz show this irregular morphology.

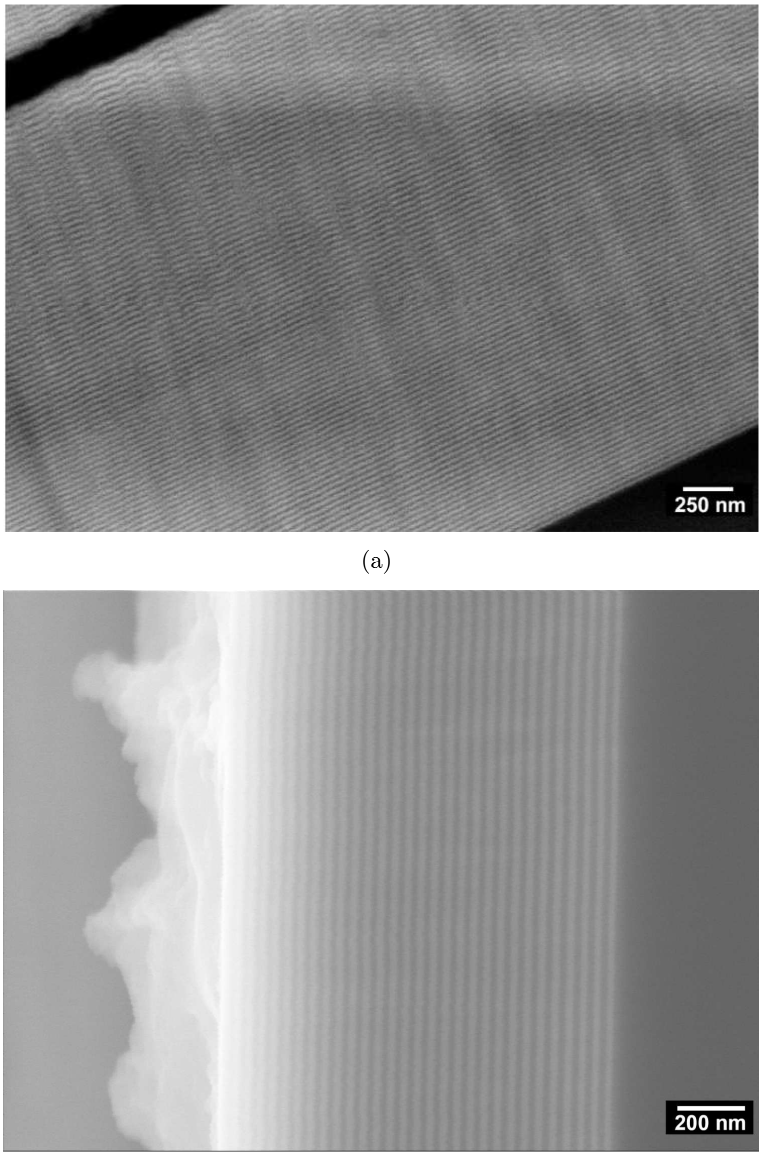

(a)

(b)

**Figure 7.8:** a) SEM image of the sample YSc100-2 (100 individual layers of each phase, $d$ about 16 nm). The substrate is in the lower right corner. The distortion in the the middle of the picture is an image artefact. b) SEM image of the sample YSc30 (30 individual layers of each phase, $d$ about 28 nm). The substrate is in the right side of the picture. Both samples were deposited at 10 Hz. The brighter layers consist of YSZ.

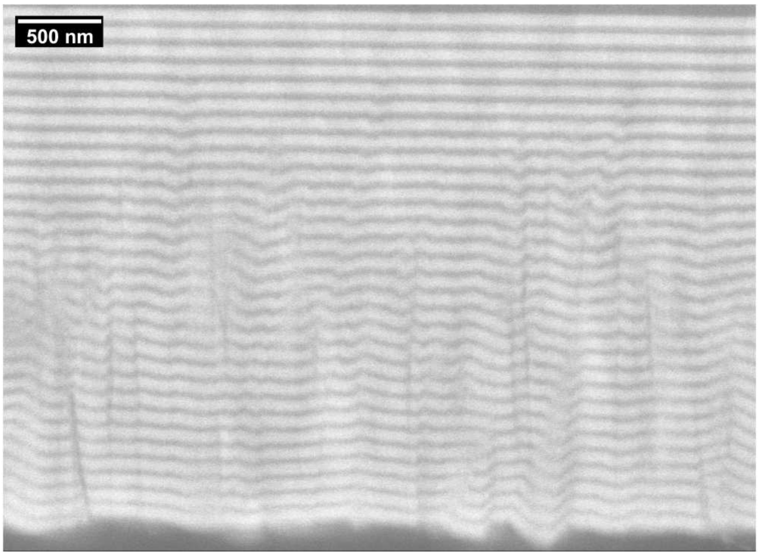

**Figure 7.9:** SEM image of the sample YSc303 ($n$ = 30, $d$ = 58 nm, deposited at a rate of 2 Hz). The substrate is located at the upper edge of the picture. Dark layers consist of $Sc_2O_3$.

A slight decrease of the individual layer thickness with increasing distance to the substrate can be seen in all samples but it is most pronounced in samples with rather thin individual layers. This phenomenon is most probably due to effects during the deposition, for example the gradual roughening of the target surface. Therefore, the thicknesses of the YSZ layers as given in tables 12.1-12.4 are mean values.

### (HR)TEM, HR-STEM and SAED Results

The TEM micrographs show the overall structure of the multilayers very clearly (see figure 7.10). Especially in dark field exposures, the columnar growth structure is visible (figure 7.11). The individual columns extend through several individual layers, often even through the whole width of the multilayer. In the samples deposited at 10 Hz, the individual columns are about 40-60 nm wide. In the samples deposited at 2 Hz, the columnar structure is more uniform and the mean column size is larger, being about 60-100 nm.

All interfaces between YSZ and $Sc_2O_3$ are sharp and well ordered. No transition regions or additional phases were found in the HRTEM micrographs. Instead, the close packed lattice planes are interconnected 1:1 across the interfaces. Also, in all YSZ | $Sc_2O_3$ samples investigated by HRTEM, the interface between the sapphire substrate and the first layer did not contain any visible transition region. This could have been expected because of the high theoretical misfit between $Al_2O_3$ and $Sc_2O_3$ and the different geometries of the bixbyite and the $\alpha$-corundum

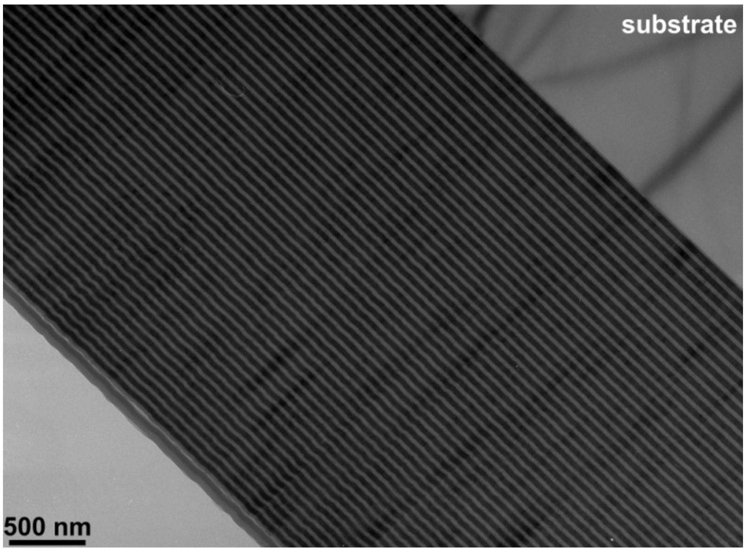

**Figure 7.10:** TEM image of the sample YSc50-3 with 50 individual YSZ layers (dark), deposited at a rate of 2 Hz.

structure. In the system YSZ | $Y_2O_3$, a disordered transition region of about 1-2 nm thickness had been found between the substrate and the first layer [19].

### Orientation Relationships

The SAED measurements agree well with the results obtained by XRD regarding the preferred orientation relationship in the multilayers. This can be seen in figure 7.12, where a TEM micrograph of the sample YSc100 (100 individual YSZ layers, *d* about 8 nm) is shown. The inset shows the associated SAED pattern, which was recorded from an area being approximately 18 double layers wide. The pattern is corrected in its rotation according to the accelerating voltage and magnification of the measurement. All indexed reflections in figure 7.12 refer to YSZ. At many signal positions, secondary reflections are clearly visible. The additional reflections belong to $Sc_2O_3$ and are all very close to the reflections belonging to YSZ. This is best visible at the positions of the (222) and ($\bar{2}\bar{2}\bar{2}$) YSZ reflections, were the (444) and ($\bar{4}\bar{4}\bar{4}$) $Sc_2O_3$ reflections are clearly distinguishable from the YSZ signals. The coincidence of corresponding reflections for both phases agrees with the pole figure measurements (figure 7.6c,d), indicating that the orientation relationship between YSZ and $Sc_2O_3$ in the multilayers also exists for the azimuthal rotation.

The reflections belonging to the (111) planes of YSZ and $Sc_2O_3$ are arranged on one line which is directed perpendicular to the layers respectively to the substrate surface. This proves that both phases in this sample are orientated along the $\{111\}$ axis. Closer analysis of all reflections in the SAED reveals that two

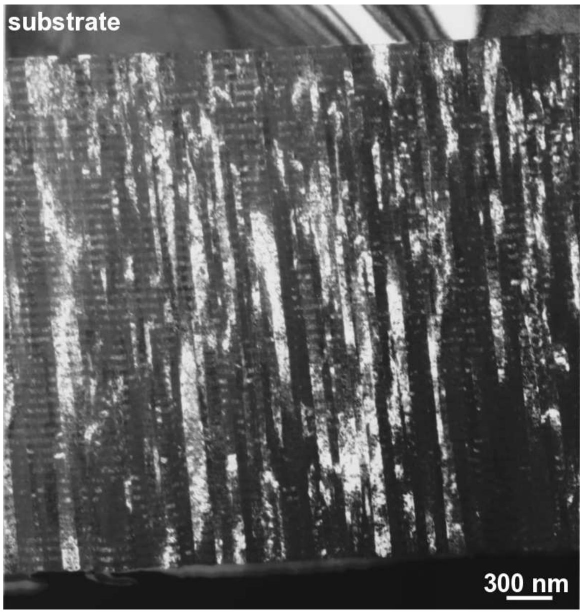

**Figure 7.11:** HR-TEM dark field exposure of the sample YSc50-3, showing the columnar structure.

azimuthal orientations of the crystallites contribute to the pattern, the signals being superimposed: the first is marked by white, the second by red (hkl) indices. We can identify these azimuthal orientations as:

1) $[\bar{1}10]$ YSZ $\parallel$ $[\bar{1}10]$ $Sc_2O_3$ $\parallel$ $\vec{\mathrm{B}}$

2) $[11\bar{2}]$ YSZ $\parallel$ $[11\bar{2}]$ $Sc_2O_3$ $\parallel$ $\vec{\mathrm{B}}$

$\vec{\mathrm{B}}$ denotes the beam direction relative to the crystal lattices.
In the SAED in figure 7.13, reflections from the substrate and the first 3 to 4 individual layers of the multilayer sample YSc150-2 (deposited at 10 Hz, $n = 150$, $d$ about 11 nm) are visible. The reflections from the substrate are marked red, as well as the associated relative beam vector $\vec{\mathrm{B}}$ in square brackets. The azimuthal orientation relationship between the substrate and the first layers, found in this SAED, is:

$[1\bar{1}0]$ $Al_2O_3$ $\parallel$ $[\bar{1}10]$ $Sc_2O_3$ $\parallel$ $[\bar{1}10]$ YSZ

The local structure as well as local orientation relationships in the multilayers were analysed in detail by fast Fourier transformation (FFT) of selected areas in the HRTEM micrographs. Periodic structures in the HRTEM micrographs lead to signals in the FFT results which are comparable to those in SAED and can be analysed in the same way. Some of the FFT results are shown in figure 7.14, 7.15, 7.20 and 7.21. In all Fast-Fourier transformations of selected areas in the

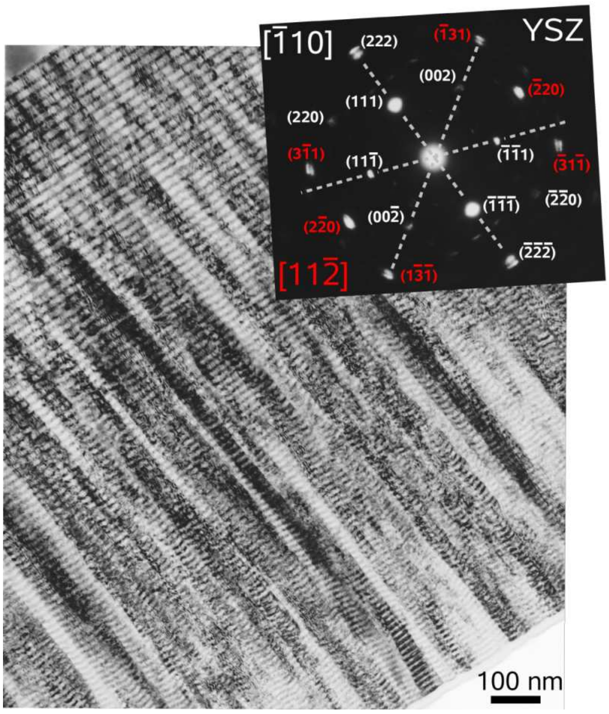

**Figure 7.12:** TEM micrograph of a YSZ | $Sc_2O_3$ multilayer with 100 individual YSZ layers and associated SAED result. The area of interest for the SAED pattern was about 18 double layers wide. (hkl) values in the SAED pattern refer to YSZ. The red indices belong to a superimposed second variant of the azimuthal orientation. Indices in square brackets denote the beam direction $\vec{\mathrm{B}}$ relative to the crystal lattices. The substrate is situated in the upper left corner.

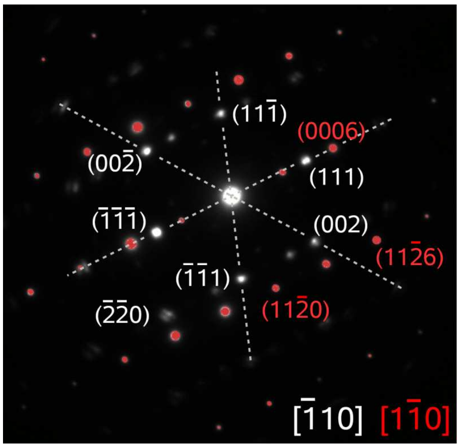

**Figure 7.13:** SAED of a multilayer with $n = 150$, deposited at 10 Hz (YSc150-2). An aperture of about 0.1 µm was used, so that information from the substrate and the first 3 to 4 individual layers could be gained. Reflections originating from the substrate are marked red, as well as the direction of the vector $\vec{\mathrm{B}}$ relative to the substrate.

HRTEM micrographs, a line of signals belonging to the (111) (or (222)) planes of YSZ or $Sc_2O_3$ is perpendicular to the layers. FFT analysis therefore agrees with the XRD, pole figure and SAED measurements regarding the preferred crystal orientation of the layers.
An overview of the orientation relationship between the substrate and the different layers is presented in figure 7.14. The two HRTEM micrographs in the figure display different positions in the same column, the lower micrograph showing the substrate and the first layers whereas the upper micrograph shows a region at some distance to the substrate. From all layers but the first $Sc_2O_3$ layer, FFT results are shown. It is very easy to recognize the diffraction patterns of the bixbyite type rare earth oxide by the larger number of reflections. In all patterns, the direction perpendicular to the interfaces is indicated by an arrow and the associated reflex is given in round brackets. All layers are oriented along the (111) direction on the (0001) sapphire substrate. Also, the azimuthal orientation is the same for each of the layers. The azimuthal orientation relationship between the layers and the substrate in this crystal column is:

$$[100]\ \mathrm{Al_2O_3} \parallel [1\bar{1}0]\ \mathrm{Sc_2O_3} \parallel [1\bar{1}0]\ \mathrm{YSZ}$$

As evident from the different SAED and HRTEM investigations, different variants are possible for the azimuthal orientation relationship between the substrate, YSZ and $Sc_2O_3$. Unfortunately, the FFT of the HRTEM micrographs in figures 7.20 and 7.21 did not deliver any information about the orientation of the substrate. In the HRTEM micrograph in figure 7.15, showing the interface between the substrate and the first layers of the sample YSc150-2, the substrate orientation could be analysed. It revealed the same orientation relationship between the substrate and the first layer which was found before in the SAED in figure 7.13. A mirror-inverted variant is also present. Two mirror inverted crystallites are marked with 2 and 3, respectively, with the associated FFT results numbered in the same way. The FFT from the substrate is numbered with 1. FFT 4 is an analysis of an area in the first YSZ layer, exhibiting exactly the same orientation as the adjacent $Sc_2O_3$ layer marked with 3.

Summarizing, we can identify all found variants for the azimuthal orientation relationships in the YSZ | $Sc_2O_3$ multilayers:

1a) $[1\bar{1}0]\ \mathrm{Al_2O_3} \parallel [\bar{1}10]\ \mathrm{Sc_2O_3} \parallel [\bar{1}10]\ \mathrm{YSZ}$

1b) $[1\bar{1}0]\ \mathrm{Al_2O_3} \parallel [1\bar{1}0]\ \mathrm{Sc_2O_3} \parallel [1\bar{1}0]\ \mathrm{YSZ}$

2a) $[1\bar{1}0]\ \mathrm{Al_2O_3} \parallel [11\bar{2}]\ \mathrm{Sc_2O_3} \parallel [11\bar{2}]\ \mathrm{YSZ}$

2b) $[1\bar{1}0]\ \mathrm{Al_2O_3} \parallel [\bar{1}\bar{1}2]\ \mathrm{Sc_2O_3} \parallel [\bar{1}\bar{1}2]\ \mathrm{YSZ}$

3) $[100]\ \mathrm{Al_2O_3} \parallel [1\bar{1}0]\ \mathrm{Sc_2O_3} \parallel [1\bar{1}0]\ \mathrm{YSZ}$

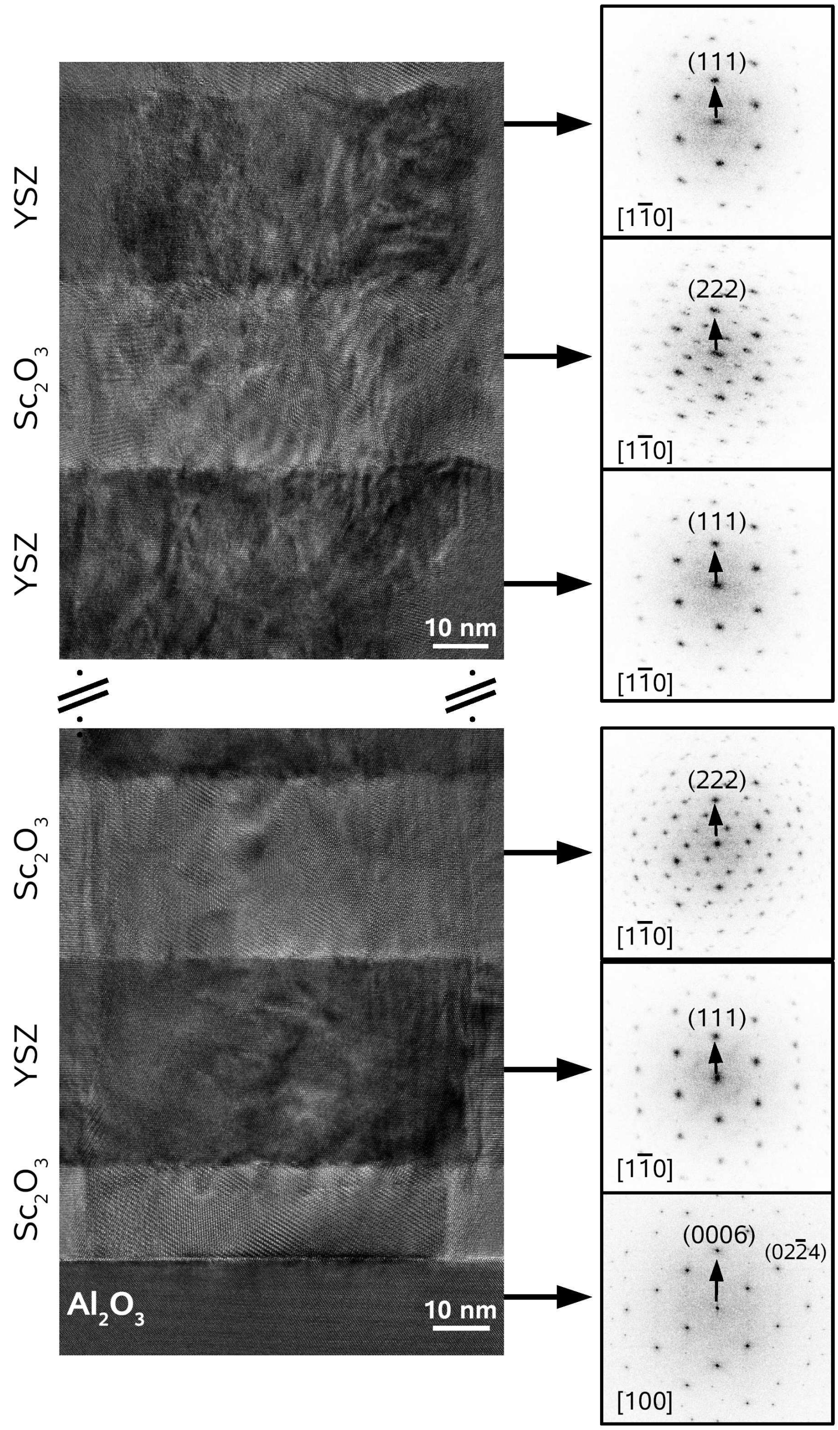

**Figure 7.14:** HRTEM micrographs of the sample YSc50-3. Lower micrograph: at the substrate. Upper micrograph: same column, at some distance to the substrate. The small pictures on the right hand side show FFT results from the different layers (the associated layers are marked by arrows). (hkl) indices in square brackets denote the direction of the beam vector. The strict orientation relationship between the substrate and the different phases in the multilayer can easily be determined from the FFT results. (FFT results by B. Butz, Karlsruhe)

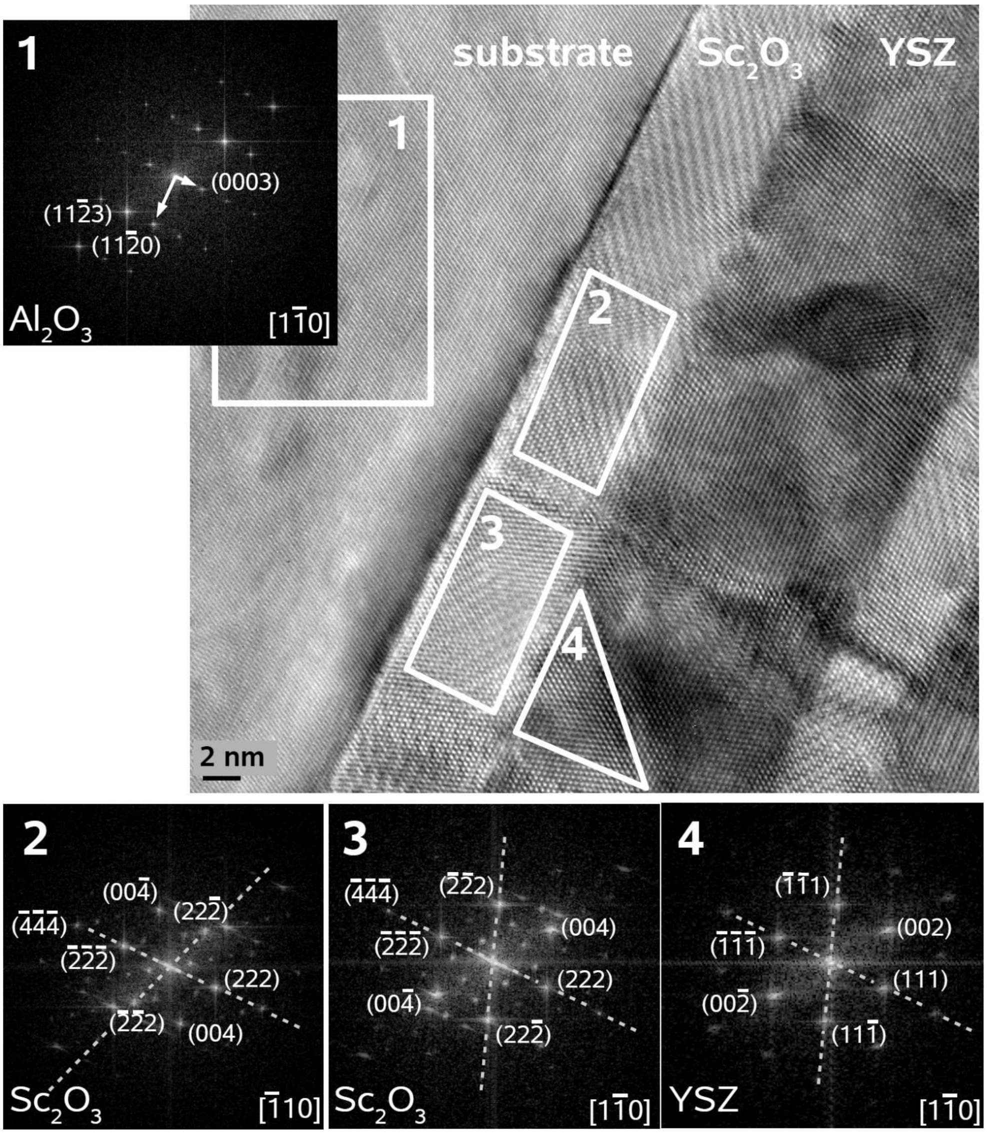

**Figure 7.15:** HRTEM micrograph of the sample YSc150-2. The substrate and the first two layers are shown. The small pictures are FFT analyses of the marked regions, their numbering correspondent. FFT 1 belongs to the substrate, FFT 2 and 3 show two mirror-inverted variants of the azimuthal orientation.

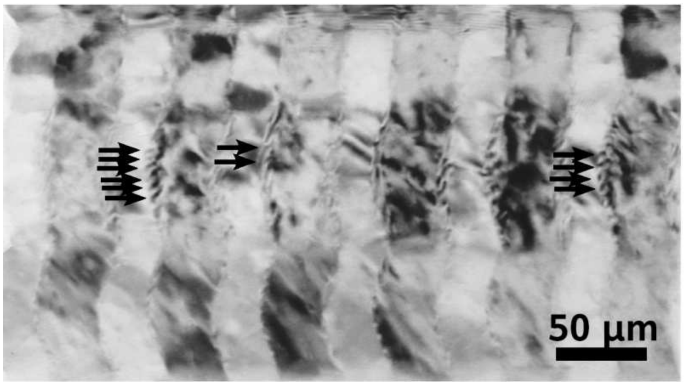

**Figure 7.16:** TEM picture of the sample YSc50-3. At the phase boundaries regular contrast variations are visible (some are marked with arrows).

1a) and 1b) as well as 2a) and 2b) are mirror inverted variants of each other. In the case of 1a) and 1b), these variants can be distinguished in the FFT images (see FFT 2 and 3 in figure 7.15, FFT 2 in figure 7.20 and FFT 1 in figure 7.21). This is not possible for 2a) and 2b). Variant 3) was only found in the HRTEM micrograph of one column of the sample YSc50-3.
It is important to emphasize that in all samples investigated by HRTEM, the azimuthal orientation stays the same within one column, respectively is identical for both phases in this column (see figure 7.14 and FFT 1 and 2 in figure 7.21). The orientation variants:

4a) $[1\bar{1}0]$ $Al_2O_3$ $\|$ $[\bar{1}10]$ $Sc_2O_3$ $\|$ $[1\bar{1}0]$ YSZ

4b) $[1\bar{1}0]$ $Al_2O_3$ $\|$ $[1\bar{1}0]$ $Sc_2O_3$ $\|$ $[\bar{1}10]$ YSZ

can therefore be excluded on the basis of the HRTEM analyses.

### Dislocation Density

From the analysis of the (HR)TEM images, also some statements can be made regarding the strain and defect structure of the interfaces. In figure 7.16, a TEM micrograph of the sample YSc50-3, showing an overview over some layers, is depicted. At the interfaces, contrast variations are visible (some marked with arrows). Such contrast variations typically appear as a consequence of strain fields.
Despite the calculated misfit, only few dislocations were found at the interfaces in samples deposited at 10 Hz. In figure 7.17, a HR-STEM Z-contrast image of the sample YSc150-2 is shown (150 YSZ layers, $d$ about 11 nm). It was recorded from a region near the sample surface. The smaller picture shows an enlarged image of the marked area. Here, almost fully epitaxial growth is found at the

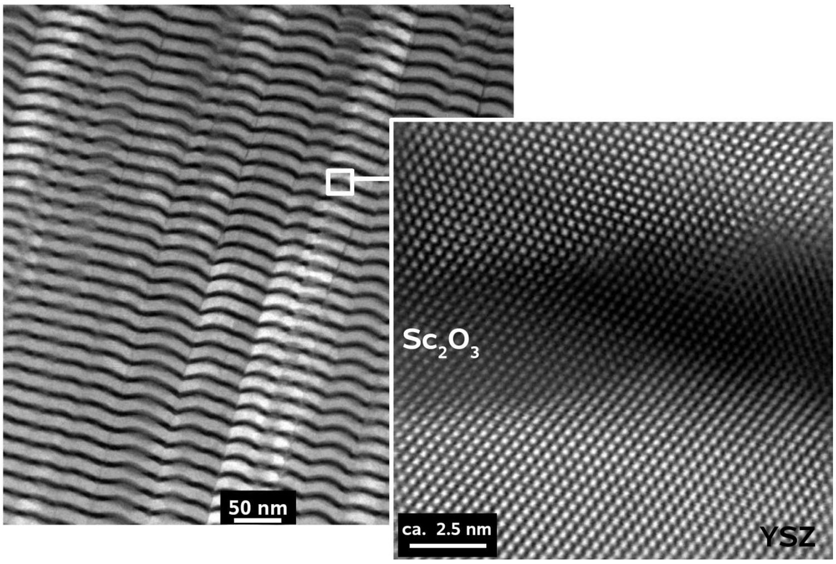

**Figure 7.17:** HR-STEM Z-contrast picture of the sample YSc150-2 ($n$ = 150, $d$ about 11 nm), in the upper part of the multilayer (near the sample surface). The inset shows a zoomed picture from the marked region. Almost fully epitaxial growth is visible at the phase boundaries.

interfaces between YSZ and $Sc_2O_3$ (one dislocation is visible at the upper right part of the $Sc_2O_3$ layer). The 1:1 interconnection of the lattice planes can easily be recognized.

The HRTEM micrographs of a sample deposited at 2 Hz (YSc50-3) revealed two different types of dislocations: the first type has Burgers vectors with the main components being parallel to the interfaces (the angle of inclination of the dislocations being dependent on the lattice planes in which they are situated), the second type has Burgers vectors perpendicular to the interfaces. Either type of dislocations is not restricted to the interfaces but can also be found at irregularities in the layer volume. Regular networks of dislocations could only be found in a few regions.

An example for the arrangement of dislocations of the first type is shown in figure 7.18. The HRTEM micrographs are overlays of the raw (unfiltered) micrographs in figure 7.14 and the black and white results of a Fourier filtering, focusing on the (111) reflections. Thereby, the (111) lattice planes in YSZ (respectively the (222) planes in $Sc_2O_3$) are enhanced and the phase contrast is preserved. In the figure, different locations of the same column are shown: directly at the substrate (lower micrograph) and at some distance to it (upper micrograph). At the first $Sc_2O_3$ | YSZ interface, a quite regular arrangement of dislocations is found in the $Sc_2O_3$ phase (see also the smaller picture at the right hand side, which is a magnification of this region). However, the dislocations are more

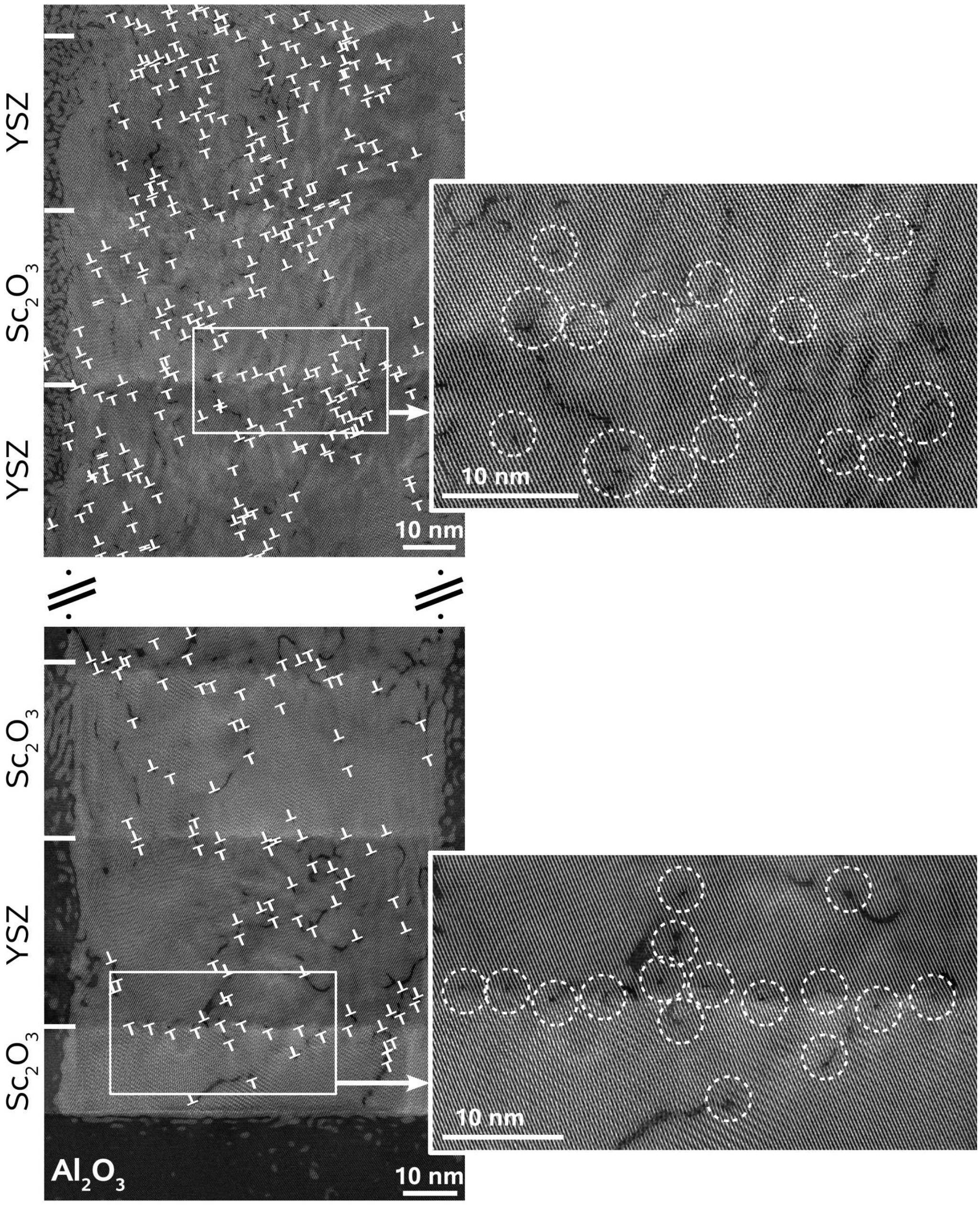

**Figure 7.18:** HRTEM micrographs from different positions in the multilayer sample YSc50-3. Lower micrograph: directly at the substrate. Upper micrograph: at some distance from the substrate. Dislocations are marked with $\perp$. The smaller pictures on the right hand side are magnifications of the indicated areas (shown in larger scale in the appendix, section 12.3). Because of the high number, not all dislocations are marked in the upper small picture.

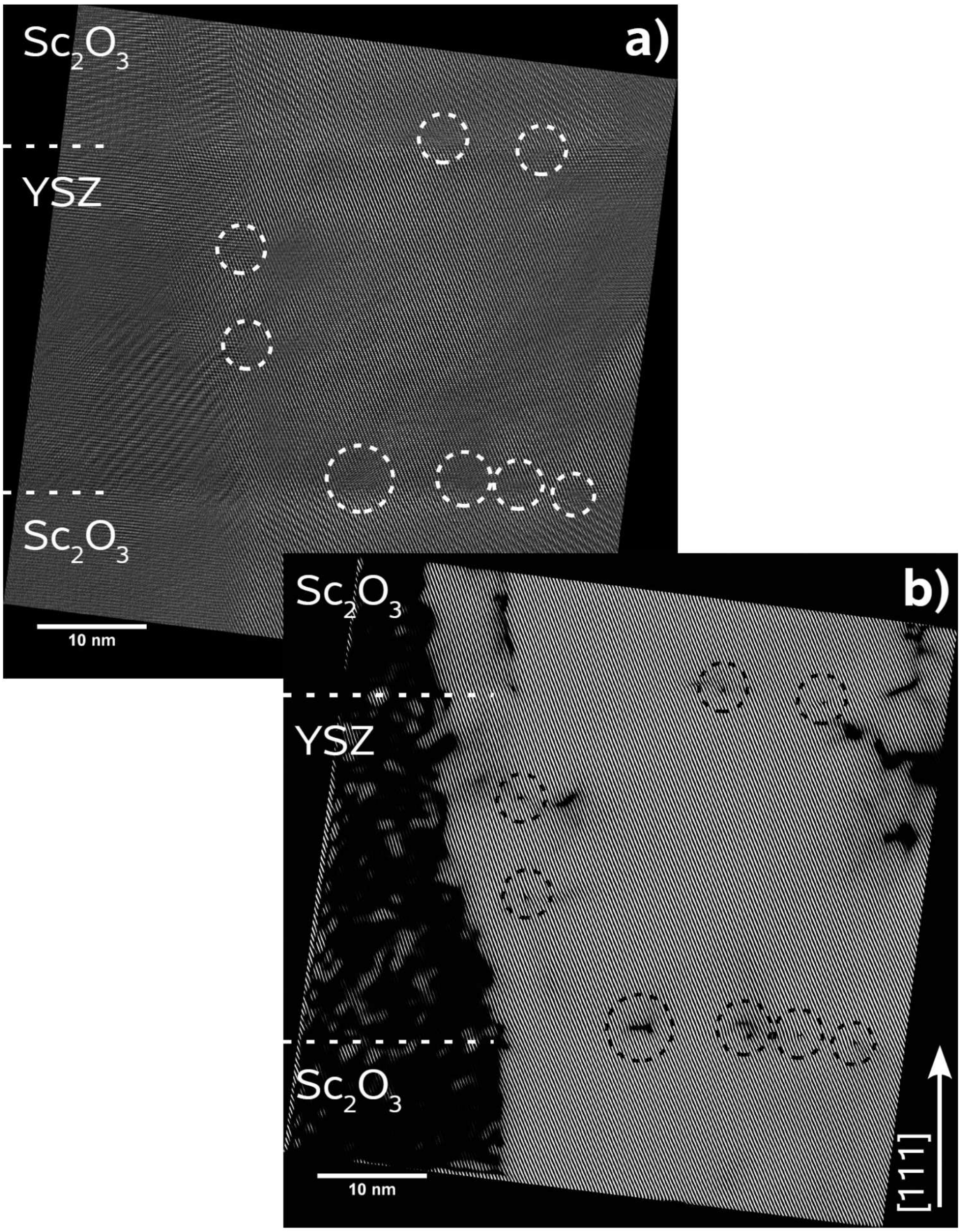

**Figure 7.19:** HRTEM micrograph from an area in the sample YSc50-3, situated at a middle distance between the substrate and the sample surface. a) Raw micrograph. b) [001] filtered micrograph. Dislocations are highlighted. The phase boundaries are marked by dashed lines. The pictures are shown in larger scale in the appendix, section 12.3

irregularly arranged in subsequent layers. At some distance to the substrate, as is shown in the upper HRTEM micrograph in figure 7.18, a very high number of dislocations can be found. These dislocations are distributed statistically over the layers. No accumulation at the interfaces and no regular arrangements are present. Also, two orientations with anti-parallel Burgers vectors are visible for the dislocations. There seems to be no preference for either of the two possible orientations. Often, anti-parallel dislocations are situated directly next to each other.

The high dislocation density in figure 7.18 is not found in all HRTEM micrographs of this sample and may therefore be an extreme example. Figure 7.19 shows a HRTEM micrograph from a region in a larger column, situated at a middle distance between the substrate and the sample surface. Only few dislocations are visible in this micrograph (they can be seen more easily in the [001] filtered image in figure 7.19b)). These dislocations are situated in the $Sc_2O_3$ layers close to the interfaces and also in the YSZ layer near a grain boundary.

Dislocations of the second type were found in smaller densities (see figure 7.20). A slightly increased number of these dislocations was found in the vicinity of the grain boundaries. As an example, the small inset in the upper right corner in figure 7.21 shows an enlarged region near a grain boundary where some dislocations can be seen. Close to the substrate, the number of visible dislocations of the second type is lower, as can be seen figure 7.21.
The strain release caused by dislocations takes place in the direction of their Burgers vector. Typical misfit dislocations are therefore ideally edge type dislocations inclined between 90° to 60° towards the interface. This is the case for the first type of dislocations found in this multilayer sample, but not for the second type.

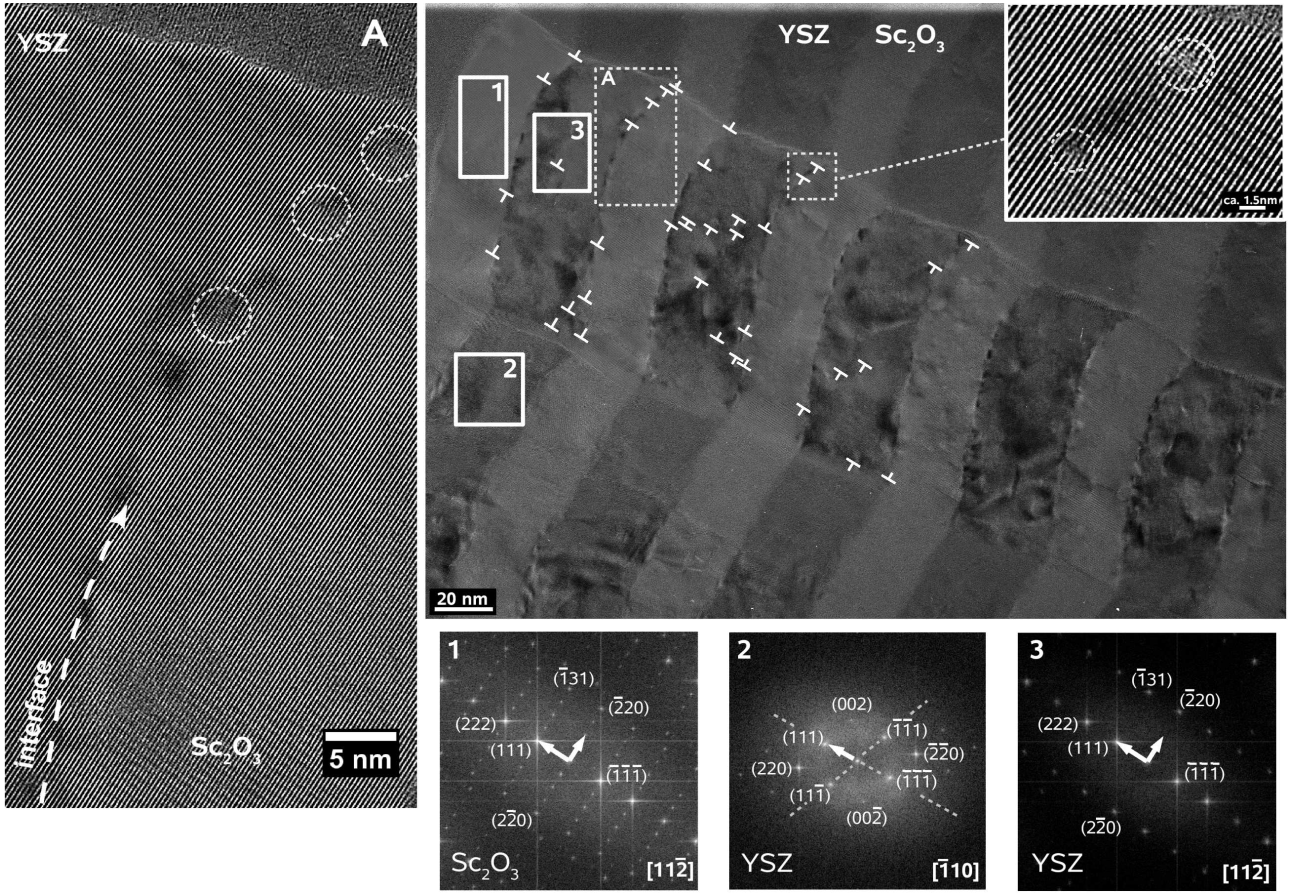

**Figure 7.20:** HRTEM micrograph of the sample YSc50-3, showing dislocations along the phase boundaries (marked with ⊥). Dark layers: YSZ. The YSZ layers are about 31 nm thick, the column shown is 98-99 nm thick. Small picture: magnification from the marked area.

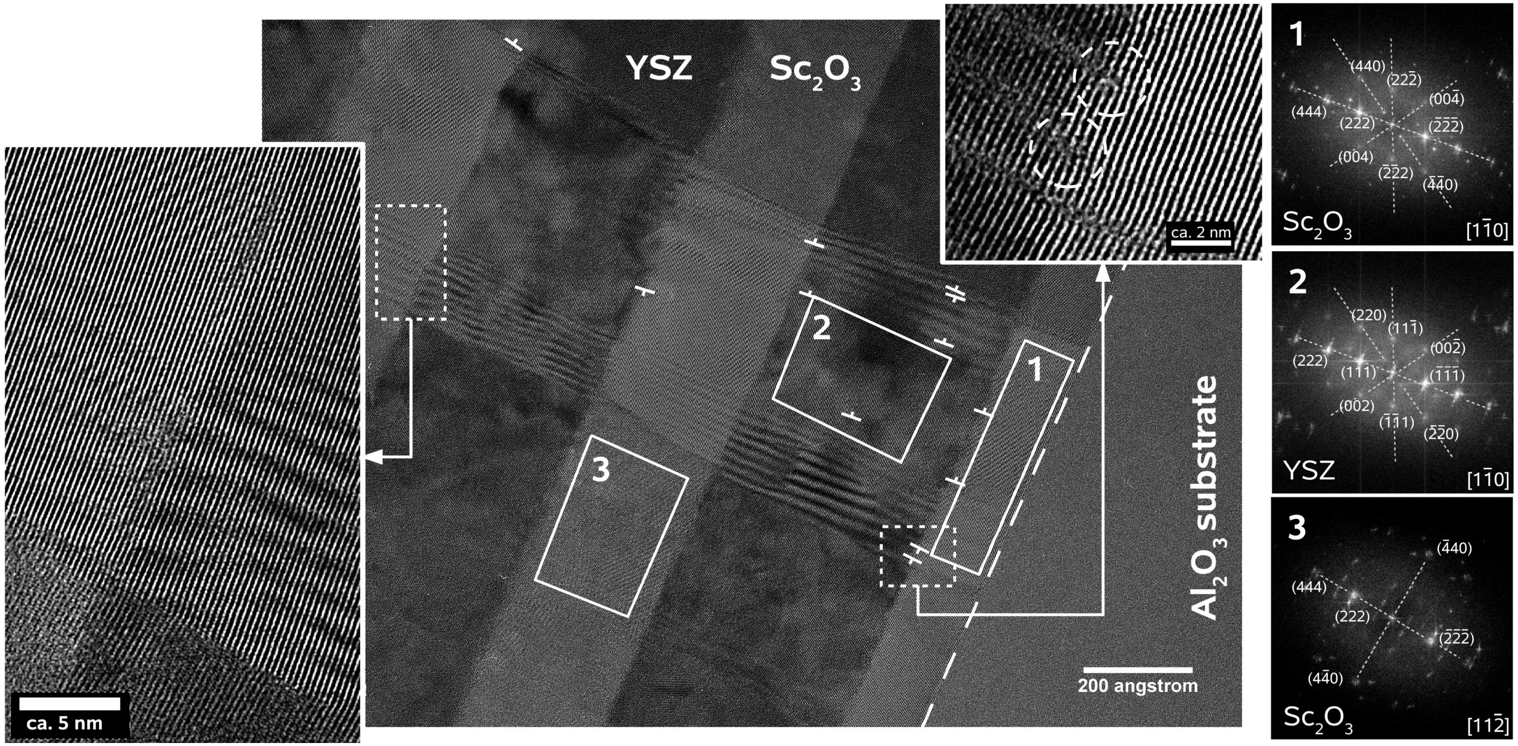

**Figure 7.21:** HRTEM micrograph of the sample YSc50-3, near the substrate. Small picture: magnification from the marked area. Dislocations are marked with ⊥.

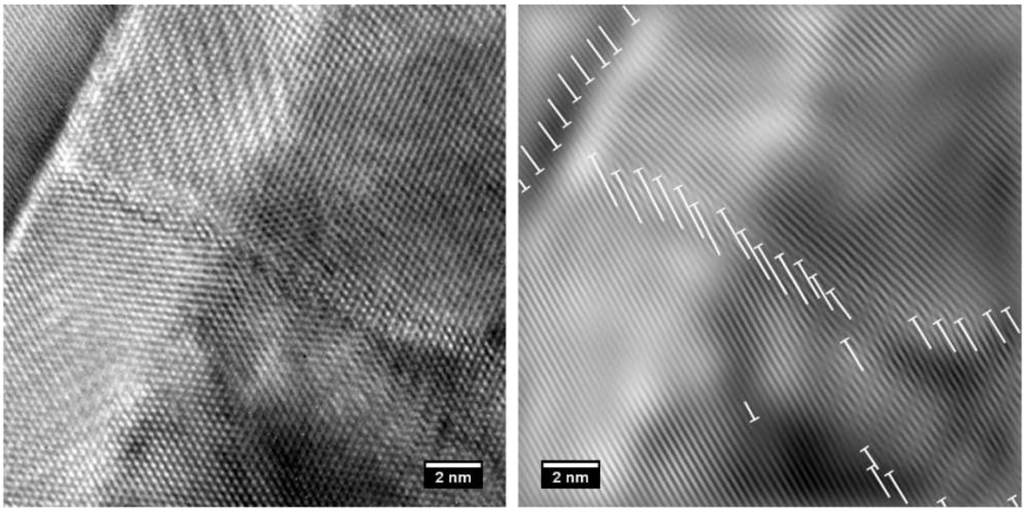

**Figure 7.22:** HRTEM micrograph of the sample YSc150-2, at the substrate. Right hand side: [001], $[11\bar{1}]$ $Sc_2O_3$ and $[11\bar{2}\bar{3}]$ $Al_2O_3$ Fourier filtered image of the same region.

### Grain Boundary Structure

The structure of the grain boundaries was closely investigated in the sample YSc150-2 (deposited at 10 Hz). In figure 7.22, a detail of the HRTEM micrograph in figure 7.15 is shown, comprising the substrate and the first two layers. The width of the region associated with the grain boundary in this picture is roughly 1 nm. Fourier filtering with respect to the [001] and $[11\bar{1}]$ $Sc_2O_3$ and the $[11\bar{2}\bar{3}]$ $Al_2O_3$ reflections[12] was used to make the periodic structures perpendicular to the substrate / layer interface clearly visible (right hand side of the picture). The investigated grain boundary is situated between two crystallites exhibiting the mirror inverted azimuthal orientations 1a) and 1b) (see figure 7.15), as defined above. A dense network of dislocations if found in the grain boundary, their distance being only one or two lattice planes (the dislocations are marked in the Fourier filtered picture). This structure can be expected for a grain boundary with a certain degree of misorientation between the crystallites, in this case mainly rotational (twist) and only a minor degree of tilt misorientation. Dislocations in the vicinity of grain boundaries can also be seen in figure 7.20 and 7.21 and were mentioned before.

Another feature is visible in the Fourier filtered image in figure 7.22: a regular network of dislocations exists in the interface between the substrate and the first $Sc_2O_3$ layer. The mean distance of the dislocations is 4.25 lattice planes. This is comparable to investigations on the system YSZ | $Y_2O_3$ [19].

---

[12] Because of the mirror inverted azimuthal orientation between the neighbouring crystallites, two sets of reflections were used which were very close in the FFT pattern: for the upper crystallite, $[11\bar{1}]$ reflections were used and [001] reflections for the lower crystallite. The FFT result in which these reflections are marked is shown in the appendix in figure 12.1.

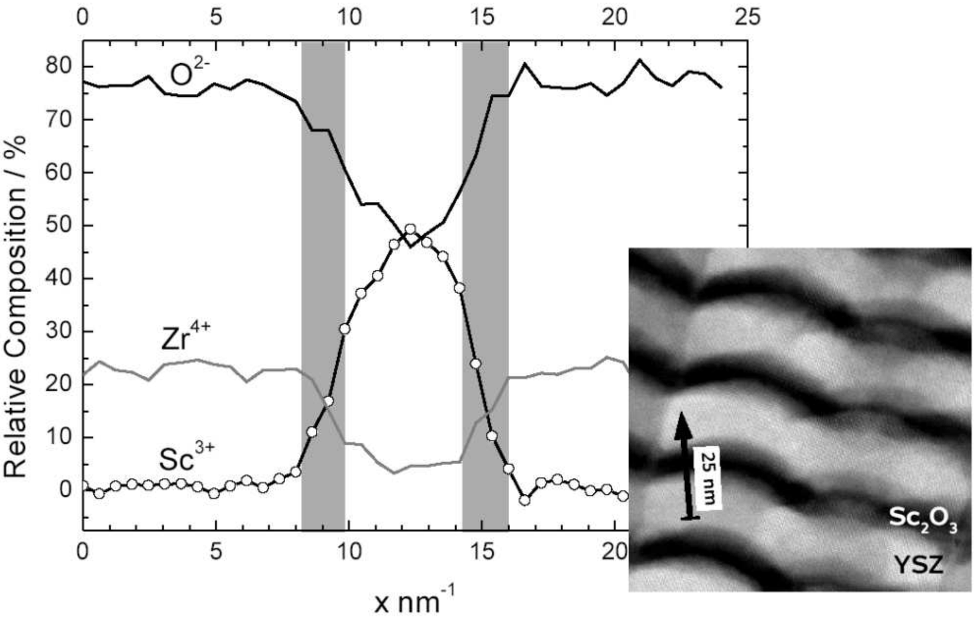

**Figure 7.23:** Quantified EEL spectrum for the sample YSc150-2. The relative composition is given in atomic %. Oxygen is overestimated. The inset picture is a Z-contrast HR-STEM micrograph. The position of the line scan is marked with an arrow.

### EELS Measurements

EELS line scans were performed across selected interfaces in the samples YSc150-2 (10Hz) and YSc50-3 (2Hz). The relative local composition (in atomic %) of the sample YSc150-2 as a result of a line scan is shown in figure 7.23. The oxygen content is overestimated. It can be seen that the signals of Zr and Sc overlap over a distance of several nm. From point measurements, the real overlap between both phases was estimated as $x$ = 1.5 - 2 nm, which is also marked in the plot. This indicates only a slight interdiffusion of both phases. The reason that the interdiffusion zone in the plot in figure 7.23 appears broader is most probably due to the fact that the wavy layer morphology leads to an overlap of the different layers below the investigated lateral surface. This overlap is visible as gray shadows at the layer interfaces in the inset Z-contrast image.

In the sample YSc50-3, EELS line scans were performed from two different regions in the multilayer: close to the substrate and at some distance to the substrate (see figure 7.24). Figure 7.24a) shows the result of a line scan over a length of 190 nm at some distance to the substrate. The wavy layer morphology in this region can easily be seen in the inset Z-contrast HRSTEM micrograph, in which

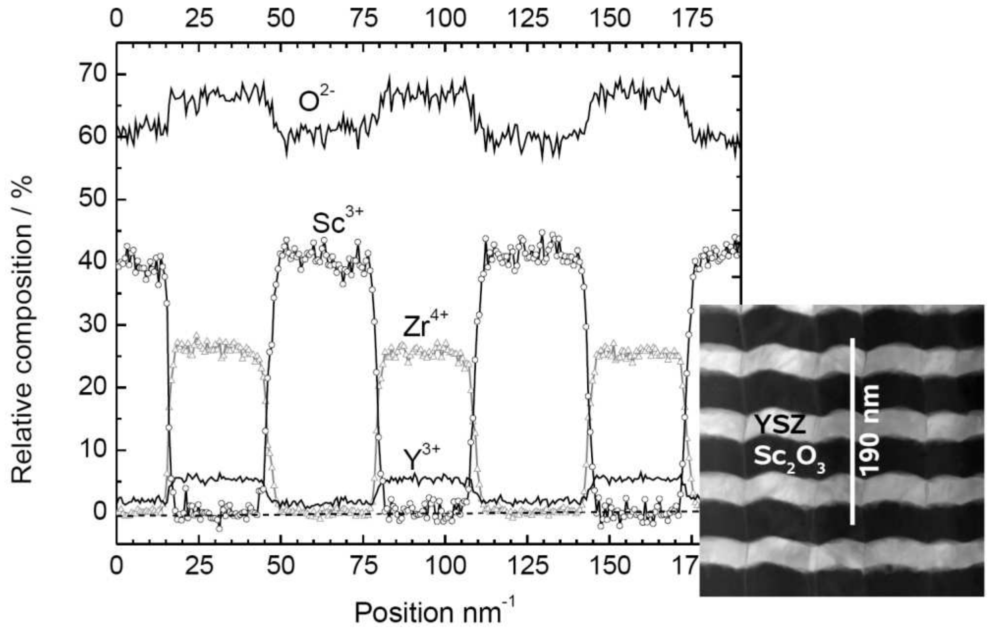

(a)

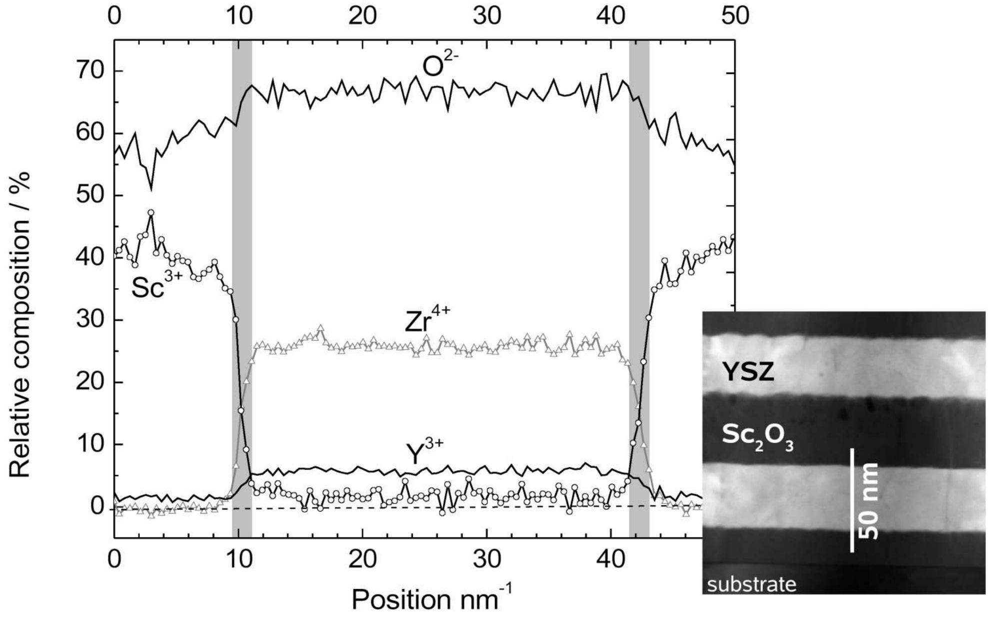

(b)

**Figure 7.24:** Quantified EELS line scans of the sample YSc50-3. The relative composition is given in atomic % and the position of the line scans is marked in the small inset HR-STEM micrographs. a) A line scan performed over a distance of 190 nm. The overlap between the different layers estimated from this picture is about 2.5 nm. b) EELS line scan performed over a distance of 50 nm. The overlapping zones are about 1.5 nm wide and highlighted light gray.

the position of the line scan is marked[13]. From this line scan, an overlap of about 2.5 nm between the different materials is found at the phase boundaries.

Figure 7.24b) shows the result of a line scan over a length of 50 nm near the substrate, were the layers are flat. The width of the interdiffusion zone estimated from this line scan is about 1.5 nm. This means that the phase boundaries in the YSZ | $Sc_2O_3$ multilayers actually are very sharp and almost no interdiffusion takes place. The broader overlap of the signals in figure 7.24a) is due to the wavy layer morphology. It is important to say that the actual width of the interdiffusion zones may be even smaller because the determined width is close to the resolution limit of the measurement[14].

### TOF-SIMS-Results

Dynamic TOF-SIMS measurements show that the overall contamination level in the multilayers is low. Figure 7.25 depicts the result for the sample YSc50-3, deposited at 2 Hz. An $O_2^+$ ion source was used for sputtering, operating at 1 kV accelerating voltage.

The undulating signal intensities for Sc, Zr and Y reflect the alternating layer structure of the sample. A broadening of the intensity maxima associated with the different phases in the multilayer is due to an increased intermixing induced by the ion beam. As the signal intensity in TOF-SIMS is dependent on the ionization probability of each detected species and on the given matrix, absolute concentrations can not be evaluated without a suitable calibration.

As expected, the relative oxygen content is higher in the YSZ layers. The amount of possible impurities like Fe, Ti, Si, Mg and Cr in the samples is very low and in the order of the background level. The associated signals are therefore not included in figure 7.25. In the YSZ layers, a somewhat enhanced concentration of Ca, Al, K and C was found. The $Sc_2O_3$ layers contain a slightly enhanced amount of Na if compared to the YSZ layers. If the high ionization probability for Na and K are considered, their relative content in the multilayers is inconspicuous.

A steep increase of the intensities directly at the beginning of the profile as well as single sharp peaks in the curves can be attributed to measurement artefacts.

The TOF-SIMS investigation of a $Sc_2O_3$ single layer delivered similar results, with Na and K being the impurities with the highest intensity in the profile, followed by Ca and Al at much lower intensities.

---

[13] Because of the software based background correction in the quantified EEL spectra, the relative chemical composition in these plots shows a stronger variation than that of the net signals (not shown; the variation of the net signal intensity obtained from one material layer is very low).

[14] The resolution limit in the EEL spectra is mainly determined by the broadening of the electron beam inside the sample.

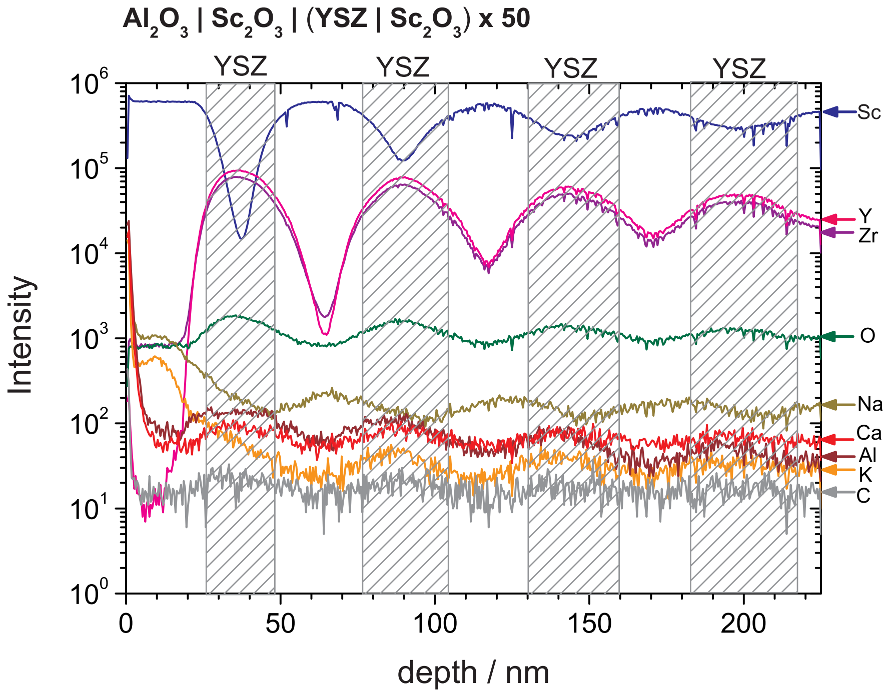

**Figure 7.25:** Positive ion mode SIMS depth profile of the topmost layers of the sample YSc50-3.

### 7.2.2 YSZ | $Lu_2O_3$ Multilayers

#### X-Ray Diffraction

Similar to the system YSZ | $Sc_2O_3$, all YSZ | $Lu_2O_3$ multilayers were crystalline directly after preparation. But the crystallinity could be improved by a heat treatment. No significant change of the relative intensities of the signals was observed during annealing, showing that the orientation of the crystallites was determined during the deposition process and did not change afterwards.

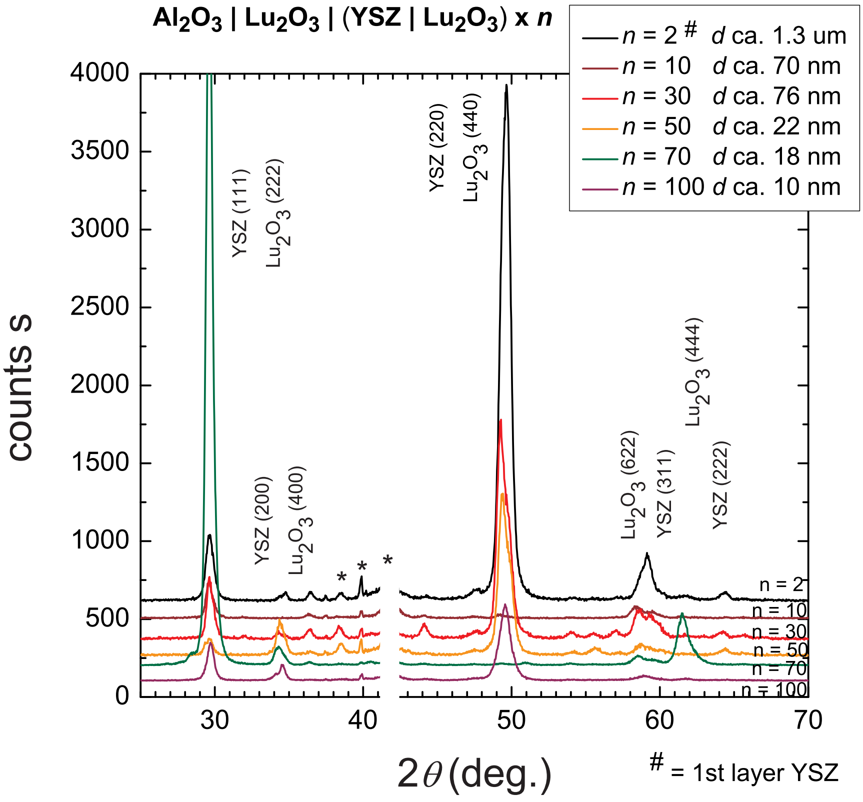

**Figure 7.26:** Overview showing the XRD results for different samples of the system YSZ | $Lu_2O_3$, deposited at 2 Hz. "$*$" denotes the position of substrate reflections.

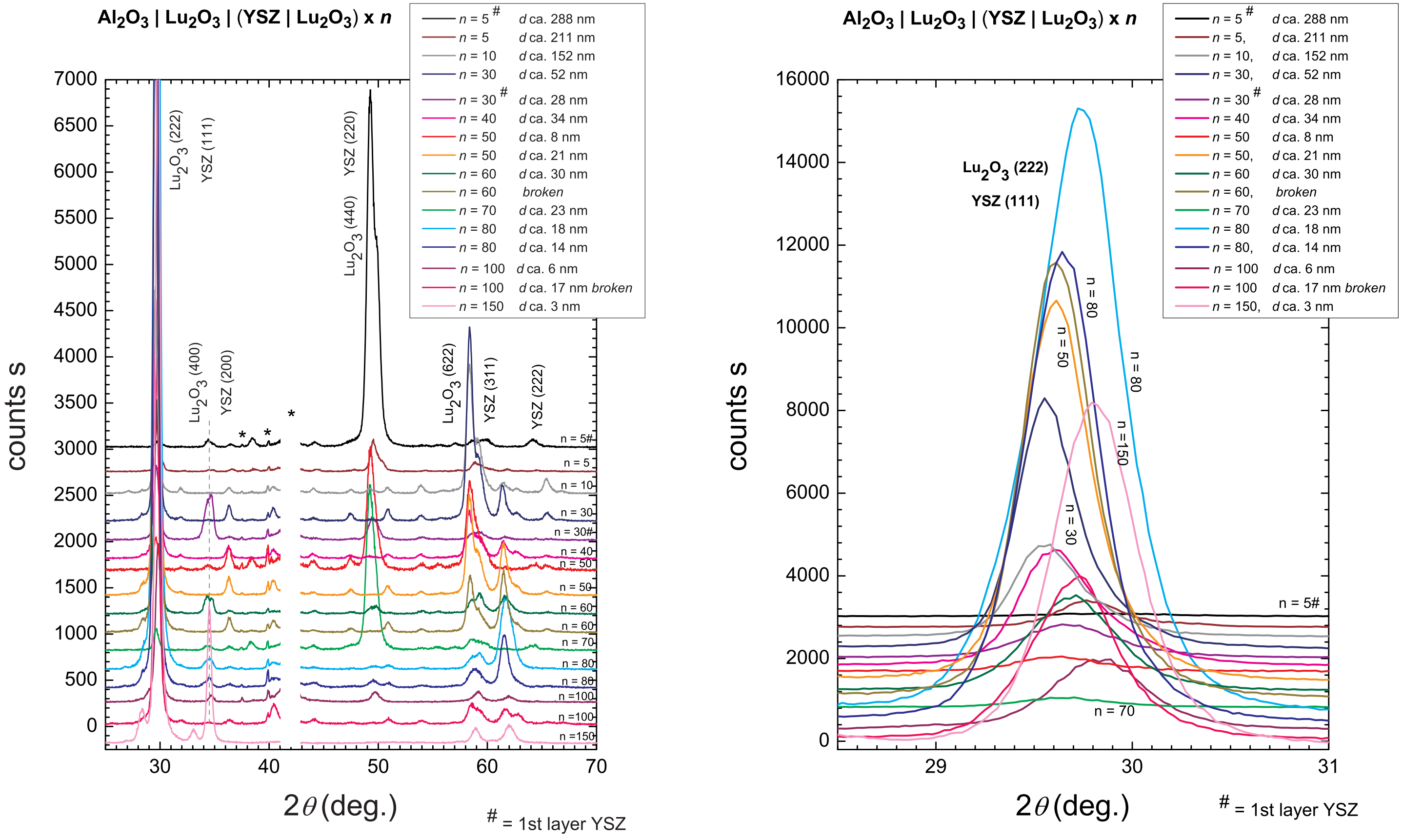

(a)

(b)

**Figure 7.27:** Overview showing the results of XRD measurements for different samples of the system YSZ | $Lu_2O_3$, deposited at 10 Hz. b) Enlarged part of a), showing the (111) YSZ respectively (222) $Lu_2O_3$ reflexes. "$*$" denotes the position of substrate reflections.

It is already apparent from the XRD results in figure 7.26 and 7.27 that the texture of the multilayers was not as highly developed as in the system YSZ | $Sc_2O_3$. This is independent from the deposition frequency. Mainly two variants for the axial orientation relationship were found:

A) $Al_2O_3$ (0001) ‖ $Lu_2O_3$ (111) ‖ YSZ (111)

B) $Al_2O_3$ (0001) ‖ $Lu_2O_3$ (110) ‖ YSZ (110)

Variant A) was mostly preferred in samples with thin individual layers ($d <$ 20 nm), variant B) in samples with thick individual layers.
Orientation variants which were found in smaller amounts were:

C) $Al_2O_3$ (0001) ‖ $Lu_2O_3$ (100) ‖ YSZ (100)

D) $Al_2O_3$ (0001) ‖ $Lu_2O_3$ (311) ‖ YSZ (311)

A splitting of the (111) YSZ and (222) $Lu_2O_3$ reflections was observed for a sample with $n = 150$ and $d \approx 3$ nm (see figure 7.28), but not for any other sample of this system. The additional reflections appear at a mean distance of 1.425°. As in the system YSZ | $Sc_2O_3$, these are most probably superlattice reflections. The $d$ value of the superlattice can be calculated using Bragg´s equation. Assuming a 2nd order reflection, a value of 6.2 nm results. From HRTEM measurements, the width of a double layer YSZ/$Lu_2O_3$ (which is assumed to be one period of the superlattice) was calculated to be ≈ 5.6 nm.

Due to the similar lattice spacings, the reflections of YSZ and $Lu_2O_3$ could not be separated in the XRD measurements, resulting in broadened combined signals. Therefore, analysing the position of the merged (111) YSZ and (222) $Lu_2O_3$ reflection leads to a common value for both phases. Comparing this value to the literature values for both materials (see table 4.1), only a very coarse evaluation of the out-of-plane lattice parameters in the multilayers can be made (see tables 12.3 and 12.4). An overview over the calculated mean lattice dilation in YSZ and $Lu_2O_3$ perpendicular to the film plane is given in table 7.2. Because of the rather big uncertainty of these calculations, no FWHM values for the reflections are given.
As a consequence of the method which was used to obtain these values, the calculated lattice dilatation of $Lu_2O_3$ is always much lower than that of YSZ. A shrinking of $\Delta a$ after the heat treatment can be observed for both materials and deposition rates. In contrast to the values obtained for the system YSZ | $Sc_2O_3$, the lattice dilatation is greater for samples deposited at 2 Hz compared to those deposited at 10 Hz.

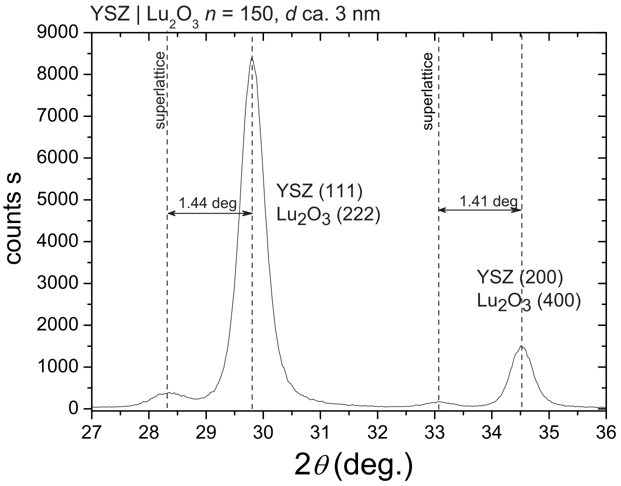

**Figure 7.28:** Enlarged range from the XRD of the sample YLu150. The superlattice reflections are marked.

**Mean Lattice Dilatation of YSZ in the System YSZ | $Lu_2O_3$**

| | 10 Hz deposition rate | | 2 Hz deposition rate | |
|---|---|---|---|---|
| | $\Delta a$ YSZ [%] | $\Delta a$ $Lu_2O_3$ [%] | $\Delta a$ YSZ [%] | $\Delta a$ $Lu_2O_3$ [%] |
| as deposited | 1.61 | 0.60 | 1.92 | 0.92 |
| after annealing | 1.17 | 0.17 | 1.39 | 0.39 |

**Table 7.2:** Mean deviance $\Delta a$ of the lattice parameter of YSZ and $Lu_2O_3$ from the literature values.

### Texture Analysis

Rocking curves revealed that some tilt misorientation is present in all multilayer samples. The results obtained for different samples deposited at 10 Hz and 2 Hz are shown in figure 7.29. All rocking curves were recorded for the (111) YSZ, respectively (222) $Lu_2O_3$ reflection. In figure 7.29a), it can easily be seen that the FWHM value of the reflections increases with increasing thickness $d$ of the individual layers. It is only 7.23° for the sample YLu804, for which $d$ is about 14 nm. The FWHM values for the samples YLu304 ($d$ = 52 nm) and YLu5-2 ($d$ = 211 nm) are almost twice as high, being 13.54° and 13.70°, respectively. A value of 12.02° was measured for the sample Ylu40 ($d$ = 34 nm). This behaviour is opposite to the results obtained for the system YSZ | $Sc_2O_3$ (see figure 7.5 in section 7.2.1). The FWHM value for the sample YLu70-3, deposited at 2 Hz and shown in figure 7.29b), is only about 6.06°. It is somewhat smaller than the FWHM value of the sample YLu804, deposited at 10 Hz, even though the individual layers are slightly thicker.

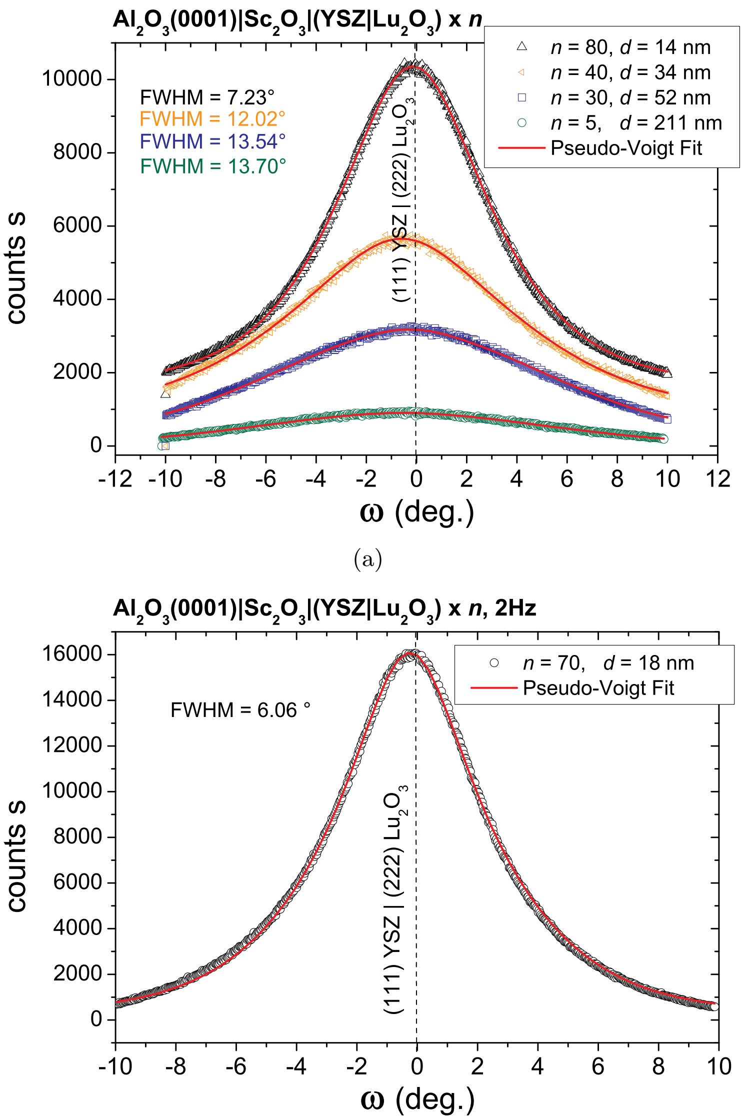

(a)

(b)

**Figure 7.29:** Rocking curves for different samples of the system YSZ | $Lu_2O_3$. a) Samples deposited at 10 Hz (YLu5-2, YLu304, YLu804). b) sample Ylu70-3, deposited at 2 Hz

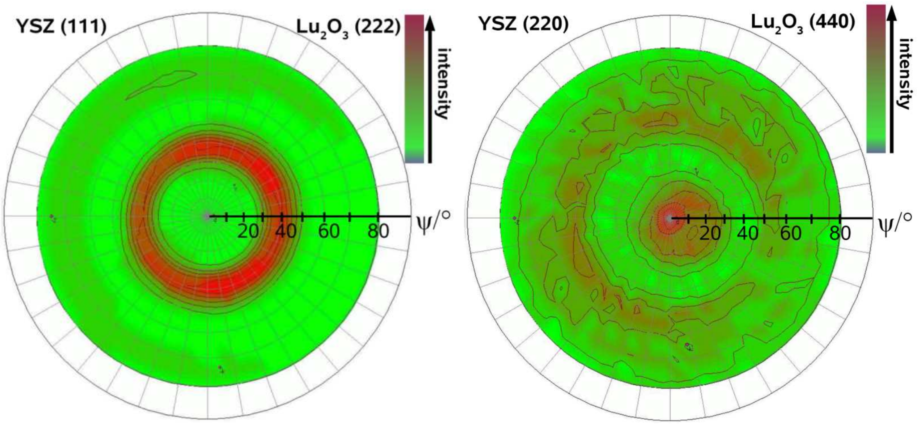

(a) (b)

**Figure 7.30:** Pole figures for a sample with n = 70, deposited at 10 Hz.

The intensity of the signals in the rocking curve measurements cannot directly be interpreted in terms of crystallinity, because the investigated samples were not always mainly oriented along the (111) direction. Thus, the (111) reflection sometimes is not very intensive in the XRD pattern.

Figure 7.30 shows pole figure measurements of a sample with $n = 70$ and $d =$ 23 nm, deposited at 10 Hz. The pole figures were recorded for the (111) YSZ, respectively (222) $Lu_2O_3$ and the (220) YSZ, respectively (440) $Lu_2O_3$ reflections. In figure 7.30a), the maximum signal intensity for the reflections of the [111] direction appears at $\Psi \approx 30° - 40°$ and is equally distributed over all azimuthal (in-plane) angles $\Phi$ (the red spot in the centre of the figure is not due to signal intensity, it is just a marker). $\Psi$ roughly corresponds to the theoretic angle between the (111) and the (110) planes, which is 35.26°.

The maximum signal intensity for the (220) YSZ (or (440) $Lu_2O_3$) signals in figure 7.30b) is found at the centre of the pole figure. Together with the $\Psi$ value obtained for the (111) signal, this shows that the crystallites are mainly oriented along the [110] direction, which complies well with the results found by standard XRD measurements for this sample (see figure 7.27). At $\Psi \approx$ 50°-60°, again some signal intensity is visible in figure 7.30b). This is expected because in cubic structures the equivalent [110] axes are oriented at 60° to each other. As in figure 7.30a), the signal intensity is more or less equally distributed over all azimuthal (in-plane) angles. That means that no preferred azimuthal orientation for the crystallites exists.

In both pole figures, the signal intensities are dispersed over a small range of the angle $\Psi$. In figure 7.30a), the intensity for the signals belonging to the [111] direction is dispersed over $\Delta\Psi \approx 10°$. The signal intensity for the [110] direction in figure 7.30b) is distributed somewhat asymmetrically, leading to a spreading of the central signal intensity over more than $\Delta\Psi = 20^\circ$ in a broad range of of azimuthal angles $\Phi$. This scattering of the signal intensity with respect to $\Psi$ is caused by a certain amount of tilt misorientation present in the sample (compare to figure 7.29). The reason that $\Delta\Psi$ is larger for the [110] signals is that the contributions of YSZ and $Lu_2O_3$ cannot be separated in this measurement. Because the difference in $2/theta$ of the (220) YSZ and (440) $Lu_2O_3$ reflections is larger than that of the (111) YSZ and (222) $Lu_2O_3$ reflections, $\Delta\Psi$ is also larger.

### SEM Measurements

As described for the system YSZ | $Sc_2O_3$, SEM mainly delivered information about the thickness of the individual layers and about the overall morphology of the multilayers. The determined mean thicknesses of the YSZ layers in samples of the system YSZ | $Lu_2O_3$ are given in the appendix in tables 12.3 and 12.4. Two examples for SEM measurements are shown in figure 7.31.

As in the system YSZ | $Sc_2O_3$, the individual layers of the multilayers were perfectly flat near the substrate. A wavy layer morphology developed with increasing distance to the substrate and was especially found in samples with rather thin individual layers ($\leq$ 20 nm). However, this wavy morphology is less strongly developed compared to the YSZ | $Sc_2O_3$ multilayers (compare figure 7.31b) to figure 7.8a)). Even in samples deposited at 2 Hz, no significant coarsening of the columnar structure was observed.

Again, a slight decrease in the thickness of the individual layers with increasing distance to the substrate was observed in all samples. It is most probably due to effects typical for pulsed laser deposition.

### (HR)TEM, HR-STEM and SAED Results

The samples which were investigated by (HR)TEM methods were: Ylu50, Ylu70, Ylu150 (10 Hz) and Ylu50-3 (2 Hz) (see table 12.3).

Comparable to the system YSZ | $Sc_2O_3$, a well-developed columnar structure was the main morphological feature of all multilayer samples. This can clearly be seen in the dark field exposure of the sample YLu70 in figure 7.32 and in the HRTEM micrograph of the sample YLu150 (figure 7.33). The width of the columns shows a strong variation, reaching from about 30 nm to over 100 nm. For the sample YLu70 ($n = 70$, $d =$23 nm), a mean column width of about 70 nm was determined. As can be seen in the dark field exposure, the columnar structure close to the substrate is very irregular, containing small crystallites, but it gets more uniform after 10 to 15 double layers. In the HRTEM micrograph of the sample YLu150, the columns close to the substrate are more regular, but the crystallites are also small. Again, the column width and uniformity increases with increasing distance to the substrate. In this picture, one can also see that the individual layers in this sample, which are only about 3 nm thick, are nonetheless continuous throughout

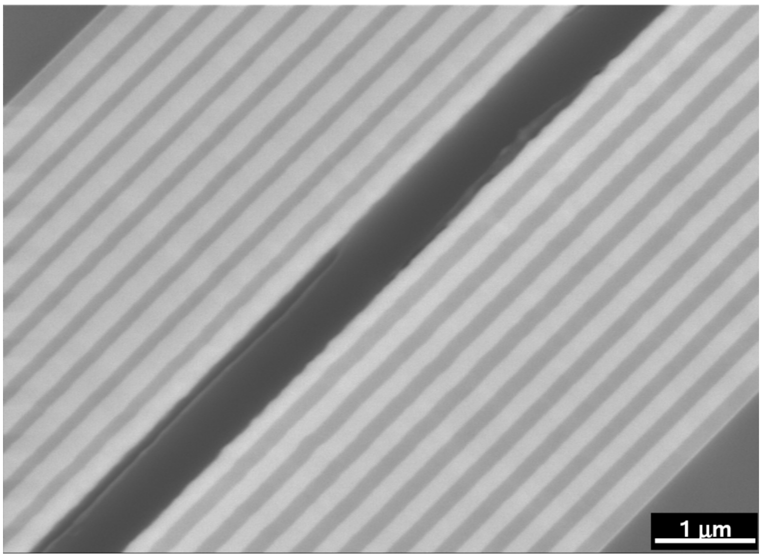

(a)

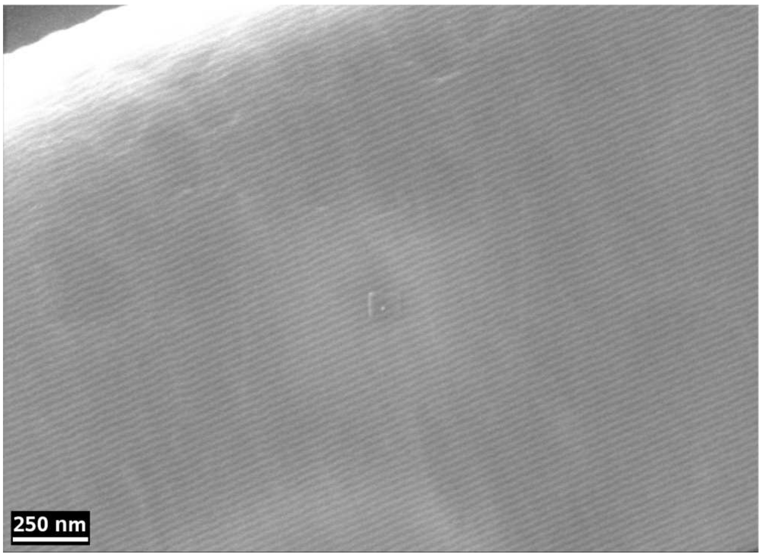

(b)

**Figure 7.31:** SEM images of two YSZ | $Lu_2O_3$ multilayers. a) Sample YLu10-2, $n$ = 10, $d$ = 152 nm, deposited at 10 Hz. The substrate can be seen in the upper left and lower right corner. b) Sample YLu1003, $n$ = 100, $d$ = 10 nm, deposited at 2 Hz. The substrate is located in the lower right corner of this picture.

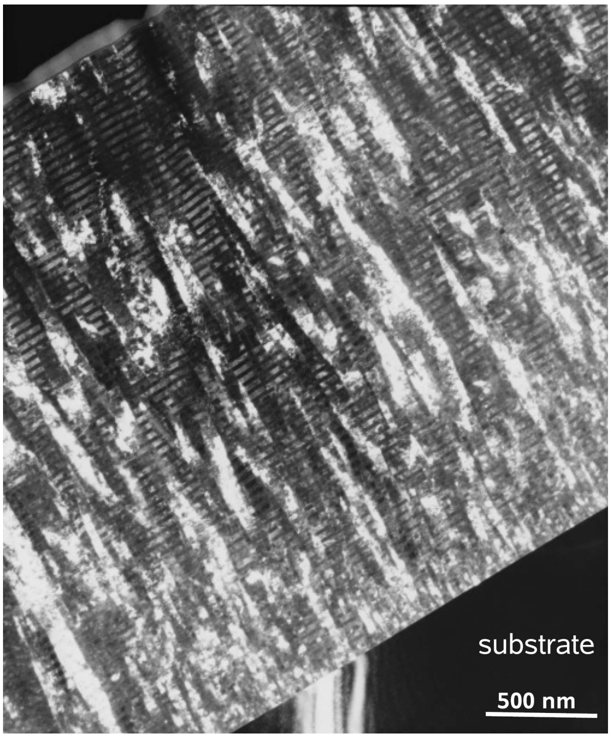

**Figure 7.32:** Dark field exposure of the multilayer YLu70, deposited at 10 Hz and consisting of 70 individual YSZ layers.

the whole multilayer and are not interrupted at the boundaries between individual columns.
The interfaces between YSZ and $Lu_2O_3$ are sharp. A disordered transition region was found between the substrate and the first $Lu_2O_3$ layer. The thickness of this region is about 1-2 nm, similar to transition regions found in the system YSZ | $Y_2O_3$. The transition region can be seen very clearly in figure 7.34, figure 7.38 a) and b) and as a bright band above the substrate in figure 7.38.

### Orientation Relationships

In figure 7.35, a TEM micrograph of the sample YLu50 is shown together with an SAED pattern obtained from an area comprising approximately 10 double layers YSZ | $Lu_2O_3$ (inset picture). The SAED pattern is corrected in its rotation in relation to the accelerating voltage and magnification. Thereby, the alignment of the reflections can directly be compared to the TEM micrograph. The reflections are sharp, indicating a highly textured local crystal structure. However, the scattering of the signal intensities over an angular range of up to 30° indicates some amount of tilt misorientation of the crystallites. No line of strong reflections

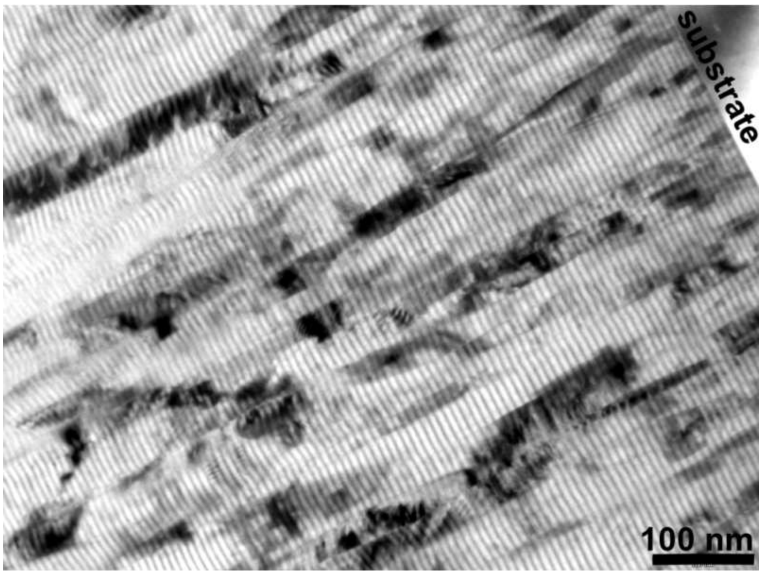

**Figure 7.33:** TEM micrograph of the sample YLu150, deposited at 10 Hz and containing 150 individual layers of YSZ being ca. 3 nm thick. The substrate can be seen in the upper right corner.

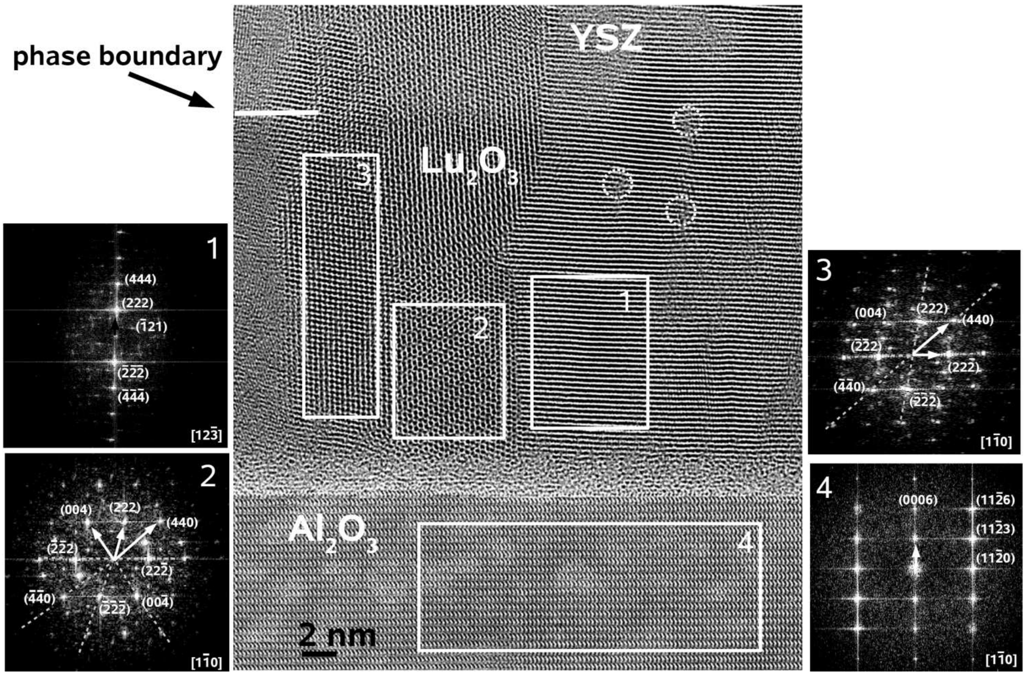

**Figure 7.34:** HRTEM micrograph of the sample YLu50 ($n$ = 50, $d$ about 8 nm). At the interface between the substrate and the first layer, a disordered transition region is visible. The indices given in square brackets denote the direction of the beam vector $\vec{\mathrm{B}}$.

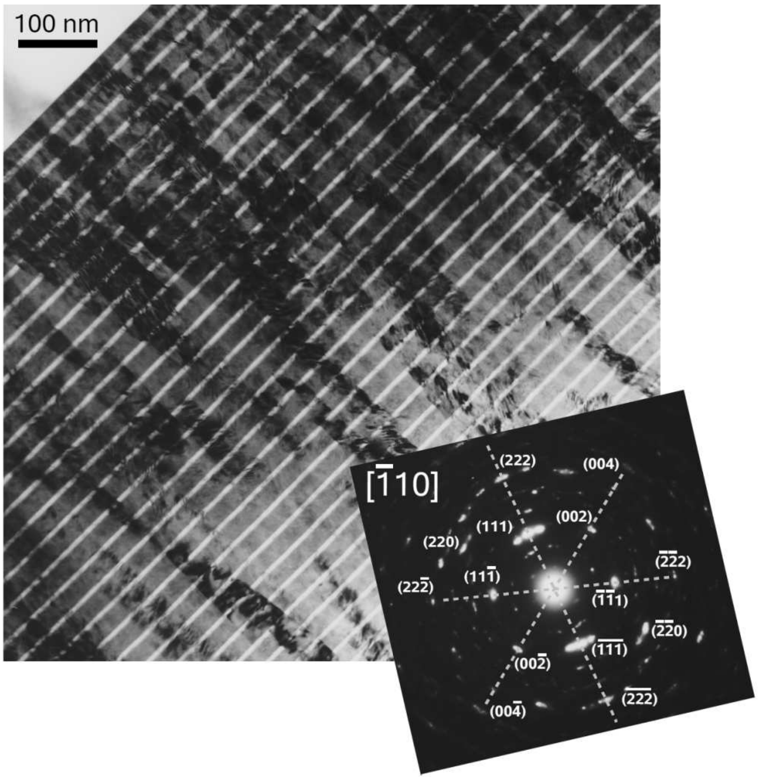

**Figure 7.35:** TEM picture of the sample YLu50. The substrate can be seen in the upper left corner. The inset picture shows an SAED of an area comprising about 10 double layers YSZ | $Lu_2O_3$. The SAED was corrected in its rotation and the alignment of the reflections can directly be compared to the TEM micrograph. (hkl) indices refer to YSZ, indices in square brackets denote the beam direction $\vec{B}$.

is perpendicular to the layers. The (110) plane is tilted by 10° to 20° to the substrate surface. In the XRD patterns, the strongest reflections were those for the [110] and [311] direction in both phases, the signals being rather broad. Unfortunately, the position of the area from which the SAED was recorded is unknown.

Figure 7.36 shows an SAED from the sample YLu150. The size of the aperture corresponded to the width of the whole multilayer. The area from which the SAED was recorded comprised the substrate and a part of the multilayer. The substrate reflections are those with the highest intensity in the SAED, being aligned in parallel lines. The signal intensities from the multilayer are distributed over a wide range of angles, leading to arc-like patterns. Similar patterns were also observed for the other samples of the system YSZ | $Lu_2O_3$ when the aperture used for the SAED was large. It proves that the overall tilt and twist misorientation in these samples is high. On the local scale, the texture is better developed, as indicated by the only slightly scattered reflections in figure 7.35.

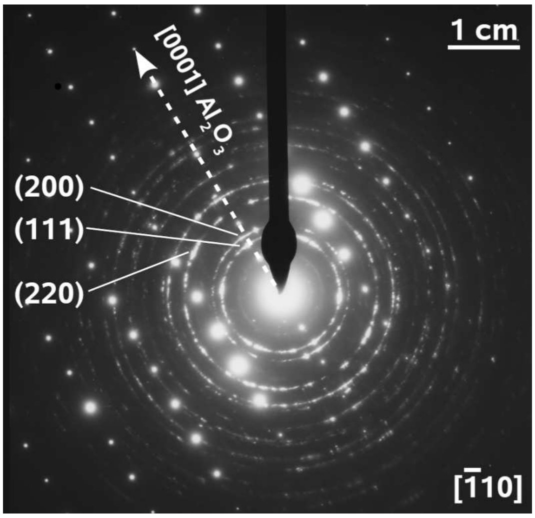

**Figure 7.36:** SAED of the sample YLu150. An aperture corresponding to the size of the whole multilayer was used and the SAED was recorded from an area comprising the substrate and part the multilayer. (hkl) indices refer to YSZ, the indices in square brackets denote the beam vector $\vec{B}$.

Some reflections are indexed, the indices referring to YSZ. Parallel to the line of reflections belonging to the [0001] direction of the substrate, reflections from the [111] and [100] direction in YSZ are visible. This corresponds to the results obtained by XRD.

Information on the local microstructure or the orientation of single crystallites was obtained by Fourier transformation of selected areas in HRTEM micrographs. As can be seen for example in figure 7.37 or figure 7.38, FFTs obtained from different phases in the same column are identical with respect to the position of the reflections. This shows that within the columns, a uniform axial crystal orientation is retained for YSZ as well as $Lu_2O_3$. The same is valid for the azimuthal orientation. The azimuthal orientation varies between neighboring columns. Since the texture of the YSZ | $Lu_2O_3$ multilayers is not as well developed as in the system YSZ | $Sc_2O_3$, also the axial orientation may vary from one column to another. In figure 7.34, three neighboring crystallites are shown. One crystallite is oriented (111) $\|$ (0001) $Al_2O_3$ (FFT 1), but the FFTs from the other two crystallites reveal a tilt misorientation of about 18° and 9° (FFT 2 and 3). Also, the azimuthal orientations of the crystallites differ. Whereas the crystallites 2 and 3 show the azimuthal orientation $[1\bar{1}0] \parallel \vec{B}$, which can be identified as $[1\bar{1}0] \parallel [1\bar{1}0]$ $Al_2O_3$ if the FFT results from the substrate are taken into account, crystallite 1 is oriented $[12\bar{3}] \parallel [1\bar{1}0]$ $Al_2O_3$.

An example for completely different axial crystal orientations visible in the HRTEM micrographs of one multilayer sample can be seen in figure 7.37. In figure 7.37a), the crystallites are roughly oriented (111) $\|$ (0001) $Al_2O_3$ with a tilt misorientation of 12° (FFT 2 and 3) and 6° (FFT 4 and 5). In figure 7.37b), the orientation of the crystallites can be identified as (001) $\parallel$ (0001) $Al_2O_3$ with only a minor tilt misorientation of about 3°. Both orientations can also be found in the XRD results for this sample.

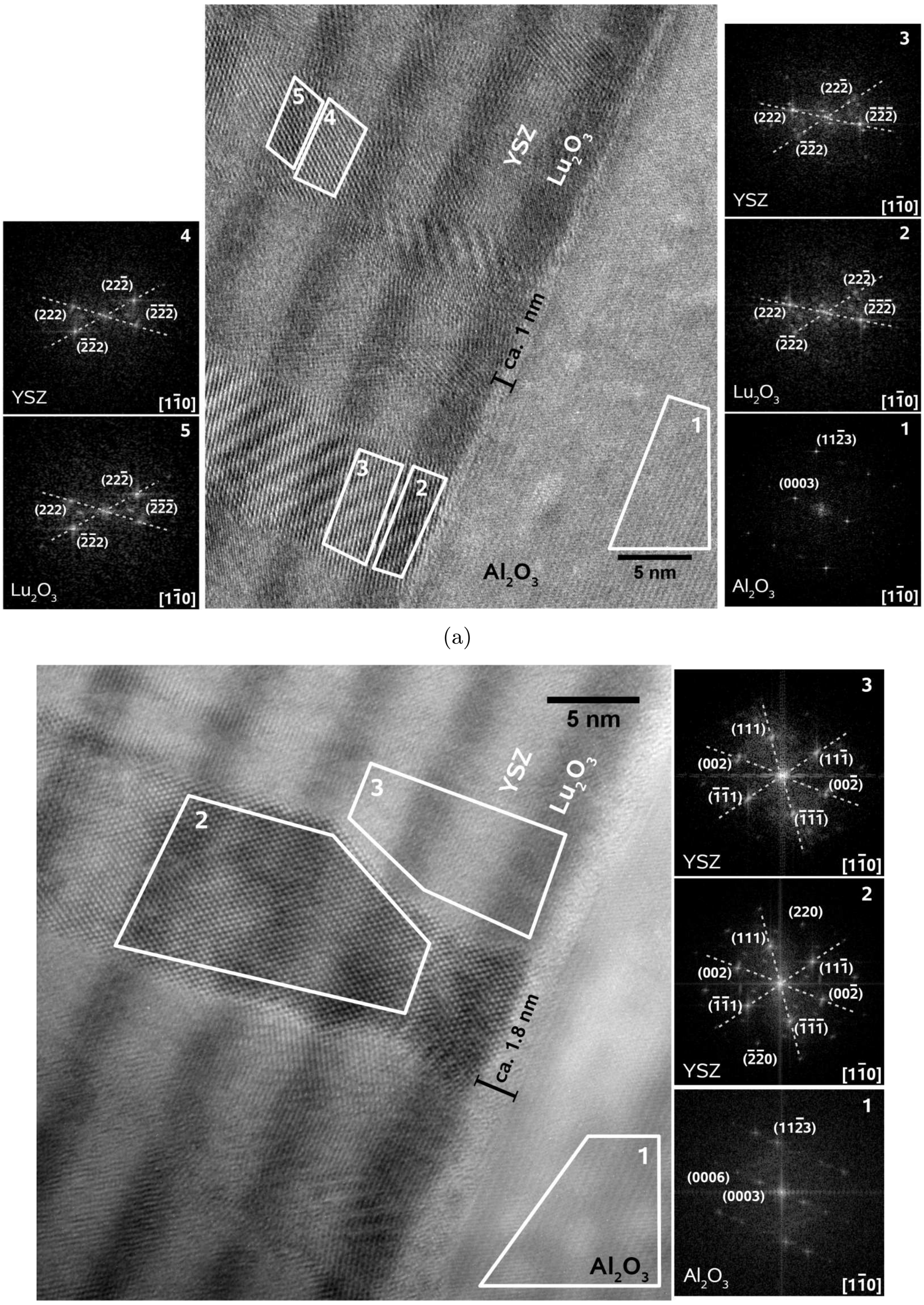

(a)

(b)

**Figure 7.37:** HRTEM pictures of the sample YLu150. The transition region between the substrate and the first layer is marked. In every inset FFT, the indices in square brackets denote the beam vector $\vec{\mathrm{B}}$.

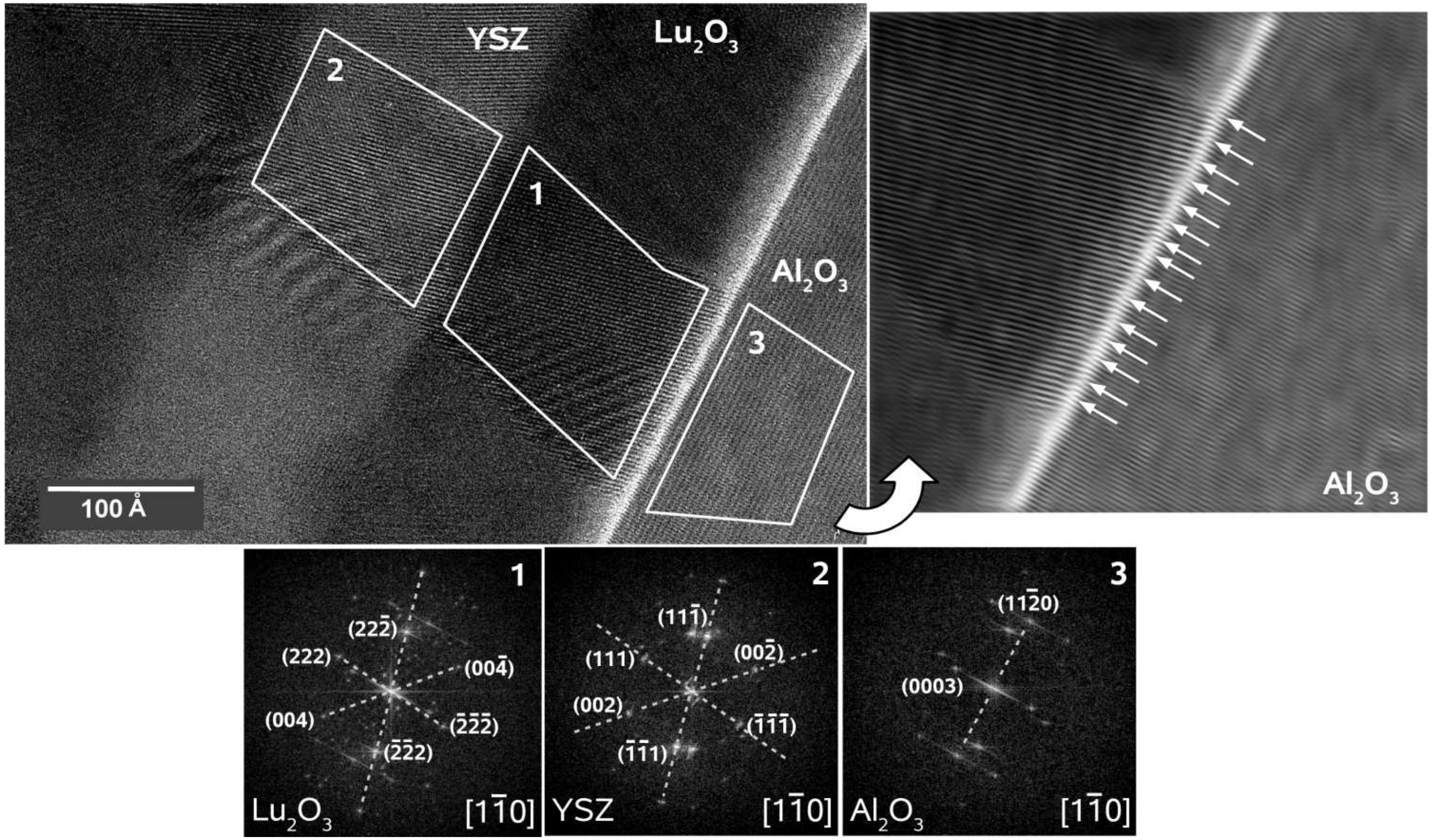

**Figure 7.38:** HRTEM micrograph of the sample YLu70, deposited at 10 Hz. The smaller picture is a Fourier filtered image of the interface between the substrate and the first Lu$_2$O$_3$ layer. Dislocations in this picture are marked by arrows. The three small pictures are Fourier transformations of the marked areas 1-3, with the associated beam vector $\vec{\mathrm{B}}$ given in square brackets.

The azimuthal orientation of the YSZ and $Lu_2O_3$ crystallites in figure 7.37 is given in every FFT as $[1\bar{1}0] \parallel \vec{B}$, which corresponds to $[1\bar{1}0] \parallel [1\bar{1}0]$ $Al_2O_3$ according to the FFT results obtained from the substrate. However, for the crystallites in figure 7.37a), this is not really true. As can be deduced from the appearance of the FFTs, the true azimuthal alignment is slightly twisted with respect to the mentioned orientation, the twist seeming to be similar in the two crystallites which were analysed.

Summarizing the results concerning the orientation relationship between the substrate, YSZ and $Lu_2O_3$, the following relationships were found in the HRTEM micrographs or by SAED measurements:

A) $Al_2O_3$ (0001) ∥ $Lu_2O_3$ (111) ∥ YSZ (111)

C) $Al_2O_3$ (0001) ∥ $Lu_2O_3$ (001) ∥ YSZ (001)

Some tilt with respect to these orientations was found in all samples, ranging between 3° and 18°.
For the azimuthal orientation, the following variants could clearly be identified (indexed in relation to orientation relationship A)):

1) $[1\bar{1}0]$ $Al_2O_3$ ∥ $[1\bar{1}0]$ $Lu_2O_3$ ∥ $[1\bar{1}0]$ YSZ

2) $[1\bar{1}0]$ $Al_2O_3$ ∥ $[12\bar{3}]$ $Lu_2O_3$ ∥ $[12\bar{3}]$ YSZ

In some FFTs (figure 7.37a)), the azimuthal orientation was most probably slightly twisted with respect to variant 1). As indicated by the pole figure measurements, a lot more variants may be possible, but those could not explicitly be found in the HRTEM micrographs.

### Dislocation Density

In YSZ | $Lu_2O_3$ multilayers, which were deposited at 10 Hz, no dislocations were found at the interfaces, at least not in crystallites were the periodic structures were clearly visible in the HRTEM micrographs.
A detailed insight in the interface structure is provided by Z-contrast HR-STEM micrographs, as shown in figure 7.39. In this image, the interfaces do not contain any visible dislocations or disordered regions. The lattice planes continue smoothly across the interface, a complete epitaxial growth is found. Both lattices are strained to establish a 1:1 fit at the phase boundary.

In the sample YLu50-3, which was deposited at 2 Hz, Fourier filtering of a HRTEM micrograph revealed a high number of dislocations. This can be seen in figure 7.40, were the HRTEM micrograph is shown together with an overlay

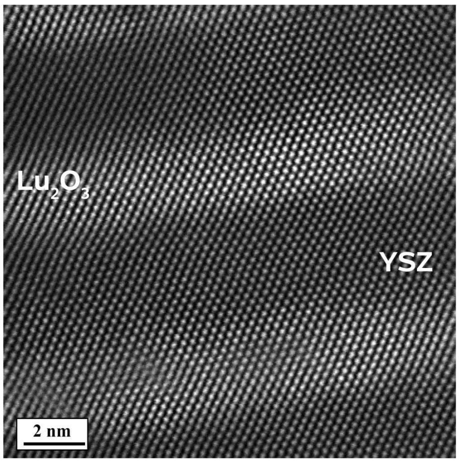

**Figure 7.39:** Z-contrast HR-STEM micrograph of the sample YLu150, $d \approx 3$ nm (mean value).

picture including the result of a Fourier filtering with respect to the (200) reflections. The dislocations are marked. High dislocation densities are found in regions were strain contrasts are visible in the raw micrograph and also at the grain boundaries. To give an impression of these dislocation arrangements, selected regions in the HRTEM micrographs are enlarged and shown in the small pictures on the left hand side. A characteristic feature of the overall dislocation configuration is that seemingly equal numbers of dislocations with anti-parallel Burgers vectors are present, often situated directly next to each other. There are no regular dislocation networks at the interfaces.

An important observation concerning the interface between the substrate and the first $Lu_2O_3$ layer can be made in figure 7.38. There, a part of the image was Fourier filtered to enhance the periodic structures perpendicular to the interface (smaller picture on the right hand side of figure 7.38). The Fourier filtered image shows the region marked 3 and approximately half of the region marked 1 in the normal HRTEM picture. The lattice planes in $Al_2O_3$ and $Lu_2O_3$ perpendicular to the interface can clearly be seen in the filtered image. Directly at the interface, a regular array of misfit dislocations is visible in $Al_2O_3$. These basically constitute the transition region mentioned earlier. The mean distance between the dislocations are 4.3 atomic rows in of $Al_2O_3$ but only about 3.4 atomic rows of $Lu_2O_3$.

### HR-EDX and EELS Measurements

HR-EDX measurements provide a means to evaluate the interdiffusion of YSZ and $Lu_2O_3$ at the phase boundaries. Figure 7.41 shows the result of a line scan across the approximate width of a double layer in the sample Ylu150 (deposited with 10 Hz). The small inset picture shows a Z-contrast image of the multilayer

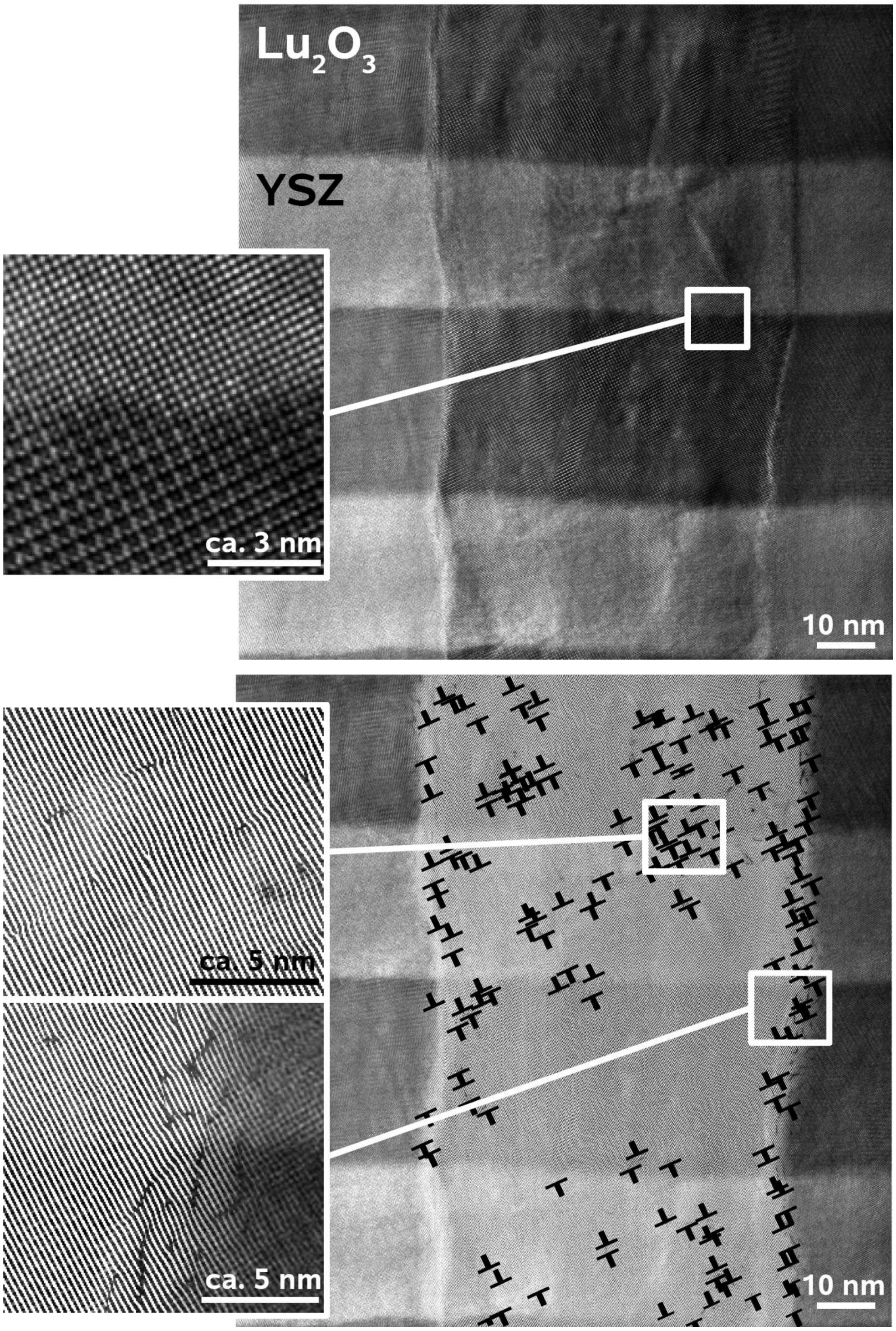

**Figure 7.40:** HRTEM micrograph of the sample YLu50-3, deposited at 2 Hz. The lower picture shows and overlay of the raw micrograph and the result of Fourier filtering with respect to the (200) YSZ reflections. Dislocations are marked with $\perp$. A high dislocation density is found in regions were strain contrasts are visible in the raw micrograph and at the grain boundaries. The small pictures on the left hand side show enlarged regions of the micrographs on the right hand side.

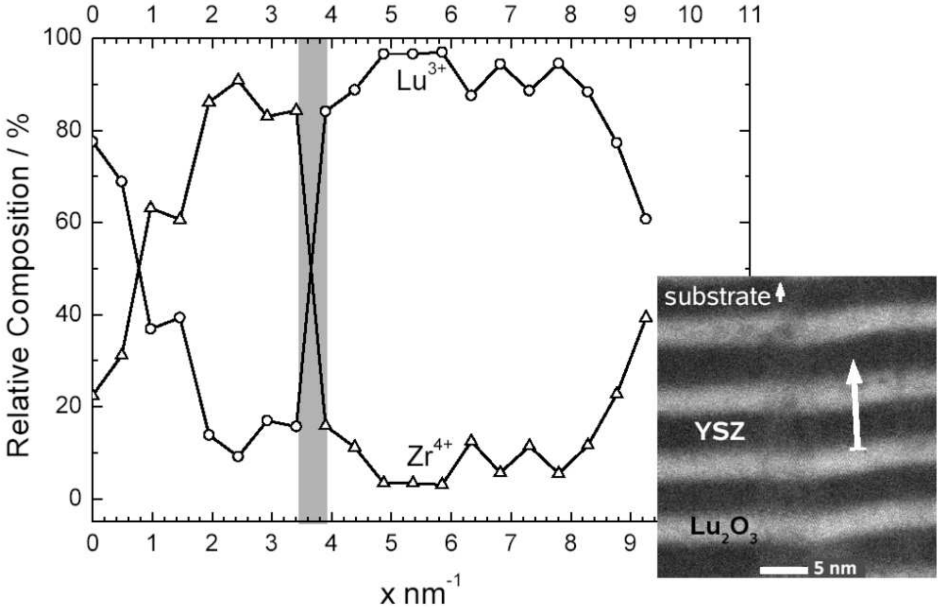

**Figure 7.41:** High resolution EDX line scan of the sample Ylu150. The counts, plotted on the y-axis, are relative values, scaled so that the sum of the signals of Zr and Lu amounts to 100 %. The white arrow in the inset Z-Contrast STEM picture shows the position of the line scan.

where the position of the line scan is marked with an arrow. In the graph, the relative intensities of Zr and Lu are shown in relation to the position. Because of a short acquisition time, which was used to prevent sample drift, the errors in the diagram are large for low concentrations. But point measurements showed that the concentration of Zr in $Lu_2O_3$ and Lu in YSZ drops to almost zero. Thus, the interdiffusion zones were estimated to be $\leq 1$ nm wide.

EELS measurements of the sample YLu50-3, deposited with 2 Hz, delivered somewhat different results. In figure 7.42, two different line scans are shown. The upper plot shows a scan over a distance of 190 nm, the lower plot a line scan over 50 nm. The position of the line scans is marked in the small inset HR-STEM micrographs. Contrary to the EELS measurements of the sample YSc50-3 in section 7.2.1, the net intensities are plotted with relation to the position. From both line scans, the width of the interdiffusion zone was determined to be about 4 nm, highlighted in light gray in figure 7.42b). The decline of the signal for $Zr^{4+}$ in $Lu_2O_3$ is steeper than that of $Lu^{3+}$ in the YSZ Phase, which can best be seen in figure7.42a). That means that mainly $Lu^{3+}$ diffuses into YSZ.

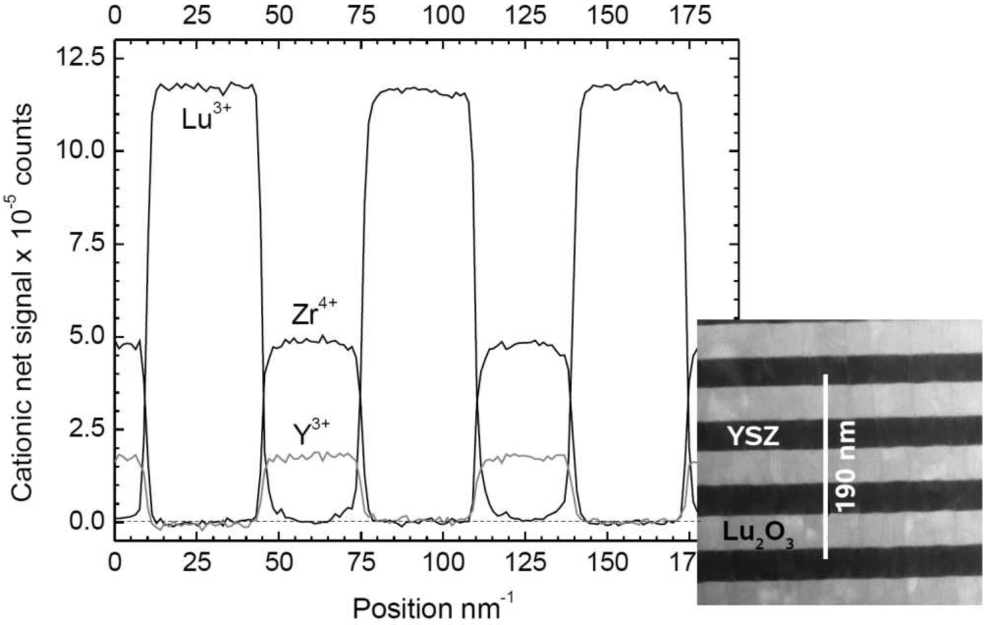

(a)

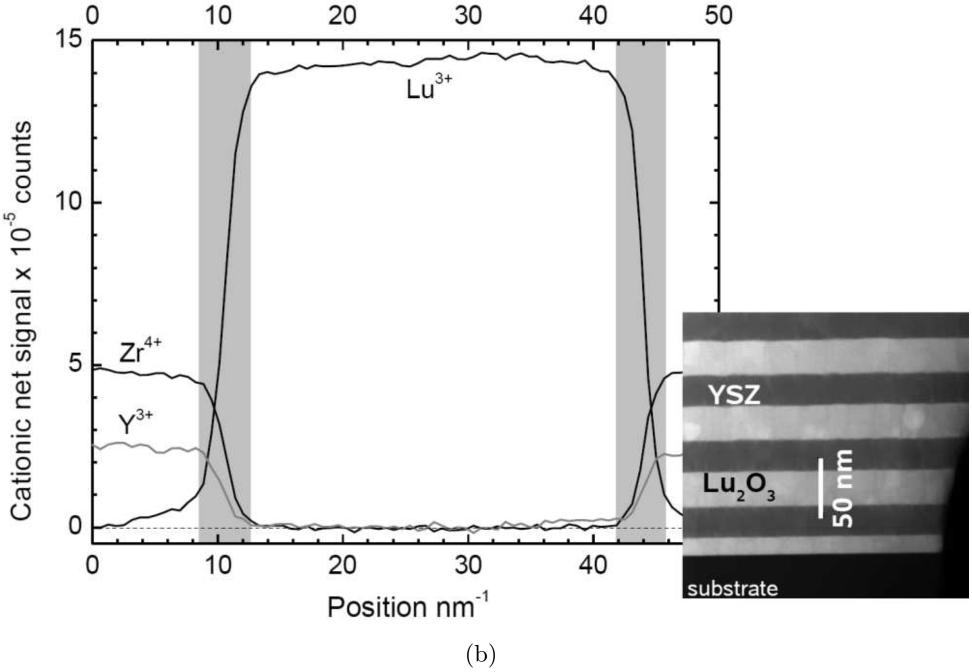

(b)

**Figure 7.42:** EELS line scans of the sample YLu50-3, showing the net signal intensity. The position of the line scans is marked in the inset HR-STEM micrographs. a) A line scan performed over a distance of 190 nm. b) EELS line scan performed over a distance of 50 nm. The overlapping zones are about 4 nm wide and highlighted light gray.

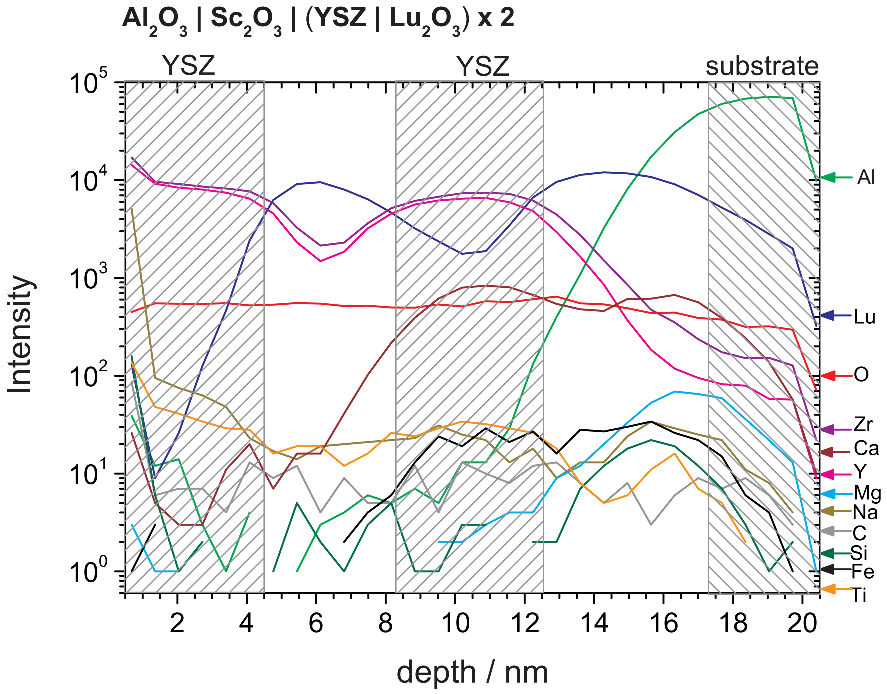

**Figure 7.43:** Negative ion mode SIMS depth profile of a sample wit 2 double layers YSZ / $Lu_2O_3$.

### TOF-SIMS-Results

TOF-SIMS measurements were performed on a multilayer for which the deposition had to be canceled due to problems with the target rotation mechanism of the PLD system. Only two thin double layers YSZ | $Lu_2O_3$ were deposited. A Cs ion source was used for sputtering.

The undulation of the Lu and the Zr and Y signals indicates the individual layers. They are broadened because of the intermixing of the individual layers caused by the ion beam. The relative oxygen content is quite constant. Near the substrate, the Al signal rises steeply. A rather high amount of Ca is found in this region, too. A 3D reconstruction (see appendix, figure 12.2) of the TOF-SIMS data showed that Ca was more or less equally distributed in a diffuse layer on top of the substrate. Other impurities like Na, Mg, Fe, Si and Ti are present in lower amounts and also show a slight enrichment close to the substrate. Only Ti seems to be distributed over a larger region. The Cr content is negligible and therefore not shown. If impurities precipitate on the surface of the targets used in PLD during heating or are deposited during the alignment of the laser beam, they are expected to be incorporated in the first layers of a thin film sample. Therefore, it is probable that all multilayer samples may be contaminated in the first 10 to 20 nm.

# 8 Electrochemical Investigations

## 8.1 Measurement Setup

Impedance spectroscopy was used for the electrochemical characterisation of the samples. The basic setup consisted of a cylindrical furnace equipped with a shielded sample holder for four-probe measurements (see figure 8.2). The furnace as well as all measurement devices could be controlled by a computer unit.
Working and counter electrode in the sample holder were made of silver nets[1] fastened to ceramic slices. Each net was connected to two wires, supplying one junction apiece as reference. The platinum feed lines in the sample holder were shielded by ceramic capillaries surrounded by platinum tubes.

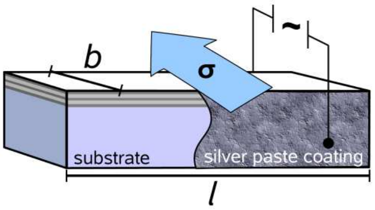

**Figure 8.1:** scheme showing a sample prepared for electrochemical measurements.

Slices with a thickness of around 2 mm were cut from the annealed samples (see figure 8.1). All edges were cut to ensure a defined geometry of the thin films. The lateral surfaces were polished down to 9 µm and silver paste[2] was applied as oxygen permeative electrode. It was sintered for 10 h at 800 °C in air to provide a good contact to the thin film. After a sample was inserted in the sample holder, it was heated up to about 775 °C for 2 hours to ensure sufficient contact between the silver paste and the silver nets. Then, electrochemical measurements were performed in air from about 420 °C to about 775 °C in temperature steps between 40° and 60°, first during heating and a then during cooling of the sample. Impedance measurements were performed with a PARSTAT Model 2273 potentiostat/galvanostat and impedance analyser[3]. The impedance was measured from 2 MHz down to 1 Hz, in some cases down to 100 mHz. An amplitude of 50 mV was used.

---

[1] More temperature stable platinum nets reacted with silver paste and led to a deterioration of the electrical contact.

[2] Leitsilber 200, Hans Wolbring GmbH

[3] Princeton Applied Research, 801 S. Illinois Avenue, Oak Ridge, 37830 Tennessee

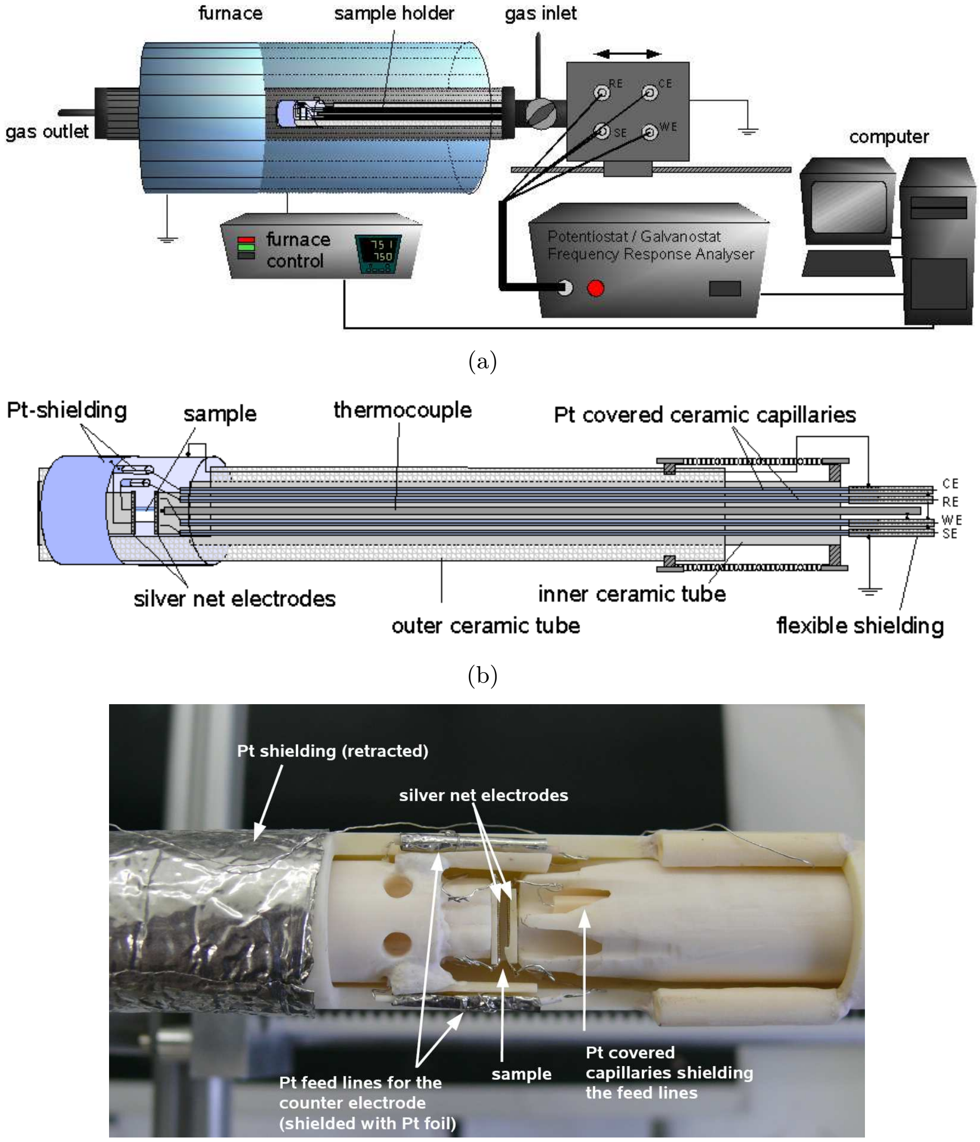

(c)

**Figure 8.2:** a) sketch of the measurement setup; b) schematic picture of the sample holder used for electrochemical measurements; c) photo of the sample holder.

DC-measurements could also be performed with the PARSTAT Model 2273 as control for the results obtained by the AC-measurements. The software *Electrochemistry Power Suite* was used for data collection. The data was fitted using the software *ZSimpWin 3.21*.

## 8.2 Results

### 8.2.1 Sapphire Substrate and Sample Holder

In order to exclude any influence of the substrate or the sample holder on the results of the conductivity measurements, a slice of an uncoated c-plane sapphire substrate was cut, polished and supplied with silver electrodes in the same way as described for the multilayer samples. The conductivity was then measured parallel to the (0001) sapphire plane from 450 °C to 800 °C in air. The result is shown in figure 8.3.

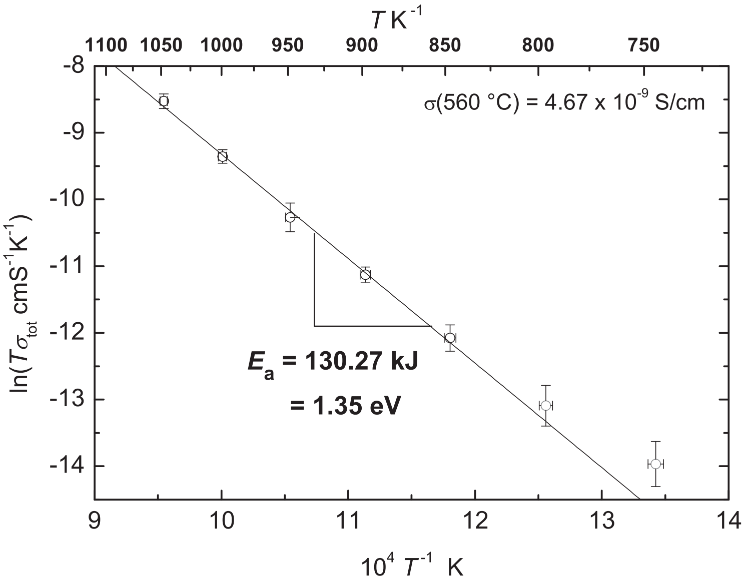

**Figure 8.3:** Conductivity measurement of a slice of an uncoated sapphire substrate.

At low temperatures, a deviation of the measured values from the expected Arrhenius type behaviour is visible. This agrees with investigations by J. A. Champion [114].

From the linear fit, a conductivity of $4.67 \cdot 10^{-9}$ S/cm at 560 °C is obtained. This is approximately one order of magnitude higher than the value obtained by Champion for this temperature [114]. However, the conductivity values reported in literature differ significantly at temperatures below 1000 °C. An overview is given in [115]. The activation energy calculated from the linear fit is 1.35 eV, which is somewhat lower than the results of Champion for this temperature range [4].

---

[4] Champion calculated a mean activation energy of about 1.7 eV for the temperature range between 450 °C to 850 °C. The value was obtained from four different samples with different impurity contents.

The conductivity of the sample holder was below the detection limit in the temperature range from 450 °C to 800 °C. It was measured with the standard setup but without inserting a sample so that a gap existed between the electrodes.

### 8.2.2 Rare Earth Oxides

The conductivity of the rare earth oxides in the multilayers was determined by depositing thick single films of $Lu_2O_3$ and $Sc_2O_3$ on c-plane sapphire substrates and preparing samples for impedance spectroscopy in the same way as described in section 8.1. Only one semicircle was visible in the impedance plots, therefore the data were fitted using a parallel $(RC)$ element. Arrhenius plots show a linear relationship between $\ln(T\sigma_{\mathrm{tot}})$ and $1/T$. For RE $=$ Lu, the measured resistances were higher for the cooling cycle of the sample, which results in a larger uncertainty of these measurements. The results can be seen in figure 8.4.
The measured conductivity of $Lu_2O_3$ is about three orders of magnitude higher than that reported in the literature [23]. The literature value for $Sc_2O_3$ [20] (see section 4.2.2) is even about ten orders of magnitude lower than the value measured in this work. A substrate effect can be ruled out because the measured substrate conductivity in section 8.2.1 was almost three orders of magnitude lower and the activation energy determined for the substrate is significantly higher.
One has to consider that the literature values were obtained from pressed and sintered powder samples, which have a lower density than films deposited by PLD and may suffer more from blocking grain boundaries. In the case of [20], a Pt wire was pressed on the sample surface to establish the electrical contact. This contact may have been not sufficient and an additional electrode resistance may have occurred. However, a discrepancy of ten orders of magnitude can not be explained sufficiently in this way.

### 8.2.3 YSZ | $Sc_2O_3$ Multilayers

#### Samples deposited with 10 Hz

A typical impedance measurement of a multilayer of the system YSZ | $Sc_2O_3$ showed one clearly distinguishable and nearly ideal semicircle (see figure 8.5a)). Fitting the measurement to a parallel $(RC)$ element in most cases delivered good results. The scattered signals from lower frequencies could not be fitted in a reasonable way and were therefore omitted for the fit. Much scattering can be observed in the frequency range around 50 Hz; it is due to a distortion of the signal by the outer power supply. This distortion can best be seen in the Bode plots (see figure 8.5b)).
Arrhenius plots show a perfectly linear relationship between $\ln(T\sigma_{\mathrm{tot}})$ and the reciprocal temperature (see figure 8.6). Deviations between the values of $\ln(T\sigma_{\mathrm{tot}})$ measured during heating and cooling of the samples were about 10 % at maximum. The resistance of the samples typically increased in subsequent measurement cycles, but the major increase took place in the first cycle and was negligible

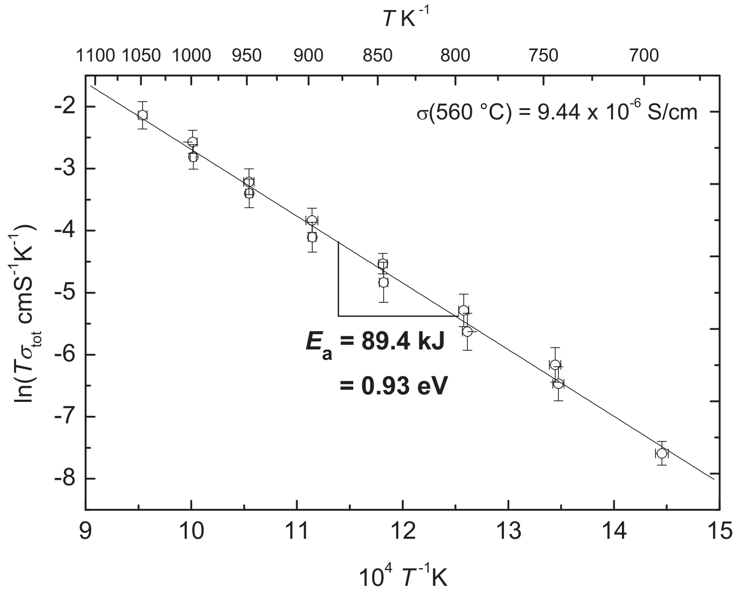

(a)

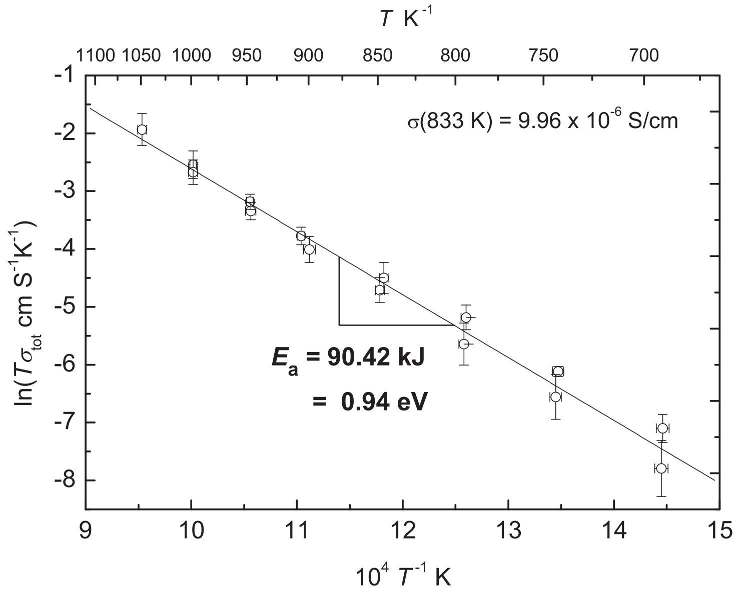

(b)

**Figure 8.4:** a) Arrhenius plot for a 4.26 µm thick $Sc_2O_3$ layer; b) Arrhenius plot for a 2.93 µm thick $Lu_2O_3$ layer.

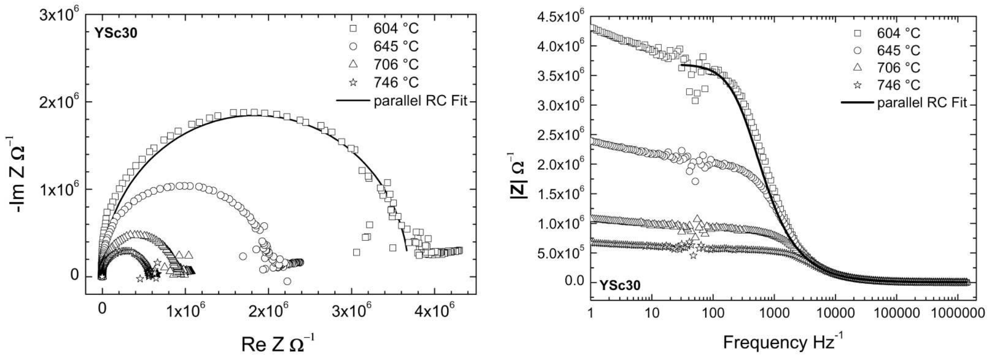

(a) (b)

**Figure 8.5:** a) Nyquist plots for the sample YSc30 ($n$ = 30, $d$ = 20 nm) at four different temperatures. A fit to a parallel ($RC$) element is shown for the measurement at 604 °C; b) Bode plots for the same sample at the same temperatures.

**Activation Energy YSZ | $Sc_2O_3$ (10 Hz)**

| Name | $n$ | $d$ YSZ [nm] | $E_a$ [kJ] | $E_a$ [eV] |
|---|---|---|---|---|
| YSc5 | 5 | 252 | 107.71 | 1.11 |
| YSc20 | 20 | 43 | 104.73 | 1.09 |
| YSc60-4 | 60 | 30 | 109.97 | 1.14 |
| YSc40 | 40 | 24 | 116.03 | 1.20 |
| YSc120 | 120 | 23 | 108.92 | 1.12 |
| YSc30 | 30 | 20 | 109.53 | 1.14 |
| YSc70-2 | 70 | 18 | 116.11 | 1.20 |
| YSc80-4 | 80 | 17 | 111.28 | 1.15 |
| YSc1002 | 100 | 16 | 122.24 | 1.27 |
| YSc150-2 | 150 | 11 | 111.19 | 1.15 |

**Table 8.1:**

in further cycling. The increase of the resistance during the first cycle could be reduced to practically zero by reducing the maximum measurement temperature by 30 °C to about 745 °C.

A small tendency to higher activation energies with decreasing thickness $d$ of the individual YSZ layers can be seen in figure 8.6. The calculated values for the activation energy are also shown in table 8.1. However, this tendency is not very pronounced.

The conductivity of the samples clearly decreases with decreasing individual layer thickness, as can be seen in figure 8.6 and more clearly in figure 8.7. For the sample YSc5 ($n = 5$, $d = 252$ nm), a value of $8.58 \cdot 10^{-4}$ S/cm was measured whereas the sample YSc150-2 ($n = 150$, $d = 11$ nm) has a conductivity of $4.02 \cdot 10^{-4}$ S/cm, which is approximately half the value of the sample YSc5. The conductivity of

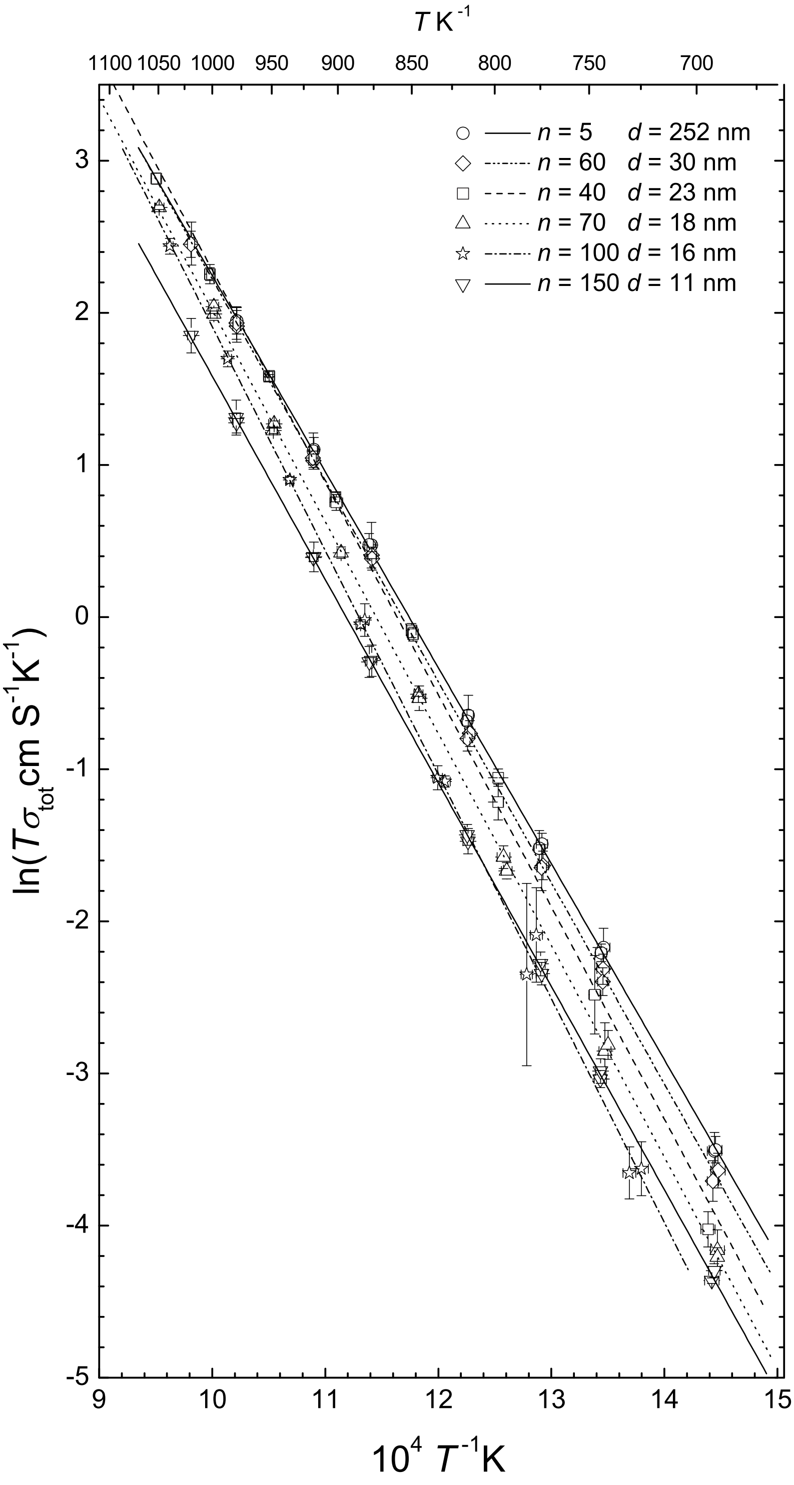

**Figure 8.6:** Arrhenius plots for six samples of the system YSZ | $Sc_2O_3$, deposited with 10 Hz. For the sake of clarity, not all samples are shown.

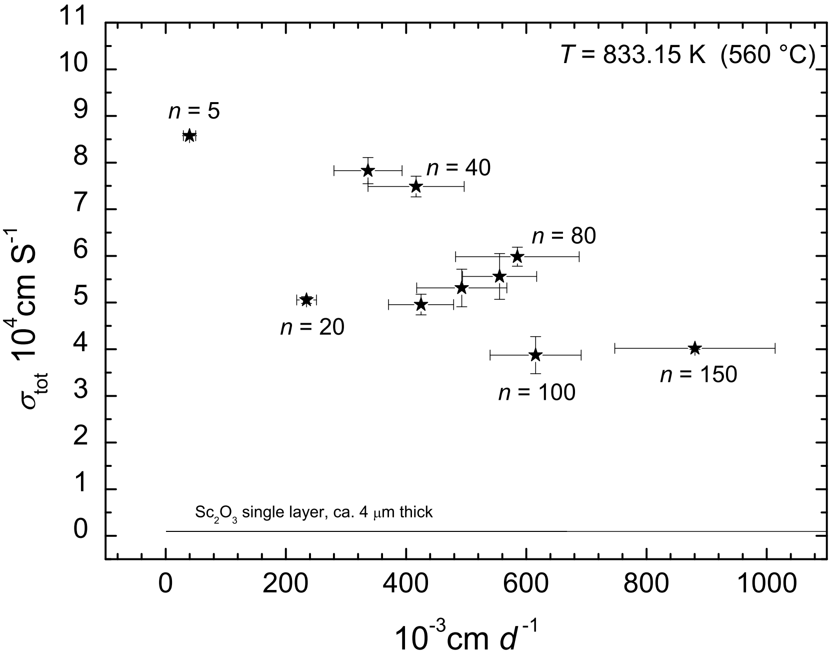

**Figure 8.7:** Plot of total conductivity $\sigma_{\mathrm{tot}}$ of the multilayers YSZ | $Sc_2O_3$, deposited with 10 Hz, in relation to the inverse layer thickness $d$.

the $Sc_2O_3$ single layer sample is shown for comparison (see also section 8.2.2). It is much lower than the lowest value obtained for a multilayer sample.

### Samples deposited with 2 Hz

The behaviour of the samples deposited with 2 Hz was similar to those deposited with 10 Hz. The appearance of the impedance measurements was the same and the Arrhenius plots showed no deviations from linearity (see figure 8.2). A more or less regular increase of the activation energy with decreasing individual layer thickness $d$ can be recognized in figure 8.8 and table 8.2. Only the sample with $n = 70$ does not confirm this trend.

In general, the conductivity $\sigma_{\mathrm{tot}}$ of the samples deposited with 2 Hz was lower than that of the samples deposited with 10 Hz.

A clear decrease of $\sigma_{\mathrm{tot}}$ with decreasing $d$ was observed for four of five investigated samples of this system (see figure 8.9). One sample, YSc403, showed a conductivity which was higher than expected. This may be due to impurities in this case; it is suspected that the sample was contaminated during the deposition because the laser hit the substrate shutter for the first few pulses. Therefore, the conductivity of this sample will be omitted for further analyses.

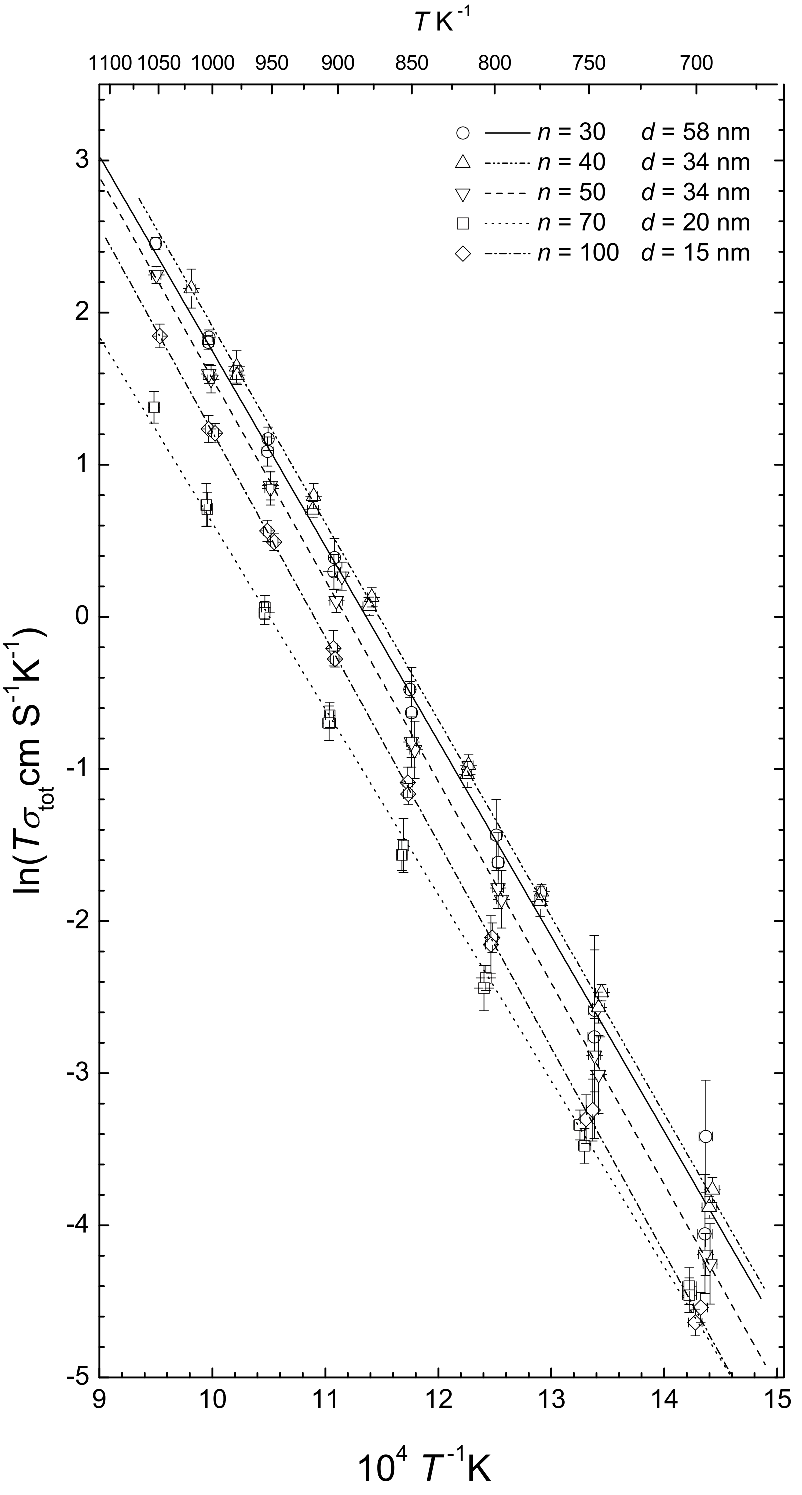

**Figure 8.8:** Arrhenius plots for samples of the system YSZ | $Sc_2O_3$, deposited with 2 Hz.

**Activation Energy YSZ | $Sc_2O_3$ (2 Hz)**

| Name | $n$ | $d$ YSZ [nm] | $E_a$ [kJ] | $E_a$ [eV] |
|---|---|---|---|---|
| YSc303 | 30 | 58 | 106.61 | 1.10 |
| YSc403 | 40 | 34 | 106.87 | 1.11 |
| YSc503 | 50 | 34 | 109.89 | 1.14 |
| YSc703 | 70 | 20 | 101.63 | 1.05 |
| YSc1003-2 | 100 | 15 | 112.20 | 1.16 |

**Table 8.2:**

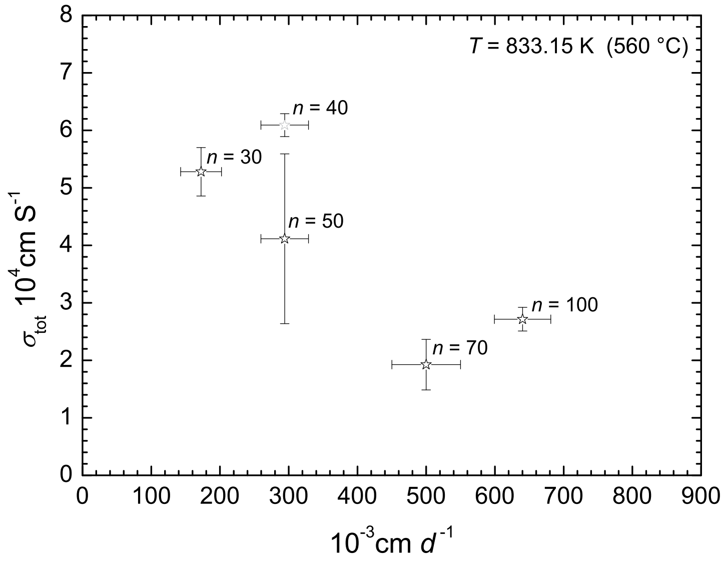

**Figure 8.9:** Plot of total conductivity $\sigma_{\mathrm{tot}}$ of the multilayers YSZ | $Sc_2O_3$, deposited with 2 Hz, in relation to the inverse layer thickness $d$. The grey shaded value was omitted for further analyses.

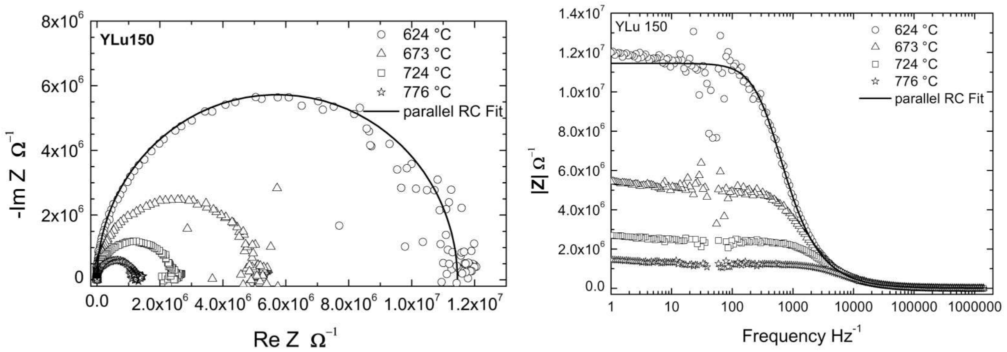

(a) (b)

**Figure 8.10:** a) Nyquist plots for the sample YLu150 ($n$ = 150, $d \approx$ 3 nm) at four different temperatures. A fit to a parallel ($RC$) element is shown for the measurement at 624 °C; b) Bode plots for the same sample at identical temperatures.

### 8.2.4 YSZ | $Lu_2O_3$ Multilayers

#### Samples deposited with 10 Hz

Regarding the appearance of the impedance spectra, the system YSZ | $Lu_2O_3$ delivered the same results as the system YSZ | $Sc_2O_3$: Only one semicircle was observed. Again, the data were fitted to a parallel ($RC$) element. Examples for impedance spectra (Nyquist and Bode plot) are shown in figure 8.10. The Bode plot shows that the measured data deviates from the fit at low frequencies and that a strong scattering of the data can be observed at frequencies near 50 Hz.

Arrhenius plots for samples of the system YSZ | $Lu_2O_3$, deposited with 10 Hz, can be seen in figure 8.11. They show a linear behaviour for all samples. For the sake of clarity, only the results for six different samples are shown. One can already see in this plot that the slopes of the linear fits have quite different values and do not change in a systematic way in relation to the interface densities ($\propto d^{-1}$) in the different samples.

The activation energies calculated from the Arrhenius plots of all samples are listed in table 8.3. No relation between the activation energy and the thickness $d$ of the individual layers can be observed.

Plotting the total conductivity of the samples at 560 °C in relation to the reciprocal layer thickness (figure 8.12) shows a high scattering of the conductivity values for samples with $d > 10$ nm ($d^{-1} = 1000 \cdot 10^3$ cm$^{-1}$). No definite trend can be recognized in this regime. For samples with thinner individual layers ($d < 10$ nm), the conductivity decreases markedly. The conductivity of the sample YLu150, for which $d$ is only about 3 nm, is only about 40 % of the conductivity of the sample Ylu5, for which $d$ is about 211 nm. For comparison, the conductivity of the $Lu_2O_3$ single layer sample is shown (see also section 8.2.2).

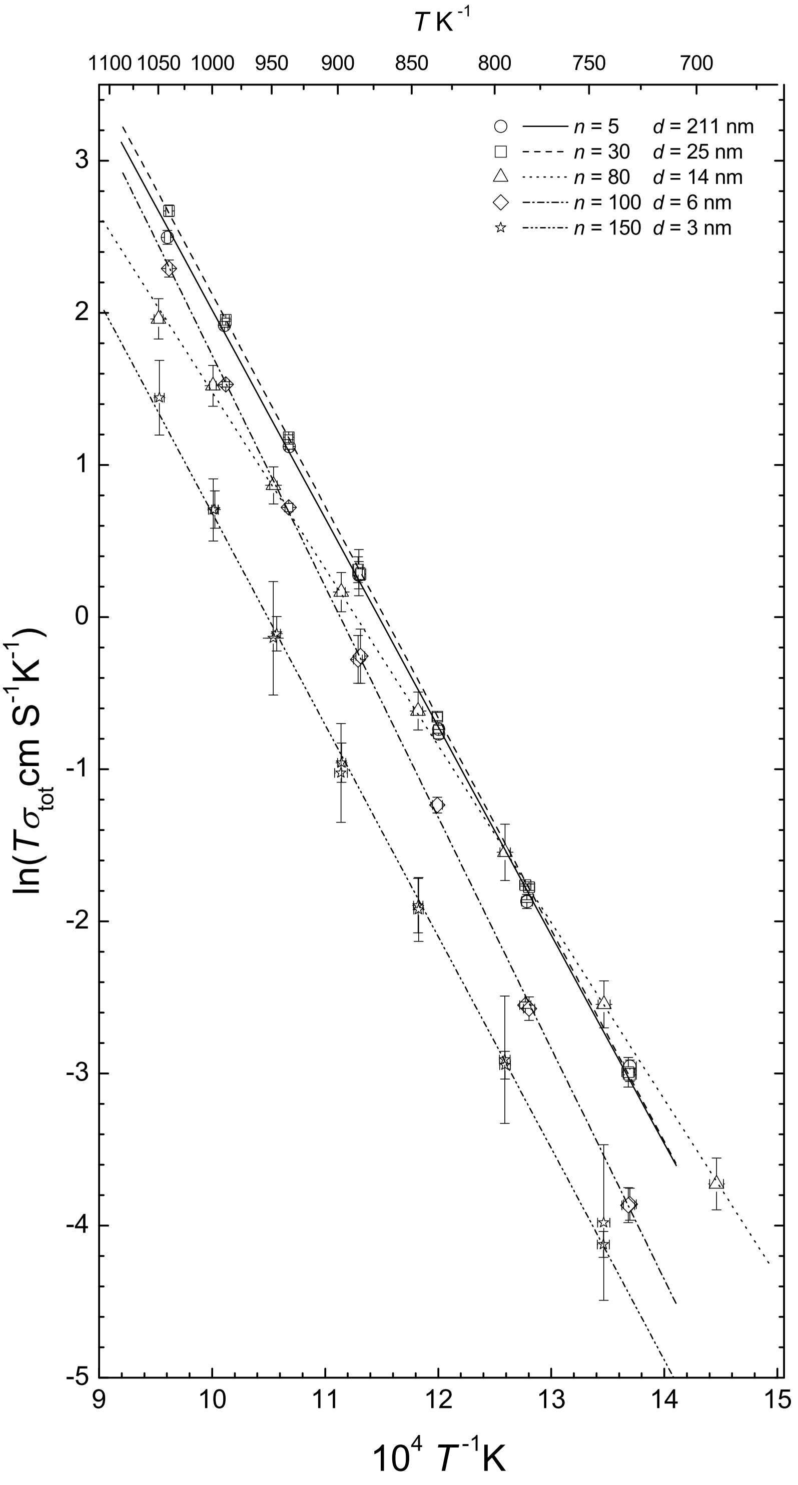

**Figure 8.11:** Arrhenius plots for six samples of the system YSZ | $Lu_2O_3$, deposited with 10 Hz. For the sake of clarity, not all samples are shown.

**Activation Energy YSZ | $Lu_2O_3$ (10 Hz)**

| Name | $n$ | $d$ YSZ [nm] | $E_a$ [kJ] | $E_a$ [eV] |
|---|---|---|---|---|
| YLu5-2 | 5 | 211 | 113.93 | 1.18 |
| YLu10-2 | 10 | 152 | 97.92 | 1.01 |
| YLu304 | 30 | 52 | 102.68 | 1.06 |
| YLu30 | 30 | 25 | 115.78 | 1.20 |
| YLu50(2) | 50 | 24 | 105.04 | 1.09 |
| YLu504 | 50 | 21 | 106.26 | 1.10 |
| YLu70 | 70 | 20 | 114.25 | 1.18 |
| YLu804 | 80 | 14 | 96.70 | 1.00 |
| YLu1002 | 100 | 6 | 126.30 | 1.31 |
| YLu150 | 150 | 3 | 115.73 | 1.20 |

**Table 8.3:**

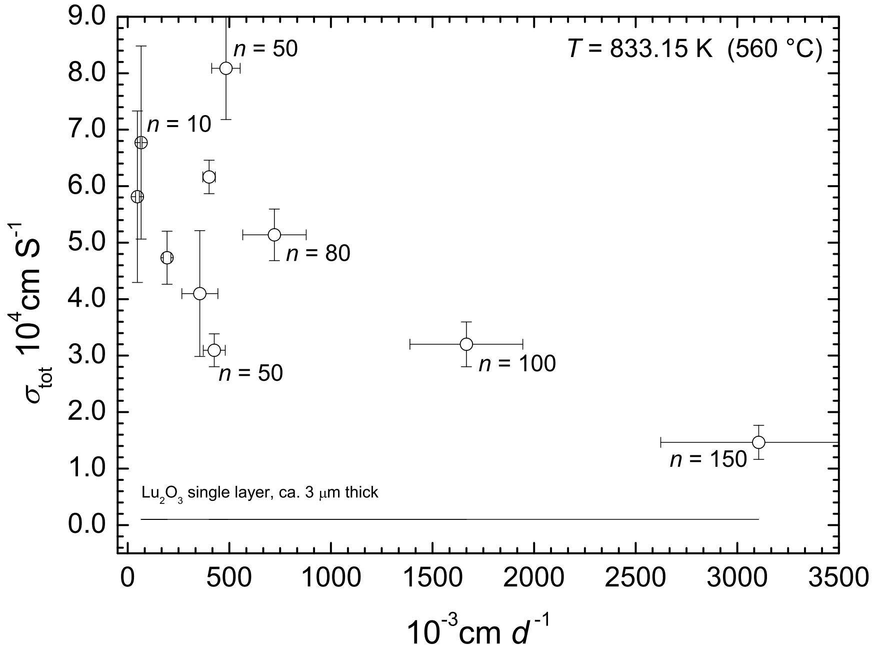

**Figure 8.12:** Plot of total conductivity $\sigma_{\text{tot}}$ of the multilayers YSZ | $Lu_2O_3$, deposited with 10 Hz, in relation to the inverse layer thickness $d$.

**Activation Energy YSZ | $Lu_2O_3$ (2 Hz)**

| Name | $n$ | $d$ YSZ [nm] | $E_a$ [kJ] | $E_a$ [eV] |
|---|---|---|---|---|
| YLu20 | 10 | 71 | 107.45 | 1.11 |
| YLu303 | 30 | 76 | 105.86 | 1.10 |
| YLu503 | 50 | 22 | 111.26 | 1.15 |
| YLu703 | 70 | 22 | 113.81 | 1.18 |
| YLu1003 | 100 | 10 | 114.90 | 1.19 |

**Table 8.4:**

### Samples deposited with 2 Hz

The general remarks which were made for the YSZ | $Lu_2O_3$ multilayers deposited with 10 Hz, regarding the shape of the impedance spectra and the Arrhenius type temperature dependence of the conductivities, are also valid for the samples deposited with 2 Hz.

In contrast to the results for the samples deposited with 10 Hz, the Arrhenius plots of the samples deposited with 2 Hz (figure 8.13) show a regular variation of the slope of the linear fit in relation to the interface density.

This relation can be recognized more easily in table 8.4, where the calculated activation energies for all samples of this system are listed. An increase in the activation energy of 0.8 eV is observed when $d$ is decreased from 71 nm to 10 nm. As for the samples deposited with 10 Hz, the scattering of the conductivity values is high. Because of the small number of measured samples, no reliable conclusion can be drawn for the dependency of the conductivity on $1/d$, which is shown in figure 8.14. In total, a decrease takes place.

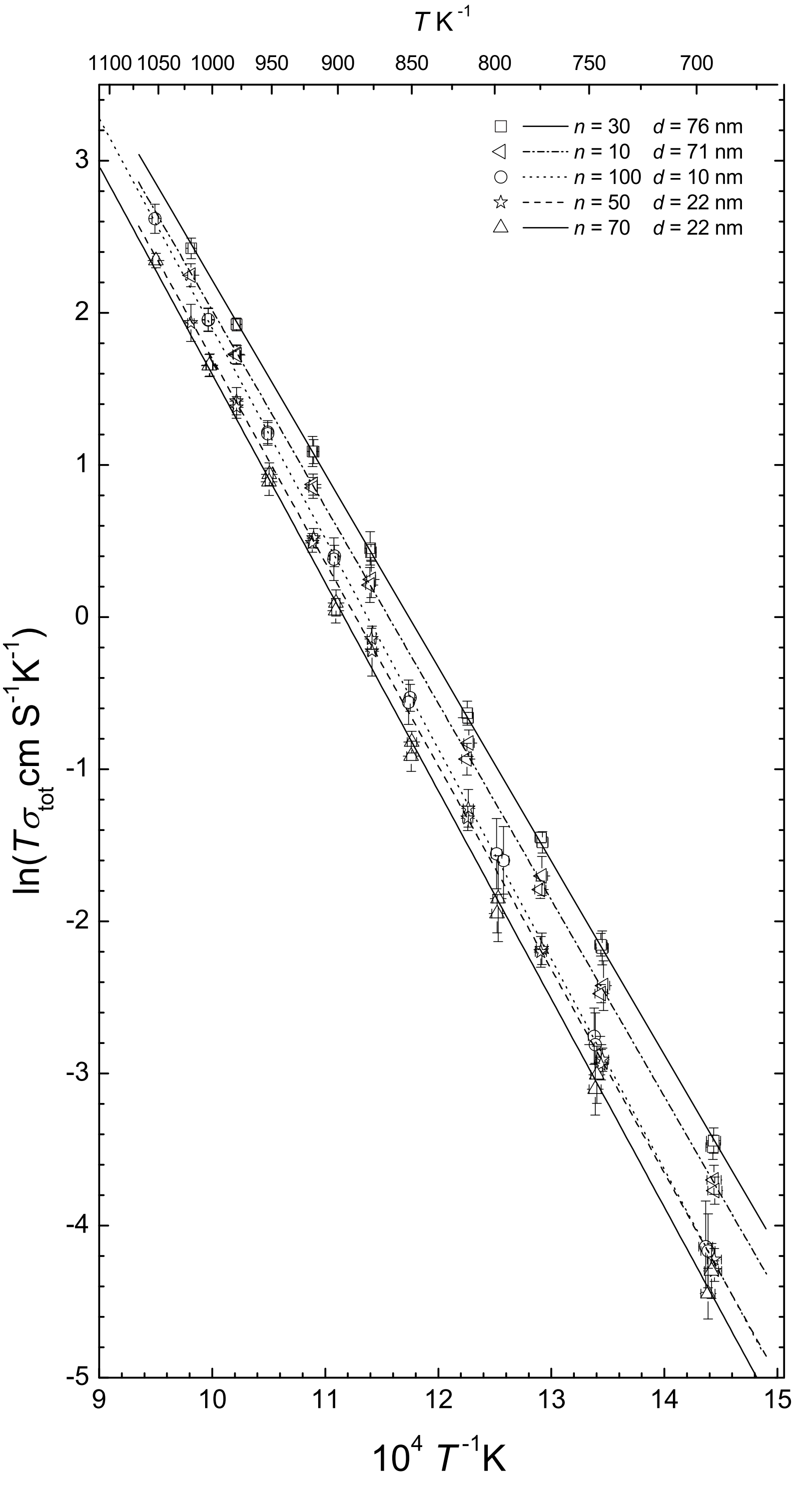

**Figure 8.13:** Arrhenius plots for six samples of the system YSZ | $Lu_2O_3$, deposited with 2 Hz.

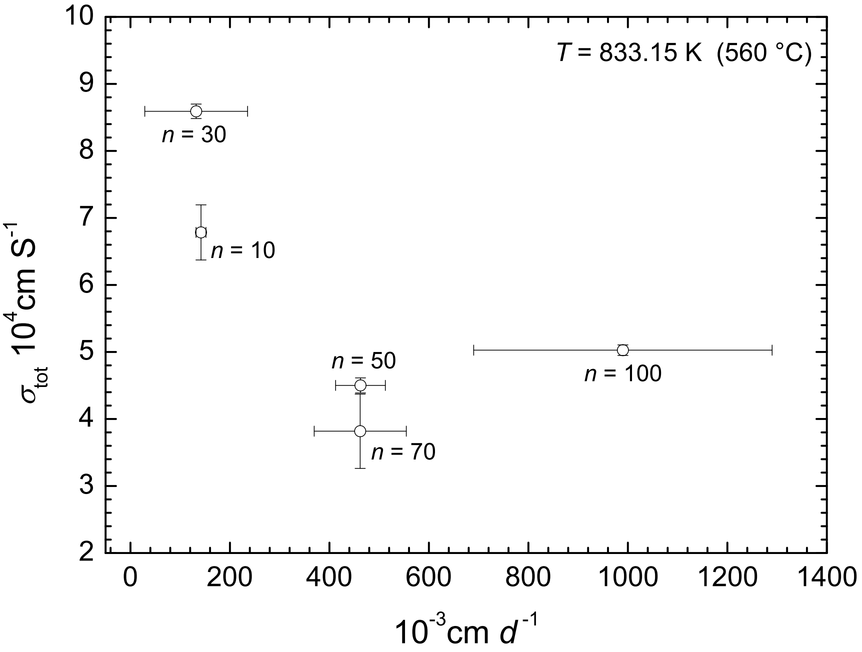

**Figure 8.14:** Plot of total conductivity $\sigma_{\text{tot}}$ of the multilayers YSZ | $Lu_2O_3$, deposited with 10 Hz, in relation to the inverse layer thickness $d$.

# Part V

# Discussion and Outlook

# 9 Discussion of the Results

## 9.1 Structural Properties of the Multilayers

### 9.1.1 Orientation Relationships

#### Orientation Relationship YSZ ∥ $RE_2O_3$

Based on former investigations on the system YSZ | $Y_2O_3$ [19], also for YSZ | $Sc_2O_3$ and YSZ | $Lu_2O_3$ systems highly textured multilayers were expected with a preferred axial orientation relationship between the different phases as follows:

$$(0001)\ Al_2O_3 \parallel (111)\ RE_2O_3 \parallel (111)\ YSZ$$

In the system YSZ | $Sc_2O_3$, this orientation relationship was found in almost all samples. It is depicted schematically in figure 9.1. Two variants for the azimuthal orientation (and their mirror images) were found, which is comparable to the YSZ | $Y_2O_3$ system. The strict orientation relationship between YSZ and $Sc_2O_3$ is also valid in the azimuthal regime.

In the system YSZ | $Lu_2O_3$, though, the texture was not as highly developed. Instead, different variants for the orientation relationship were found. The expected orientation (0001) $Al_2O_3$ ∥ (111) $RE_2O_3$ ∥ (111) YSZ dominates only in samples with thin individual layers.

No preference for the azimuthal orientation of the crystallites could be found in the system YSZ | $Lu_2O_3$, which is evident from the pole figure and SAED measurements. In the HRTEM micrographs, some crystallites showed the same azimuthal orientations as those found in the system YSZ | $Sc_2O_3$, but also other orientations and variants which could not unambiguously be defined were revealed by FFT. Interpreting HRTEM measurements, one always has to consider that the obtained results only provide insight into very small regions and may not always be representative for the whole sample. However, the orientation relationship between the two phases of the multilayer was as strict as in the system YSZ | $Sc_2O_3$. This means that within one column, the orientation did not change and was also preserved in the azimuthal regime.

#### Orientation Relationship $RE_2O_3$ ∥ $Al_2O_3$

The fact that two distinct variants for the azimuthal orientation of the crystallites in the system YSZ | $Sc_2O_3$ (and their mirror images) were found, indicates that

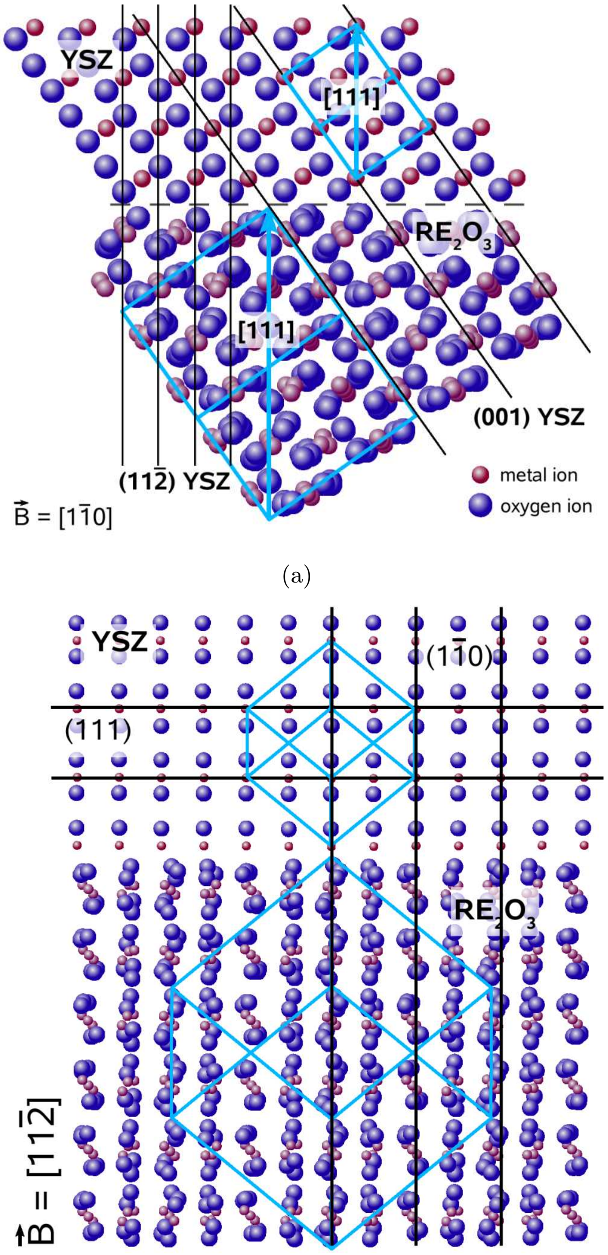

(a)

(b)

**Figure 9.1:** Schematic picture showing (ideal, non-deformed) YSZ and $RE_2O_3$ lattices stacked (111) YSZ ∥ (111) $RE_2O_3$. a) The viewing direction is along the $[1\bar{1}0]$ axis. b) The viewing direction is along the $[11\bar{2}]$ axis. The unit cells are drawn in light blue. Atomic radii in this picture are not realistic for the sake of clarity.

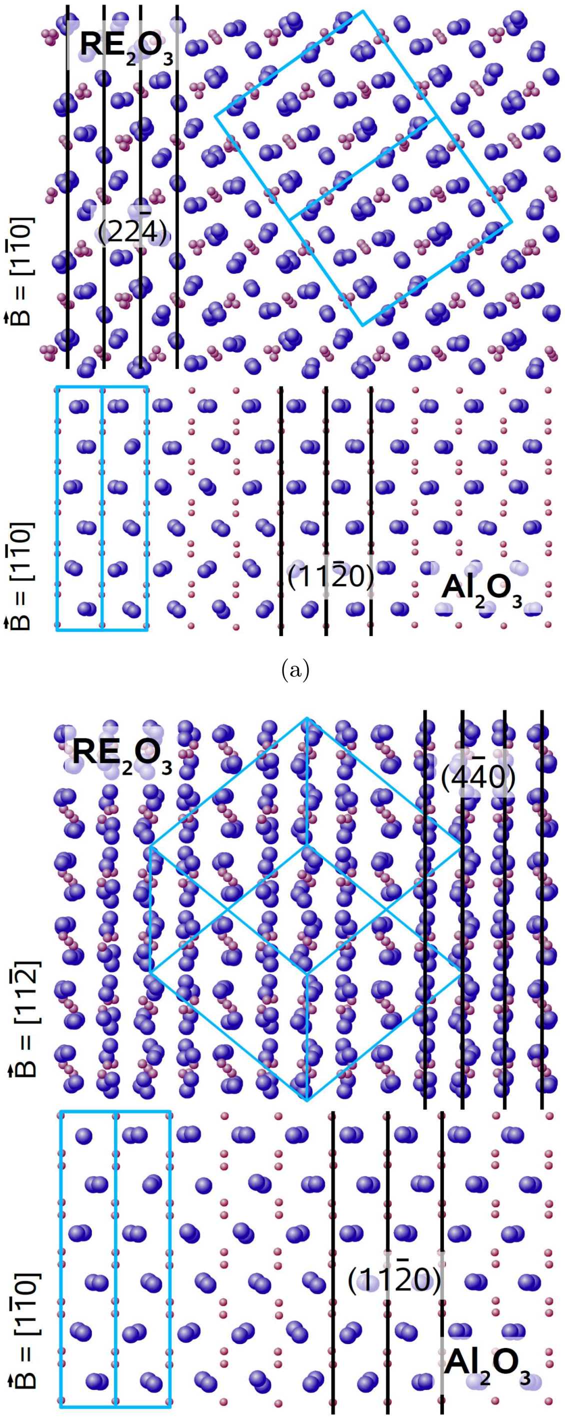

(a)

(b)

**Figure 9.2:** Schematic picture showing the orientation relationship between RE$_2$O$_3$ and the sapphire substrate. a) [1$\bar{1}$0] Al$_2$O$_3$ ∥ [1$\bar{1}$0] RE$_2$O$_3$; b) [1$\bar{1}$0] Al$_2$O$_3$ ∥ [11$\bar{2}$]

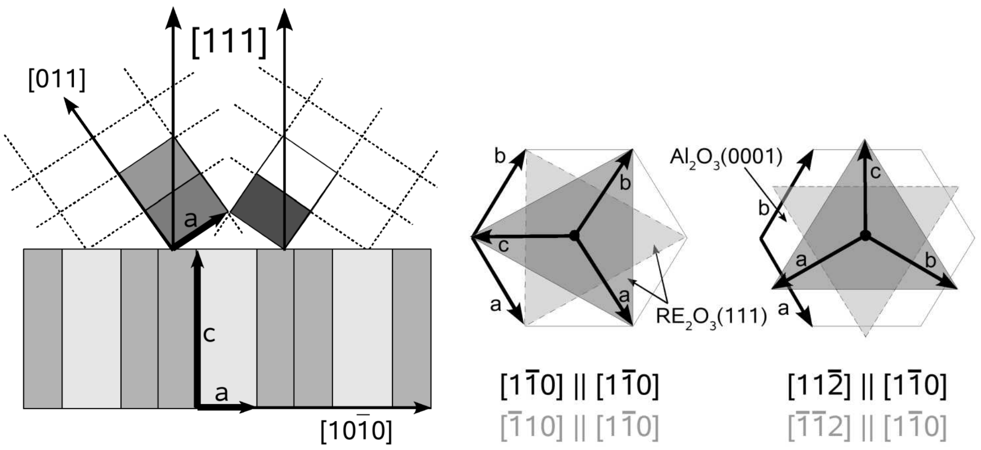

(a) (b)

**Figure 9.3:** Scheme depicting possible alignments of the $RE_2O_3$ crystallites on the sapphire substrate. a, b and c denote the basis vectors of the elementary cells. a) lateral view for the orientation relation (0001) $Al_2O_3$ ∥ (111) $RE_2O_3$ (the elementary cells are not shown in realistic proportion); b) top view, emphasis on the possible azimuthal orientations. The orientation relation between the substrate and the rare earth oxide is given in square brackets in the form $[RE_2O_3] \parallel [Al_2O_3]$. The black written relationship belongs to the dark grey shaded (111) $RE_2O_3$ plane (triangle), the grey written one the associated mirror image (light grey shaded (111) $RE_2O_3$ plane).

two energetically favourable alignments exist for the $Sc_2O_3$ crystallites on the sapphire substrate. The two variants are depicted schematically in figure 9.2 and 9.3. Because variant 1), in detail

1a) $[1\bar{1}0]$ $Al_2O_3$ ∥ $[\bar{1}10]$ $Sc_2O_3$ ∥ $[\bar{1}10]$ YSZ

1b) $[1\bar{1}0]$ $Al_2O_3$ ∥ $[1\bar{1}0]$ $Sc_2O_3$ ∥ $[1\bar{1}0]$ YSZ

(two mirror inverted sub-variants) was found most often, it can be concluded that these variants mark the minimum for the interface energy. However, no such minimum seems to exist for the system YSZ | $Lu_2O_3$ because no azimuthal orientation of the crystallites was preferred. The reason for this difference between the two systems must be the mismatch between the substrate and the particular rare earth oxide.

The misfit between the sapphire substrate and the first $RE_2O_3$ layer can be calculated similar to the misfit between YSZ and the rare earth oxide. Because $Al_2O_3$ and $RE_2O_3$ crystallise in structures of different symmetry, the mismatch is expected to be high. Sapphire crystallises in the $\alpha$-corundum structure with a hcp anion sublattice. The (0001) surface has a threefold symmetry (space group R$\bar{3}$c). The best match is expected to be achieved with the (111) $RE_2O_3$ plane, which also has a threefold symmetry. This is proven by the found orientation relationship (0001) $Al_2O_3 \parallel$ (111) $RE_2O_3$. Therefore, the spacings of the $(\bar{1}100)$ $Al_2O_3$ and $(\bar{1}10)$ $RE_2O_3$ planes, respectively those of the $(11\bar{2}0)$ $Al_2O_3$ and $(11\bar{2})$ $RE_2O_3$ planes, have to be considered to calculate the misfit because these planes are perpendicular to the interface plane.

The relevant data for sapphire are [116]:

$Al_2O_3$:
trigonal, $\alpha$-corundum type ($R\bar{3}c$),
$a_{Al_2O_3} = b_{Al_2O_3} = 4.7540$ Å,
$c_{Al_2O_3} = 12.9900$ Å
$d_{(\bar{1}100)} = \frac{1}{2}\sqrt{3}\; a_{Al_2O_3} = 4.1171$ Å
$d_{(11\bar{2}0)} = \frac{1}{6}\sqrt{6}\; a_{Al_2O_3} = 2.3770$ Å

If the misfit is calculated according to equation 4.1, assuming a 1:1 commensurability between the $(11\bar{2}0)$ $Al_2O_3$ and the $(22\bar{4})$ $Lu_2O_3$ planes, very high values for $f$ are obtained. Taking into account the actual atomic distances in the close packed lattice planes (these are cation planes in $RE_2O_3$, but anion planes in $Al_2O_3$), an additional factor of 3/2 has to be considered:

$$f = \frac{d_{(11\bar{2}0)}(Al_2O_3) - \frac{3}{2}d_{(22\bar{4})}(RE_2O_3)}{\frac{3}{2}d_{(22\bar{4})}(RE_2O_3)} \cdot 100\% \tag{9.1}$$

The results are $f = 18.3$ % for $Sc_2O_3$ and 13.8 % for $Lu_2O_3$. Analysing the dislocation network visible at the substrate/$RE_2O_3$ interface in the Fourier filtered HRTEM micrographs in figure 7.38 and 7.22, the mean distance of dislocations is found to be about 4 atomic rows in $Al_2O_3$ but only about 3 atomic rows in $Lu_2O_3$ or $Sc_2O_3$. Similar results have been found earlier for the system YSZ | $Y_2O_3$ [19, 26]. Therefore, a 4:3 commensurability condition between $Al_2O_3$ and $RE_2O_3$ can be assumed. Thus, the misfit yields to:

$$f = \frac{4 \cdot d_{(11\bar{2}0)}(Al_2O_3) - 3 \cdot \frac{3}{2}d_{(22\bar{4})}(RE_2O_3)}{3 \cdot \frac{3}{2}d_{(22\bar{4})}(RE_2O_3)} \cdot 100\% \tag{9.2}$$

For $Sc_2O_3$, a value of $f = 5.13$ % is obtained. For $Lu_2O_3$, a value of $f = 5.51$ % results. These values are both quite high and the value for $Lu_2O_3$ is somewhat higher than that for $Sc_2O_3$. This difference seems to be too small to explain why the orientation relationship between $Lu_2O_3$ and the substrate is not as strict as that found for $Sc_2O_3$. The high misfit may be the reason for the transition region which was found in some samples between the substrate and the first $Lu_2O_3$ layer, but then it would also be reasonable to expect a transition region for the system YSZ | $Sc_2O_3$.

### 9.1.2 Layer Morphology and Dislocation Density

Two samples of the system YSZ | $Sc_2O_3$ were investigated by HRTEM. The sample YSc150-2 ($n = 150$, $d$ about 11 nm) was deposited at 10 Hz. In this sample, dislocations were clearly visible after Fourier filtering of the HRTEM micrograph in figure 7.15; the result is shown in figure 9.4. These dislocations are slightly accumulated near the interfaces and have Burgers vectors with components parallel to the layers, but are not arranged regularly. An interesting point is that the Burgers vectors of these dislocations are often anti-parallel, so that there should be almost no release of misfit strain.
In the sample YSc50-3, which was deposited at 2 Hz, many dislocations with a Burgers vector partly parallel to the interfaces were found after Fourier filtering (see figure 7.19 and 7.18). A regular arrangement of these dislocations is seldom, an example is visible at the first $Sc_2O_3$ | YSZ interface in figure 7.18. Also, the density of dislocations is not uniform in the different columnar crystallites. Whereas the dislocation density is very high in the rather narrow column in figure 7.18, much less dislocations were found in a larger column as shown in figure 7.19. In the raw (unfiltered) micrograph of the narrow column in figure 7.14, strong strain contrasts are visible, which is also not the case in larger columns. Thus, the strain state of different crystallites in the multilayers may be quite different, depending on the crystallite size.

With rising distance to the substrate, the arrangement of the dislocations in figure 7.18 gets irregular. No accumulation at the interfaces takes place. Often, dislocations with anti-parallel Burgers vectors are found next to each other. There seems to be no preference for either of the anti-parallel orientations. The net effect of such dislocation arrangements on the overall strain in the multilayer is therefore zero and the strain release is restricted to very small regions around irregularities, marked by strain contrasts in the unfiltered micrographs.
In figure 7.19 as well as figure 7.18, dislocations which are arranged more or less regularly and not paired with anti-parallel dislocations are situated in the $Sc_2O_3$ layer. From the negative misfit between YSZ and $Sc_2O_3$, one would expect such dislocation networks in the YSZ phases. This leads to the assumption that tensile strain arising from the large misfit between the first $Sc_2O_3$ layer and the substrate or caused during the film growth and crystallisation is compensated in these dislocation networks rather than misfit strain.
Some dislocations of a second type with regard to their orientation were found in figure 7.20 and 7.21. These dislocations are also not aligned in a regular

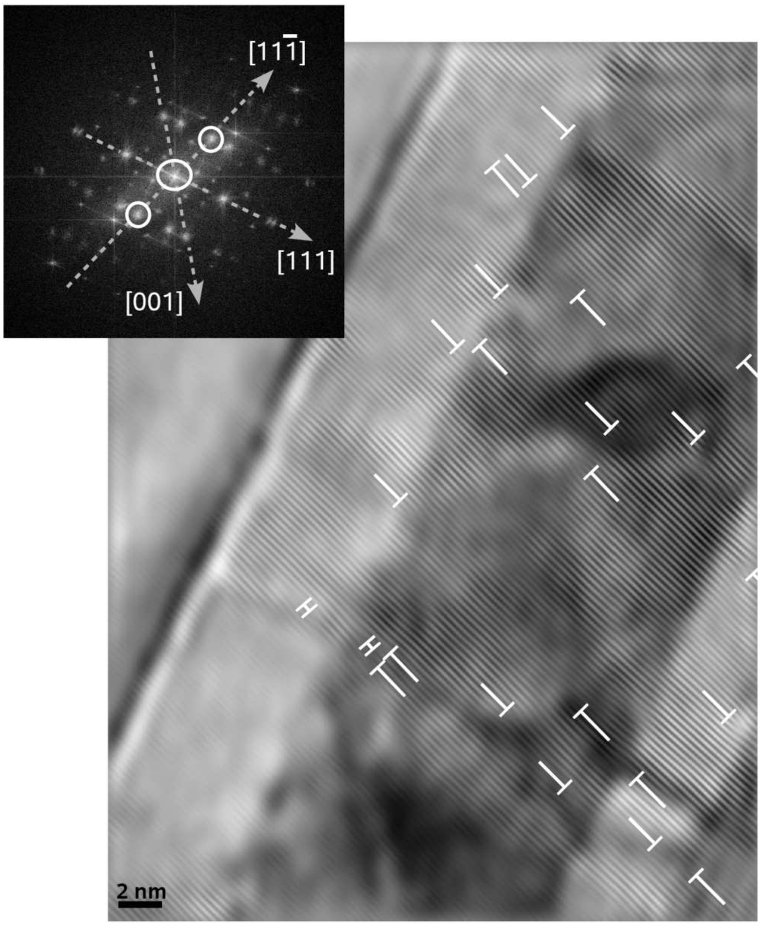

**Figure 9.4:** [11$\bar{1}$] Fourier filtered HRTEM image of the sample YSc150-2 (the original HRTEM micrograph is shown in figure 7.15). Identified dislocations are marked. The inset shows the associated FFT, obtained from the HRTEM micrograph by excluding the substrate region. The signals used for the filtering are marked; all other signals were excluded.

array and some are distributed in the bulk of the layers. More important, the found dislocations of the second type have Burgers vectors perpendicular to the individual layers. Dislocations of this geometry are not suited to release misfit strain acting parallel to the interfaces.

The exact orientation of the Burgers vectors of the found dislocations can not be determined. This is because the HRTEM micrographs are only two dimensional projections of the real three dimensional structures. Thus, a part of the structural information will be lost.
In evaluating the high density of anti-parallel dislocations found in figure 7.18 and discussed above, one has to take into account that such dislocation arrangements are very unfavourable with regard to the strain energy. It is a known fact that dislocation loops, which may dissociate into anti-parallel dislocations, can be created as a result of irradiation damage [117]. However, since the strain contrasts visible in the HRTEM bright field micrographs did not change during the time needed for the HRTEM investigations, this is not probable in this case. But it is possible that anti-parallel dislocations visible in the filtered micrographs are an artifact of the filtering.

Two samples of the system YSZ | $Lu_2O_3$, deposited at 10 Hz, were investigated by HRTEM: YLu150 and YLu70. In these samples, no dislocations were found near the phase boundaries as far as the HRTEM micrographs could be analysed. One sample deposited at 2 Hz was investigated: the sample YLu50-3. In this sample, a dislocation configuration very similar to that found in the sample YSc50-3, as described above, was found. The density of dislocations seems slightly lower than in the sample YSc50-3, but since only very small volumes of both samples were investigated by HRTEM, this statement may not be reliable. As the net strain effect of an irregular dislocation network with anti-parallel Burgers vectors is practically zero, the origin of the dislocations most likely is not the structural misfit between the different layers but microstrain caused during the layer and grain growth.

In all multilayer samples, a wavy layer morphology developed with increasing distance of the individual layers from the substrate. The effect was more strongly pronounced in the YSZ | $Sc_2O_3$ multilayers, being most severe for samples deposited at 2 Hz. The fact that the misfit in the system YSZ | $Sc_2O_3$ is larger than in the system YSZ | $Lu_2O_3$ and that the effect of lattice strain at the interfaces is more pronounced when the grain size is increased, indicates that the development of the wavy layer morphology is an important mechanism by which lattice strain is released. Similar suggestions have been made before by JIN-PHILLIP et al. [33, 118]. They found that this relaxation mechanism is important in systems with a medium mismatch at the interfaces. They also observed a distinctive lattice parameter change directly at the interfaces of the wavy layers which is assumed to lead to a partial relaxation of the misfit strain. For large misfits,

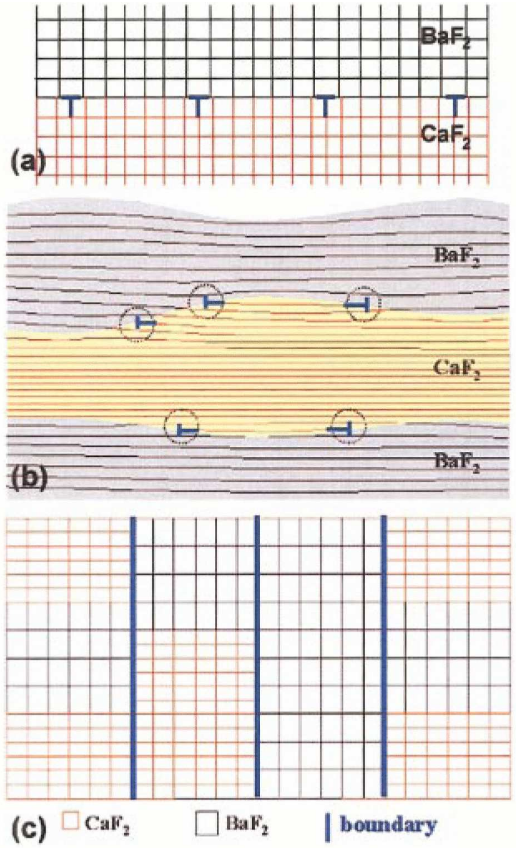

**Figure 9.5:** Scheme showing the different mechanisms for strain release in $CaF_2$ / $BaF_2$ multilayer systems, as suggested by JIN-PHILLIP et al.à) Large misfit strain leads to the formation of dislocation networks. b) Intermediate misfit strain is released by the development of a wavy layer morphology. c) Small misfit strain is compensated by the elastic deformation of the adjoining lattices. Picture taken from [33].

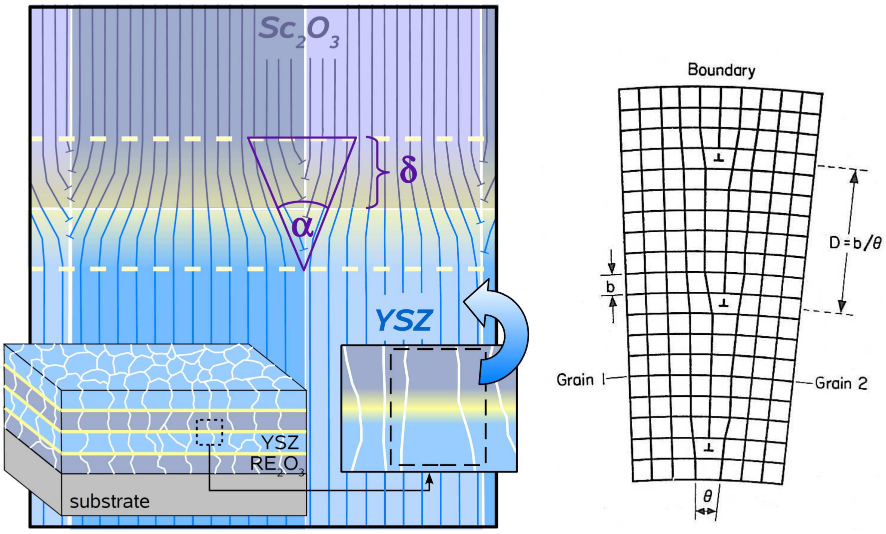

(a) (b)

**Figure 9.6:** Schematic illustration of the possible arrangement of dislocations in grain boundaries. a) Near an interface, where the misfit induced lattice strain is compensated through dislocation arrays in the grain boundaries. The situation is similar to that of a low angle tilt grain boundary. b) A low angle tilt grain boundary between two grains with a mutual tilt misorientation $\theta$. Picture taken from [44].

the relaxation takes place through dislocation networks and a small misfit can be compensated by the elastic deformation of the adjoining crystal lattices. An overview of the different relaxation mechanisms, as suggested by Jin-Phillip, is shown in figure 9.5

Most probably the number of dislocations near the phase boundaries in the system YSZ | $Sc_2O_3$, which have a Burgers vector perpendicular to the interfaces, is linked to the morphological structure of the individual layers. These dislocations may be formed as a consequence of the wavy layer morphology rather than being a direct consequence of the lattice misfit. They may be responsible for the release of the additional strain caused by this morphology, which acts perpendicular to the layers and in the same direction as the dislocations Burgers vector. Accordingly, the number of these dislocations is much lower close to the substrate, where the individual layers are flat (see figure 7.21).

### 9.1.3 The Grain Boundary Structure

Concerning the structural parameters of the multilayers, especially the amount of lattice strain present, the grain boundaries may be an important factor for strain release.

Firstly, the contact area between the different phases adjacent to the interface is determined by the grain size. Thus, the strained areas are confined. The stress distribution in confined systems was investigated by FISCHER et al. for patterned structures. They found that the strain per unit area in a film on a rigid substrate can be reduced to a great extend by pattering the system and creating small insular (mesa-like) structures instead of large continuous films [119, 120]. It was assumed that the stress falls to zero at the edges of the mesa-like islands. In the grain boundaries, the stress will also reach a minimum due to a high density of dislocations. Therefore, the total strain in a film consisting of small grains will be lower than in a film with larger grains or in a single crystalline film.

The influence of grain nucleation on the stress states in thin films during deposition was investigated by SPAEPEN [121]. He found that during grain growth, additional tensile stresses can be caused when isolated islands coalesce to a continuous film, creating grain boundaries. However, the stress state present during the deposition of a thin film in most cases cannot be compared to the relaxed (annealed) state.

Secondly, the grain boundaries are also capable of releasing a part of the misfit strain in the multilayers through the accumulation of structural defects, especially dislocations. A dense array of dislocations with a suitable geometry was found in the grain boundaries of the sample YSc150-2, as is illustrated in figure 7.15. In the shown grain boundary, the dislocations are arranged in a quite regular network and all Burgers vectors are parallel. The origin of these dislocations is for the most part the grain-to-grain misorientation. It is mainly due to twist in this case since the two adjoining grains have mirror inverted azimuthal rotations (twin grain boundary). But one can also expect that the lattice strain parallel to the layers is partly released by this dislocation arrangement.

If no dislocations are existent at the phase boundaries inside the grains, a part of the misfit strain can be released by dislocations in the grain boundaries. This is demonstrated in figure 9.6, where a possible dislocation arrangement is derived schematically. The elastic lattice deformation of neighbouring grains at the interface is expected to lead to an accumulation of dislocations in the grain boundary, creating a low angle tilt grain boundary with the tilt angle $\alpha$. If $\alpha$ is known, the spacing $\vec{D}$ of the dislocations can be calculated as follows [44]:

$$\vec{D} = \frac{\vec{b}}{2\sin\left(\alpha/2\right)} \tag{9.3}$$

Or, for small values of $\alpha$ (in radians):

$$\vec{D} \approx \frac{\vec{b}}{\alpha} \tag{9.4}$$

The tilt angle $\alpha$, in turn, depends on the diameter $l$ of the adjoining crystallites, the misfit $f$ and the extension of the strained interface region $\delta$. For small values of $\alpha$ (in radians), we obtain:

$$\alpha \approx \frac{l}{2\delta} f \tag{9.5}$$

$\vec{D}$ then yields to:

$$\vec{D} \approx \frac{2\vec{b}\delta}{lf} \tag{9.6}$$

If we assume $\vec{b} = d_{(220)}(\text{YSZ}) = 1.81$ Å, $l = 60$ nm, $f = 0.0437$ (misfit YSZ | $Sc_2O_3$) and $\delta = 10$ nm, then equation 9.6 yields $\vec{D} \approx 13.8$ Å. $\alpha$ would then be $\approx 7.5°$. For smaller values of $\delta$, $\vec{D}$ is of course smaller.

The simple picture in figure 9.6 is of course strongly exaggerated and only valid if no additional tilt or twist misorientation is present between the grains. Those misorientations increase the number of dislocations, which may be arranged in more or less regular and dense arrays.

### 9.1.4 Microstrain in the Multilayers

As evident from the XRD measurements, both YSZ and the rare earth oxide layers are strained to some extent even after the heat treatment. The mean deviation of the lattice parameter from the literature values was always positive and in the range of 0.5 % to 1.4 % (see tables 7.1, 7.2 and 12.1 - 12.4).

The lattice deformation of the system YSZ | $Lu_2O_3$ cannot be analysed reliably because the strong signals of YSZ and $Lu_2O_3$ overlap in XRD and can not be separated with the means given. Thus, the values for $\Delta a$ in table 7.2 and the calculated lattice parameters in table 12.3 and 12.4 are highly uncertain and will therefore not be interpreted further.

A. Peters found that $\Delta a$ is about 1 % in the multilayer system YSZ | $Y_2O_3$ after annealing [107]. This is comparable to the mean value of $\Delta a$ found in this work for the system YSZ | $Sc_2O_3$ deposited at 10 Hz.

Most probably, the major part of the residual strain in both phases of the different multilayer systems is due to microstrain. Like thermal strain, it acts in every direction. Microstrain present in thin films was investigated in detail by Rupp et al.The microstrain was determined in films of undoped and Gd doped $CeO_2$ during crystallization [122]. In (partly) amorphous films, e.g. directly after deposition, a high amount of microstrain is present because the molar volume of an amorphous phase is typically larger than that of the crystalline modification. However, the microstrain decreases considerably during the first 10 h of annealing at temperatures over 600 °C. Similar investigations on 8 mol-% YSZ showed that, influenced by the microstrain, the ionic conductivity in amorphous thin films is about half an order of magnitude lower than in crystalline films [123].

Even if the microstrain decreases during the thermal treatment of a sample, it does not vanish completely in thin films constrained by a much thicker and rigid substrate. The strain contributions arising from the misfit and possible thermal strains are superimposed to the microstrain. However, the microstrain and the thermal strains are only dependent on the deposition rate and the thermal treatment. In this work, all samples deposited at the same pulse rate underwent exactly the same temperature treatment, so that the contributions of microstrain and thermal strain are equal for all multilayers with the same preparation parameters but independent from the used rare earth oxide[1]. A difference between the structural (and electrochemical) properties of the different systems investigated here must therefore be due to the misfit strain contribution.

### 9.1.5 Interdiffusion at the Interfaces

Interdiffusion between the different layers in a multilayer system alters the ideal interface structure and also influences strain fields or space charges present at the interfaces. In interdiffusion zones, the transport properties may be significantly different from those in the bulk.

Kilo et al. investigated the diffusion of different cations in stabilized zirconia [124, 125]. Extrapolating their experimental results to a temperature of 800 °C, the following diffusion coefficient are obtained:

**Diffusion Coefficients in YSZ at 1073 K**

| Cation | D [$10^{23}$ cm$^2$s$^{-1}$] |
|---|---|
| $Zr^{4+}$ | 0.85 |
| $Y^{3+}$ | 46.66 |
| $Lu^{3+}$ | 1.19 |
| $Sc^{3+}$ | 0.60 |

**Table 9.1:**

Using a diffusion coefficient of $1 \cdot 10^{-22}$ cm$^2$ s$^{-1}$, annealing for one month at 800 °C leads to a diffusion length[2] of about 0.4 nm. This seems negligible. However, the real diffusion lengths may be larger due to a lowered activation energy for diffusion in strained crystal lattices. Also, a slight intermixing of both phases may occur during the pulsed laser deposition because of a certain roughness of the layer surfaces caused by an island-like growth process or because of contaminated target surfaces which is hard to avoid in the used PLD setup.

---

[1] This assumption is made on the basis that the thermal expansion coefficients of $Lu_2O_3$, $Sc_2O_3$ and $Y_2O_3$ can be considered as similar.

[2] This value was calculated as: $\Delta x = \sqrt{6 \Delta t D}$

The width of interdiffusion zones in both multilayer systems was determined by HREDX and EELS line scan measurements. In the system YSZ | $Sc_2O_3$, the maximal width of the interdiffusion zones was 2 nm for both of the investigated samples (one deposited with 10 Hz, one with 2 Hz; see section 7.2.1). A similar width was determined for a sample of the system YSZ | $Lu_2O_3$, deposited at 10 Hz (section 7.2.2). In a sample deposited at 2 Hz, the interdiffusion zone was twice as wide, the value determined from the EELS line scans being 4 nm. From the shape of the signals for $Zr^{4+}$ and $Lu^{3+}$, it is deduced that mainly the $Lu^{3+}$ ions diffuse.

Summarising, one can conclude that interdiffusion between the different material layers in the multilayer system is not very pronounced at temperatures up to 800 °C. However, it may influence the strain state at the interfaces, especially in the system YSZ | $Lu_2O_3$.

## 9.2 Ionic Conductivity

### 9.2.1 General Remarks

DC measurements in general produced the same results as AC measurements. As an example, the AC and DC results for the sample YSc1002 are shown in figure 9.7 for comparison. A perfectly Ohmic behaviour of the samples was observed in the DC measurements. If a significant deviation of the DC from the AC results was observed, the measured DC resistance was always higher. The corresponding Nyquist plots showed additional, often scattered signals at lower frequencies, exceeding the diameter of the semicircle attributed to the sample response. Thus, the DC resistances were equal to or a little higher than the total real part of Z, which at low frequencies includes electrode polarisation phenomena. The electrode polarization resistance is typically higher in DC than in AC measurements.

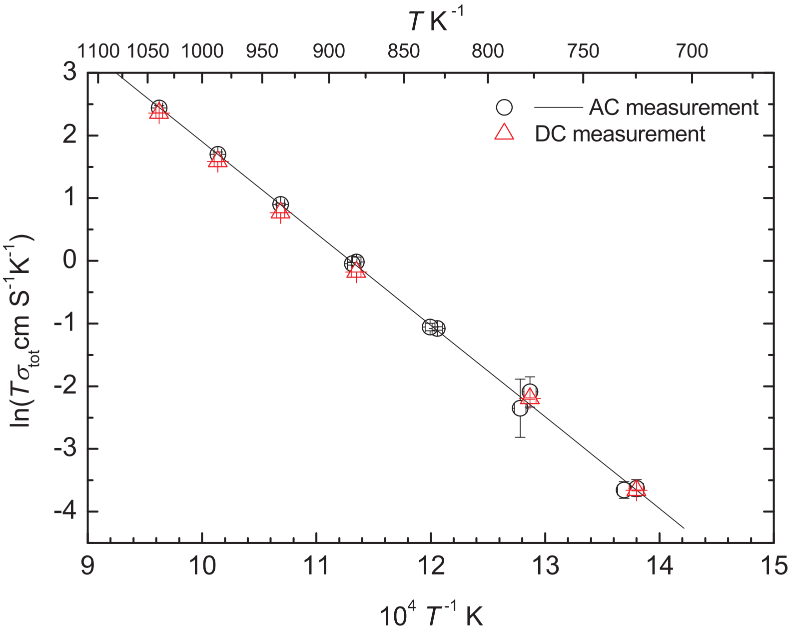

**Figure 9.7:** AC and DC results for the ionic conductivity of the sample YSc1002. The line fit relates to the AC results.

To evaluate the influence of the sample polishing, the sample YSc1002 was prepared in two ways: The first sample was polished down to a polishing foil roughness of 9 µm, the second sample was prepared almost in the same way as described in section 7.1.2 for SEM investigations (two pieces glued together, polished down to 0.1 µm, no ion polish) and the polishing was checked with an optical microscope. Within the error margins, both samples delivered the same results in the conductivity measurements. This shows that a polish down to 9 µm, without gluing the sample on top of another crystal, was sufficient for the electrochemical measurements.

If the conductivity values obtained for the different multilayer samples are compared to the conductivities of the $RE_2O_3$ single layers presented in section 8.2.2, one can see that the conductivity of the rare earth oxide is always at least one order of magnitude lower than $\sigma_{\text{tot}}$ of the multilayers. Since the thickness of the $RE_2O_3$ and the YSZ layers is similar in every multilayer, the conductivity of the rare earth oxides can be neglected for $\sigma_{\text{tot}}$. The same is valid for the conductivity of the substrate. The thickness of the substrate is about 3 orders of magnitude larger than the total thickness of the multilayers (which is 2 - 4 µm), but its conductivity is about 5 orders of magnitude lower than any conductivity value measured for the multilayer samples (see section 8.2.1).

### 9.2.2 Derivation of a Suitable Equivalent Circuit

The fact that only one semicircle was observed in the impedance spectra of all investigated samples is consistent with results found in literature about other thin film systems, see e.g. investigations on YSZ films on (001) MgO by KOSACKI [6]. KARTHIKEYAN obtained similar impedance spectra for YSZ | $SiO_2$ multilayers on (001) MgO [12] (see also part II). The same was reported by A. PETERS for investigations on the multilayer systems CSZ | $Al_2O_3$ and YSZ | $Y_2O_3$ [19, 107].
To understand the impedance properties of the samples, a theoretical model must be derived resulting in an equivalent circuit. The elements which contribute to the overall AC response are the substrate (index s), the grain volume (vol), the grain boundaries (gb) (perpendicular to the direction of the current), the interfaces between YSZ and the rare earth oxide (int), the electrodes (el) and the feed lines (feed) in the sample holder. The grain boundaries parallel to the direction of the current are included in the grain volume element for the sake of simplicity. Every contribution can be expressed by a parallel ($RC$) element. The resistance of the feed lines and the ($RC$) elements of the electrodes, the grain boundaries perpendicular to the current direction and the grain volume are connected in series. The elements of the interfaces and the substrate and the capacity of the feed lines are connected parallel. In figure 9.8, the resulting equivalent circuit is shown.
The resistance of the feed lines can be neglected. Because of the low electrode polarisation, the same is valid for the electrode resistance. The resistance of the substrate, on the other hand, is much higher than the resistance of the multilayer (see section 8.2.1), so that the current flow takes place only through the thin film; $R_{\text{s}}$ does not contribute to the measurement. The capacities associated with the layer volume and the layer-to-layer interfaces are also considered to be low.
Values for the sample capacities, obtained by fitting the various impedance measurements, were always around $3.5 \cdot 10^{-11}$ F. To analyse the origin of the measured

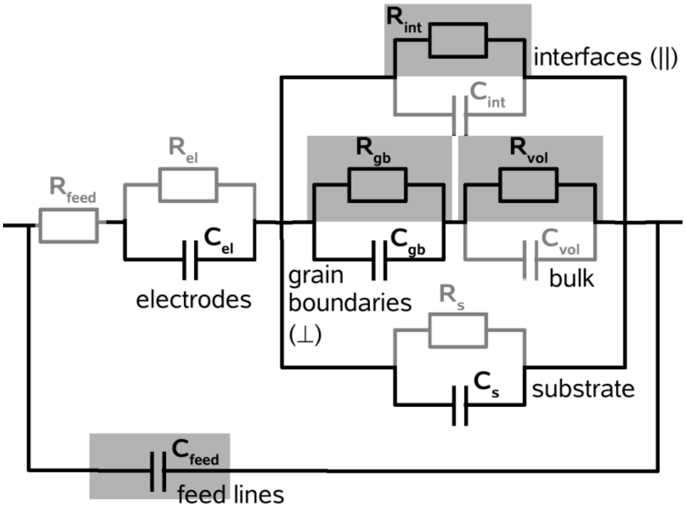

**Figure 9.8:** Equivalent circuit for a polycrystalline thin film multilayer sample. The important contributions are marked dark grey.

capacities, they have to be compared to theoretic values for different parts of the multilayer sample or the measurement setup.

The theoretic geometric capacity of the sample (including the silver paste electrodes) can be calculated using the equation for a simple parallel plate type capacitor:

$$C = \varepsilon_0 \varepsilon_r \cdot \frac{A}{b} \tag{9.7}$$

$\varepsilon_r$ corresponds to the dielectric constant of the substrate, which is much thicker than the thin film and therefore constitutes the major part of the sample capacity. Assuming a value of 9.5 for $\varepsilon_r$ ($Al_2O_3$) [126], a lateral surface $A$ of $8 \cdot 10^{-6}$ m$^2$ and a sample thickness $b$ of 2 mm, the calculated value for the capacity is about $3.9 \cdot 10^{-13}$ F. This value is two orders of magnitude smaller than the one obtained by the impedance measurements of the multilayer samples.

If the shielding of the cables or Pt wires inside the sample holder is not sufficient, there will be a considerable capacity between neighbouring feed lines. This capacity can be calculated using the equation for a Lecher system:

$$C = \pi \varepsilon_0 \varepsilon_r \cdot \frac{1}{\operatorname{arcosh}(\frac{a}{d})} \tag{9.8}$$

$a$ is the distance between two feed lines and $d$ denotes their diameter. $\varepsilon_r$ again denotes the dielectric constant of $Al_2O_3$, because the sample holder basically consists of this material. If we assume $a$ to be 1 cm and $d$ to be 0.25 mm, then the calculated capacity between the two voltage measuring feed lines inside the sample holder is $6 \cdot 10^{-11}$ F.

The grain boundary capacity was measured by GUO to be 40-50 nF/cm$^2$ in 8 mol-% YSZ [27]. For the lateral surface of a multilayer, which is assumed to be 3 µm thick and 8 mm wide, a capacity of about $1 \cdot 10^{-11}$ F results.

If these calculated values are compared to the measured sample capacity, it is evident that the geometric capacity of the samples does not play a role. The capacities of the grain boundaries and of the feed lines, calculated for the case that the shielding is not sufficient, are in the same order of magnitude as the measured value and can therefore not be neglected. An impedance measurement of a dummy cell, consisting of a parallel $(RC)$ element with nominal values of $R = 10$ MΩ and $C = 1$ pF, delivered $C = 3.203 \cdot 10^{-11}\text{F} \pm 2.783$ %. This result is very similar to the one obtained for the multilayers (see figure 9.9). The dummy cell was placed in the same sample holder that was used for all electrochemical investigations and measured with the same impedance bridge. Measuring the same dummy cell outside the sample holder delivered $C = 2.451 \cdot 10^{-11}\text{F} \pm 3.173$ %. It can therefore be concluded that indeed the major part of the measured sample capacities arises from the feed lines, especially from the cables outside the sample holder. Since the value of the grain boundary capacity is in the same order of magnitude, it can not be separated from the feed line contribution.

With the above defined limitations

$$R_\text{s} >> R_\text{vol} + R_\text{gb}, R_\text{int} >> R_\text{el} >> R_\text{feed}$$

$$C_\text{feed}, C_\text{gb} >> C_\text{s+el} >> C_\text{vol}, C_\text{int}$$

the semicircle in figure 9.8 can be simplified to a single parallel $(RC)$ element were $R$ is given by a combination of $R_\text{vol}$, $R_\text{gb}$ and $R_\text{int}$ and $C$ by a combination of $C_\text{gb}$ and $C_\text{feed}$. Consequently, only one semicircle appears in the impedance plots.

### 9.2.3 Expectations for the Strain Induced Change of the Ionic Conductivity

Considering the theoretical approach in section 3.2, the expected effect of lattice strain on the ionic conductivity can be calculated for the different material combinations. For YSZ, $Lu_2O_3$ and $Sc_2O_3$, we can assume the elastic properties to be similar. Therefore, lattice deformation will take place in YSZ as well as in the rare earth oxide and the lattice strain splits up in two nearly equal parts.

$$f_{\text{YSZ/RE}_2\text{O}_3} \approx 2\varepsilon_{\text{YSZ/RE}_2\text{O}_3} \tag{9.9}$$

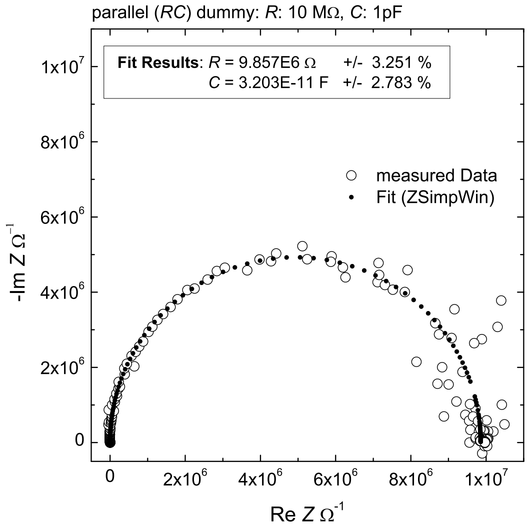

**Figure 9.9:** Impedance result for a dummy cell consisting of 10 M$\Omega$ resistor parallel to a 1 pF capacitor, which was placed in the sample holder used for the multilayer measurements. The small dots represent the fit result; the calculated values for $R$ and $C$ are also given in the figure.

Necessarily, the strain in the rare earth oxide has the opposite sign than in YSZ. The identity of the sign depends on whether the material is strained compressively (−) or dilatively (+).

$$\varepsilon_{\text{YSZ/RE}_2\text{O}_3} \approx -\varepsilon_{\text{RE}_2\text{O}_3\text{/YSZ}}$$

The relation between the ionic conductivity $\sigma_{\text{int}}$ along the strained interface regions and the bulk conductivity $\sigma_{\text{vol}}$ can be calculated using equations 3.28, 3.29 and 9.9:

$$\ln\frac{\sigma_{\text{int}}}{\sigma_{\text{vol}}} \approx \frac{1}{3}\frac{\Delta V^{\text{M}}_{\text{V}_\text{O}^{\cdot\cdot}}}{RT}\frac{\text{Y}_{\text{YSZ}}}{1-\nu_{\text{YSZ}}}\cdot f_{\text{YSZ/RE}_2\text{O}_3} \tag{9.10}$$

With the following values [127–129]:

| | |
|---|---|
| $\Delta V^{\text{M}}_{\text{V}_\text{O}^{\cdot\cdot}}$ | $2.08 \cdot 10^{-6}$ m$^3$ mol$^{-1}$ [127] |
| Y | 180 GPa [128] |
| $\nu$ | 0.3 [129] |
| T | 833 K |
| $f_{\text{YSZ/Sc}_2\text{O}_3}$ | 0.0428 (see table 4.2) |

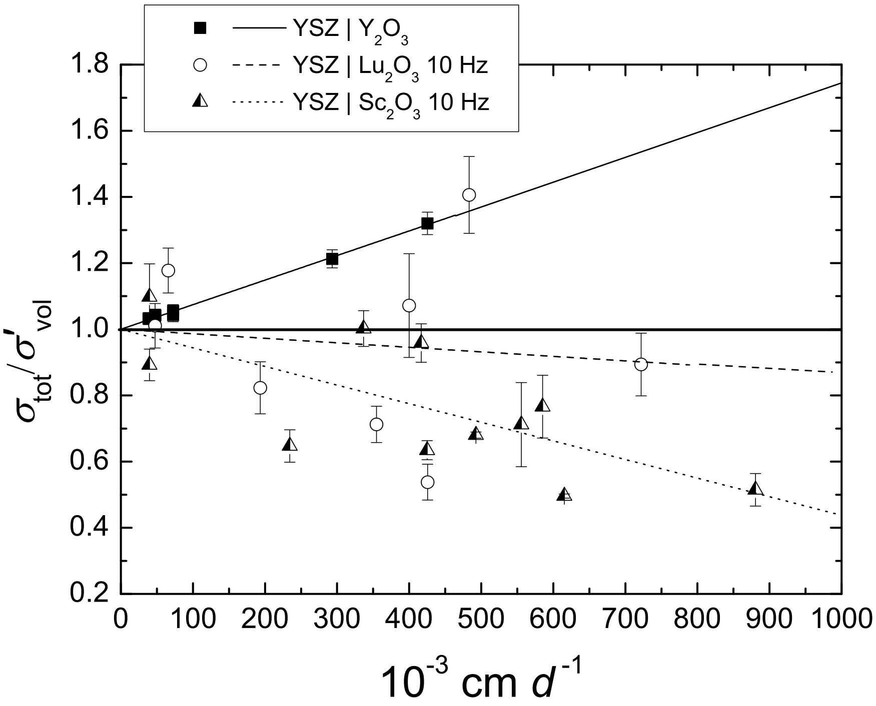

**Figure 9.10:** Relative conductivity versus $1/d$ for the different systems YSZ | $RE_2O_3$. RE = Y (data taken from [107]), RE = Lu and RE = Sc. Only samples with $d \geq 10$ nm were taken into account.

$f_{\mathrm{YSZ/Lu_2O_3}}$ 0.0102 (see table 4.2)

$\ln \frac{\sigma_{\mathrm{int}}}{\sigma_{\mathrm{vol}}}$ yields to −1.10 for YSZ | $Sc_2O_3$ and 0.26 for YSZ | $Lu_2O_3$.
Using the values given above, the slope for a plot of $\ln \frac{\sigma_{\mathrm{int}}}{\sigma_{\mathrm{vol}}}$ in relation to the misfit $f$ can be estimated theoretically as 25.74.

### 9.2.4 Comparison of the Different Systems YSZ | $RE_2O_3$

To be able to compare the three systems YSZ | $RE_2O_3$ with RE = Y, Lu and Sc, only samples with $d \geq 10$ nm were taken into account. We expect that above a single layer thickness of 10 nm, the structurally and chemically altered interface regions do not overlap. Thus, the relationship between the total conductivity and the inverse layer thickness can safely be assumed as linear. The resulting plots, showing the relative conductivity $\frac{\sigma_{\mathrm{tot}}}{\sigma'_{\mathrm{vol}}}$, are shown in figure 9.10 for the samples RE = Y, RE = Lu and Sc deposited at 10 Hz and in figure 9.11 for the samples deposited at 2 Hz.
The values obtained from the linear fits are summarized in table 9.2.

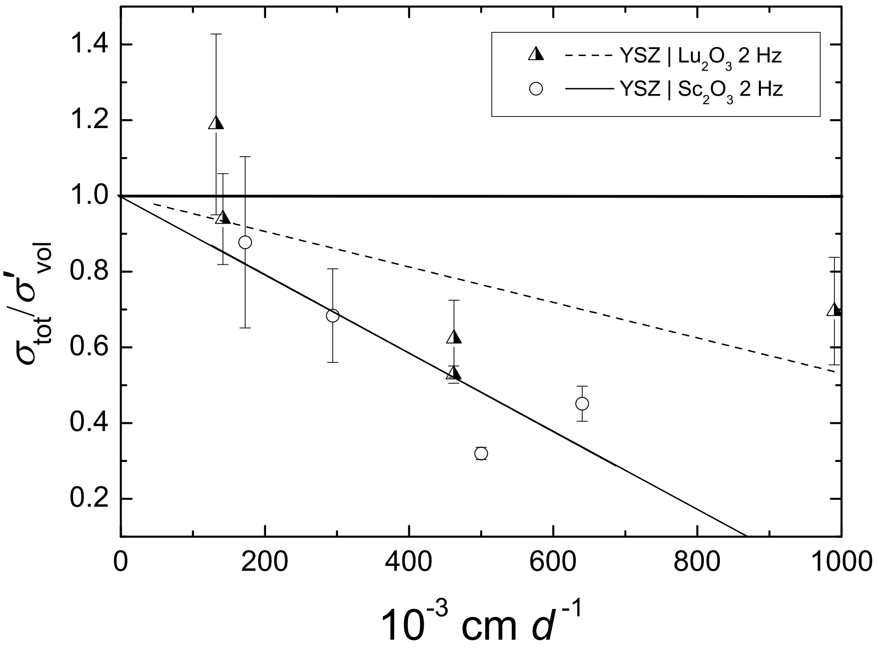

**Figure 9.11:** Relative conductivity versus $1/d$ for the different systems YSZ | RE$_2$O$_3$ with RE = Lu and RE = Sc, deposited at 2 Hz.

| $RE_2O_3$ | $\sigma'_{\text{vol}}$ $[10^{-4}\ \text{S/cm}]$ | $2\delta\,(\sigma_{\text{int}} - \sigma_{\text{vol}})$ $[10^{-10}\ \text{S}]$ | $\sigma_{\text{int}}$ $[10^{-4}\ \text{S/cm}]$ | $\frac{\sigma_{\text{int}}}{\sigma_{\text{vol}}}$ | $\ln(\frac{\sigma_{\text{int}}}{\sigma_{\text{vol}}})$ |
|---|---|---|---|---|---|
| $Y_2O_3$ | 1.85 | 1.37 | 3.22 | 1.74 | 0.56 |
| $Lu_2O_3$ | 5.75 | –0.79 | 4.97 | 0.86 | –0.15 |
| $Sc_2O_3$ | 7.81 | –4.39 | 3.42 | 0.44 | –0.83 |
| $Lu_2O_3$ 2 Hz | 7.23 | –3.39 | 3.84 | 0.53 | –0.63 |
| $Sc_2O_3$ 2 Hz | 6.02 | –6.25 | –0.23 | –0.04 | – |

**Table 9.2:** Summary of the data obtained from the linear fits in figure 9.10 and 9.11. Data for the system YSZ | $Y_2O_3$ taken from [107].

According to equation 4.14, $\sigma'_{\text{vol}}$ corresponds to the intercept of the linear fit for the conductivity data versus $1/d$ down to $d = 10$ nm and $2\delta\,(\sigma_{\text{int}} - \sigma_{\text{vol}})$ to the slope. $\sigma_{\text{int}}$ is estimated as the value of $\sigma_{\text{tot}}$ for $d = 10$ nm as calculated from the data of the fit.

The increase of the conductivity with decreasing $d$ in the system YSZ | $Y_2O_3$ is described in detail in [107] and [19]. It is in good agreement with the expectations for interfacial ionic transport in case of tensile lattice strain. For RE = Lu (10 Hz), a small decrease of the conductivity takes place, but the calculated conductivity of $d = 10$ nm is still 86 % of the determined volume conductivity. A much stronger decrease is determined for RE = Sc (10 Hz), where the conductivity for $d = 10$ nm is only 44 % of the volume conductivity. The decrease in conductivity for RE = Sc is also in agreement with the influence of lattice strain on ionic transport (see section 3.2.2). The value of $\ln(\frac{\sigma_{\text{int}}}{\sigma_{\text{vol}}})$, being -0.83, is somewhat lower than the value of -1.10 calculated in section 9.2.3 ($\sigma_{\text{vol}}$ here is approximated by $\sigma'_{\text{vol}}$). It may be that a more realistic value of the interface conductivity in this system is obtained when $d$ is reduced to under 10 nm.

For RE = Lu, a small increase of the conductivity would have been in accordance with the expectations, but considering the high scattering of the conductivity values and therefore the high error in determining the change in conductivity, the theoretical approach in section 3.2.2 is not disproved.

For the samples deposited at 2 Hz, the interpretation of the obtained results is not straightforward. The error for the change in conductivity is large because of the small number of investigated samples and the scattering of the values. The scattering is again stronger for RE = Lu. For both systems, a significant decrease of the total conductivity was determined, being stronger than for the samples deposited at 10 Hz. For RE = Sc, this can be explained by the enhanced influence of compressive lattice strain at the interfaces. This influence is larger when the columnar grains in the thin film are bigger, leading to an increased contact area between the two adjoining phases and less strain release at the grain boundaries. For RE = Lu, no satisfactory explanation of the conductivity behaviour can be given. The volume conductivity may be overestimated through the strong scattering of the measured conductivities.

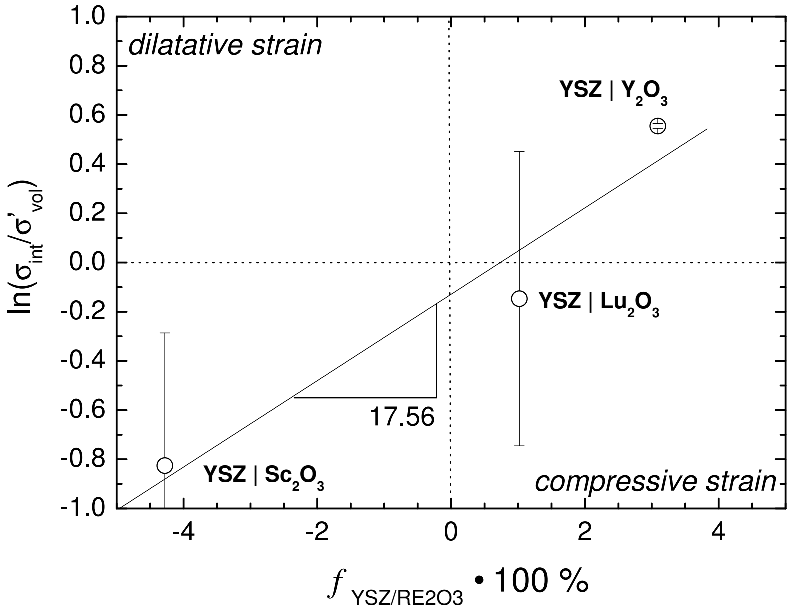

**Figure 9.12:** Change of the conductivity in relation to the misfit. The results for the samples deposited at 2 Hz were not taken into account.

The value of $\sigma_{\text{int}}$ estimated for $d = 10$ nm in the system YSZ | $Sc_2O_3$ (2 Hz) is negative and makes therefore no sense. The reason may be that due to the small number of samples the slope of the linear fit does not represent the real change in conductivity very well. It may also be that for this system, the conductivity behaviour is not linear down to $d = 10$ nm. If $\sigma_{\text{int}}$ is calculated as the total conductivity at $d = 15$ nm, a value of $1.85 \cdot 10^{-4}$ S/cm is obtained. $\frac{\sigma_{\text{int}}}{\sigma_{\text{vol}}}$ then is 0.31 and $\ln\frac{\sigma_{\text{int}}}{\sigma_{\text{vol}}}$ yields -1.18.

The three systems YSZ | $RE_2O_3$ with RE = Sc, Lu and Y can best be compared by plotting $\ln\frac{\sigma_{\text{int}}}{\sigma_{\text{vol}}}$ in relation to $f_{\text{YSZ/RE}_2\text{O}_3}$ as it is done in figure 9.12. For RE = Sc and Lu, only the samples deposited at 10 Hz were taken into account. From the plot, a slope of 17.56 is obtained. The error for this value is large, which is mainly due to the scattering of the conductivity values mentioned before. The experimentally determined slope is about two thirds of the slope calculated theoretically in section 9.2.3. This theoretical value is based on considerations taking only into account elastic strain as an influence on conductivity. However, the structural measurements indicated that the effective strain may not be as high as anticipated because grain boundaries and the development of a wavy layer structure act as mechanisms reducing the strain at the interfaces.

The measured activation energies $E_a$ for the ionic conduction in the different multilayers were between 1.05 eV and 1.27 eV for the system YSZ | $Sc_2O_3$ (table 8.1 and 8.2) and between 1.00 eV and 1.31 eV for the system YSZ | $Lu_2O_3$ (table 8.3 and 8.4). In general, the measured activation energies for samples with thick individual layers are in the range of the literature values given in table 9.3. Samples with smaller values of $d$ (below 20 nm) tend to show somewhat higher activation energies, independent on the nature of the rare earth oxide.

**Literature Values of the Activation Energy in YSZ**

| $Y_2O_3$ [mol-%] | $E_a$ [eV] | $T$ [K] | Ref. |
|---|---|---|---|
| 8.7 | 1.09 | 623-973 | [36] |
| 9.5 | 0.89 | 833-1473 | [37] |
| 9.9 | 1.15 | 623-673 | [36] |
| 10.3 | 1.06 | 873 | [38] |

**Table 9.3:**

If the course of the activation energy for the different systems with RE = Sc and Lu is compared, it must be stated that for the samples deposited at 10 Hz this trend is not very well developed (see section 8.2.3 and 8.2.4). For the samples deposited at 2 Hz, a more or less regular increase of $E_a$ with decreasing $d$ can be observed. PETERS measured a quite regular decrease of $E_a$ in the system YSZ | $Y_2O_3$ [107]. The literature values indicate that $E_a$ is also dependent on the dopant level, but not in a regular way.

Since the measured values of the activation energy include all possible contributions to the transport in the multilayers, in detail the volume, the interface and the grain boundary fractions, the influence of lattice strain at the interfaces may be covered by other effects. That may be the reason for the scattering of $E_a$ and for the unexpected decrease in the system YSZ | $Lu_2O_3$. A very serious influence on the activation energy and the ionic conductivity may be caused by impurities, which may segregate at the interfaces and grain boundaries. As was shown in SIMS measurements (figure 7.25 and 7.43), the impurity content is low in layers at some distance to the substrate, but may be higher near the substrate. However, no segregation phases were found at the interfaces using HRTEM methods. Since only two samples were investigated with SIMS, the obtained results are not sufficient to further clear the role of impurities in the multilayers.

### 9.2.5 The Influence of Grain Boundaries

The grain boundary conductivity is an important part of the volume conductivity $\sigma'_{\mathrm{vol}}$ estimated from plotting $\sigma_{\mathrm{tot}}$ in relation to $1/d$. It has been mentioned before that the grain boundaries in YSZ are blocking with respect to ionic transport. This is on one hand due to the segregation of impurities, most important Si, on the other hand space charge regions are considered to play an important role. Also,

the local dopant content in YSZ may differ at the grain boundaries. Guo et al. found an increase of the $Y^{3+}$ concentration at the grain boundaries in YSZ [27,28], which is considered as the main source for the evolution of space charge regions in this material. This dopant segregation takes place at elevated temperatures, e.g. at sintering temperatures of 1000 °C. As a consequence, the grain boundary core is positively charged and a depletion of oxygen vacancies takes place in the space charge region. Whereas the crystallographic width of a grain boundary is in the range of 1 nm (see for example figure 7.22), the segregation of $Y^{3+}$ was found to take place in a region of 4 nm to 8 nm around the grain boundaries in 2.5 mol-% YSZ [64, 130, 131]. This 'chemical' grain boundary width may be lower in YSZ with a higher dopant content, but it may nevertheless play a role. Concerning the temperature dependence of the grain boundary blocking effect, it was found to be most pronounced at low temperatures (below 400 °C - 500 °C, see [27]).
The segregation of Si at the grain boundaries was also investigated by Guo and Maier [27]. They reported that the grain boundary resistivity is insensitive to the amount of the Si segregation phase. To their understanding, a Si segregation phase does not influence the activation energy for the grain boundary transport, but rather narrows the available pathways. As the Si content in the multilayers investigated here was found to be low according to SIMS measurements (see section 7.2.1), the influence of Si segregation can be considered as small.
Because the grain boundary density in the thin film samples is mainly influenced by the deposition rate used in PLD and the subsequent temperature treatment, the above described properties of the grain boundaries should be a constant influence factor for all samples being prepared equally. Most importantly, they are not dependent on the number of individual layers in a multilayer sample.

### 9.2.6 The Role of Space Charge Regions

Since space charge regions have an extension in the order of the materials Debye length, they play a major role in systems with large Debye lengths, that means for a highly diluted carrier situation. The Debye length of highly doped YSZ is in the range of 0.1 nm [3]. Compared to this, the extension of strained lattice regions at the interfaces in YSZ can safely be considered much larger. However, Guo et al. noticed that the real extension of a space charge region may be exceeding the Debye length significantly due to segregation effects, being most severe

---

[3] The Debye length can be calculated according to the Debye-Hückel theory as

$$\lambda = \sqrt{\left(\frac{\varepsilon_0 \varepsilon_r kT}{2N_A e^2 I}\right)} \qquad I = \sum_i z_i^2 c_i \tag{9.11}$$

with $c_i$ being the concentration of charge carriers, $z_i$ their charge, $e$ the electron charge and $N_A$ Avogadro´s constant. $\varepsilon_r$ for YSZ is about 55-60 [27, 132, 133]. $c_i$ is interpreted as the extrinsically fixed concentration of oxygen vacancies, which is half the concentration of the $Y^{3+}$ ions. It is about $4.6 \cdot 10^3$ mol/m$^3$ for 9.5 mol-% YSZ with a density of about 6 g/cm$^3$ [128]. For 833 K, the Debye length yields to $\lambda \approx 0.14$ nm.

at temperatures below 500 °C (see section 9.2.5). But it was also mentioned that at higher temperatures, where the cations in YSZ are sufficiently mobile, the space charge width may be negligible [27]. Summing all these arguments up and considering that the number of grain boundaries in the multilayers is much larger than the number of layer-to-layer interfaces, the major influence of the space charge regions is limited to the grain boundary resistance. Only in multilayers with very thin individual layers and a high density of layer-to-layer interfaces, the space charge effects have to be taken into account. If $d$ is in the range of only a few nm, even non-trivial size effects may occur. Similar to the grain boundaries in YSZ, the YSZ | $RE_2O_3$ interfaces may then be assumed to be blocking. Especially in the system YSZ | $Lu_2O_3$, where the mismatch strain is small, a space charge effect can explain the low conductivity of multilayer samples with $d$ below 10 nm.

# 10 Open Questions - Further Required Investigations

To improve the results for the dependence of the conductivity on the interface density, the scattering of the measured conductivity values has to be reduced. This can be done by investigating a larger number of samples to rule out statistical errors. It is especially important for multilayers deposited at 2 Hz, because the number of investigated samples is far to small to draw reliable conclusions.

Considering the relationship between $\frac{\sigma_{\mathrm{int}}}{\sigma_{\mathrm{vol}}}$ and the misfit $f$, the same can be said. The value obtained in this work seems reasonable when compared to theory, but the investigation of more multilayer systems with different cubic and insulating rare earth oxides would improve the understanding of this relationship considerably. A promising rare earth oxide is $Gd_2O_3$, which has a quite large positive mismatch of 5.08 %. Some trials to deposit and investigate multilayers containing $Gd_2O_3$ have already been made within this work, but have not been presented because only one sample with crystalline layers was obtained and characterised by XRD and AC impedance measurements. The other samples contained amorphous layers or chipped off due to the high interfacial strain.

For the evaluation of the conductivities obtained for the different multilayers in this work, purely ionic conduction was assumed. This assumption was solely based on the well known conductivity properties of YSZ. However, an electronic contribution to the total conductivity can not be excluded for sure. To answer the question of the identity of the charge carriers, accurate measurements of the electromotoric force (EMF) have to be carried out using an oxygen concentration cell setup in which the multilayer works as electrolyte. If the measured EMF is not equal to the theoretic value obtained for the given oxygen chemical potential gradient, the difference is directly linked to the transference number for oxygen vacancies in the electrolyte phase. First attempts to measure the EMF of a multilayer have been made, but because of experimental problems so far delivered no results.

Another way to identify potential electronic conduction in the multilayers is to carry out Wagner-Hebb polarization cell measurements. By the choice of suitable electrodes (purely electronic or purely ionic conductivity), the flow of either the ionic or the electronic charge carriers can be blocked. The conductivity associated with the non-blocked charge carrier can then be measured.

Measurements in relation to the oxygen partial pressure have to be performed to analyse the defect chemistry in the multilayer systems, especially with respect to electronic charge carriers and electronic conduction in the rare earth oxides or the interfaces.
Diffusion experiments are a means to further investigate the preferred transport paths for oxygen in the samples. $^{18}O$ and $D_2^{18}O$ tracer experiments in connection with SIMS investigations are already in progress in a subsequent doctoral thesis. Those experiments will be performed with multilayers of different material combinations to vary the degree of disorder present at the interfaces.

In order to rule out influences of the grain boundaries and thereby to be able to measure the conductivity more accurately, an attempt may be made to deposit single crystalline multilayer films. A suitable method for this would be molecular beam epitaxy (MBE).

# 11 Conclusion

By the systematic investigation of two YSZ | $RE_2O_3$ multilayer systems with RE = Sc and Lu, which differ in the sign as well as the size of the lattice mismatch at the phase boundaries, the influence of misfit induced strain on the ionic conduction in thin film multilayer systems could be shown. The main results are:

- In the system YSZ | $Sc_2O_3$, where a compressive lattice strain in YSZ is caused by the negative misfit between the two phases, the conductivity decreases with increasing interface density. This agrees well with the theoretic expectations that increased local pressure or compressive strain cause a hindrance for ionic transport (see section 3.2.2 or for example [80–84, 86]).
- In the system YSZ | $Lu_2O_3$, where only a small misfit strain is present, no remarkable change of the conductivity with increasing interface density was observed. Because space charges should be of equal magnitude in both systems, this rules out the possibility that the conductivity change in the system YSZ | $Sc_2O_3$ is caused by a space charge effect.
- As the impurity level in both multilayer systems was low, blocking segregation phases at the interfaces appear not to play an important role.
- The structural characterisation offers valuable information: It delivers the basis for a better understanding of different strain relaxation mechanisms in thin electrolyte films on a rigid substrate. In addition to the emergence of dislocations, the development of a wavy layer morphology was identified as an important mechanism for strain release. Similar observations were made by JIN-PHILLIPP et al. [33].
- The role of electronic charge carriers in the multilayers has still to be clarified. The most promising investigations with regard to this are tracer diffusion experiments which will be accomplished in a subsequent work. These are expected to prove that the interfaces are indeed preferred transport paths for oxygen ions.

Summarising, the results of this work add information to those obtained by other authors on transport in related thin film or thin film multilayer systems (see section II or for example [5–8, 10–12, 27, 34]). A closely related work is that of A. PETERS on the two systems CSZ | $Al_2O_3$ and YSZ | $Y_2O_3$ [18, 19], in which, like in this work, an attempt is made to develop a model for the interfacial transport properties of ionic conductors, based on relations to structural parameters rather

than space charge effects. A common result of the present work and that of PETERS is that the influence of strain on ionic conduction lies in a range of 1 to maximal 2 orders of magnitude. The effect of disorder and a high dislocation density at the interfaces is somewhat larger, as shown in [18].
It is expected that structural effects on the conductivity are more pronounced in intrinsic ionic conductors with a lower bulk conductivity. But in these materials, the effect of space charges cannot be neglected due to a much larger Debye length.

The results of this work may help to improve the design of micro- and nanostructured thin film devices such as sensors, thin film solar cells or other semiconductor applications by influencing the choice of the utilised materials with respect to their structural relation and lattice misfit.

# 12 Appendix

## 12.1 Fourier Filtering Details

The following picture shows the FFT result of the HRTEM micrograph in figure 7.22, excluding the substrate. The reflections used for creating the filtered image on the right hand side of this figure are marked with circles. The [001] reflections originate from the lower crystallite in figure 7.22. Both crystallites visible in the micrograph are oriented along the [111] direction, so the associated reflections appear at identical positions in the FFT. However, the azimuthal orientation of the crystallites is mirror-inverted.

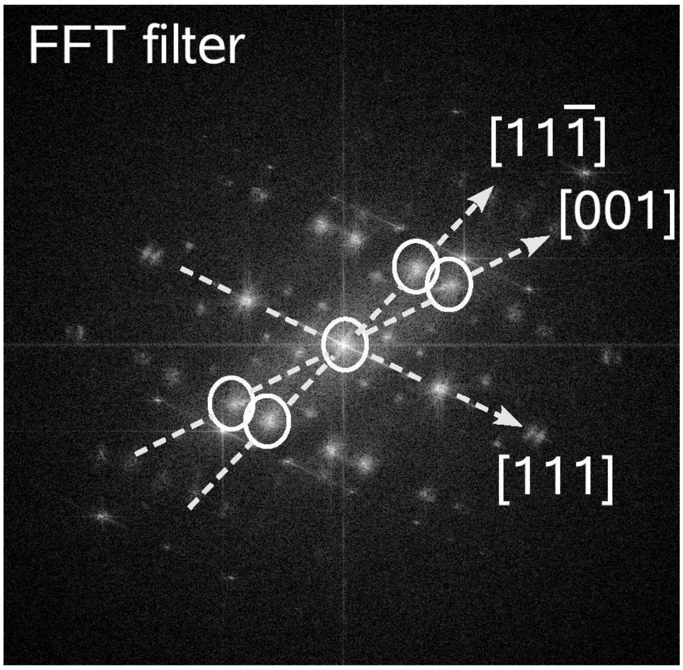

**Figure 12.1:** FFT result of figure 7.22.

## 12.2 TOF-SIMS: Additional Graphical Material

The following figure shows a 3D reconstruction of the $Ca^+$ signal measured by dynamic TOF-SIMS in the sample YLu3 (see section 7.2.2). The signal intensity is brightness encoded.

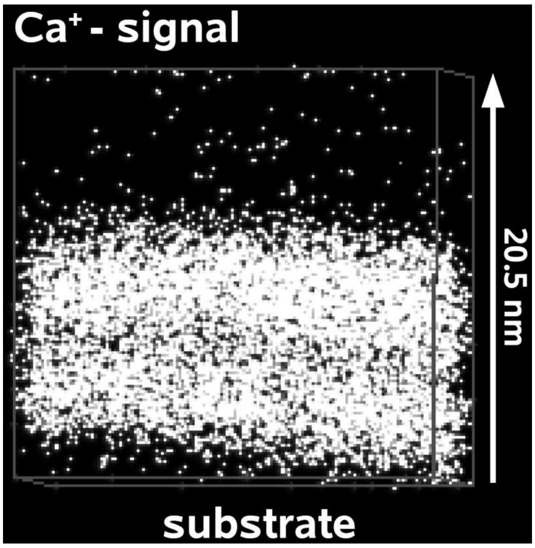

**Figure 12.2:** 3D reconstruction of the dynamic SIMS result for the sample YLu3.

## 12.3 HRTEM Mictrographs

In the following, some HRTEM micrographs from section 7.2.1 are shown enlarged to make details like the dislocation arrangement better visible.

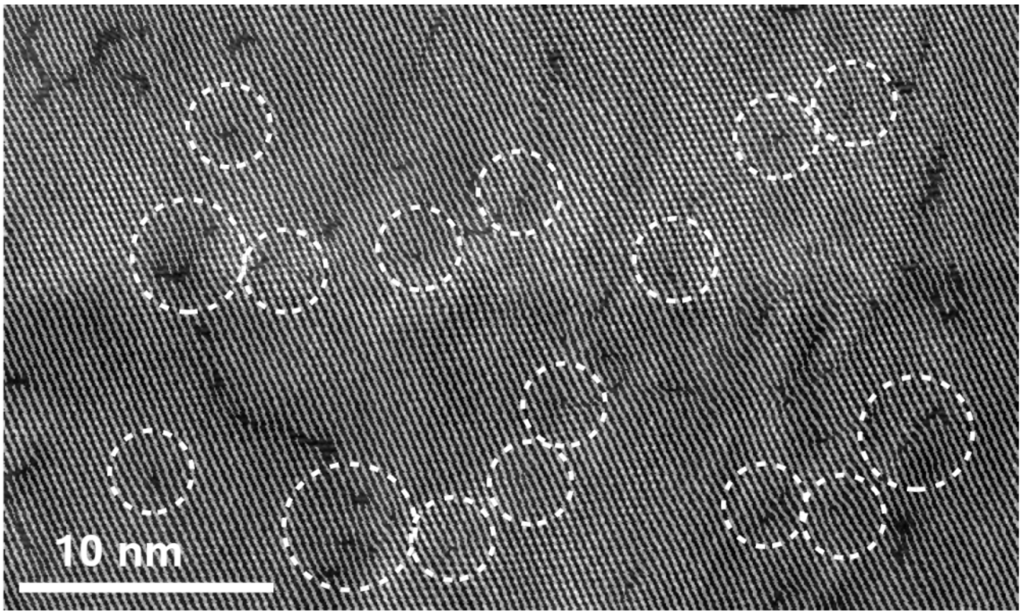

**Figure 12.3:** Enlarged region of a Fourier filtered micrograph as shown in figure 7.18. A phase boundary between $Sc_2O_3$ (upper layer) and YSZ (lower layer) in the sample YSc50-3 is shown. Some dislocations are highlighted.

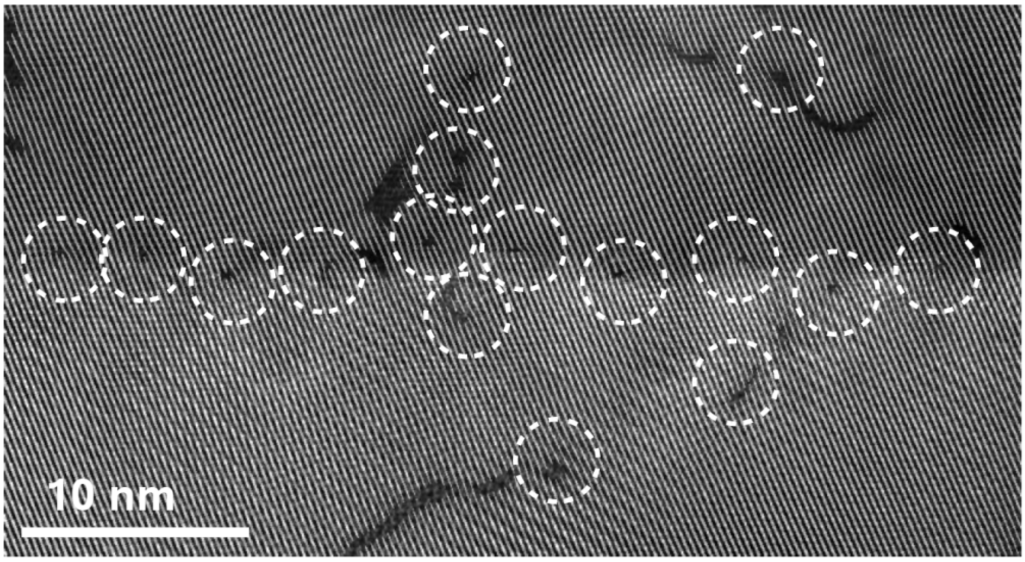

**Figure 12.4:** Enlarged region of a Fourier filtered micrograph of the sample YSc50-3, as shown in figure 7.18. A region at the substrate is shown. Upper layer: YSZ; lower layer: $Sc_2O_3$. The dislocations are highlighted.

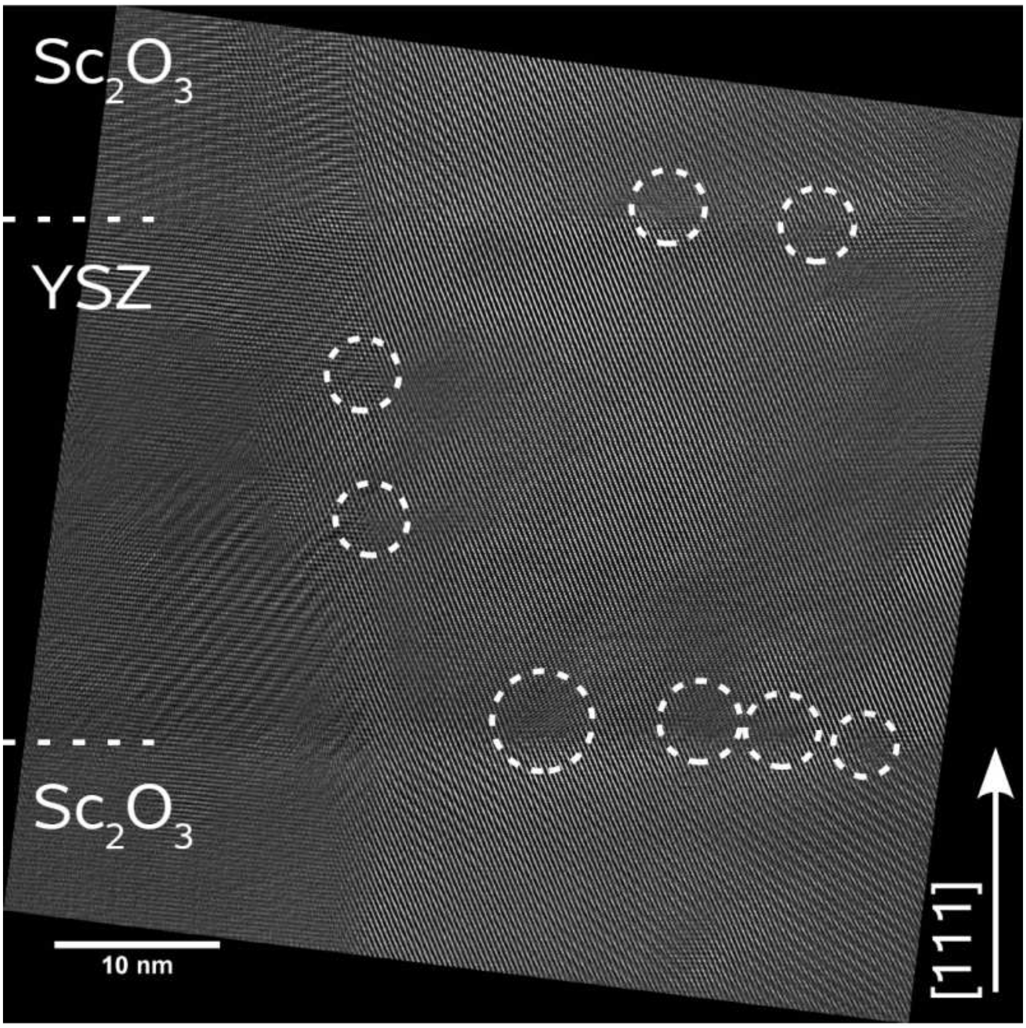

**Figure 12.5:** Unmachined HRTEM micrograph from an area in the sample YSc50-3, as shown in figure 7.19a). The phase boundaries are marked by dashed lines.

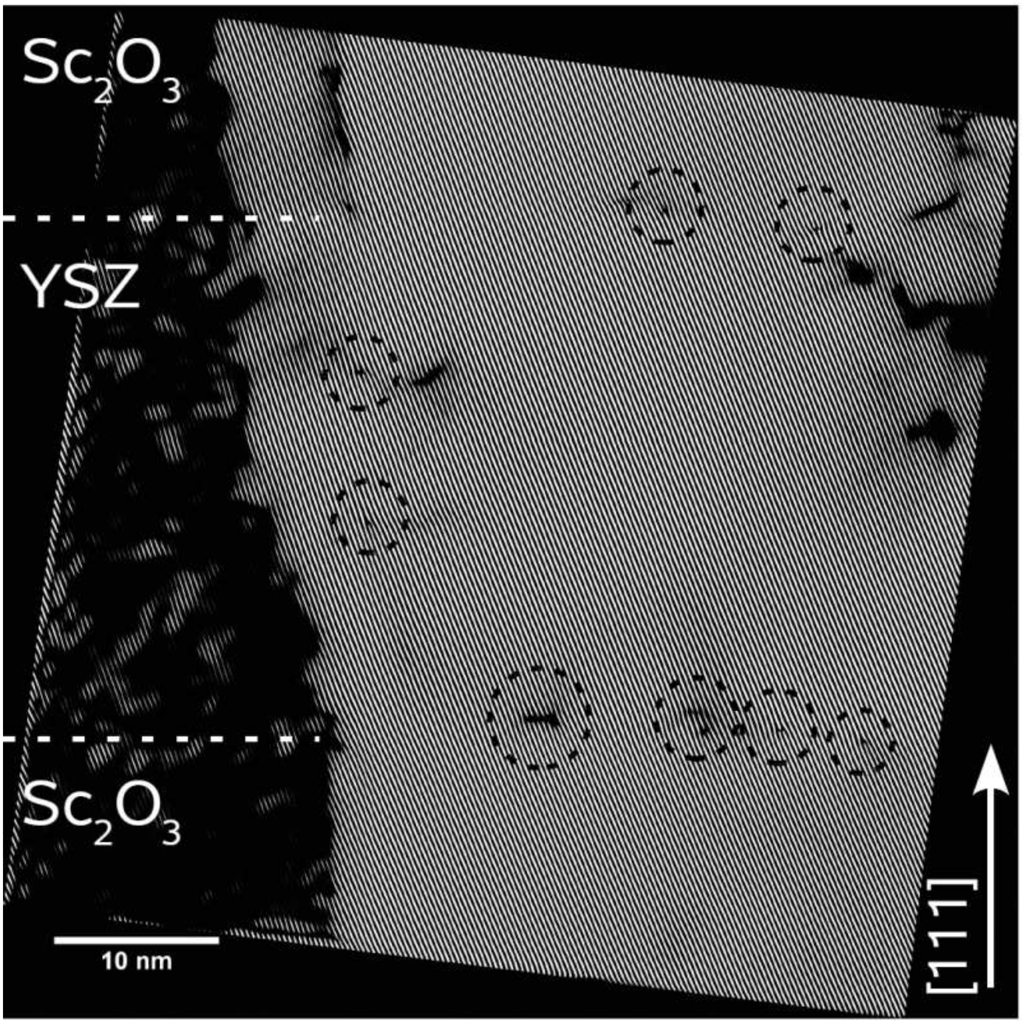

**Figure 12.6:** [001] filtered micrograph, as shown in figure 7.19b). Dislocations are highlighted.

## 12.4 Sample Data

In the following tables, data of the preparation and the structural parameters of the multilayers are presented. If two values are given, the upper one refers to investigations before heat treatment, the lower one denotes the value after heat treatment. Values denoted with "-" were not measured.

For the system YSZ | $Lu_2O_3$, the (111) YSZ and (222) $Lu_2O_3$ reflection could not be separated in the XRD measurements. Therefore, only a coarse lattice parameter for YSZ was calculated and no FWHM value was determined.

If not denoted otherwise in the comment column, all samples were deposited as described in the experimental section, see chapter 6. The number of pulses per layer refer to all YSZ and $Sc_2O_3$ layers but the first one, which was typically deposited with 500 pulses of rare earth oxide. $l$ and $d$ refer to the sample dimensions as defined in figure 8.2a).

**Multilayers YSZ | $Sc_2O_3$, deposited at 10 Hz.**

| Name | $n$ | $l \times b$ [$mm^2$] | Pulses per Layer | $d$ YSZ | $a$ YSZ [Å] | FWHM YSZ | $a$ $Sc_2O_3$ [Å] | FWHM $Sc_2O_3$ | Comment |
|---|---|---|---|---|---|---|---|---|---|
| YSc2 | 2 | - | ? | 70-80 | 5.242<br>5.233 | 0.5185<br>0.5170 | 9.881<br>9.823 | 0.3100<br>0.3061 | student project |
| YSc5 | 5 | 7.47 × 2.24 | 10000 | ca. 252 | 5.215<br>5.165 | 0.8790<br>0.4919 | 9.883<br>9.877 | 0.7930<br>0.7228 | |
| YSc20 | 20 | 7.68 × 1.88 | 720 | 43 | 5.207<br>5.195 | 0.8085<br>0.6315 | 9.968<br>9.930 | 0.4466<br>0.4225 | by A. Rein |
| YSc30 | 30 | 7.65 × 2.05 | 1667 | 20 | 5.222<br>5.192 | 0.8613<br>0.7205 | 9.857<br>9.816 | 0.5915<br>0.3993 | 24 h annealed, A. Rein |
| YSc40 | 40 | 7.42 × 1.75 | 1250 | 23 | 5.221<br>5.163 | 0.8490<br>0.8526 | 9.861<br>9.836 | 0.6213<br>0.6374 | |
| YSc60-4 | 60 | 8.17 × 1.87 | 834 | 30 | 5.200<br>5.172 | 0.7417<br>0.5636 | 10.000<br>9.925 | 0.9842<br>0.8135 | |
| YSc70 | 70 | - | 715 | 18 | 5.246<br>5.193 | 0.9816<br>0.9515 | 9.965<br>9.966 | 0.7080<br>0.7188 | irregular layers |
| YSc70-2 | 70 | 7.93 × 1.78 | 715 | 18 | 5.187<br>5.175 | 0.8296<br>0.8715 | 9.907<br>9.906 | 0.6388<br>0.6324 | 2nd preparation |
| YSc80-4 | 80 | 7.70 × 1.96 | 625 | 17 | 5.184<br>5.181 | 0.9033<br>0.7347 | 9.801<br>9.857 | 0.6042<br>0.5801 | |
| YSc100 | 100 | - | 360 | 8 | 5.221<br>5.155 | 1.3168<br>0.9571 | 9.957<br>9.900 | 0.8648<br>0.7739 | sample destroyed |
| YSc1002 | 100 | 7.68 × 1.50 | 500 | 16 | 5.228<br>5.180 | 1.0609<br>0.7982 | 9.997<br>9.920 | 1.0053<br>0.8307 | 2nd preparation |
| YSc120 | 120 | 7.79 × 1.90 | 417 | 24 | 5.216<br>5.186 | 0.7147<br>0.6406 | 9.873<br>9.861 | 0.6874<br>0.6900 | |
| YSc150 | 150 | 7.27 × 1.81 | 417 | 3-4 | - | - | - | - | broken |
| YSc150-2 | 150 | 7.58 × 2.08 | 417 | 11 | - 5.205 | - 0.7712 | - 10.047 | - 1.0765 | 2nd preparation |

**Table 12.1:**

**Multilayers YSZ | $Sc_2O_3$, deposited at 2 Hz.**

| Name | $n$ | $l \times b$ [$mm^2$] | Pulses per Layer | $d$ YSZ | $a$ YSZ [Å] | FWHM YSZ | $a$ $Sc_2O_3$ [Å] | FWHM $Sc_2O_3$ | Comment |
|---|---|---|---|---|---|---|---|---|---|
| YSc20-3 | 20 | - | 2500 | - | - | - | - | - | very irregular layers |
| YSc20-3(2) | 20 | - | 2500 | - | - | - | - | - | 2nd preparation, bad crystallinity |
| YSc30-3 | 30 | 7.57 × 1.66 | 1667 | 58 | 5.213<br>5.160 | 0.8743<br>0.5626 | 9.850<br>9.836 | 0.3963<br>0.4005 | |
| YSc40-3 | 40 | 7.64 × 2.02 | 1250 | 34 | 5.232<br>5.174 | 0.7353<br>0.5554 | 9.863<br>9.852 | 0.4202<br>0.4011 | maybe contaminated |
| YSc50-3 | 50 | 7.77 × 2.02 | 1000 | 34 | 5.219<br>5.171 | 0.7337<br>0.6449 | 9.876<br>9.856 | 0.4354<br>0.4120 | |
| YSc70-3 | 70 | 7.90 × 1.65 | 715 | 20 | 5.189<br>5.149 | 0.7909<br>0.6885 | 9.857<br>9.854 | 0.4545<br>0.4478 | |
| YSc1003 | 100 | - | 500 | - | 5.212<br>5.180 | 0.8388<br>0.7796 | 9.862<br>9.874 | 0.6614<br>0.6548 | broken |
| YSc1003-2 | 100 | 7.83 × 1.84 | 500 | 15 | 5.192<br>5.193 | 0.7567<br>0.7639 | 9.865<br>9.872 | 0.7699<br>0.7556 | 2nd preparation |

**Table 12.2:**

### Multilayers YSZ | $Lu_2O_3$, deposited at 10 Hz.

| Name | $n$ | $l \times b$ [mm$^2$] | Pulses per Layer | $d$ YSZ | $a$ YSZ [Å] | $a$ $Lu_2O_3$ [Å] | Comment |
|---|---|---|---|---|---|---|---|
| YLu5 | 5 | - | 10000 | ca. 288 | 5.188<br>5.173 | 10.375<br>10.347 | 1st layer: YSZ |
| YLu5-2 | 5 | 8.50 × 1.57 | 10000 | ca. 211 | 5.234<br>5.200 | 10.468<br>10.400 | |
| YLu10-2 | 10 | 7.60 × 1.77 | 5000 | 152 | 5.255<br>5.231 | 10.510<br>10.462 | |
| YLu30 | 30 | 8.26 × 2.10 | 1667 | 25 | 5.235<br>5.219 | 10.469<br>10.438 | 1st layer: YSZ |
| YLu304 | 30 | 7.40 × 1.73 | 1667 | 51.7 | 5.243<br>5.231 | 10.486<br>10.462 | |
| YLu40 | 40 | 7.41 × 1.53 | 1250 | 33.7 | 5.239<br>5.221 | 10.477<br>10.442 | contaminated |
| YLu50 | 50 | - | 720 | 7.8 | | | by A. Rein |
| YLu50(2) | 50 | 7.64 × 2.15 | 1000 | 23.5 | 5.236<br>5.195 | 10.472<br>10.390 | 1st layer: 800 counts, 200 mJ |
| YLu504 | 50 | 7.61 × 1.78 | 1000 | 20.7 | 5.237<br>5.221 | 10.474<br>10.442 | |
| YLu60 | 60 | 7.40 × 1.94 | 834 | 30 | 5.216<br>5.207 | 10.433<br>10.414 | contaminated |
| YLu604 | 60 | - | 834 | | 5.237<br>5.221 | 10.474<br>10.442 | broken |
| YLu70 | 70 | 7.25 × 1.60 | 715 | 20 | 5.221<br>5.216 | 10.442<br>10.431 | |
| YLu80 | 80 | 7.35 × 1.78 | 625 | 18.2 | 5.217<br>5.160 | 10.434<br>10.319 | contaminated |
| YLu804 | 80 | 7.46 × 1.65 | 625 | 13.9 | 5.232<br>5.216 | 10.464<br>10.431 | |
| YLu1002 | 100 | 8.19 × 1.54 | 500 | ca. 6 | 5.209<br>5.187 | 10.419<br>10.373 | 1st layer: YSZ |
| YLu1004 | 100 | 7.19 × 1.65 | 500 | 16.9 | 5.224<br>5.200 | 10.449<br>10.400 | broken |
| YLu150 | 150 | 7.85 × 1.85 | 333 | 3.2 | 5.209<br>5.159 | 10.417<br>10.317 | |

**Table 12.3:**

### Multilayers YSZ | $Lu_2O_3$, deposited at 2 Hz.

| Name | $n$ | $l \times b$ [$mm^2$] | Pulses per Layer | $d$ YSZ | $a$ YSZ [Å] | $a$ $Lu_2O_3$ [Å] | Comment |
|---|---|---|---|---|---|---|---|
| YLu3 | 2 | - | 34000 | ca. 1300 | 5.289<br>5.216 | 10.578<br>10.431 | 1st layer: YSZ |
| YLu20 | 10 | 7.45 × 1.82 | 2500 | 70.6 | 5.248<br>5.215 | 10.496<br>10.429 | |
| YLu303 | 30 | 7.99 × 2.27 | 1000 | 75.6 | 5.235<br>5.216 | 10.469<br>10.431 | |
| YLu503 | 50 | 7.67 × 2.26 | 1000 | 22 | 5.227<br>5.222 | 10.454<br>10.445 | |
| YLu703 | 70 | 7.29 × 1.52 | 1000 | 22 | 5.227<br>5.219 | 10.454<br>10.438 | |
| YLu1003 | 100 | 7.38 × 1.68 | 1000 | 10 | 5.237<br>5.207 | 10.473<br>10.414 | |

**Table 12.4:**

## 12.5 List of Abbreviations and Symbols

| | |
|---|---|
| $A$ | Area |
| $a$ | Lattice parameter |
| AFM | Atomic Force Microscopy |
| $b$ | Sample depth |
| $C$ | Capacity in F |
| CPE | Constant phase element |
| $d$ | Layer thickness |
| $\varepsilon$ | strain |
| $\varepsilon_r$ | dielectric constant |
| $\varepsilon_0$ | dielectric vacuum constant $= 8.85419 \cdot 10^{-12}$ A s $\mathrm{V}^{-1}$ $\mathrm{m}^{-1}$ |
| EBSD | Electron Backscatter Diffraction |
| EELS | Electron Energy-Loss Spectroscopy |
| EDX | Energy Dispersive X-ray Analysis |
| EIS | Electrochemical Impedance Spectroscopy |
| EMF | Electromotive Force in V |
| F | Faraday constant $= F \cdot e = 9.64846 \cdot 104\ C \cdot mol^{-1}$ |
| $f$ | Misfit |
| $\varphi$ | Galvani potential |
| FFT | Fast Fourier Transformation |
| FWHM | Full Width at Half Maximum value of a signal |
| G | second Lamé constant (shear modulus) |
| $I$ | Electric current in A |
| $i$ | Current density $I/A$ |
| $j_i$ | Flux of the component i |
| $l$ | Sample width |
| $L_i$ | Transport coefficient of i |
| $\lambda$ | first Lamé constant |
| M | Biaxial Modulus $\mathrm{M} = \mathrm{Y}/(1-\nu)$ |
| $\mu_i$ | Chemical potential of i |
| $\tilde{\mu}_i$ | Electrochemical potential of i |
| $n$ | Number of individual YSZ layers within a multilayer |
| PLD | Pulsed Laser Deposition |
| R | Universal gas constant $= 8.314472 J \cdot \mathrm{mol}^{-1} \cdot K^{-1}$ |
| $R$ | Resistance in Ohm ($\Omega$) |
| $(RC)$ | Parallel connection of $R$ and $C$ |
| $\mathrm{RE_2O_3}$ | Rare earth oxide |
| $\sigma$ | Specific conductivity in S/cm; stress |
| SAED | Selected-Area Electron Diffraction |
| SEM | Scanning Electron Microscopy |
| SIMS | Secondary Ion Mass Spectrometry |
| STEM | Scanning Transmission Electron Microscopy |

| | |
|---|---|
| $T$ | Temperature |
| $\tau$ | Relaxation time |
| TEM | Transmission Electron Microscopy |
| $U$ | Voltage |
| $\nu$ | Frequency; Poisson´s ratio $= -\varepsilon_{transverse}/\varepsilon_{axial}$ |
| $\omega$ | Radial frequency |
| XRD | X-Ray Diffraction |
| Y | Young´s modulus $= \sigma/\varepsilon$ |
| YSZ | Yttria stabilized zirconia |
| $Z$ | Impedance |
| $Z'$ | Real part of the impedance (also: Im $(Z)$) |
| $Z''$ | Imaginary part of the impedance (also: Re $(Z)$) |

# Bibliography

[1] Jiang, S. & Wagner, J. B. A theoretical model for composite electrolytes – I. space charge layer as a cause for charge-carrier enhancement. *J. Phys. Chem. Solids* **56**, 1101–1111 (1995).

[2] Indris, S., Heitjans, P., Ulrich, M. & Bunde, A. Ac and dc conductivity in nano- and microcrystalline $Li_2O$: $B_2O_3$ composites: Experimental results and theoretical models. *Z. Phys. Chem.* **219**, 89–103 (2005).

[3] Albinet, G., Debierre, J. M., Knauth, P., Lambert, C. & Raymond, L. Enhanced conductivity in ionic conductor-insulator composites: numerical models in two and three dimensions. *Eur. Phys. J. B* **22**, 421–427 (2001).

[4] Beniere, F. & Reddy, K. V. Enhanced ionic transport in NaCl-$Al_2O_3$ heterogeneous electrolytes. *J. Phys. Chem. Solids* **60**, 839–847 (1999).

[5] Kosacki, I., Rouleau, C. M., Becher, P. F., Bentley, J. & Lowndes, D. H. Surface/interface-related conductivity in nanometer thick YSZ films. *Electrochem. Solid State Lett.* **7(12)**, A459–A461 (2004).

[6] Kosacki, I., Rouleau, C. M., Becher, P. F., Bentley, J. & Lowndes, D. H. Nanoscale effects on the ionic conductivity in highly textured YSZ thin films. *Solid State Ionics* **176**, 1319–1326 (2005).

[7] Guo, X. *et al.* Ionic conduction in zirconia films of nanometer thickness. *Acta Mater.* **53(19)**, 5161–5166 (2005).

[8] Karthikeyan, A., Chang, C.-L. & Ramanathan. High temperature conductivity studies on nanoscale yttria-doped zirconia thin films and size effects. *Appl. Phys. Lett.* **89(18)**, 183116 (2006).

[9] Lubben, D. & Modine, F. A. Enhanced ionic conduction mechanisms at LiI/$Al_2O_3$ interfaces. *J. Appl. Phys.* **80**, 5150–5157 (1996).

[10] Sata, N., Eberman, K., Eberl, K. & Maier, J. Mesoscopic fast ion conduction in nanometre-scale planar heterostructures. *Nature* **408**, 946–949 (2000).

[11] Azad, S. *et al.* Nanoscale effects on ion conductance of layer-by-layer structures of gadolinia-doped ceria and zirconia. *Appl. Phys. Lett.* **86**, 131906/1–131906/3 (2005).

[12] Karthikeyan, A. & Ramanathan, S. Temperature-dependent interfacial carrier transport in low-dimensional oxides using ionic conductor-insulator (YDZ-$SiO_2$) superlattices. *J. Appl. Phys.* **104**, 124314 (2008).

[13] Guo, X. & Maier, J. Inionically conducting two-dimensional heterostructures. *Adv. Mater.* **21**, 2619–2631 (2009).

[14] Maier, J. Point-defect thermodynamics and size effects. *Solid State Ionics* **131**, 12–22 (2000).

[15] Maier, J. Transport in electroceramics: micro- and nano-structural aspects. *J. Eur. Ceram. Soc.* **24**, 1251–1257 (2004).

[16] Maier, J. Ionic transport in nano-sized systems. *Solid State Ionics* **175**, 7–12 (2004).

[17] Maier, J. Nanoionics: ion transport and electrochemical storage in confined systems. *Nature Materials* **4**, 805–815 (2005).

[18] Peters, A., Korte, C., Hesse, D., Zakharov, N. & Janek, J. Ionic conductivity and activation energy for oxygen ion transport in superlattices - the multilayer system CSZ ($ZrO_2$+CaO)/$Al_2O_3$. *Solid State Ionics* **178**, 67–76 (2007).

[19] Peters, A., Korte, C., Janek, J., Hesse, D. & Zakharov, N. Ionic conductivity and activation energy for oxygen ion transport in superlattices - the semicoherent multilayer system YSZ ($ZrO_2$ + 9.0 mol% $Y_2O_3$)/$Y_2O_3$. *Phys. Chem. Chem. Phys.* **10**, 4623–4635 (2008).

[20] Noddack, W., Walch, H. & Dobner, W. Leitfähigkeitsmessungen an Oxyden der Seltenen Erden. I. *Z. Phys. Chem.* **211**, 180–193 (1959).

[21] Tare, V. B. & Schmalzried, H. Ionen- und Elektronenleitung in einigen seltenen Erdoxiden. *Z. Phys. Chemie* **43**, 30 (1964).

[22] Rao, G. V. S., Ramdas, S., Mehrotra, P. N. & Rao, C. N. R. Electrical transport in rare-earth oxides. *J. Solid State Chem.* **2**, 377–384 (1970).

[23] Yun, S. H., Kim, K. & Choi, J. S. Defect structure and electrical conductivity of pure and doped lutetium sesquioxides. *J. Phys. Chem. Solids* **50**, 291–296 (1989).

[24] Uvarov, N. F. Estimation of composites conductivity using a general mixing rule. *Solid State Ionics* **136-137**, 1267 – 1272 (2000).

[25] Yuan, S. L. *et al.* Percolation model of the temperature dependence of resistance in doped manganese perovskites. *Applied Physics Letters* **79**, 90–92 (2001).

[26] Korte, C. Zur Wechselwirkung von Ionentransport und Mikrostruktur in inneren Grenzflächen. Habilitationsschrift; Justus-Liebig Universität Gießen (2008).

[27] Guo, X. & Maier, J. Grain boundary blocking effect in zirconia: A schottky barrier analysis. *J. Electrochem. Soc.* **148**, E121–E126 (2001).

[28] Guo, X. & Waser, R. Space charge concept for acceptor-doped zirconia and ceria and experimental evidences. *Solid State Ionics* **173**, 63–67 (2004).

[29] Terwilliger, C. D. & Chiang, Y. M. Size-dependent solute segregation and total solubility in ultrafine polycrystals: Ca in $TiO_2$. *Acta Metall. Mater.* **43**, 319–328 (1995).

[30] Chiang, Y., Lavik, E. & Blom, D. Defect thermodynamics and electrical properties of nanocrystalline oxides: pure and doped $CeO_2$. *Nanostruct. Mater.* **9**, 633–642 (1997).

[31] Maier, J. Ionic conduction in space charge regions. *Progr. Solid State Chem.* **23**, 171–263 (1995).

[32] Karthikeyan, A., Tsuchiya, M. & Ramanathan, S. Studies on structure-electrochemical conduction relationships in doped-zirconia thin films. *Solid State Ionics* **179**, 1234–1237 (2008).

[33] Jin-Phillipp, N. Y. *et al.* Structures of $BaF_2$-$CaF_2$ heterolayers and their influences on ionic conductivity. *J. Chem. Phys.* **120**, 2375–2381 (2004).

[34] Wang, C. M. *et al.* Microstructure of $ZrO_2/CeO_2$ hetero-multi-layer films grown on YSZ substrate. *Acta Mater.* **7**, 1921–1929 (2005).

[35] Wang, C. M. *et al.* Distribution of oxygen vacancies and gadolinium dopants in $ZrO_2$–$CeO_2$ multi-layer films grown on $\alpha$-$Al_2O_3$. *Solid State Ionics* **177**, 1299–1306 (2006).

[36] Ikeda, S., Sakurai, O., Uematsu, K., Mizutani, N. & Kato, M. Electrical conductivity of yttria-stabilized zirconia single crystals. *J. Mater. Sci.* **20**, 4593–4600 (1985).

[37] Filal, M., Petot, C., Mokchah, M., Chateau, C. & Carpentier, J. L. Ionic conductivity of yttrium-doped zirconia and the "composite effect". *Solid State Ionics* **80**, 27–35 (1995).

[38] Weller, M. *et al.* Oxygen mobility in yttria-doped zirconia studied by internal friction, electrical conductivity and tracer diffusion experiments. *Solid State Ionics* **175**, 409–413 (2004).

[39] Garcia-Barriocanal, J. *et al.* Colossal ionic conductivity at interfaces of epitaxial $ZrO_2$:$Y_2O_3$/$SrTiO_3$ heterostructures. *Science* **321**, 676–680 (2008).

[40] Bruce, P. G. (ed.) *Solid State Electrochemistry* (Cambridge University Press, Great Britain, Cambridge, 1997).

[41] West, A. R. *Solid State Chemistry and its Applications* (John Wiley and Sons, Chichester, 1992).

[42] Sutton, A. P. & Balluffi, R. W. *Interfaces in Crystalline Materials*. Monographs on the Physics and Chemistry of Materials, 51 (Oxford University Press, USA, 1997).

[43] Wolf, D. *Materials Interfaces: Atomic-Level Structure and Properties* (Chapman and Hall, London, 1992).

[44] Hull, D. & Bacon, D. J. *Introduction to Dislocations*, vol. 37 of *International Series on Materials Science and Technology* (Pergamon Press, Oxford, 1984), 3. edn.

[45] Zepeda-Ruiz, L. A., Maroudas, D. & Weinberg, W. H. Theoretical study of the energetics, strain fields, and semicoherent interface structures in layer-by-layer semiconductor heteroepitaxy. *J. Appl. Phys.* **85**, 3677–3695 (1999).

[46] Freund, L. B. & Nix, W. D. A critical thickness condition for a strained compliant substrate/epitaxial film system. *Appl. Phys. Lett.* **69**, 173–175 (1996).

[47] Lo, Y. H. New approach to grow pseudomorphic structures over the critical thickness. *Appl. Phys. Lett.* **59**, 2311–2313 (1991).

[48] MarÉe, P. M. J. *et al.* Generation of misfit dislocations in semiconductors. *J. Appl. Phys.* **62**, 4413–4420 (1987).

[49] Merwe, J. H. V. D. Crystal interfaces. part II. finite overgrowths. *J. Appl. Phys.* **34**, 123–127 (1963).

[50] Merwe, J. H. V. D. Erratum: Crystal interfaces: Part II. finite overgrowths. *J. Appl. Phys.* **34**, 3420–3420 (1963).

[51] Matthews, J. W. & Blakeslee, A. E. Defects in epitaxial multilayers I. misfit dislocations. *J. Cryst. Growth* **27**, 118–125 (1974).

[52] Matthews, J. W. & Blakeslee, A. E. Defects in epitaxial multilayers II. dislocation pile-ups, threading dislocations, slip lines and cracks. *J. Cryst. Growth* **29**, 273–280 (1975).

[53] Matthews, J. W. & Blakeslee, A. E. Defects in epitaxial multilayers III. preparation of almost perfect multilayers. *J. Cryst. Growth* **32**, 265–273 (1976).

[54] Matthews, J. *Dislocation in Solids* (North Holland, Amsterdam, 1979).

[55] Eshelby, J. D. *Dislocations in Solids*, vol. 1, chap. 3, 167 (North-Holland, Amsterdam, 1979).

[56] People, R. & Bean, J. C. Calculation of critical layer thickness versus lattice mismatch for $\mathrm{Ge}_x\mathrm{Si}_{1-x}/\mathrm{Si}$ strained-layer heterostructures. *Appl. Phys. Lett.* **47**, 322–324 (1985).

[57] People, R. & Bean, J. C. Erratum: Calculation of critical layer thickness versus lattice mismatch for $\mathrm{Ge}_x\mathrm{Si}_{1-x}/\mathrm{Si}$ strained-layer heterostructures [appl. phys. lett. 47, 322 (1985)]. *Appl. Phys. Lett.* **49**, 229 (1986).

[58] Nabarro, F. R. N. *Theory of Crystal Dislocations* (Clarendon, Oxford, 1967).

[59] Huang, F. Y. Effect of strain transfer on critical thickness for epitaxial layers grown on compliant substrate. *Appl. Phys. Lett.* **76**, 3046–3048 (2000).

[60] Chidambarrao, D., Srinivasan, G. R., Cunningham, B. & Murthy, C. S. Effects of Peierls barrier and epithreading dislocation orientation on the critical thickness in heteroepitaxial structures. *Appl. Phys. Lett.* **57**, 1001–1003 (1990).

[61] Fox, B. A. & Jesser, W. A. The effect of frictional stress on the calculation of critical thickness in epitaxy. *J. Appl. Phys.* **68**, 2801–2808 (1990).

[62] Etsell, T. H. & Flengas, S. N. Electrical properties of solid oxide electrolytes. *Chem. Rev.* **70**, 339–376 (1970).

[63] Verkerk, M. J., Middlehuis, B. J. & Burggraaf, A. J. Effect of grain boundaries on the conductivity of high-purity zirconium oxide - yttrium oxide ceramics. *Solid State Ionics* **6**, 159–170 (1982).

[64] Guo, X. X. & Maier, J. Ionic conductivity of epitactic MBE-grown $\mathrm{BaF}_2$ films. *Surf. Sci.* **549**, 211–216 (2004).

[65] Liang, C. C., Mallory, P. R. & Co. Conduction characteristics of the lithium iodide-aluminum oxide solid electrolytes. *J. Electrochem. Soc.* **120**, 1289–1292 (1973).

[66] Sata, N., Jin-Philipp, N. Y., Eberl, K. & Maier, J. Enhanced ionic conductivity and mesoscopic size effects in structures of $\mathrm{BaF}_2$ and $\mathrm{CaF}_2$. *Solid State Ionics* **154-155**, 497–502 (2002).

[67] Chowdhary, P. & Jr., J. W. The influence of a dispersion of $\mathrm{Al}_2\mathrm{O}_3$ on the second- or higher-order phase transition temperature in AgI. *Mater. Lett.* **3**, 78 – 79 (1985).

[68] Maier, J. Defect chemistry and conductivity effects in heterogeneous solid electrolytes. *J. Electrochem. Soc.* **134**, 1524–1535 (1987).

[69] Wagner, C. The electrical conductivity of semiconductors involving inclusions of another phase. *J. Phys. Chem. Solids* **33**, 1051–1059 (1972).

[70] Jamnik, J. & Maier, J. Defect chemistry and chemical transport involving interfaces. *Solid State Ionics* **119**, 191–198 (1999).

[71] Maier, J. Nano-sized mixed conductors (Aspects of nano-ionics. Part III). *Solid State Ionics* **148**, 367–374 (2002).

[72] Maier, J. Mass storage in space charge regions of nano-sized systems (Nano-ionics. Part V). *Faraday Discuss.* **134**, 51–56 (2007).

[73] Maier, J. Space charge regions in solid two-phase systems and their conduction contribution–I. conductance enhancement in the system ionic conductor-'inert' phase and application on AgCl:$Al_2O_3$ and AgCl:$SiO_2$. *J. Phys. Chem. Solids* **46**, 309 – 320 (1985).

[74] Guo, X., Fleig, J. & Maier, J. Separation of electronic and ionic contributions to the grain boundary conductivity in acceptor-doped $SrTiO_3$. *J. Electrochem. Soc.* **148**, J50–J53 (2001).

[75] Maier, J. Defect chemistry at interfaces. *Solid State Ionics* **70-71**, 43–51 (1994).

[76] Maier, J. Defect chemistry and ion transport in nanostructured materials part II. Aspects of nanoionics. *Solid State Ionics* **157**, 327–334 (2003).

[77] Nachtrieb, N. H., Resing, H. A. & Rice, S. A. Effect of pressure on self-diffusion in lead. *J. Chem. Phys.* **31**, 135–138 (1959).

[78] Ott, A. Effect of hydrostatic pressure on the diffusion of silver in indium. *Physica Status Solidi B* **43**, 213–219 (1971).

[79] Antonelli, A. & Bernholc, J. Pressure effects on self-diffusion in silicon. *Phys. Rev. B: Condens. Matter* **40**, 10643–10646 (1989).

[80] Kim, K. S. & Paik, W.-K. Effects of temperature and pressure on conductance of solid electrolyte, rubidium silver iodide. *J. Chem. Eng. Data* **20**, 356–359 (1975).

[81] Hoshino, H., Yanagiya, H. & Shimoji, M. Effect of hydrostatic pressure on the electrical conductivity of $Ag_3SBr$ and $\beta$-$Ag_3SI$. *J. Chem. Soc., Faraday Trans. 1* **70**, 281–286 (1974).

[82] Samara, G. A. Pressure and temperature dependences of the ionic conductivities of cubic and orthorhombic lead fluoride ($PbF_2$). *J. Phys. Chem. Solids* **40**, 509–522 (1979).

[83] Oberschmidt, J. & Lazarus, D. Ionic conductivity and activation volumes in the lead halides $PbCl_2$, $PbBr_2$, and $PbI_2$. *Phys. Rev. B: Condens. Matter* **21**, 5813–5822 (1980).

[84] Pierce, C. B. Effect of hydrostatic pressure on ionic conductivity in doped single crystals of sodium chloride, potassium chloride, and rubidium chloride. *Phys. Rev.* **123**, 744–754 (1961).

[85] Cowern, N. E. B., Zalm, P. C., van der Sluis, P., Gravesteijn, D. J. & de Boer, W. B. Diffusion in strained Si(Ge). *Phys. Rev. Lett.* **72**, 2585–2588 (1994).

[86] Yoon, D. N. & Lazarus, D. Pressure dependence of ionic conductivity in KCl, NaCl, KBr, and NaBr. *Phys. Rev. B: Condens. Matter* **5**, 4935–4945 (1972).

[87] Aziz, M. J. Thermodynamics of diffusion under pressure and stress: Relation to point defect mechanisms. *Appl. Phys. Lett.* **70**, 2810–2812 (1997).

[88] Radzilowski, R. H. & Kummer, J. T. The hydrostatic pressure dependence of the ionic conductivity of $\beta$-aluminas. *J. Electrochem. Soc.* **118**, 714–716 (1971).

[89] Molten, G. M. Diffusionless phase transformations in zirconia and hafnia. *J. Am. Ceram. Soc.* **46**, 418–422 (1963).

[90] Kroeger, F. A. Electronic conductivity of calcia-stabilized zirconia. *J. Am. Ceram. Soc* **49**, 215–218 (1966).

[91] Aldebert, P. & Traverse, J.-P. Structure and ionic mobility of zirconia at high temperature. *J. Am. Ceram. Soc.* **68**, 34–40 (1985).

[92] Howard, C. J., Hill, R. J. & Reichert, B. E. Structures of $ZrO_2$ polymorphs at room temperature by high-resolution neutron powder diffraction. *Acta Cryst.* **B44**, 116–120 (1988).

[93] Yashima, M. *et al.* Oxygen-induced structural change of the tetragonal phase around the tetragonal–cubic phase boundary in $ZrO_2$–$YO_{1.5}$ solid solutions. *Acta Cryst.* **B50**, 663–672 (1994).

[94] Hanic, F., Hartmanová, M., Knab, G. G., Urusovskaya, A. A. & Bagdasarov, K. S. Real structure of undoped $Y_2O_3$ single crystals. *Acta Crystallogr. B: Struct. Sci* **40**, 76–82 (1984).

[95] Ishibashi, H., Shimomoto, K. & Nakahigashi, K. Electron density distribution and chemical bonding of $Ln_2O_3$ (Ln=Y, Tm, Yb) from powder X-ray diffraction data by maximum-entropy method. *J. Phys. Chem. Solids* **55**, 809–814 (1994).

[96] Douglass, D. L. & Wagner, C. The oxidation of oxygen-deficient zirconia and its relationship to the oxidation of zirconium. *J. Electrochem. Soc.* **113**, 671–676 (1966).

[97] Kofstad, P. & Ruzicka, D. J. On the defect structure of $ZrO_2$ and $HfO_2$. *J. Electrochem. Soc.* **110**, 181–184 (1963).

[98] Kumar, A., Rajdev, D. & Douglass, D. L. Effects of oxide defect structure on the electrical properties of $ZrO_2$. *J. Am. Ceram. Soc.* **55**, 439–445 (1972).

[99] Vest, R. W., Tallan, N. M. & Tripp, W. C. Zirconia: I, monoclinic phase. *J. Am. Ceram. Soc.* **47(12)**, 635–640 (1964).

[100] Valov, I. *Nitrogen doped zirconia (N-YSZ): preparation , characterization and electrode processes.* Ph.D. thesis, Justus-Liebig Universität Gießen (2006).

[101] Butler, E. P. *Microstructural-electrical property relationships in high-conductivity zirconia*, 572–584 (The American Ceramic Society, Columbus, Ohio, 1983).

[102] Butler, V., Catlow, C. & Fender, B. The defect structure of anion deficient $ZrO_2$. *Solid State Ionics* **5**, 539 – 542 (1981). Proceedings of the International Conference on Fast Ionic Transport in Solids.

[103] Nakamura, A. & J. Bruce Wagner, J. Defect structure, ionic conductivity, and diffusion in yttria stabilized zirconia and related oxide electrolytes with fluorite structure. *J. Electrochem. Soc.* **133**, 1542–1548 (1986).

[104] Manning, P. S., Sirman, J. D., Souza, R. A. D. & Kilner, J. A. The kinetics of oxygen transport in 9.5 mol crystal yttria stabilised zirconia. *Solid State Ionics* **100(1-2)**, 1–10 (1997).

[105] Janek, J. & Korte, C. Electrochemical blackening of yttria-stabilized zirconia - morphological instability of the moving reaction front. *Solid State Ionics* **116**, 181–195 (1999).

[106] Park, J.-H. & Blumenthal, R. N. Electronic transport in 8 mole percent $Y_2O_3$-$ZrO_2$. *J. Electrochem. Soc.* **136(19)**, 2867–2876 (1989).

[107] Peters, A. W. *Transporteigenschaften von mikro- / nanostrukturierten oxidischen Multischichten.* Ph.D. thesis, Justus-Liebig-Universität Gießen (2009).

[108] Maxwell, J. C. *A Treatise on Electricity and Magnetism, 2nd Ed.* (Claredon Press, Oxford, 1881).

[109] Hodge, I. M., Ingram, M. D. & West, A. R. Impedance and modulus spectroscopy of polycrystalline solid electrolytes. *J. Electroanal. Chem.* **74**, 125–143 (1976).

[110] Beekmans, N. M. & Heyne, L. Correlation between impedance, microstructure, and compositions of calcia-stabilized zirconia. *Electrochimica Acta* **21**, 303–310 (1976).

[111] van Dijk, T. & Burggraaf, A. J. Grain boundary effects on ionic conductivity in ceramic $Gd_xZr_{1-x}O_{2-(x/2)}$ solid solutions. *Physica Status Solidi (a)* **63**, 229–240 (1981).

[112] Näfe, H. Ionic conductivity of $ThO_2$- and $ZrO_2$-based electrolytes between 300 and 2000 K. *Solid State Ionics* **13**, 255–263 (1984).

[113] Macdonald, J. R. (ed.) *Impedance Spectroscopy* (John Wiley & Sons, 1987).

[114] Champion, J. A. The electrical conductivity of single-crystal alumina. *Brit. J. Appl. Phys.* **15**, 633–638 (1964).

[115] Brook, R. J., Yee, J. & Kröger, F. A. Electrochemical cells and electrical conduction of pure and doped $Al_2O_3$. *J. Am. Ceram. Soc.* **54**, 444–451 (1971).

[116] Ishimata, N., Miyata, T., Minato, J., Marumo, F. & Iwai, S. A structural investigation of $\alpha$-$Al_2O_3$ at 2170 K. *Acta Crystallogr. B: Struct. Sci* **36**, 228–230 (1980).

[117] Baufeld, B., Baither, D., Messerschmidt, U., Bartsch, M. & Merkel, I. *In Situ* study on the generation of radiation damage in cubic-zirconia in the high-voltage electron microscope. *J Am Ceram Soc* **76**, 3163–3166 (1993).

[118] Jin-Phillipp, N. Y. & Phillipp, F. Atomic structures of dislocations in $BaF_2/CaF_2$ strained multilayers. *Phil. Mag.* **84**, 3509–3516 (2004).

[119] Fischer, A. & Richter, H. Elastic misfit stress relaxation in heteroepitaxial SiGe/Si mesa structures. *Appl.Phys. Lett.* **61**, 2656–2658 (1992).

[120] Fischer, A., Kiihne, H., Roos, B. & Richter, H. Elastic strain relaxation in patterned heteroepitaxial structures. *Semicond. Sci. Technol.* **9**, 2195–2198 (1994).

[121] Spaepen, F. Interfaces and stresses in thin films. *Acta Mater.* **48**, 31–42 (2000).

[122] Rupp, J. L., Infortuna, A. & Gauckler, L. J. Microstrain and self-limited grain growth in nanocrystalline ceria ceramics. *Acta Mater.* **54**, 1721–1730 (2006).

[123] Heiroth, S., Lippert, T., Wokaun, A. & Döbeli, M. Microstructure and electrical conductivity of YSZ thin films prepared by pulsed laser deposition. *Appl. Phys. A: Materials Science and Processing* **93**, 639–643 (2008).

[124] Kilo, M. *et al.* Cation transport in yttria stabilized cubic zirconia: $^{96}$Zr tracer diffusion in $(Zr_xY_{1-x})O_{2-x/2}$ single crystals with $0.15 \leq x \leq 0.48$. *J. Eur. Ceram. Soc.* **20**, 2069–2077 (2000).

[125] Kilo, M. *et al.* Lanthanide transport in stabilized zirconias: Interrelation between ionic radius and diffusion coefficient. *J. Chem. Phys.* **121**, 5482–5487 (2004).

[126] Petzhold, A. & Ulbricht, J. *Aluminiumoxid: Rohstoff – Werkstoff – Werkstoffkomponente*, vol. I. (Deutscher Verlag der Grundstoffindustrie, Leipzig, 1991), I edn.

[127] Park, E. T. & Park, J.-H. Pressure effect on ionic conduction in yttrium-oxide-doped single crystal zirconium oxide. In *Proceedings of the 3rd International Meeting of Pacific Rim Ceramic Societies* (Kyungju, Korea, 1998).

[128] Kandil, H. M., Greiner, J. D. & Smith, J. F. Single-crystal elastic constants of yttria-stabilized zirconia in the range 20 °C to 700 °C. *J. Am. Ceram. Soc.* **67**, 341 – 346 (1984).

[129] Tracy, C. A. & Quinn, G. D. Fracture toughness by the surface crack in flexure (scf) method. In Logan, K. (ed.) *Ceramic Engineering and Science Proceedings*, vol. 15, 837–845 (American Ceramic Society, 1994).

[130] Ikuhara, Y., Thavorniti, P. & Sakuma, T. Solute segregation at grain boundaries in superplastic $SiO_2$-doped TZP. *Acta Mater.* **45**, 5275–5284 (1997).

[131] Guo, X. & Waser, R. Electrical properties of the grain boundaries of oxygen ion conductors: Acceptor-doped zirconia and ceria. *Prog. Mater Sci.* **51**, 151–210 (2006).

[132] Steil, M. C., Thevenot, F. & Kleitz, M. Densification of yttria-stabilized zirconia. *Journal of The Electrochemical Society* **144**, 390–398 (1997).

[133] Santos, A. P., Domingues, R. Z. & Kleitz, M. Grain boundary blocking effect in tetragonal yttria stabilized zirconia. *Journal of the European Ceramic Society* **18**, 1571 – 1578 (1998).

Ich erkläre: Ich habe die vorgelegte Dissertation selbständig und ohne unerlaubte fremde Hilfe und nur mit den Hilfen angefertigt, die ich in der Dissertation angegeben habe. Alle Textstellen, die wörtlich oder sinngemäß aus veröffentlichten Schriften entnommen sind, und alle Angaben, die auf mündlichen Auskünften beruhen, sind als solche kenntlich gemacht. Bei den von mir durchgeführten und in der Dissertation erwähnten Untersuchungen habe ich die Grundsätze guter wissenschaftlicher Praxis, wie sie in der „Satzung der Justus-Liebig-Universität Gießen zur Sicherung guter wissenschaftlicher Praxis“ niedergelegt sind, eingehalten.

Gießen, 12. April 2010

Nicole Schichtel